DYNAMIC FRACTURE TOUGHNESS OF FIBER REINFORCED CONCRETE

by

Vivek Srinivasan Bindiganavile

B.Tech., Institute of Technology, Banaras Hindu University, 1996

M.A.Sc., The University of British Columbia, 1998

A THESIS SUBMITTED IN PARTIAL FULFILLMENT OF
THE REQUIREMENTS FOR THE DEGREE OF
DOCTOR OF PHILOSOPHY

in

THE FACULTY OF GRADUATE STUDIES
(The Department of Civil Engineering)

We accept this thesis as conforming
to the required standard

THE UNIVERSITY OF BRITISH COLUMBIA

March, 2003

In presenting this thesis in partial fulfilment of the requirements for an advanced degree at the University of British Columbia, I agree that the Library shall make it freely available for reference and study. I further agree that permission for extensive copying of this thesis for scholarly purposes may be granted by the head of my department or by his or her representatives. It is understood that copying or publication of this thesis for financial gain shall not be allowed without my written permission.

Department of ___CIVIL ENGINEERING___

The University of British Columbia
Vancouver, Canada

Date ___20th March 2003.___

DE-6 (2/88)

Abstract

The technique of instrumented drop-weight impact testing is often adopted to perform impact tests on cement-based materials. However, to date, no uniformity in the testing methods exists, which makes it difficult to enable reasonable comparisons between data emerging from different laboratories. Test machines come with widely varying hammer-mass systems, different ranges of drop-heights and various release mechanisms. As the University of British Columbia houses three such machines yielding a wide range of impact possibilities, one of the objectives for this research was to conduct a parametric study of drop-weight impact testing to study the effect of drop-height and hammer mass on the impact response of plain concrete. It was found that the test machine significantly influences the apparent stress-rate sensitivity. For the same incident energy, a heavier mass simulates a flatter pulse (i.e. a slower impact rate) but a higher drop-height (or approach velocity) simulates a sharper pulse (and consequently, a higher rate of impact). It is established that drop-height is the most important and critical parameter for a comparison of data across machines. Any future standard for impact testing of cement-based materials should emphasize drop-height of impact and not the hammer mass.

Fiber reinforced concrete (FRC) is a heterogeneous material comprising of distinct components so that the mechanical properties of this composite are in effect, a sum of individual responses, which are affected by their mutual interactions. Many applications demand from FRC, an enhanced resistance to impact loading. Designing for impact involves understanding the impact response of each of the various phases within the material, viz. the concrete matrix, the fibers, and the fiber-matrix interface, the last one being the most critical component. Although plain concrete and, to a lesser extent, steel fiber reinforced concrete have been the subject of high stress-rate testing, limited data exists on the impact response of polymeric fiber reinforced concrete. Given that both the matrix (plain concrete) and the fibers (metallic or polymeric) depict widely varying

stress-rate sensitivities, it is a moot point as to how the resultant multi-phase material behaves under impact loading.

The properties of FRC were investigated at the level of a) the fiber-matrix interface, b) crack growth & bridging and c) as a structural material. To this end, over 300 single fiber pull-out tests, 60 crack growth tests and over 300 flexural tests were carried out. In this program, three drop-weight impact machines and an air-gun driven dynamic pull-out machine were utilized. For the first time, a drop-weight impact machine was configured to conduct fracture studies of Contoured Double Cantilevered FRC beams under impact loading. The thesis reports a complete dynamic analysis, which was performed to identify and account for the inertial effects during crack growth testing. The results reveal that inertial correction was significant in the case of plain and polypropylene fiber reinforced concrete but was negligible when steel fiber was used.

Pull-out of single-fibers reveal that bond stiffening occurred under impact. This was evident through higher peak loads and lower corresponding slip values. Polymeric fibers had higher slip values under static conditions, but under impact, their slip values approached that of steel fibers at all angles of orientation. This capacity of polymeric fibers to approach the behaviour of a higher modulus material such as steel was repeatedly evident in fracture tests as well as flexural tests. The flexural toughness of steel and polypropylene FRC converged at higher drop-heights.

Specimen size-effect on the impact response of FRC has not received adequate attention and hence forms a significant part of this study. The results indicate that, provided the self-weight is ignored, both plain and fiber reinforced concrete exhibit size-effects on their flexural strength under impact. However, the nature of this size-effect was not clear from the present work as the data appeared to fit conflicting empirical models as given by Bažant's Size Effect Law and by the Multifractal Scale Law. Under impact, the flexural toughness with both types of fibers demonstrated size effects, a phenomenon that was not seen during quasi-static tests. Size effect under impact also appeared to intensify with an increase in the drop-height for both plain and fiber reinforced concrete.

Table of Contents

List of Tables

List of Figures

xiv

List of Symbols

Chapter 4

$\ddot{u}_0(t)$.   Acceleration at the load-point at time t

F Normal reaction to wedge load

$F_v,$ Wedge load in a CDCB test under quasi-static and impact cases, respectively

$F_v(t)$

g Acceleration due to gravity

h Drop-height of hammer in a drop-weight machine

OL Opening load after resolution for a MODE I crack

V_f Fiber volume fraction

v_h Velocity of impacting hammer

α Angle of wedge

γ Coefficient of friction between the wedge and the CDCB specimen

Chapter 5

$u(x,t)$ Deflection at any point x, on the beam at a given time t

$u_0^b(t)$ Mid-span deflection of the beam at an instant t

$P_i(t)$ Generalized inertial load at a time t

$P_b(t)$ Generalized true bending load at a time t

$P_t(t)$ Generalized tup load at a time t

$\Delta E(t)$ Total energy lost by the hammer at time t

$E_m(t)$ Machine losses at time t

$E_{KEr}(t)$ Rotational kinetic energy of the beam at time t

$E_b(t)$ Bending energy at any time t

σ_n, σ_u Nominal strength under consideration according to BSEL and MFSL, respectively

f_u, f_t Nominal flexural strength according to BSEL and MFSL, respectively

β Brittleness number

ρ Mass density of the material of the beam

A Area of cross-section for the beam

B, d_0 Empirical curve-fitting parameters for BSEL

d Beam depth

G_f Fracture energy

l Clear span of the beam

l_{ch} Characteristic length arising empirically from MFSL

N Rate-sensitivity index

ov Symmetric over-hang for a simply supported, beam

x Distance along the length of the beam

Chapter 7

μ Poisson's ratio for the beam material

δ Deflection of the beam

D Depth of the beam

EI Flexural rigidity of the beam

l Clear span

P Applied quasi-static load

Chapter 8

Δ Deflection of the free-end of the cantilever

$\overset{*}{M}$ Generalized mass for a cantilever arm

$P_i(t)$ Generalized inertial load at a time t

$P_b(t)$	Generalized true bending load at a time t
$P_t(t)$	Generalized tup load at a time t
$z(t)$	Displacement history for a cantilever arm
$\dot{z}(t)$	Velocity history for a cantilever arm
$\ddot{z}(t)$	Acceleration history for a cantilever arm
$\psi(x)$	Shape function for the cantilever arm
$u(x,t)$	Transverse deflection at any point x, along the length of the beam at time t
$\mu(x)$	Mass distribution per unit length of the cantilever arm
W_0, W_L	Width of one arm of the CDCB at its narrowest and widest, respectively
ρ	Mass density of the material of the cantilever
$P_{iu}(t), P_{ic}(t)$	Inertial loads in the cantilever before and after cracking, respectively
a	Crack length for the DCB
a_{act}	Actual crack length
a_{eff}	Effective crack length
B, H	Width and height of one arm of a rectangular double cantilever beam
C	Compliance of a fracture specimen
$CMOD$	Crack mouth opening displacement
E	Elastic modulus for the material of the specimen
E_p	Numerical value of the initial tangent modulus as obtained from a fiber pull-out test
K_I	Mode I stress intensity factor
K_{IC}	Mode I Fracture toughness
L	Length of the cantilever arm
M	Mass of a cantilever arm
P	Opening load
x	Distance along the length of the beam

Acknowledgment

Chapter 1

INTRODUCTION

The need to understand the dynamic behaviour of cement-based composites at high rates of loading is of critical importance in applications such as airport runways, structures subjected to rock-bursts, accidental automobile impact and military installations required to withstand impact from missiles or projectiles. Under such dynamic conditions, the stress-rate dependence of the composite leads to a significantly different material behaviour from what is observed under quasi-static conditions. The extent of stress-rate dependence of the material's mechanical response (henceforth referred to as its stress-rate sensitivity) depends upon internal factors (such as its morphology) as well as external factors, such as the environment (moisture content, temperature etc.). Clearly, the design and assessment of structures prone to impulsive loading should not be based on their quasi-static evaluation.

Dynamic loading may arise due to a single cycle loading or a multi-cycle loading. Further, single cycle loading may be either a localized (single-point) impulse or a distributed impulse. It is the single-point impulsive loading that is henceforth referred to as "impact loading", which forms the subject of the present work.

While the stress-rate sensitivity of plain concrete has been the subject of active research for decades, plain concrete due to its inherent brittle nature is, for all practical purpose, incapable of carrying loads beyond the stage of crack initiation. The addition of short, randomly distributed fibers helps alleviate this problem. Little is known, unfortunately, of the dynamic response of cement-based materials reinforced with fibers. This is particularly true for polypropylene fibers, which present enormous potential not the least because of their light-weight, ease of handling and electromagnetic neutrality.

It was clear at the beginning of this program that several fundamental issues regarding our understanding of the impact resistance of fiber reinforced concrete (FRC) were yet to be resolved. These include the lack of a standard test method for characterizing the impact resistance of cement-based materials, our inability to correlate the fiber-matrix interaction under dynamic loading with the overall performance, and the understanding of the mechanisms, which govern the fracture processes in this material under impact. Equally limited is our understanding of dimensional similitude in cement-based materials under impact conditions.

Fiber reinforced concrete is composed of three distinct phases: the fiber, the cementitious matrix and the fiber-matrix interface. The material and geometry of the fiber, together with the properties of the matrix, produce a range of responses under quasi-static loading. Under impact loading, the stress-rate sensitivity of the individual phases adds a new dimension to the overall response of the composite. A comprehensive experimental program was undertaken here to characterize the role of steel and polypropylene fibers in imparting toughening capability to concrete under impact.

First of all, it was recognized that no standard test method exists to help characterize cement-based materials under impact. With three impact machines ("SMALL", "MEDIUM" and "LARGE"), conferring a wide range of capacity upon researchers at The University of British Columbia, at the very outset, this program envisaged the understanding of machine-specific parameters, which influence the observed response of the material under test. To this end, only plain concrete was employed as the subject of study in order to minimize the complexities arising from the test-material itself.

That all materials exhibit some degree of stress-rate sensitivity, is well known. Polymers are known to depict higher sensitivity than metals, but whether polymeric fibers lead to significantly better performance of the FRC under impact loading is yet to be ascertained. The present research program was designed in part to test this hypothesis. Both flexural and fracture mechanics-based assessments were made in order to discern any influence of the inherent stress-rate sensitivity of the fiber material itself.

In a composite, the interface between any two phases forms the weakest link and hence influences the overall response. In fiber reinforced concrete, the role of fibers is best understood through defining their interaction at the level of the fiber-matrix interface. In the case of steel fiber reinforced concrete, several studies have shown the correlation between the properties of the fiber-matrix bond and the flexural response of fiber reinforced concrete under quasi-static loading. However, no such correlation has been attempted under impact conditions. In this research program, significant emphasis was placed on understanding the fiber-matrix interface and its stress-rate sensitivity through bond-slip tests with steel and polypropylene fibers.

Since the primary role of fibers in a quasi-brittle composite such as fiber reinforced concrete lies in crack bridging, the capacity to bridge a fast moving crack under dynamic conditions plays a defining role in their capacity to enable post-elastic deformation. While loading-rate effect on the fracture of plain concrete has received considerable attention, relatively limited information exists on the role of fibers. A test method has been developed in this program to understand crack bridging under dynamic loading and the related dynamic analysis is described.

The effect of specimen size on the nominal strength of quasi-brittle materials has been extensively studied over the last couple of decades. However, the presence of a size-effect for concrete under impact conditions remains to be ascertained. In the same vein, the nature of this size-effect in the presence of fiber reinforcement is yet to be established. Consequently, in this research program, a significant series of tests was devoted to examining the influence of specimen size on the impact properties of both plain and fiber reinforced concrete. It was recognized that the outcome of this investigation of size-effects under impact will play an important role in the development of a standardized impact test method.

Due to advances in the related fields of chemistry, polymer science and metallurgy, a wide range of admixtures is available with the ability to suitably modify the rheology, the

morphology and the fracture toughness of concrete. Impact response of these ultra-high performance concretes is unfortunately not understood and it was therefore considered appropriate that the present program should address this issue. Accordingly, an ultra-high strength cementitious composite was investigated for its impact response, which was then compared with the performance of conventional FRC.

The primary aim of the present work is to create a data base of dynamic properties of FRC considering crack growth and bridging, both at the level of the fiber-matrix interface and at the level of a structural material involving engineering properties. It is expected that this data will be useful not only in modeling the constitutive response of FRC under impact, but also in developing design tools for structures subjected to frequent dynamic load events.

Chapter 2

SCOPE AND PRESENTATION

2.1   Problem Definition

Fiber reinforced concrete (FRC) as a building material witnesses various loading environments. The focus of this thesis is on the behaviour of FRC under short duration impulsive loads at stress rates in the range of 10^3-10^6 MPa/s. These high stress-rates correspond to loading that occurs during rock bursts, impulse from the under-carriage of aeroplanes, accidental vehicular impact etc. Although the behaviour of plain concrete at high strain-rates has been a subject of intensive study for decades, thus far, very limited research has been conducted on the impact response of FRC. Part of the problem is that even something as essential as a standardized test method for characterizing the impact performance of cement-based materials does not exist. As a result, there are many fundamental questions, which remain unanswered:

- What are the parameters, which affect the impact testing of FRC? Are there favourable test-machine and test-specimen attributes? What features must a future test-standard entail?

- How does the behaviour of FRC differ from that of plain concrete? What role do fibers play and what if any, are the effects of fiber type on the composite behaviour?

- How do fibers affect the crack-bridging processes and crack growth in a cement-based matrix under impact loading?

This thesis addresses the above related issues. It was recognized that the study of fiber reinforced concrete involves the simultaneous understanding of three related area: 1) bond-slip interaction between the fiber and the matrix, 2) crack growth and arrest mechanisms during fiber bridging, and 3) engineering properties. Accordingly, all three aspects of the impact response of FRC are systematically investigated in the following Chapters.

5

2.2   Presentation

FRC is composed of two distinct elements namely, the fiber and the surrounding plain concrete matrix. Understanding the dynamic response of this material will stem from a clear understanding of its constituents; Figure 2.1 describes the approach followed in the course of this study towards characterizing the impact response of FRC.

($\longrightarrow$ quasi-static, ---------- impact)
a_{act} = actual crack; a_{eff} = effective crack; fbz = fiber bridging zone; COD = Crack Opening Displacement
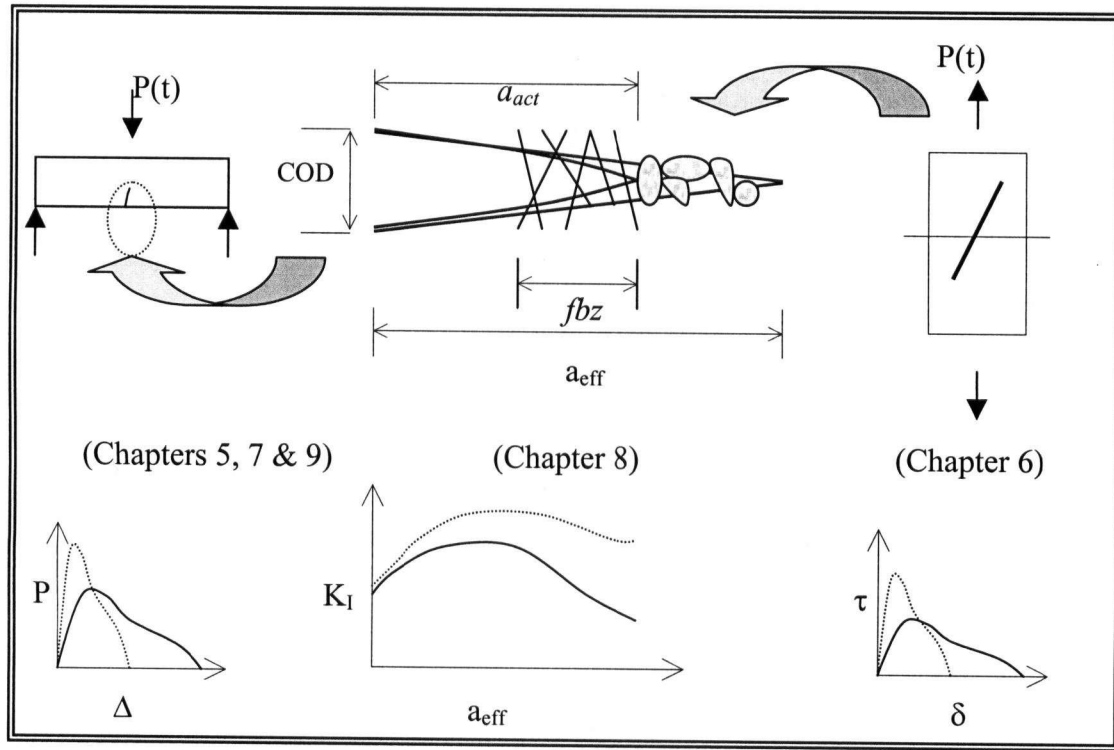
Figure 2.1   Schematic of the Research Program

The thesis is divided into 10 Chapters. Chapter 1 introduces the subject of this investigation while Chapter 2 offers the thesis outline. Chapter 3 presents an overview of the existing knowledge and the available data. The experimental set-up and the methods employed during the course of this study are described in Chapter 4. In this Chapter, particular emphasis is placed on the impact machines, which were designed and developed at The University of British Columbia. In addition, this Chapter describes their specifications, the associated instrumentation, the materials employed and the overall testing program.

6

Chapter 5 presents the results of parametric studies including machine and specimen related effects during the impact loading of plain concrete. Chapter 6 addresses the bond-slip response of a single fiber embedded in plain concrete matrix during impact loading. Both fiber material and fiber geometry are investigated. The impact response of FRC as a unified composite is presented in Chapter 7. Issues such as the type of fiber reinforcement, loading rate and the specimen size are treated at length. Some thoughts are offered on how results of Chapters 5, 6 and 7 may be used to develop a standardized test procedure for testing and characterization of the impact response of fiber reinforced concrete.

The role of fibers in improving the crack growth resistance of FRC forms the subject of Chapter 8. For this purpose, a new test configuration was developed using a Contoured Double Cantilever Beam specimen. The impact behaviour of an ultra-high performance cement composite is examined in Chapter 9 and some comparisons are made with the impact response of conventional FRC. Chapter 10 summarizes the results and conclusions inferred from this thesis. Finally, Chapter 11 offers a list of issues that remain unresolved, which it is hoped, will form the basis of future work in this area.

Chapter 3

LITERATURE REVIEW

3.1 Introduction

Concrete, in its many forms and compositions, is one of the most important materials used by man. Since the invention in 1824 of what is now termed "Portland Cement", the composite material made of sand, stone and cement, has become together with steel, the basis of modern construction. In this Chapter, the state-of-the-art on the material science of concrete is presented with special emphasis on its response to dynamic loading. This is followed by a detailed survey of literature dealing with the stress-rate sensitivity of the various phases that constitute fiber reinforced cementitious composites.

3.2 Fiber Reinforced Concrete

Fiber reinforced concrete is defined as "concrete containing short, discrete fibers randomly distributed in the matrix". In the modern age, the earliest example is of asbestos fibers, which were used to reinforce cement sheets at volume fractions of about 10 %. Later, glass fibers were employed in the USSR in the 1950s. Development of fiber reinforced cement-composites occurred in North America only in the 1960s. Today, a wide range of fiber types are used by the construction industry, among them: steel, polymers, carbon, glass and natural (cellulose) fibers.

The world-wide consumption of fibers as concrete reinforcement stood at 140,000 metric tons annually in 1998, and is growing at a rate of 5% per annum [1]. Most of this is used for slabs-on-grade (65 %), followed by shotcrete (25 %), and the remaining in pre-cast products and other sundry applications. While it is recognized that fiber reinforced concrete is not a substitute for conventional rebar-reinforced concrete, it is clear that due to the random distribution and discrete nature, several distinct advantages exist: 1) fibers provide shear reinforcement, 2) they improve the compressive toughness of concrete, 3) they reduce spalling (useful in the case of impact or blast loading), 4) control shrinkage

cracking, 5) micro-fibers modify fresh shotcrete rheology to reduce rebound. As a result of these attributes, fiber reinforced concrete/shotcrete has gained increasing popularity in the non-structural sector for concrete products.

3.3 Short Fibers for Discontinuous Reinforcement of Concrete

Bentur and Mindess [2], Balaguru and Shah [3] and Banthia [4] provide a detailed reference of all discrete fibers in use till early 1990's including steel, polypropylene, aramids, glass, carbon and cellulose-based fibers. Since then great strides have been made especially with macro polymeric fibers and the quasi-static performance of the most recent ones are given by Trottier and Mahoney [5]. New steel fibers are listed in Banthia and Armelin [6] and Naaman and Sujivorakul [7].

3.4 Impact Response of Building Materials

High loading-rates occur in a wide range of construction operations including military and strategic structures, shotcrete lining subjected to rock-bursting, aircraft landing-tarmacs, crash resistant structures in the transport industry, etc. In all such cases, the mechanical response of a material is generally observed to be different from its behaviour under normal (lower) loading rates. Typical strain rates occurring in various dynamic events are summarized in Table 3.1 [8].

Table 3.1   Typical Strain-Rates for Various Types of Loading [8]

Type of loading	Strain-rate (s^{-1})
Traffic	10^{-6}-10^{-4}
Gas explosions	5×10^{-5}-5×10^{-4}
Earthquake	5×10^{-3}-5×10^{-1}
Pile driving	10^{-2}-10^{0}
Aircraft impact	5×10^{-2}-2×10^{0}
Hard impact	10^{0}-5×10^{1}
Hypervelocity impact	10^{2}-10^{6}

3.4.1 Test Methods

A number of different methods have been used to measure the impact response of materials. The simplest and the most commonly employed is the drop-weight impact machine [9]. In this technique, a mass is raised to a pre-determined height and then dropped on a specimen. In the un-instrumented version of this test, the number of drops required to effect a prescribed level of damage is counted and used as a measure of the amount of energy absorbed by the specimen to reach this level of damage. Clearly, such a measurement is only an estimate (and a crude one at that) and no information on the load-time history is obtained. Nor is there any idea of the deformation history for the specimen.

An instrumented drop-weight impact machine [10], developed initially for metals, provides much more information than the simple drop-weight machine described above. It can be used to obtain reliable time histories of such parameters as load, acceleration and deflection. Potential energy of a hammer mass is converted to kinetic energy of impact by raising the hammer mass. The level of applied energy may be varied by means of raising or lowering the drop-height of the mass. Such machines were used in the research presented in this thesis (Figures 4.7, 4.11 & 4.13 in Chapter 4).

Another version of the instrumented drop-weight impact machine is the pendulum machine where, unlike with the version described above, the mass is not dropped vertically but is allowed to swing, which renders it a modified version of the Charpy impact testing device shown in Figure 3.1. When instrumented, this machine is equally capable of measuring the impact load, support reactions and the inertial loads.
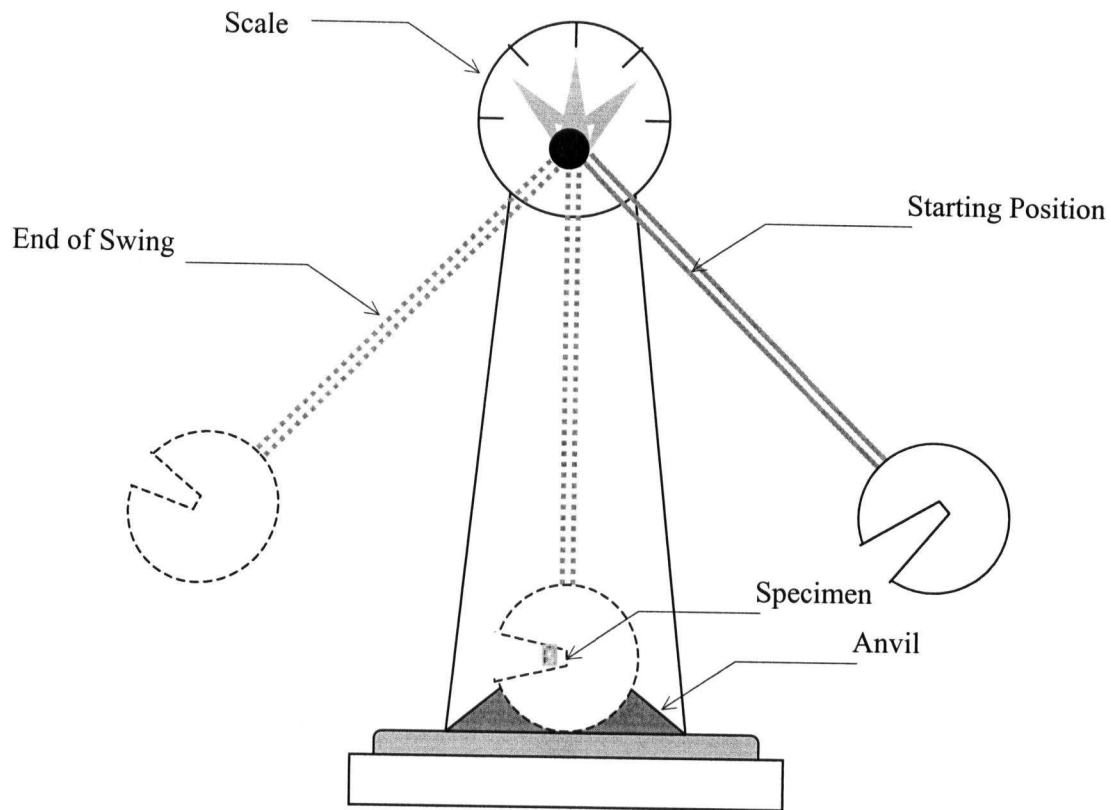
Figure 3.1   Schematic View of the Pendulum Impact Tester

Another widely used test for evaluating material response to very high strain rates (~ 10^3/s) is the Split Hopkinson Pressure Bar (SHPB) shown schematically in Figure 3.2. Developed originally by Kolsky [12], these machines are able to provide information on the duration of the event, maximum stress associated with the impact, strain-rate sensitivity, damage propagation and failure mechanisms. A typical machine consists of three major parts: the striking "tup", the incident (input) bar and the transmitted (output) bar. The driving force could be a spring mechanism or a gas-gun. Upon impact, the compression pulse from the striking bar travels along the incident bar to the specimen. When the pulse reaches the specimen, a part of it is absorbed by the specimen and a part of it is transmitted to the output bar even as a part of it is reflected back to the incident bar. All pulses are recorded and analyzed. The SHPB method is highly versatile and can be used to produce various loading configurations including compression, tension and shear.
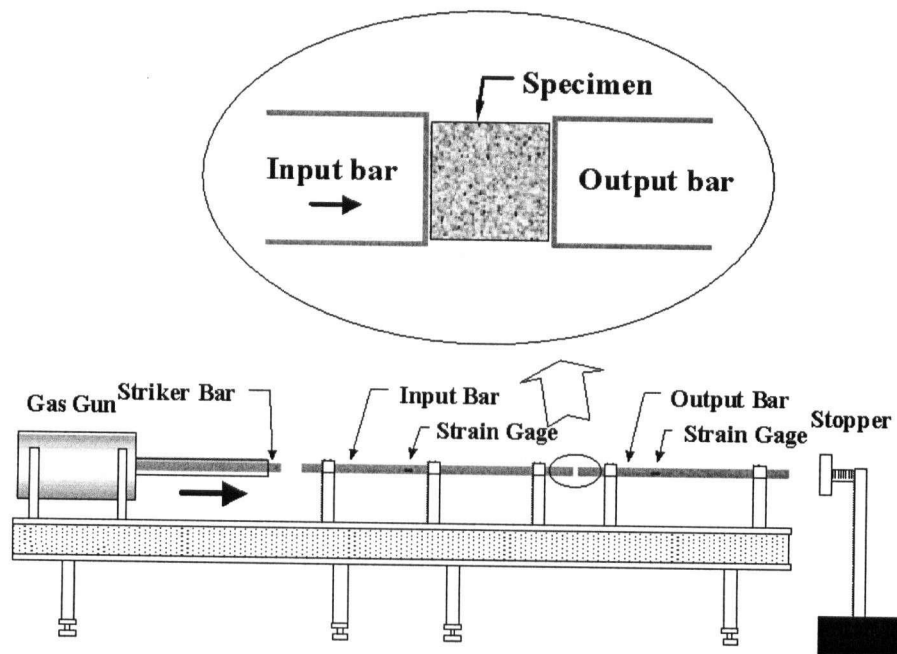
Figure 3.2   Schematic View of the Split Hopkinson Pressure Bar [11]

Although the SHPB technique generates high strain-rates and provides a large amount of information, certain limitations must be recognized. For example, the specimen length and diameter must be kept as small as possible to ensure a uniform stress distribution. The effect of friction between the end surface of the specimen and the incident bar is quite high. Perhaps the most strident criticism is the fact that the load-histories and the deflection histories are not obtained from the same device. This means that the load-deflection plot is obtained by comparing the two separate time histories and there exists the possibility of a lag between these histories, which makes it difficult to have full confidence in the analysis.

A separate class of impact testing is devoted to ballistics. In these tests, a projectile is launched at a target and the areas of interest include damage to both the projectile and the

target. Typically, these tests involve penetration or perforation of the localized target region on the one hand and scabbing to the projectile on the other. Clearly, this class of tests focuses on the localized and/or structural nature of impact and not on the constitutive response of the material. Hence it is outside the purview of the present work.

3.4.2 Plain Concrete

The macroscopic properties of concrete are known to depend upon the applied strain rate. Among the various loading configurations, while both compressive strength [13,14] and tensile strength [15] are strain-rate dependent, often the tensile strength shows a more pronounced dependence [16]. Sensitivity in the flexural mode is seen to be somewhere between those of the compressive and tensile modes [17].

There are several factors that affect the apparent strain-rate sensitivity of plain concrete. Higher quasi-static strength is seen to lead to a drop in strain-rate sensitivity [18]. Strain-rate sensitivity is also known to be influenced by the moisture content, humidity and temperature. Fully saturated concrete is expected to be more strain-rate sensitive than dry concrete. Recent work [19] suggests a link between the degree of saturation of the nano-pores (≤ 30 Å) and the strength enhancement observed at higher loading rates. According to this view, the moisture in the gel pores is thought to lead to microscopic viscous forces within the saturated nano-pores such that only concretes with saturated nano-pores exhibit dynamic strength enhancement. However, Banthia *et al.* [20] did not witness any significant change (drop) in the stress-rate sensitivity at sub-zero temperatures (- 50 °C), even though the moisture in the pores would have frozen by then.

Stress-rate sensitivity of concrete is also believed to be related to the increase in crack velocity that occurs under high stress-rate loading. Ross [13] suggests that lower strength concretes attain lower limiting crack velocities, thereby reducing crack growth and allowing for higher strengths to develop. However, much lower velocities than those theoretically predicted have been observed for concrete under impact [21,22] and are believed to be the result of the crack branching and bridging mechanisms prevalent in the microstructure.

3.4.2.1 Inertial Effects

The dynamic nature of impact testing means that a component of the applied load is utilized in accelerating the specimen and this rigid-body motion of the concrete specimen does not contribute to the material stresses. However, it is a part of the measured load, which if not identified, leads to an erroneous assessment of the impact properties of the specimen. The load that is utilized in overcoming inertia is called inertial load and it depends upon the relation between the rapidity of the loading and the lowest natural frequency of the test-specimen. Chen and Sih [23] suggest that if the time required to increase the magnitude of the applied load from zero to its maximum value is less than half the natural period of the specimen, then the formation of stress waves due to the inertial effect should be considered in the analytical treatment.

The inertial load was considered for the first time by Cotterell [24] in 1962 for tests on metallic specimens. Without excluding the inertial load, Hibbert reported a 10-15 fold increase in the tensile strength of concrete [25]. However, Suaris and Shah [26] pointed out that the specimens in Hibbert's tests failed within the first oscillation during which the inertial component was a maximum, thereby yielding an incorrect and overestimated strength. Server and his associates [27,28] postulated that for a reliable measurement of impact response, the load should be measured only after three oscillations of the specimen. However, this is clearly not applicable to the case of quasi-brittle materials like concrete, which tend to fail within the first oscillation itself.

Gopalaratnam and Shah [29] used a rubber pad to minimize the inertial component. However, in the process, the rubber pad also reduces significantly the loading rate, by absorbing large amounts of energy, which must therefore be considered in the analysis. A second approach is that suggested by Banthia et al. [30] for flexural testing and involves the direct measurement of accelerations. By mounting three accelerometers along the length of the test-beam, the acceleration distribution could be determined to obtain a distributed inertial load. This was later generalized to a point inertial load acting at the center of the beam, using the principle of virtual work. The true stressing load was then obtained by subtracting the inertial response from the recorded response. This concept

wide acceptance since, and is the one employed in this research program. As seen in Chapter 8, this method was also employed to obtain the true stressing load in the case of a relatively complex geometry of a Contoured Double Cantilevered Beam specimen.

3.4.3   Steel

There is clear experimental evidence that most metals and alloys exhibit some increase in strength with increasing strain-rate, although the degree of strain-rate sensitivity is decidedly lower than for either ceramics or polymers. The greatest strain-rate sensitivity is usually found in metals of body-centered-cubic (bcc) structure [31]. Figure 3.3 shows tensile stress-strain curves for bcc mild steel under strain rates varying from quasi-static ($\sim 10^{-3}$/s) to impact (~ 2000/s) using the tensile version of SHPB [32]. Over this range of strain rates, the lower yield stress is almost doubled, the ultimate tensile stress increases by about 50 % and there is a marked increase in the upper yield stress. The process of alloying results in a reduced strain-rate sensitivity of the flow-stress. This is shown in Figure 3.4 for a quenched and tempered alloy steel. As with high-strength concrete, alloys generally increase the quasi-static strength of the base metal but reduce its sensitivity to strain-rate. Three different regions may be identified from the behaviour of steel with increasing strain-rates as shown in Figure 3.5: Region I, corresponding to rate-independent response ; Region II, where a linear dependence of flow-stress prevails, and Region III, with a rapid increase in rate-sensitivity.
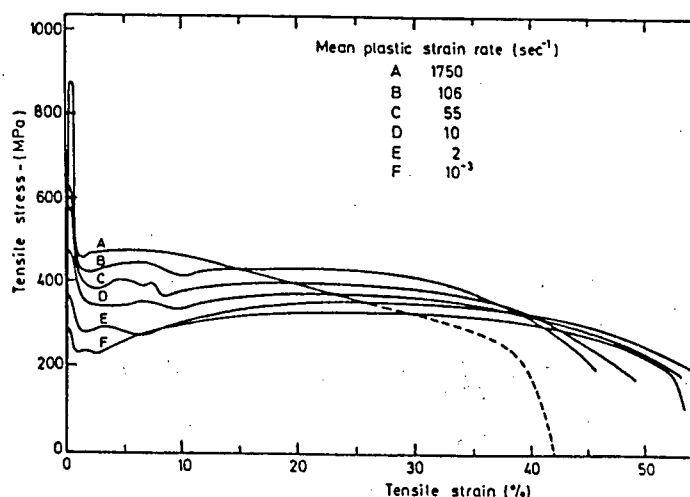
Figure 3.3   Mild Steel under Tensile Loading [32]
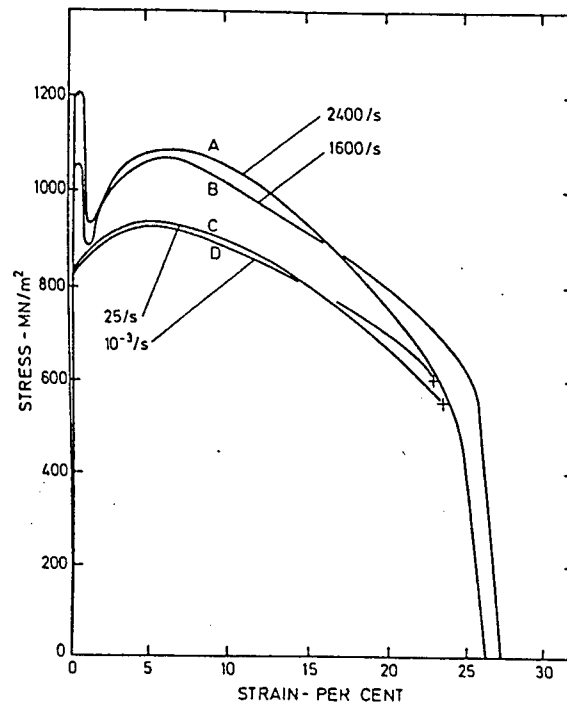
Figure 3.4   Strain-Rate Dependence of Quenched and Tempered Alloy Steel [33]
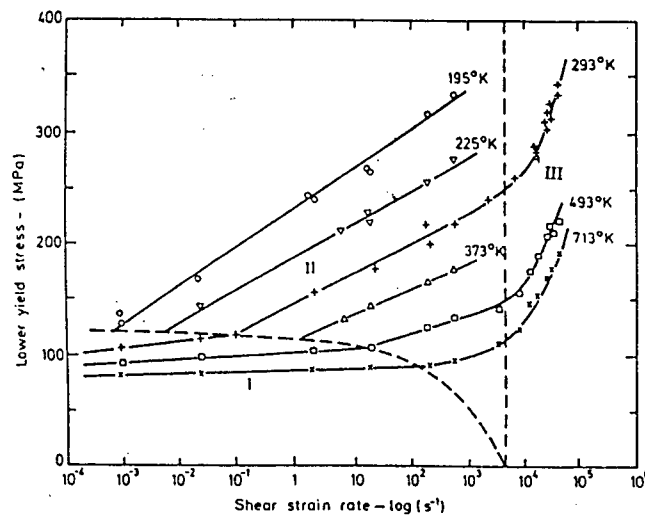
Figure 3.5   Strain-Rate Dependence of Flow-Stress of Annealed Mild Steel [31]

16

While there is no data on the rate sensitivity of steel fibers, Malvar [34] presents a review of the rate-effects on the mechanical properties of rebars. Without going into the post-yield behaviour of steel under high strain-rates, Malvar proposed an expression for the "Dynamic Impact Factor" (DIF) for both yield stress and ultimate stress:

$$DIF = \left(\frac{\dot{\varepsilon}}{10^{-4}}\right)^{\alpha} \qquad \qquad ...(3.1)$$

where, for yield stress,

$$\alpha = \alpha_{fy} = 0.074 - 0.04\frac{f_y}{60} \qquad \qquad ...(3.2)$$

and for ultimate stress,

$$\alpha = \alpha_{fu} = 0.019 - 0.009\frac{f_y}{60} \qquad \qquad ...(3.3)$$

The formulation above fails to capture the rate-sensitivity beyond a strain-rate of $3s^{-1}$. It suggests a relatively modest (20 %) increase in the DIF under impact conditions.

3.4.4 Polypropylene

Strictly speaking, viscoelastic materials like polypropylene have no well-defined and unique linear elastic regime; never-the-less one may operationally define an "elastic modulus" from the direct compression data to characterize the effects of strain-rate and temperature on material stiffness. Figures 3.6 a, b and c present the strain-rate sensitive compressive response for polypropylene under three different ambient temperatures of 20 °C, 65 °C and 110 °C, respectively [35]. Notice from Figure 3.6a that at room-temperature, a 300 % increase in the flow-stress occurs at very high strain-rates ($\sim 10^2$/s).
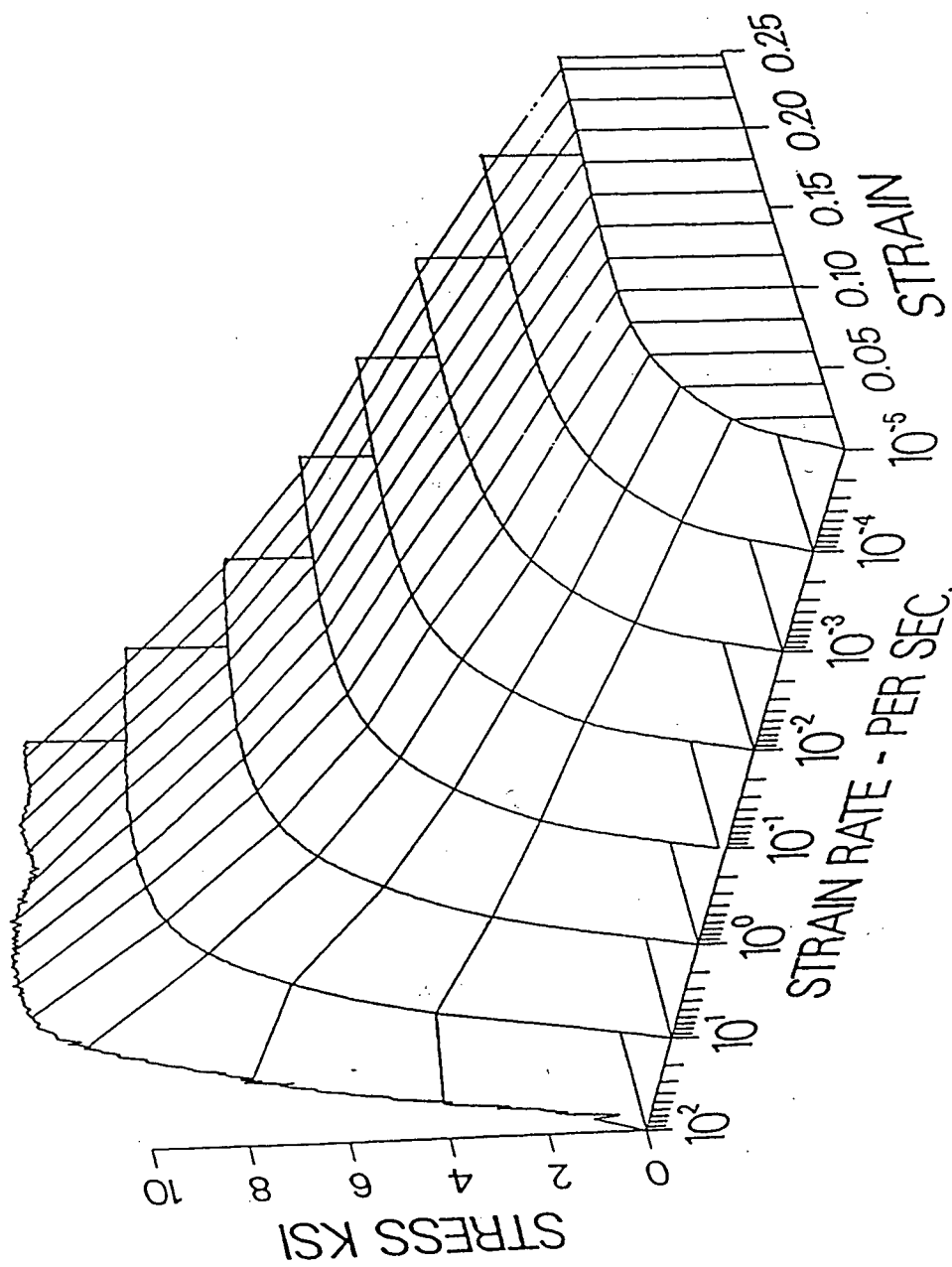
Figure 3.6a   Static and Dynamic Behaviour of Polypropylene in Direct Compression (20° C) [35]

18
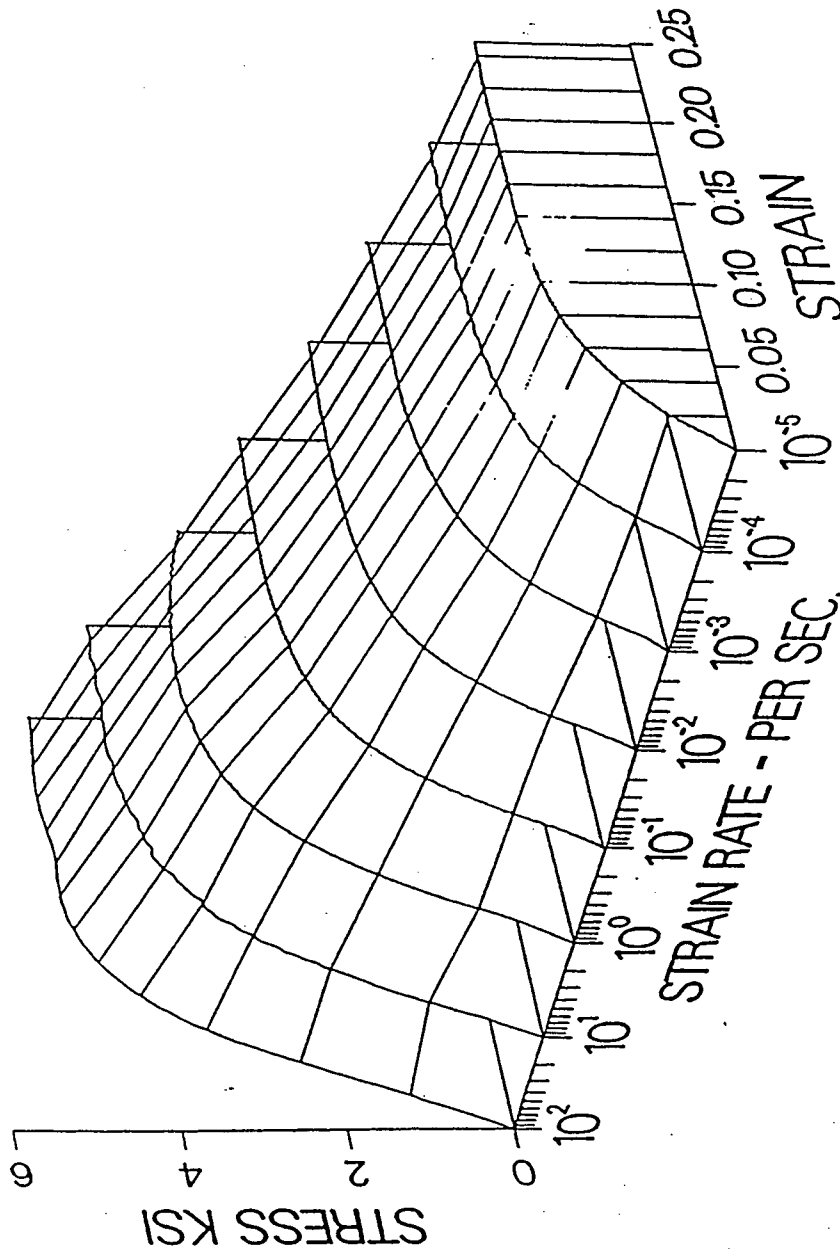
Figure 3.6b   Static and Dynamic Behaviour of Polypropylene in Direct Compression (65° C) [35]
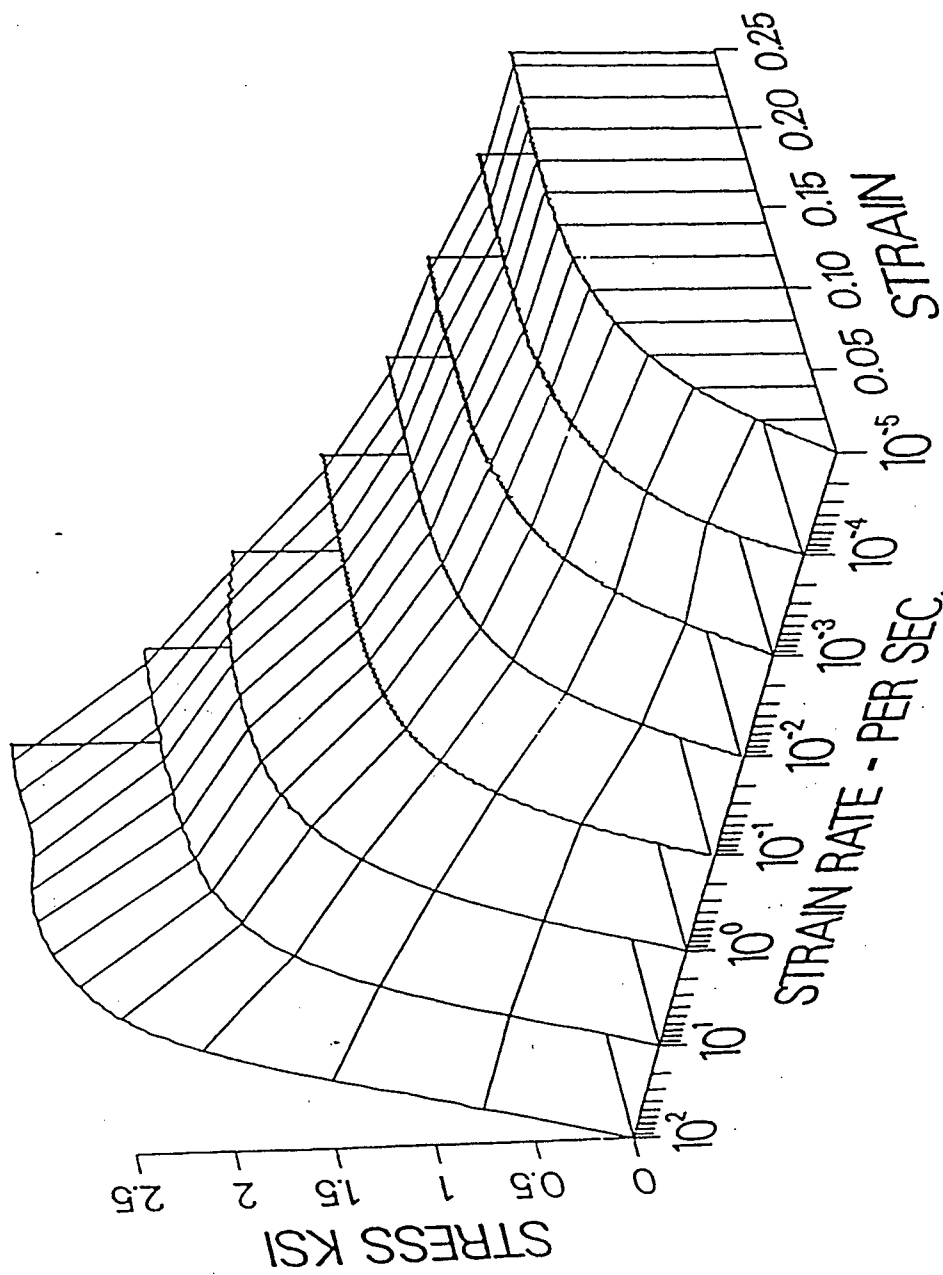
Figure 3.6c   Static and Dynamic Behaviour of Polypropylene in Direct Compression (110° C) [35]

It is reported that the degree of crystallinity bears a strong influence on the impact behaviour of polypropylene. In industrial practice, the final properties of polypropylene are a result of nucleating agents added in the course of production. Consequently, several changes occur in the crystallinity and spherulite levels. Impact properties of polypropylene have been observed to depend on these two factors [36-38]. Lower degree of crystallinity leads to lower strengths but a higher stress-rate sensitivity (similar to the effect of strength on the rate sensitivity of concrete). A higher degree of crystallinity promotes superior impact strength regardless of spherulite size. Similarly, smaller spherulites reportedly favour higher impact strength at all levels of crystallinity. However, a detailed account of the effect of manufacturing process and morphology on the impact response of polypropylene, although important is beyond the scope of this thesis.

One aspect peculiar to polymers is the phenomenon of "glass-transition". It implies that upon increasing the temperature beyond 0 °K, one reaches a certain temperature above which the hitherto amorphous and brittle polymer transforms into a soft and flexible solid, or an elastomer, or even a very viscous liquid. With specific reference to polypropylene, which is highly crystalline, its glass-transition temperature (T_g) is -10 °C. However, it has been noted that this point on the temperature scale is highly sensitive to the applied strain-rate. That is to say, strain-rate sensitivity in polymers is closely associated with T_g.

3.5 Bond-Slip Response of Fibers from a Cementitious Matrix

In a cement-based composite subjected to flexural or tensile loading, the matrix is always the first to fail by cracking. Fibers are intended to transmit stresses across these matrix cracks and preserve the load-transmitting capacity of the composite. The resistance of the cracked section to further crack opening depends largely on the bond-slip characteristics of the bridging fibers and a number of possibilities ranging from complete fiber pull-out to fiber fracture exist, which in turn affect the energy dissipation. Bartos [39] presented an excellent review on bond-slip data till the 1980's. More recently, Bentur et al. [40] offer an updated review of the fiber-matrix interaction. While some believe there is no

21

correlation between a single-fiber pull-out test and the behaviour of the composite [41,42], never-the-less, as demonstrated by Banthia and Trottier [43,44], steel fibers exhibit remarkable correlation at least qualitatively, between bond-slip and composite responses. Of late, bond-slip studies have been used as a tool to develop new geometries of fibers, optimized for their particular application [6,7,45,46].

3.5.1 Quasi-Static Response

Pull-out characteristics of steel [47-49] and (more recently) polymeric fibers [50] have been studied as a function of several variables including fiber orientation [51], matrix strength [52,53], geometry [43], surface properties [54,55] and ambient temperature [56].

The micromechanics of fiber pull-out from a relatively brittle matrix was first explained by Cox [57]. Since then, several investigators have described the pull-out response of steel fibers from a cementitious matrix using either the stress-based approach [58,59] or by using fracture mechanics [60-62]. Recently, Dubey [63] applied shear lag theory to describe the pull-out behaviour of polypropylene macro-fiber. The application of the finite element method has led to some recent modeling by Mallikarjuna et al. [64] and Li and Mobasher [65].

One of the main concerns for polypropylene fibers is its inherent hydrophobic nature that prevents the development of an adequate bond with the hydrating cement paste. In order to enhance the chemical bond between the fiber and cementitious matrix, Tu et al. [66] modified the surface chemistry of polypropylene fibers through oxyfluorination. They reported nearly 300 % increase in the interfacial bond strength of the modified fiber. However, this increase in the bond-strength was not accompanied by a commensurate increase in the bond-modulus, which means that its performance in a FRC composite at small crack openings would remain largely unchanged, in spite of oxyfluorination.

3.5.2 Impact Response

The available data concerning the rate-effects on the fiber-matrix interface is very limited. The emphasis has largely been on the quasi-static pull-out response. A study of the dynamic bond-slip response of polymeric macro-fibers has never been carried out. Table 3.2 summarizes the existing information. There is a considerable scatter in the results and a clear understanding of the mechanisms which affect the rate-sensitivity of the fiber-matrix bond, does not exist. For example, while Gokoz and Naaman [67] and Banthia and Trottier [68] found the pull-out behaviour of straight steel fibers to be rate-insensitive, Gray and Johnston [69] and Pacios et al[1]. [71] reported otherwise. Further more, Pacios et al. observed an increase in the slip-at-peak load at higher slip rates, a view not shared by others. Unlike the case of static loading, the relevance of the fiber-matrix bond-slip response to the composite performance under impact has never been investigated.

Table 3.2   Fiber Pull-Out Results under Dynamic Loading

Reference	Crack Opening Rate (mm/s)	Fiber Type	Fiber Orientation	Approx. Dynamic/Static Pull-Out Resistance
Gokoz and Naaman [66]	4.23×10^{-2}-3000	Steel, Glass and Fibrillated Polypropylene	Aligned	5 for Polypropylene Fiber
Kaadi [69]	10^{-4}-10^{-1}	Steel, Glass and Fibrillated Polypropylene	Random 3D	2 for Polypropylene Fiber
Gray and Johnston [68]	0.035-1.44	Steel	Aligned	1.3
Banthia and Trottier [67]	0.008-1500	Hooked-End Steel Fibers	Aligned	4.6
Pacios et al. [70]	0.13-500	Straight Steel Fiber	Aligned fibers	4-6 times

Provided the fiber failure mode is maintained as pull-out, Banthia and Trottier [67] cited that the energy absorbed is seen to increase at higher slip rates; a view not shared by Gokoz and Naaman [66]. However, the former also found a pull-out to fracture transition

---

[1] In the study by Pacios et al., the fiber embedment length was not equal in both halves of the matrix. The longer half was deformed to ensure pull-out from the undeformed side of the fiber.

in the failure mode in high strength matrices. Gokoz and Naaman also found that glass fibers were relatively insensitive to slip-rate. Similarly, carbon fibers are also thought to be rate-insensitive due to their inherent brittle behaviour [31].

3.6   Impact Response of Fiber Reinforced Concrete

In concrete reinforced with polymeric or metallic fibers, the sensitivity of the metals and polymers themselves and that of the fiber-matrix bond tend to make the response of these composites very much a function of the applied stress-rate. Impact tests on SFRC were conducted by Suaris and Shah [26], Gopalaratnam and Shah [72] and Li et al. [73]. Under impact, the peak load in flexure was about 40 % higher than that for plain concrete. The fracture energy increase for SFRC was about 2.5 times for normal strength FRC and about 3.5 times for high strength FRC. It was also found that the improvements in toughness due to steel fibers were much less pronounced under impact than those under quasi-static loading. This is believed to be due to the higher number of fibers fracturing instead of pulling-out, during impact loading [74]. While there is considerable experimental data for the high stress-rate response of steel fiber reinforced concrete (SFRC), tests on the impact response of concrete reinforced with other fibers is limited. Bhargava and Rehnstrom [75] found that polypropylene fiber reinforced concrete showed 15% higher impact strength than plain concrete. Gupta et al.[76] found that polypropylene and PVA fibers, although not as efficient as steel fibers, do improve significantly the toughness of shotcrete. For both fiber types, the toughness enhancement was strongly dependent on their geometry, indicating a need for optimizing the geometrical features of fibers.

3.7   From Behaviour of a Single Fiber to the Flexural Toughness of the Composite

Chanvillard [77] proposed a method to predict the flexural performance of FRC by conducting tensile tests and determining the uni-axial stress-strain behaviour. Jenq and Shah [78,79] applied fracture mechanics at the fiber-matrix interface to predict the flexural response of FRC. Armelin and Banthia [80] provide a model to predict flexural behaviour of SFRC from the bond-slip response of a single steel fiber. This is shown in
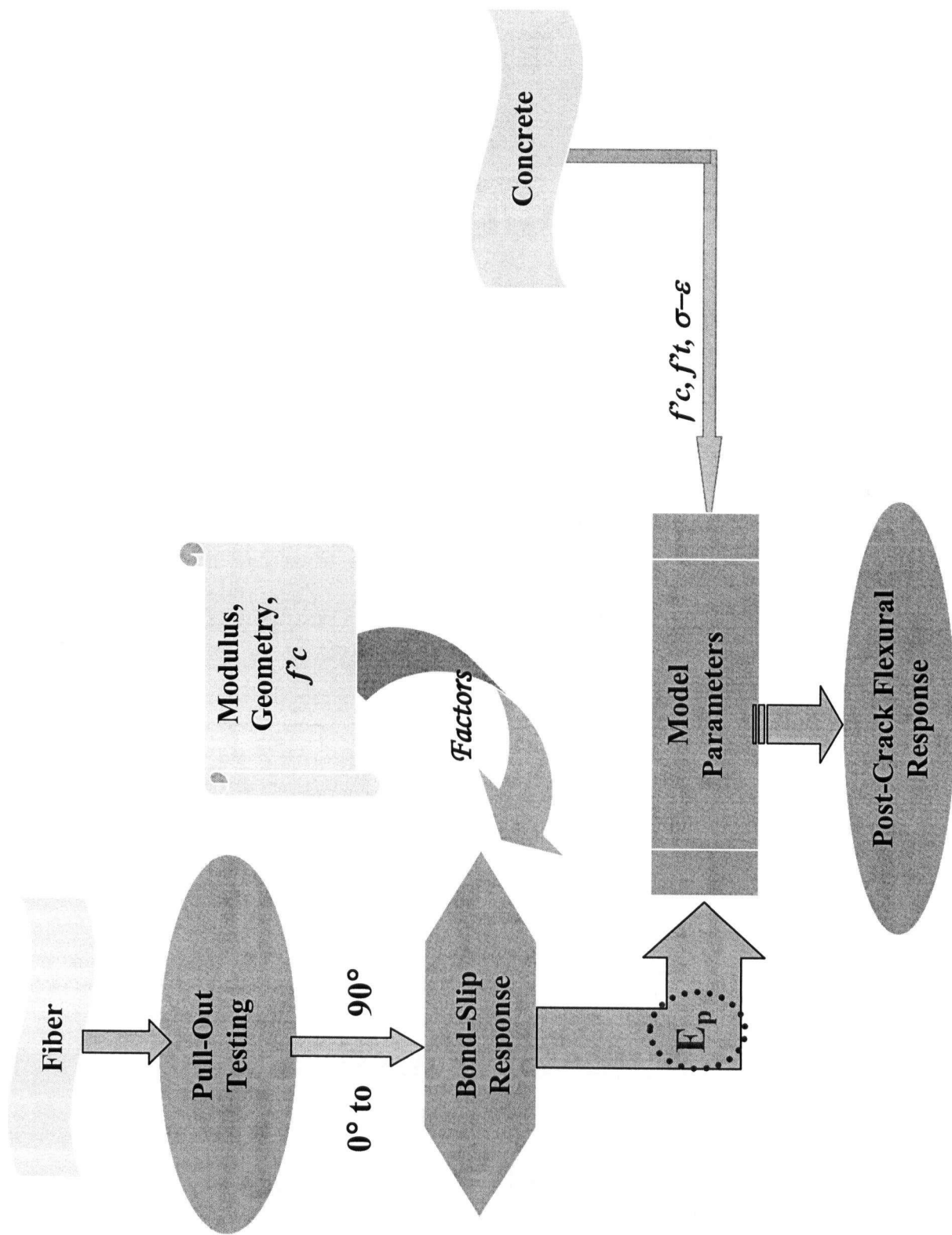
Figure 3.7 Flow-Chart to Describe the Generation of the Flexural Response from the Single-Fiber Pull-Out Data

Figure 3.7 through a flow-chart indicating the progress from single-fiber pull-out tests to the determination of flexural toughness of FRC. Their method captures the effect of fiber geometry, orientation, embedment length, fiber dosage and the matrix strength.

3.8   Fracture Mechanics of Concrete

The stress-strain response of concrete, as shown in Figure 3.8 [81], is highly non-linear due to the development of micro-cracks at the interfaces between aggregates and HCP and progressive cracking that occurs as the load increases. In spite of this, a linear-elastic behaviour is often assumed in the literature due to the simplicity of this approach and the availability of analytical solutions for elastic-brittle materials. Such methods use concepts of the stress-intensity factor K_I, for linear-elastic modeling.
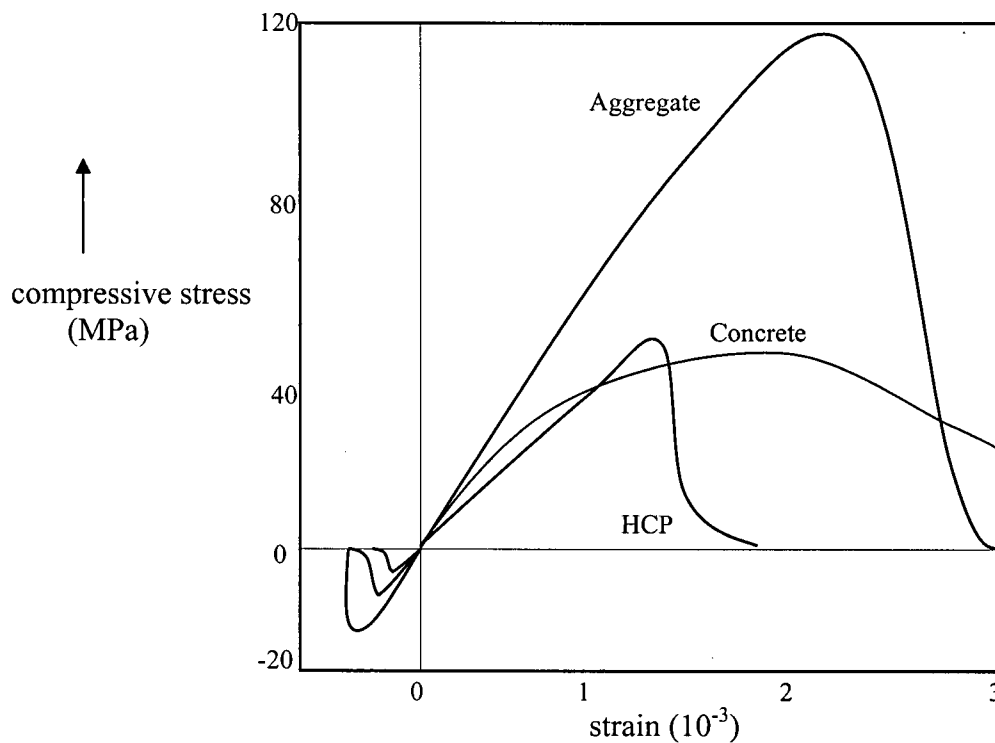
Figure 3.8   Stress-Strain Diagram of HCP, Aggregate and Concrete [81]

For the LEFM model, the distribution of stresses in front of a crack tip may be expressed as follows [82]:

26

$$\sigma_{ij} = \frac{C_1}{\sqrt{r}} f_{1ij}(\theta) + \sum_{n=2}^{\infty} C_n r^{\frac{n-1}{2}} f_{nij}(\theta) \qquad \ldots (3.4)$$

where r and θ are polar co-ordinates about the crack tip; C_i's are constants and $C_1 = K/\sqrt{(2\pi)}$; K being the stress intensity factor, which depends upon the applied load, the crack length and the shape of the specimen. K is usually expressed as:

$$K = Y\sigma\sqrt{a} \qquad \ldots (3.5)$$

where, σ is the nominal stress and Y is the finite width correction factor related to the specimen geometry and depends upon W/a; W and a being the width and crack length, respectively, in the specimen.

In the non-linear fracture mechanics (NLFM) approaches, cohesive crack models and effective crack models have been proposed. As an example of the former, Hillerborg *et al.* [83] proposed a discrete crack approach for the finite element analysis of fracture in concrete — a model often known as the "fictitious crack model" (FCM). The brittleness of the material is measured using a quantity called the characteristic length l_{ch} defined as:

$$l_{ch} = \frac{EG_f}{f_t^2} \qquad \ldots (3.6)$$

where, E is the Young's modulus in tension, f_t is the tensile strength and G_f is the fracture energy. The crack band model (CBM) of Bažant [84] is similar to the FCM except that the crack is assumed to be distributed over a region and not as a single well-defined line-crack. The effective crack models prescribe an equivalence between the actual crack and a geometrically identical elastic structure (the effective crack) using LEFM. R-curve models [85,86], the Two Parameter Fracture Model (TPFM) [78,79] and Bažant's Size Effect Law (BSEL) [87], are all extensions of this approach.

3.9 Dynamic Fracture Mechanics of Concrete

Dynamic fracture mechanics is the subfield of fracture mechanics concerned with fracture phenomena for which the role of material inertia becomes significant. Inertial effects may arise either from rapidly applied loading on a cracked solid or from rapid crack propagation. Research on crack growth under impact in the field of FRC is in its infancy with much of the work limited to plain concrete [88-90] and SFRC [91-93].

Mindess *et al.* [21] observed the crack velocities to be much lower (~ one tenth) than the theoretically predicted Rayleigh speeds and cracks further slowed down in the presence of steel fibers resulting in speeds in the range of 75 – 115 m/s. Similar values were reported by Kobayashi and his associates [94-96] for plain concrete. Banthia [17] and Sukontasukkul *et al.* [93] reported an increase in the dynamic fracture toughness K_{ID} with an increase in the hammer drop-height. No data is available for polypropylene macro-fibers.

Camacho and Ortiz [97] have noted that, when inertia is accounted for, cohesive crack model introduces a "characteristic time", which may be expressed as:

$$t_c = \frac{\rho c \delta_c}{2 f_{ts}} \qquad \qquad ...(3.7)$$

where, ρ is the mass-density, c is the longitudinal wave speed and δ_c is the critical crack opening displacement. It follows that owing to this intrinsic time scale, the material behaves differently under different loading rates. Hence, this sensitivity to the rate of loading is believed to confer upon cohesive crack models the ability to capture the stress-rate sensitivity of the mechanical response in brittle solids, such as propagation speeds, the dependence of fracture pattern and that of the dynamic strength on the stress-rate [98].

3.10 Empirical Models for the Rate-Dependence of Concrete

Experimental data is seen to obey the following general formulation for the dynamic increase in compressive strength [99]:

$$DIF = A + B\dot{\sigma} + C \log \dot{\sigma} \qquad \qquad ...(3.8)$$

Evans [100] suggested that the velocity of a moving crack (V) is related to its stress intensity factor (K_I) as:

$$V = AK_I^N \qquad \qquad ...(3.9)$$

Using this relation, Nadeau $et\ al.$ [101] obtained the dependence of strength on the loading rate by the following logarithmic expression:

$$\ln \sigma_c = \frac{1}{N+1} \ln B\dot{\sigma} + \frac{1}{N+1} \ln\left(\sigma_i^{N-2} - \sigma_f^{N-2}\right) \qquad \qquad ...(3.10)$$

where, B and N are constants. A plot of strength versus the stress-rate therefore, yields a slope of $[1/(1+N)]$. However, experiments reveal N to be itself dependent on stress-rate and on variables such as the material strength and the ambient temperature.

Reinhardt offers a model [102] which captures the rate-sensitivity of concrete over the entire range of strain-rates. Zielinski [103] proposed an empirical relationship between tensile strength and stress-rate based on the results with SHPB:

$$\ln \frac{f}{f_0} = A + B \ln \frac{\dot{\sigma}}{\dot{\sigma}_0} \qquad \qquad ...(3.11)$$

where, f and f_0 are impact and static strength, respectively, while $\dot{\sigma}$ and $\dot{\sigma}_0$ are the impact and static stress-rates, respectively.

Körmelling [104] obtained a relationship between strength and stress-rates in the case of tensile and flexural strengths as follows:

Tensile strength $\qquad \varphi_z = \left(\frac{\dot{\sigma}}{\dot{\sigma}_{st}}\right)^{0.043} \qquad \qquad ...(3.12)$

where, $\dot{\sigma}$ and $\dot{\sigma}_{st}$ are the impact and quasi-static stress rates, respectively and φ_z = dynamic increasing factor (DIF).

Comite Euro-International du Beton (CEB) suggests that in tension, the dynamic increase factor (DIF) is given by [8]:

$$
\left.
\begin{array}{l}
DIF = \left(\dfrac{\dot{\varepsilon}}{\dot{\varepsilon}_s}\right)^{1.016\delta} \quad for \dot{\varepsilon} \leq 30 s^{-1} \\[4ex]
DIF = \beta \left(\dfrac{\dot{\varepsilon}}{\dot{\varepsilon}_s}\right)^{\frac{1}{3}} \quad for \dot{\varepsilon} > 30 s^{-1}
\end{array}
\right\}
\qquad ...(3.13)
$$

where, $\dot{\varepsilon}$ and $\dot{\varepsilon}_s$ are the impact and quasi-static strain-rates, respectively and

$$\log \beta = 7.11\delta - 2.33;$$

$$\delta = \cfrac{1}{\left(10 + 6\dfrac{f_c'}{f_{co}'}\right)} \quad ; \qquad f_{co}' = 10 \text{ MPa.}$$

Asserting that the CEB recommendation under-estimates the DIF at strain-rates lower than 30 s⁻¹, Malvar and Ross [105] proposed the following modified expressions:

$$
\left.
\begin{array}{l}
DIF = \left(\dfrac{\dot{\varepsilon}}{\dot{\varepsilon}_s}\right)^{\delta} \quad for \dot{\varepsilon} \leq 1 s^{-1} \\[4ex]
DIF = \beta \left(\dfrac{\dot{\varepsilon}}{\dot{\varepsilon}_s}\right)^{\frac{1}{3}} \quad for \dot{\varepsilon} > 1 s^{-1}
\end{array}
\right\}
\qquad ...(3.14)
$$

where, $\dot{\varepsilon}_s = 10^{-6} s^{-1}$; $\log \beta = 6\delta - 2$;

and
$$\delta = \frac{1}{1 + 8\dfrac{f_c'}{f_{co}'}}$$
...(3.15)

with all other notations being the same as in the CEB recommendation.

Sercombe *et al.* [19] explain the rate-sensitivity of concrete through the viscous effects within the nano-pores. They propose the following constitutive relation:

$$\sigma = E\left(\varepsilon - \varepsilon^p - \frac{x}{\sqrt{3}}\right)$$
...(3.16)

where, ε and ε^p are the total strain and plastic strain respectively and,

$$E = E^{dyn}{}_{\infty},$$

where $E^{dyn}{}_{\infty}$ is defined as the modulus obtained from the highest possible loading rate in the experimental series. Further, x is a function representing the evolution of viscosity and is given by:

$$\eta \dot{x} = \frac{|\sigma|}{\sqrt{3}} - kx$$
...(3.17)

where, η and k are the viscosity and rigidity associated with the viscous evolution. They are to be determined experimentally.

3.11   Size-Effect

Griffith's energy based approach leads to a severe size effect given by the LEFM formulation:

$$\sigma_{N_{u\infty}} = \frac{K_{IC}}{k(\alpha_0)} D^{-\frac{1}{2}}$$
...(3.18)

where $\sigma_{Nu\infty}$ is the nominal stress at infinite size, K_{IC} is the fracture toughness of the material at given size D and $k(\alpha_0)$ is a dimensionless shape-dependent function

influenced only by the crack-to-depth ratio α_0 at initial state. Early investigations into the size-effect in concrete are due to Walsh [106] and Wright [107]. Leicester [108] appears to have been the first to model size-effects in quasi-brittle materials such as concrete and proposed a size-effect less severe than that predicted by LEFM:

$$\sigma_{N_{u\infty}} = \frac{A}{D^s} \qquad \qquad ...(3.19)$$

where, A is a constant and s is an exponent that depends upon the shape and size of the crack (or notch).

A recent review by Bažant and Chen [109] identifies several authors who have conducted various types of tests and developed theories to demonstrate and model the size-effect for large scale specimens. They identified the following basic theories of scaling in solid mechanics:

a) Statistical Size-Effect Law (SSEL)

The earliest description on the size-effect in brittle materials is based on the statistical theory of the weakest link concept proposed by Weibull [110]. Fracture is assumed to occur when the stress intensity factor at one of the flaws reaches the fracture toughness. Provided that the fracture is initiated at a single flaw (the critical flaw), the size-effect as predicted by this theory is solely dependent on the distribution of initial (pre-existing) flaws [111]. Therefore the mean strength of a smaller brittle specimen is greater than that of a larger but geometrically similar specimen simply because there is a greater probability for the existence of a critical flaw in the larger specimen. In its simplified form, failure stress, σ_N and dimension, D are related exponentially as:

$$\sigma_N \propto D^{-n/m} \qquad \qquad ...(3.20)$$

where, 'n' describes the number of dimensions and 'm' is called the Weibull modulus.

b) Bažant's Size Effect Law (BSEL)

This is based on the theory of stress redistribution and fracture energy release for large cracks. It may be stated as follows: "For concrete as a material, the size effect is intermediate between the linear elastic fracture mechanics, for which it is much too

strong and, the plastic limit analysis, for which it is absent". Bažant proposed the size effect model [87] using non-linear fracture mechanics. It is expressed as:

$$\sigma_n = Bf_u(1+d/d_0)^{-\frac{1}{2}} \qquad \qquad ...(3.21)$$

where, σ_n = nominal strength under consideration, d = characteristic dimension, and Bf_u & d_0 are the empirical parameters of the model. The ratio $d/d_0 = \beta$ is known as the brittleness number and is a measure of the structural brittleness of the material. When the size is very small ($\beta \ll 1$), the behaviour is governed by the yield criterion implying a plastic behaviour. On the other hand, for large sizes ($\beta \gg 1$), the behaviour is described by LEFM.

c) Multifractal Scale Law (MFSL)

Carpinteri and his associates [112,113] have proposed that the difference in fractal characteristics of the fracture surfaces and/or micro-crack distributions at different scales of observation is the principal source of size effect in concrete. The following equation is proposed to explain the size effect phenomenon:

$$\sigma_u(b) = f_t[1+l_h/b]^{\frac{1}{2}} \qquad \qquad ...(3.22)$$

where, f_t is the nominal tensile strength and l_{ch} is a characteristic dimension, which emerges as an empirical constant from the curve-fitting exercise.

It is important to note that both MFSL and SSEL are in complete accordance. The analogies may be summarized as follows [113]:

1. Both approaches predict an asymptotic nominal strength for large sizes.
2. In both cases, the size-effect models when plotted in the bi-logrithmic plane (ln σ_N vs. ln d), are non-linear with an upward concavity.

(Note that BSEL predicts a non-linear behaviour with *downward* concavity as seen in Figure 3.9)

Recently, Arslan and Ince [114] have indicated that neural-network modeling of concrete reveals a behaviour which would support the contention of both BSEL and MFSL, through a smooth transition between the two over the entire range of sizes.
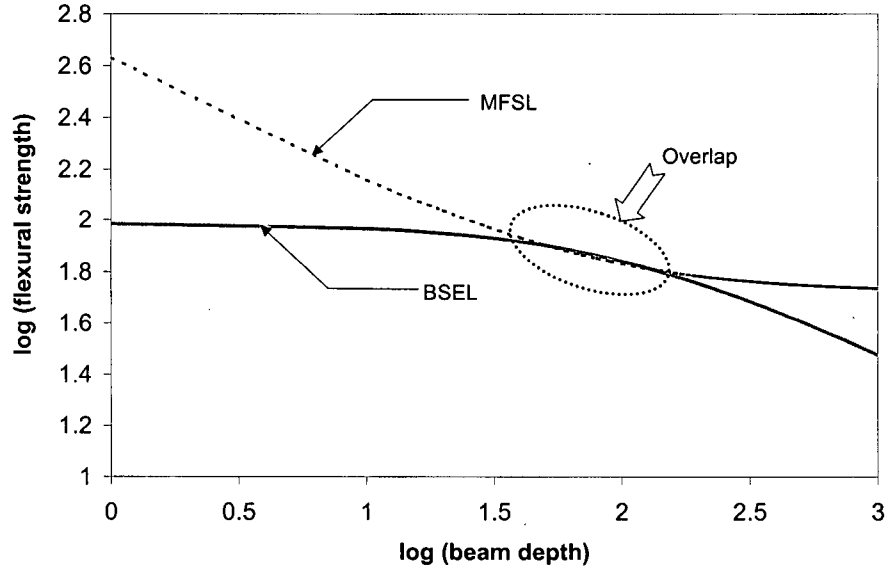
Figure 3.9   Some Scaling Laws to Describe Material Behaviour

Karihaloo's Size Effect Equation (KSEE)

Apart from the theories listed above, another approach is due to Karihaloo [115], who presented a higher-order asymptotic analysis of the size-effect in notched beams of concrete and similar quasi-brittle materials. He concluded that there is a lower bound of the specimen size below which it is not possible to determine the nominal strength. This lower bound is so large that, at least for concrete, it renders the existing size-effect laws and models meaningless. According to this view, the nominal strength for a specimen of size D, 'σ_{Nu}' is given by:

$$\frac{\sigma_{N_u}}{\sigma_{N_{u\infty}}} = \left[1 - \frac{1}{2} \frac{g'(\alpha_0)}{g(\alpha_0)} \frac{l_{p\infty}}{D} \right] \qquad \qquad ...(3.23)$$

where, $l_{p\infty}$ = size of the cohesive zone at peak load for an infinitely large specimen; $g'(\alpha_0)$ is the first derivative of the function $g(\alpha)$ at $\alpha = \alpha_0$, which is the initial crack-to-depth

ratio. Here, the nominal strength at infinite size, $\sigma_{Nu\infty}$ is given by the LEFM prediction so that,

$$\sigma_{N_{u\infty}} = \frac{K_{IC}}{k(\alpha_0)} D^{-\frac{1}{2}} \qquad \qquad ...(3.24)$$

The function $g(\alpha) = [k(\alpha)]^2$ and is introduced as a matter of convenience.

Planas *et al.* [116] critically reviewed KSEE and suggested that the predicted nominal strength deviates from other solutions (e.g. due to BSEL) with decreasing values of D. Accordingly, they state that using KSEE for small sizes does not give realistic results.

3.11.1 Quasi-Static Rates

The size-effect on the nominal strength and fracture toughness of plain concrete is well documented. Bažant and Prat [117] report an increase in the brittleness at higher temperatures. Studies by Şener [118] and Gettu *et al.* [119] show that for higher strength concrete, the size-effect appears to shift towards the LEFM predictions and thus indicates a higher brittleness. Bažant and Pfieffer [120] observed mortar to be closer to LEFM behaviour than plain concrete indicating the widely held view that concrete is less brittle that mortar. Contradictory to BSEL prediction, Perdikaris and Romeo [121] found an increase in the fracture energy with higher specimen size. This is in keeping with MFSL as shown by Carpinteri and Chiaia [112]. Mindess [122] reported that while values for both fracture energy and K_{IC} of concrete in flexure increase with an increase in the beam size, upon considering the self-weight of the specimens, no significant size-effect could be noticed.

Li *et al.* [123] studied the influence of fiber bridging on size-effects and concluded that fibers reduce the structural size effect in concrete. They related the severity of the size-effect to the characteristic length of the material, which in the case of FRC is vastly improved due to crack bridging. Similarly, Chen [124] found no significant size-effect on the flexural toughness of FRC.

3.11.2 Very Slow Rates

According to Bažant and Gettu [125], under creep rates, there is an increase in the brittleness with an increase in the time-to-peak-load. Wittmann [126] suggests that the higher brittleness arises out of a smaller fracture process zone or the localization of the energy dissipation within a smaller area at the crack tip. Under creep, the relaxation of stresses leads to a lower stress concentration at the crack tip and therefore a smaller process zone is expected.

3.11.3 Impact Loading

To the author's knowledge, a study on the size-effects in concrete or FRC under impact has never been carried out. However, data exists on the response of FRP composites under impact. Morton [127] proposed that to enable scaling for a rate-sensitive CFRP material, the time-to-peak-load (t_p) should be the same across all sizes. From tests on FRP composites, Qian et al. [128], indicated that the extent of damage depends on scale and is consistent with the predictions of fracture mechanics. Liu et al. [129] demonstrated that for laminated GFRP composite plates, the size effects arising from the plate-thickness was substantially more significant than the in-plane dimensional effect. This observation has significance in the construction industry when dealing with repairs and retro-fitting, which involve bonding and layering issues.

3.12 Ultra-high strength cement-based composites

Two directions of research have evolved in the quest for high-performance concrete. The first approach concerns compact granular matrix concrete also called DSP (Densified System containing ultra-fine Particles) and the other relates to polymer mortars mixed with aluminous cements [130]. The discussion here is focussed entirely on the DSP derivatives.

Ultra-high strength cement-composites owe their origin primarily to the development of superplasticizers. These types of concrete are being created for applications to structures designed for a 100-year design life. Typical structures include large concrete bridges exposed to severe environment and oil-drilling platforms. This type of concrete

incorporates large quantities of silica fume, high dosages of superplasticizers, low water/binder ratios and a significant amount of fibers. They may be definitely termed as "engineered materials" given that the entire mix is proportioned to achieve satisfactory grading, suitable rheology and adequate mechanical properties. To this end, the mix is usually blended with multiple mineral admixtures of various fineness moduli, hybridized fibers and the entire production process requires strict quality control.

3.12.1 Reactive Powder Concrete (RPC)

In the early 1990's, an ultra-high performance, cement-based composite with high ductility was developed by the Scientific Division of BOUYGUES, (France) through the application of certain basic principles of composition, mixing and post-set heat curing. These are:

- Enhancement of homogeneity by the elimination of coarse aggregates;
- Enhancement of compacted density and optimization of the granular mixture through pressure curing, both before and during setting;
- Enhancement of the microstructure through post-set heat treatment;
- Enhancement in the ductility by incorporating small-sized steel fibers;

Over the years, the following characteristics have been recognized to produce RPC:

a) The Portland cement must not have any C_3A and possess a minimum specific surface area of 340 m^2/kg;

b) Silica fume should be white and free from unburnt carbon;

c) Mean particle size of silica fume should be less than 0.7 μm.

Due to the increased fineness and the sustained reactivity of the dry components, this material has been called Reactive Powder Concrete (RPC). Two specific genres were developed: RPC 200, which is designed for $f'_c \geq 150$ MPa and RPC 800, which is designed for $f'_c \geq 600$ MPa. Table 3.3 summarizes the essential differences between the two types of RPC.

37

Table 3.3   Material Properties of RPC [130]

Parameter	RPC 200	RPC 800
Pre-setting Pressurization	None	10-50 MPa
Heat Treatment	20-90 °C	250-400 °C
Compressive Strength	170-230 MPa	500-800 MPa
Flexural Strength	30-60 MPa	45-140 MPa
Fracture Energy	20,000-40,000 J/m^2	1,200-20,000 J/m^2
Young's Modulus	50-60 GPa	65-75 GPa

3.12.2 Compact Reinforced Composite (CRC)

CRC is the designation for a special type of ultra-high strength fiber reinforced composite. The material incorporates large volumes of steel fibers (~6%), making it very ductile. It is a thixotropic material and even at 6 % fiber content, satisfactory slump (> 200 mm) has been reported [131]. The mechanical properties are summarized in Table 3.4. Use of densely packed, strong aggregates is believed to reduce the brittleness [132] (by increasing the characteristic length, 'EG_f/f_t^2'). This is because there is less binder in the system, and both the modulus of elasticity 'E' and the fracture energy 'G_f' are high. Such a mix has very fine mean pore size and is ideally suited for short discrete fiber reinforcement.

Table 3.4   Properties of CRC [131]

Steel Fiber Content (% Volume fraction)	2	4	6
Compressive Strength	125 MPa	135 MPa	140 MPa
Flexural Strength	16 MPa	20 MPa	25 MPa
Uniaxial Tensile Strength	6 MPa	10 MPa	14 MPa
Splitting Strength	10 MPa	15 MPa	20 MPa
Shear Strength	6 MPa	9 MPa	12 MPa
Young's Modulus	42 GPa	44 GPa	46 MPa

While both RPC and CRC are examples of ultra-high strength DSP composites, there are some essential differences between them:

- RPC is made with CSA Type 50 (ASTM Type 5) cement, while for CRC, a White Portland Cement is preferred.

- Production of RPC involves curing at elevated temperatures, which may or may not be accompanied by pressure, applied to aid in the hydration process. The need for high-temperature curing is also driven by the presence of white silica fume, which may retard the strength gain.

- Due to its higher quality control requirement, RPC is typically recommended for pre-cast applications. On the other hand, CRC may be used for in-situ applications, especially as a grout for assembling pre-cast members on site.

- CRC is typically made with up to 6% steel fiber reinforcement. RPC on the other hand may contain about 2-3% steel fibers. However, for higher grades of RPC, steel balls may be used as aggregate.

3.12.3 Impact Response of High Strength Concrete

Our understanding of the impact resistance of high strength concrete, is very limited. There are also contradictory results in the literature. For example, while Ross [13] and Bentur *et al.* [18] reported a reduced sensitivity to stress-rate with an increase in the static strength of concrete, Bischoff and Perry [133] reported otherwise.

In the case of ultra high strength concrete such as CRC, the data is still more scarce. Of the very few available studies, Lee *et al* [134] demonstrated the superior resistance of Reactive Powder Concrete (RPC, f'_c in the range of 180-400 MPa) over normal and conventional high strength concrete under projectile impact. Some tests performed in Sweden on CRC [135], have demonstrated a superior resistance of CRC to impact over traditional types of fiber reinforced concrete.

In closure, on the basis of the literature survey presented here, the following general statements may be made:

1. A systematic understanding of the dynamic bond-slip response of fibers bonded in cement-based matrices does not exist. Existing results can even be contradictory. Further more, there is no data on the bond-slip response under impact loading for polypropylene fibers.

2. No data exists on specimen size-effects in plain or fiber reinforced concrete under impact loading.

3. Stress-rate sensitivity of fracture in fiber reinforced concrete has not been understood. Very little is known about the crack growth phenomena in FRC under impact loading.

Chapter 4

EXPERIMENTAL DETAILS

4.1 Introduction

Tests on plain and fiber reinforced concrete (FRC) were conducted in this research program. The specimens ranged in shapes and sizes depending upon the parameter under investigation. The impact testing was conducted using instrumented drop-weight impact machines with various capacities and an air-pressure driven pull-out machine, — all of which were designed and built in-house. For the quasi-static tests, commercially available materials testing systems were employed. This Chapter describes the raw materials, the specimens, the testing equipment (including their configuration) and the test-program.

4.2 Materials and Mixes

4.2.1 Plain Concrete

Three different matrices were investigated with compressive strength ranging from 40 to 190 MPa. Normal strength concrete (NSC) refers to a mix as per Table 4.1 which was designed to yield a target 28-day compressive strength of 40 MPa. High strength concrete (HSC) was prepared with the proportions and properties shown in Table 4.1 for a target 28-day compressive strength of 80 MPa. The mix details for ultra-high-strength composite ($f_c > 150$ MPa) are provided in Chapter 9. For the NSC and HSC mixes, CSA Type 10 cement was used together with concrete-river-sand and 3/8" coarse aggregate (gradation as shown in Table 4.2). Silica fume and a third generation superplasticizer (GLENIUM 3000) were included as admixtures to produce the high strength mix. GLENIUM 3000 is an example of a carboxylated synthetic polymer. The carboxyl group being a relatively weak acid, is fully ionized only in an alkaline environment such as prevails in the hydrating cement paste.

Table 4.1   Mix Composition of Various Grades of Concrete

Mix	Constituent	Detail	Proportion (kg/m³)
NSC $f'_c = 40$ MPa	Cement	CSA Type 10 (ASTM Type 1)	440
	Sand	Fineness Modulus = 2.55	880
	Stone	Mean size = 10 mm	880
	Water	-	198
HSC $f'_c = 80$ MPa	Cement	CSA Type 10 (ASTM Type 1)	440
	Silica Fume	-	44
	Sand	Fineness Modulus = 2.55	880
	Stone	Mean size = 10 mm	880
	Water	-	146
	Superplasticizer	Glenium 3000	2.90

Table 4.2   Sieve Analysis of Coarse and Fine Aggregate

Sieves	ϕ (mm)	Coarse Aggregate (%passing)$_{weight}$	Sand (%passing)$_{weight}$
¾"	19.0	99.6	100
½"	13.2	89.2	100
3/8"	9.5	39.9	100
No.4	4.75	1.9	97.6
No.8	2.36	0.3	90.4
No.16	1.18	0	76.1
No.30	0.600	0	54.6
No.50	0.300	0	22.9
No.100	0.150	0	3.1
No.200	0.075	0	0.3

4.2.2   Fiber Reinforced Concrete

Four types of fibers were investigated in the course of this study (Table 4.3) The choice of fibers included steel and polymeric fibers using commercially available geometries. The mixtures are given in Table 4.4.

Table 4.3   Fiber Types Employed in this Study

| Designation | Fiber Material | Schematic | Dimensions (mm) | | Properties | |
			Length	Dia	E (GPa)	σ_y (MPa)
F1	Polyolefin		50	1.00	2.6	365
F2	Polypropylene		30	1.00	3.5	450
F3	Polypropylene		50	1.00	3.5	450
F4	Steel		30	0.70	200	1198

Table 4.4   Mix Design for FRC

| Mix Designation | Compressive Strength (MPa) | Fiber Type | Dosage[*] | |
			kg/m³	V_f (%)
MF1	38	F1	6.75	0.75
MF2	40	F2	6.75	0.75
MF3	43	F3	6.75	0.75
MF4	43	F4	60	0.75
SFRC	47	F4	60	0.75
SFRC-1	42	F4	79	1.00
SFRC-2	49	F4	158	2.00
PFRC	39	F2	6.75	0.75
PFRC-1	41	F2	9	1.00
PFRC-2	45	F2	18	2.00

* kg/m³ refers to mass fraction; V_f refers to volume fraction

The Fibers F2 and F3 were sinusoidally crimped with the deformation given by:

$$y = A \sin(2\pi x/L)$$

where, A is equal to 0.5 mm, $L = 3.9$ mm and x is measured along the fiber length.

4.3 Specimen Preparation

Four types of specimen geometries were employed during the course of this study:
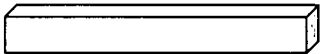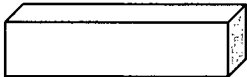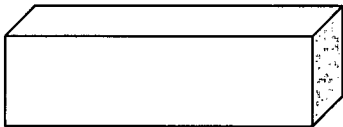
4.3.1 Cylinders

These were used to determine the compressive strengths of various mixes along with their splitting tensile strength as appropriate.

4.3.2 Beams

Flexural tests were conducted on prisms of three different sizes as shown in Table 4.5. Their depths varied from 50 mm to 150 mm, to enable a study of the specimen size effect. It is recommended that for investigating size-effects, the largest specimen be 4 times or greater than the smallest specimen. However, due to constraint on the size of the loading tup, in this program, the largest specimen chosen was only 3 times bigger than the smallest.

Table 4.5   Prisms Used for Flexural Tests

Schematic	Dimensions (mm)	Span/Depth (mm/mm)	Overhang (mm)
	50 x 50 x 450	150/50	150
	100 x 100 x 350	300/100	25
	150 x 150 x 500	450/150	25

4.3.3 Pull-Out Specimens

This type of specimen was employed to determine the bond-slip characteristics of fibers. The specimen configuration is shown in Figure 4.1. The specimen was cast in two parts: the first half was cast while keeping the fiber embedded to the desired length and

orientation, and 24 hours later, the second half was cast, thus completing a specimen. The two halves were separated by a plastic sheet (~ 0.5 mm thick) with a point-sized hole allowing the fiber to pass through it. This prevented the formation of any cementitious bond between the two concrete halves and simulated a crack in a real composite that was bridged by a fiber. The specimens were cured for a further 28 days in lime saturated water prior to test.
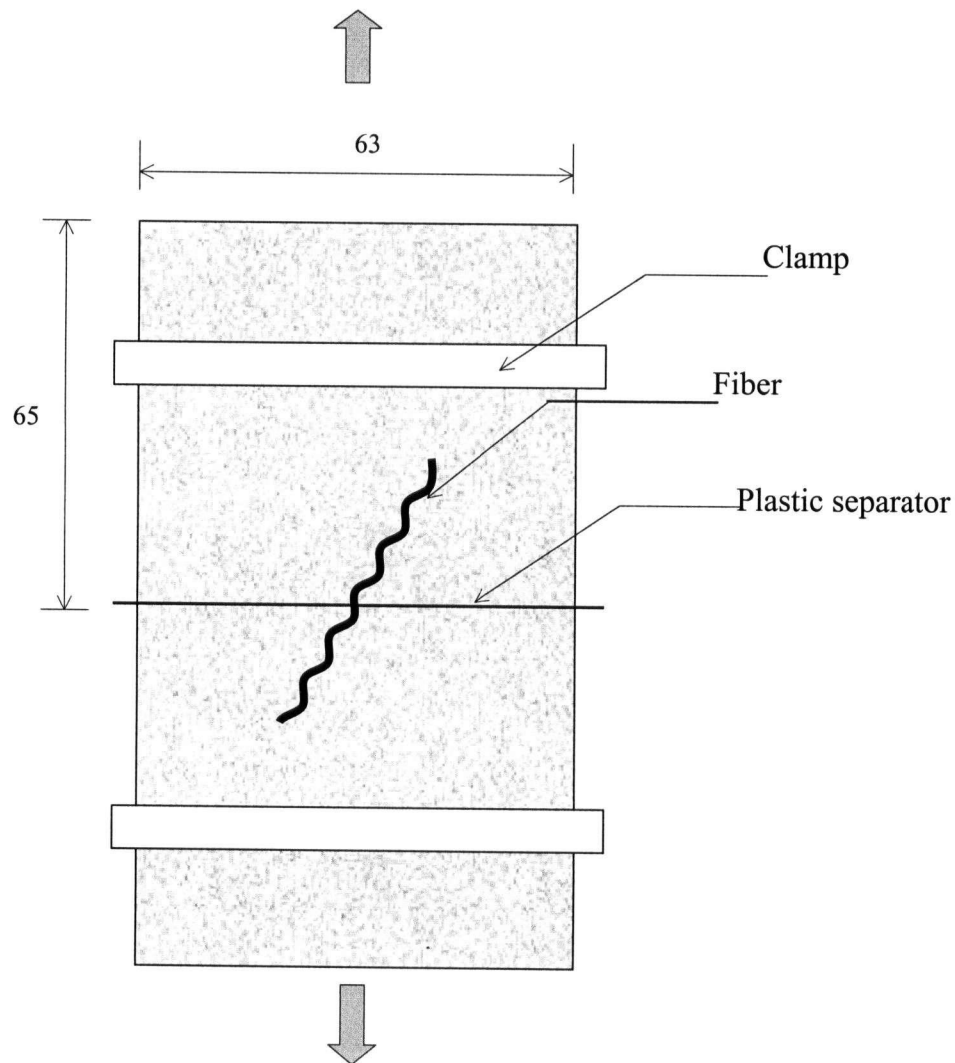
Figure 4.1   Schematic of the Pull-Out Specimen (all dimensions in mm)

4.3.4   Contoured Double Cantilevered Beam (CDCB) Specimen

The dimensions of the CDCB specimen are shown in Figure 4.2. The side groove promotes a plane strain crack state. In order to satisfy the two conditions desired for this specimen [1). propagation of the crack along the mid-plane and 2) rate of change of compliance independent of crack length], the slope of the tapering faces was calculated as $m = 0.222$ [150].
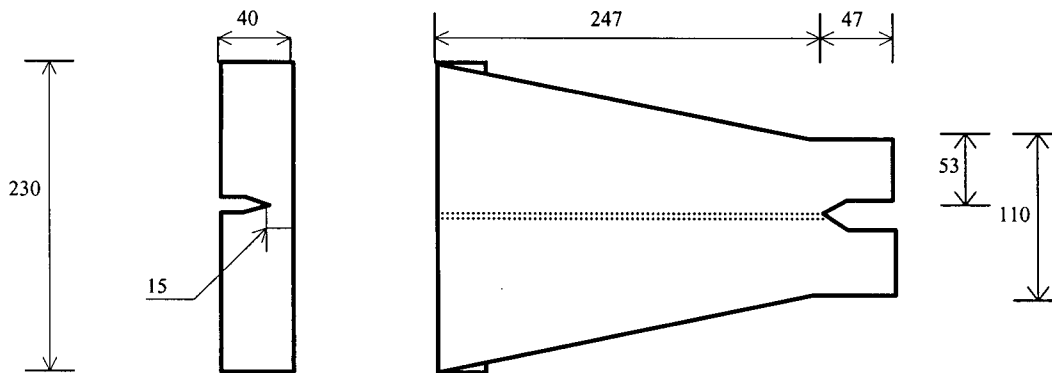
Figure 4.2   Dimensions of the CDCB Specimen (mm)

4.4   Testing Equipment and Apparatus

4.4.1   Quasi-Static Loading

4.4.1.1 The AMSLER Universal Testing Machine (UTM)

Shown in Figure 4.3, this UTM has a capacity of 220,000 lbs (981 kN) and is a hydraulically controlled machine. Both compression testing and split-cylinder testing were performed on this machine. It can measure loads as small as 50 lbs (223 N). For compression testing, load was applied at a rate of 2.67 kN/s in keeping with the requirements of ASTM C 39.
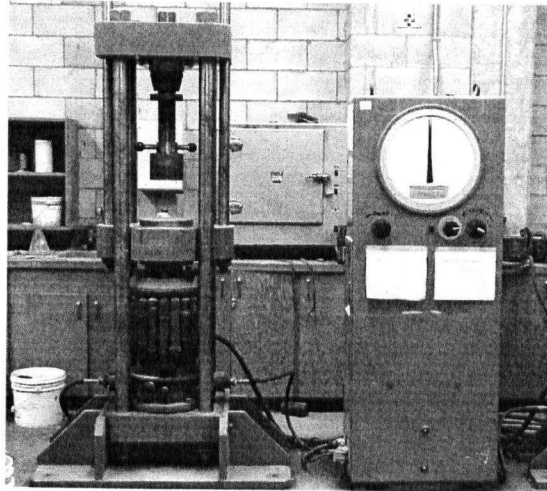
Figure 4.3   AMSLER Universal Testing Machine for Quasi-Static Compression

4.4.1.2 The INSTRON Materials Testing System

Flexural Tests

Figures 4.4 & 4.5 show quasi-static flexural testing conducted on a floor-mounted INSTRON materials testing system. It has a capacity of 150 kN and is a screw-driven machine, which allows for open-loop tests. In the former set-up, a beam is shown under flexure while in the latter, a CDCB specimen is under Mode I fracture.

Specimen

LVDT

Japanese Yoke
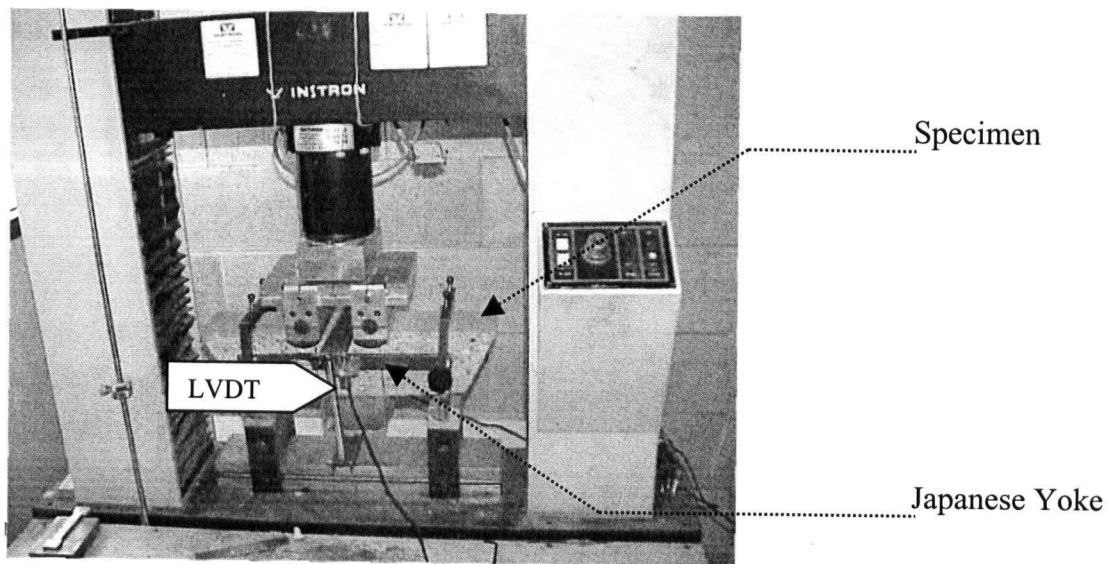
Figure 4.4   Flexural Testing of Beams under Quasi-Static 4-Point Loading
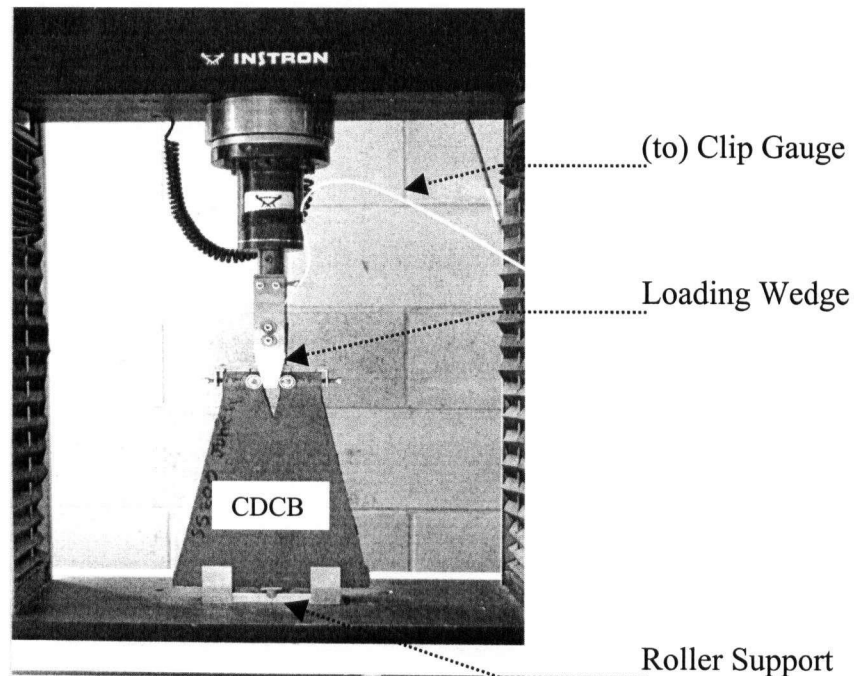
Figure 4.5   Flexural Testing of CDCB Specimen under Quasi-Static Loading

Load was applied at a cross-arm travel rate of 0.1 mm/min (resulting in a stress-rate of 0.012 MPa/s). The machine is capable of registering a load as low as 0.01 kN. For testing beams, two Linear Variable Displacement Transducers (LVDT) were placed at mid-span to record the deflection. These were later averaged to yield the mid-span deflection for each beam. During a flexural toughness test, there is crushing at the load-point and the specimen supports also tend to settle. Thus, measured beam deflections are often far greater than the true deflections at the specimen's neutral axis. In order to eliminate these extraneous effects, a "Japanese yoke", as suggested by the Japanese standard JSCE SF4, was installed around the specimens. It has been shown previously that it is only through such a yoke [145] or an equivalent deflection measuring system that true beam deflections may be measured. The applied load and deflection data was electronically recorded at a frequency of 1 Hz. The INSTRON Materials Testing System can accommodate beams with a clear span up to 450 mm. It can be used to perform both flexural and uniaxial tensile tests.

Pull-Out Tests

Quasi-static pull-out was carried out on a table-mounted INSTRON machine shown in Figure 4.6 with a load cell capacity of 5 kN (and resolution of 0.01 N). The pull-out load was applied at a cross-arm travel rate of 2 mm/min (COD rate = 3.33 x 10^{-5} m/s). The COD was measured by means of two LVDT's mounted on either side of the specimen. These LVDT's had a travel range of 40 mm and accuracy of 10^{-3} mm. The applied load and COD data were recorded at a frequency of 2 Hz by the data acquisition system.
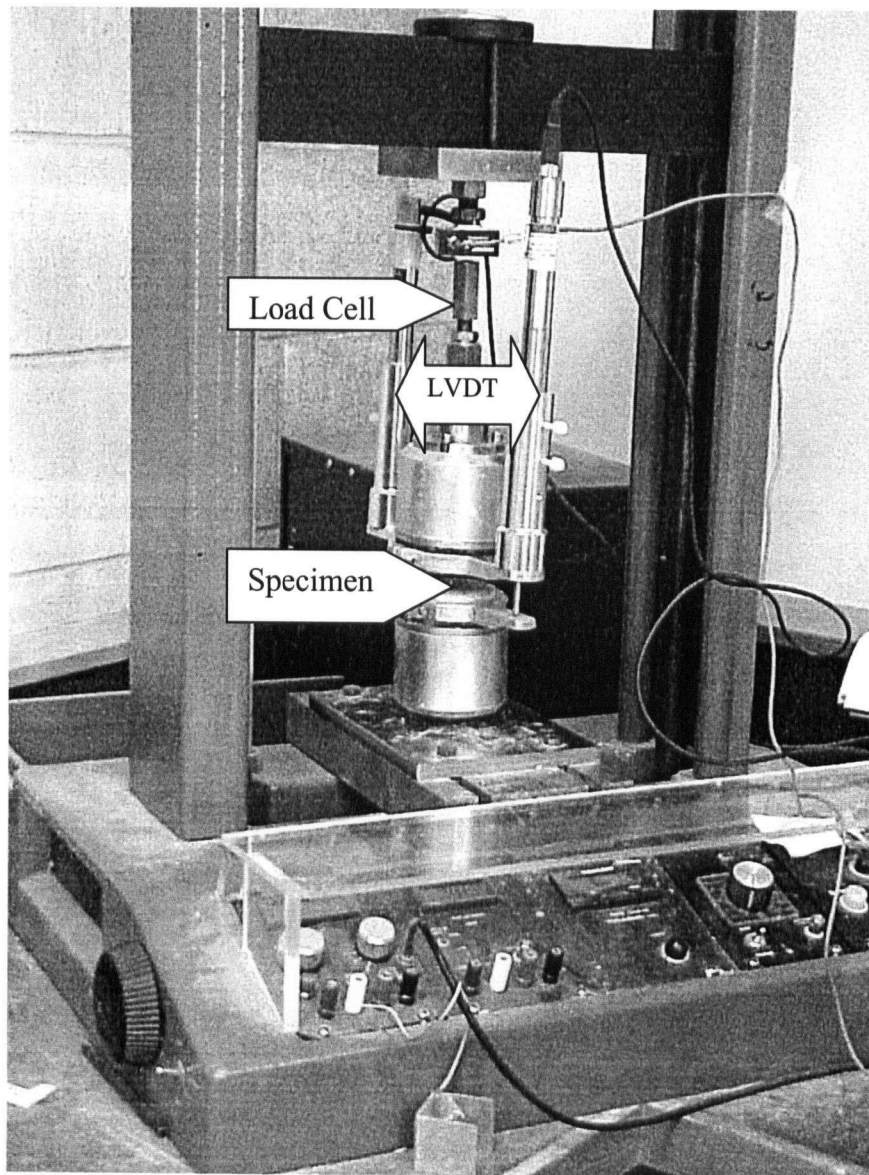
Figure 4.6   Set-Up for Quasi-Static Pull-Out Test

4.4.2 Impact Loading

Three instrumented drop-weight impact machines with varying capacities were utilized in the course of this research program. Energy is transferred from the hammer to the specimen by dropping it freely from a pre-determined height. At the instance of impact, the hammer develops a velocity v_h by:

$$v_h = \sqrt{2(0.91g)h}$$

where, v_h = the velocity of the falling hammer

  g = the acceleration due to gravity

  h = the drop height

From the work of Banthia [17], a correction factor of 0.91 was applied to g to account for frictional losses between the guide columns and the falling hammer.

4.4.2.1 The 100 J Drop-Weight Impact Machine (SMALL MACHINE)

This machine (Figure 4.7) has the capacity to drop a 12 kg mass from heights of up to 1.25 m on to a target specimen such as a beam of maximum width 100 mm. It is table-mounted and is operated electromagnetically. Figure 4.8 shows the different "tups" (dynamic load cells) that may be attached to the hammer. The 4" blade load cell was used for impact tests on beams where as, the bolt-load cell was used to perform impact tests on CDCB specimens.

As seen in Figure 4.9a, the Bolt-Load Cell consists of a single strain gauge, embedded within the bolt and the circuitry typical for this system is shown in Figure 4.9b. The strain gauge forms only one-fourth of a Wheatstone Bridge, which is why it is also called a "quarter bridge".

4.4.2.2 The 1 kJ Drop Weight Impact Machine (MEDIUM MACHINE)

This machine is floor mounted and has a reinforced concrete base. It is schematically illustrated in Figure 4.10 and the photograph is shown in Figure 4.11 along with the tup, the hammer and the support base. The hoist chain controls the hammer

electromagnetically. This machine is capable of dropping a 60 kg mass from a height of up to 2.5 m which results in a maximum possible incident energy of 1 kJ.
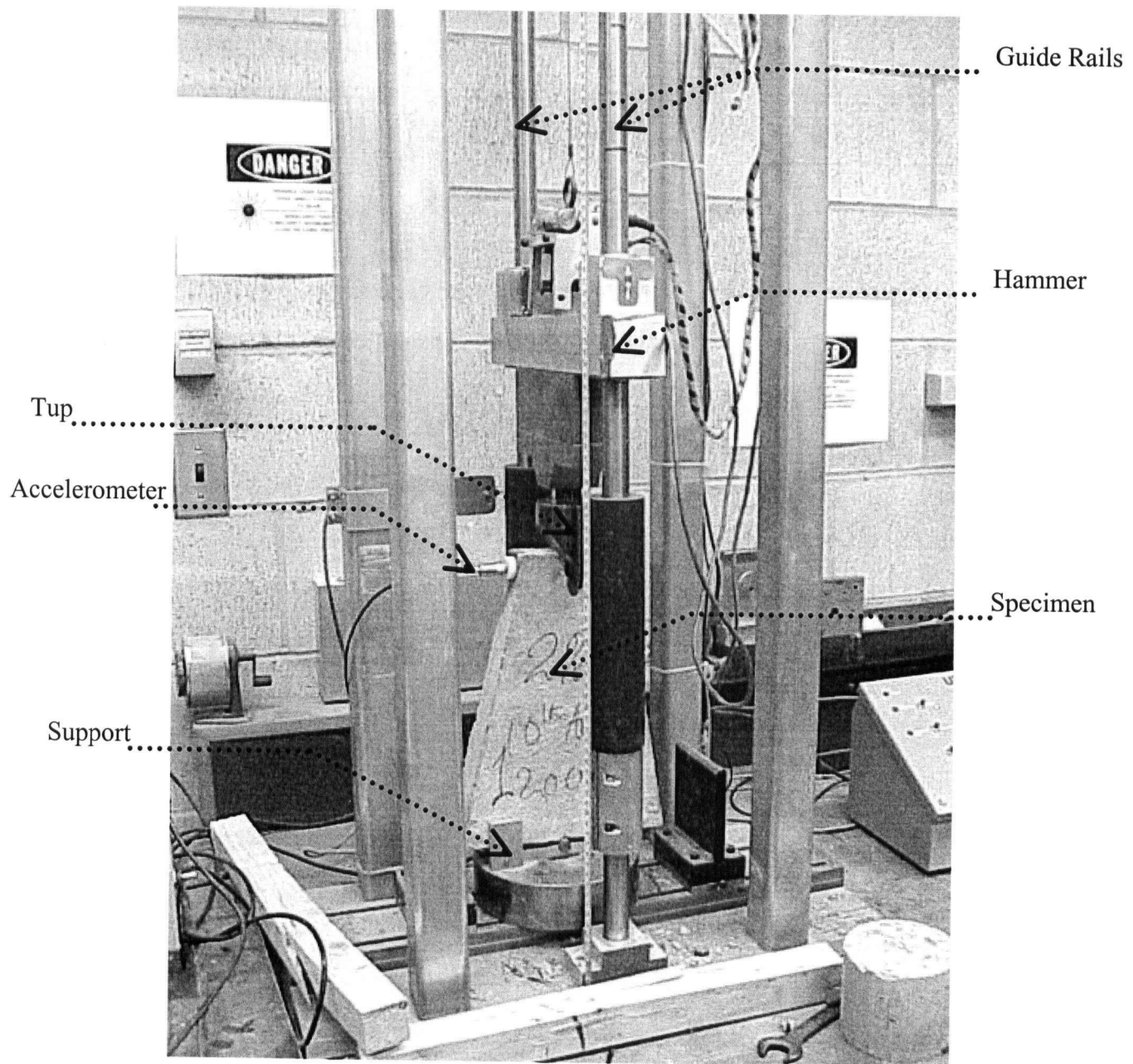
Figure 4.7   Drop-Weight Impact Machine (100 J Capacity)
(Referred to in this thesis as the SMALL MACHINE)
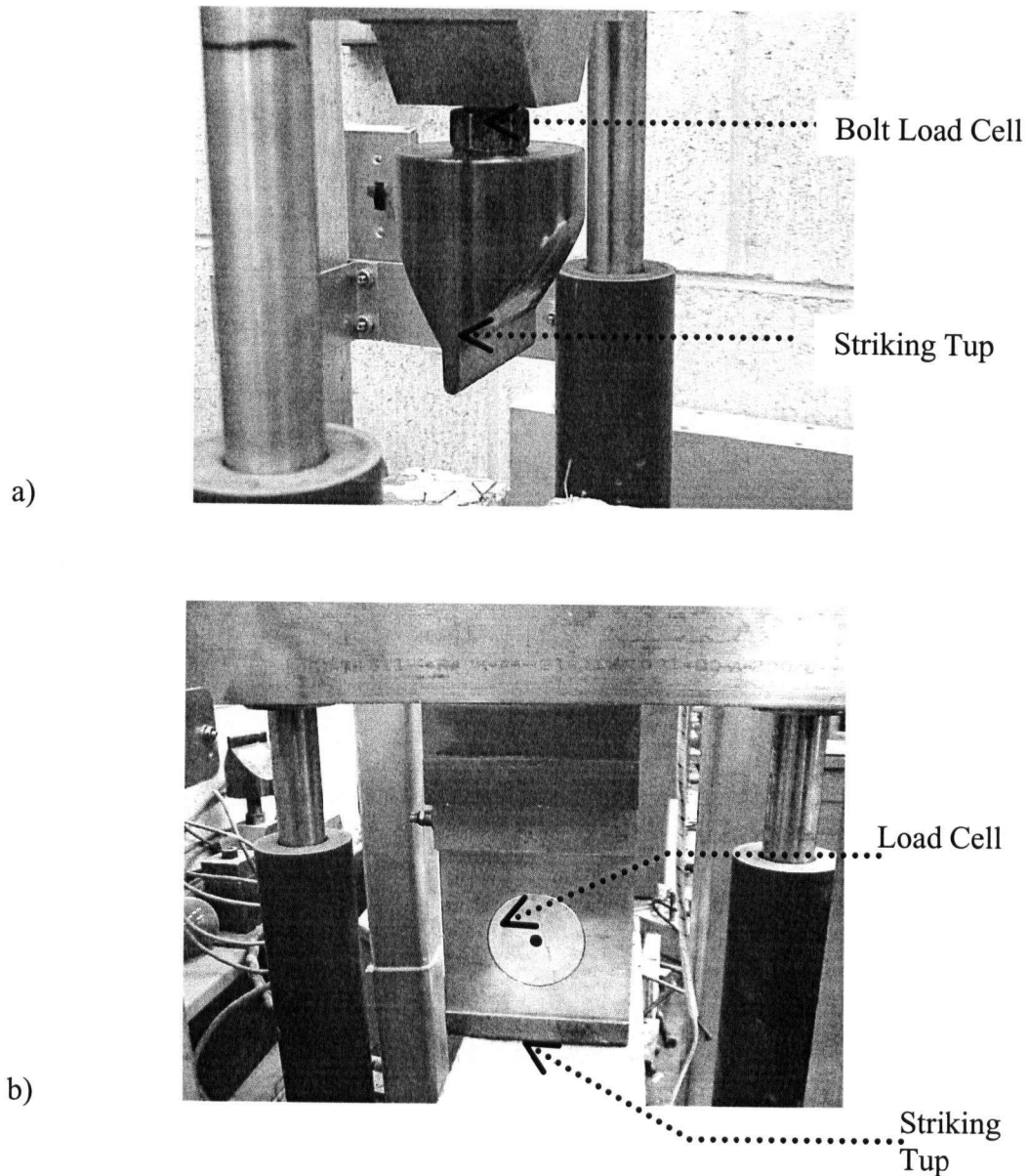
Figure 4.8   Possible Load Cells that may be Attached to the Small Machine a) Bolt Load Cell (*for CDCB Specimens*); b) 4" Blade Load Cell (*for Beam Specimens*)

4.4.2.3 The 10 kJ Drop Weight Impact Machine (LARGE MACHINE)

The largest of the drop-weight machines used is a 10 kJ impact machine that can drop a 578 kg mass from heights of up to 2.5 m (Figures 4.12 & 4.13). A 6" blade load cell, shown in Figure 4.11b was employed as the striking tup during flexural testing on both medium and large (1 kJ and 10 kJ) machines. This tup has 8 bonded strain gauges mounted within itself.

a)

b)
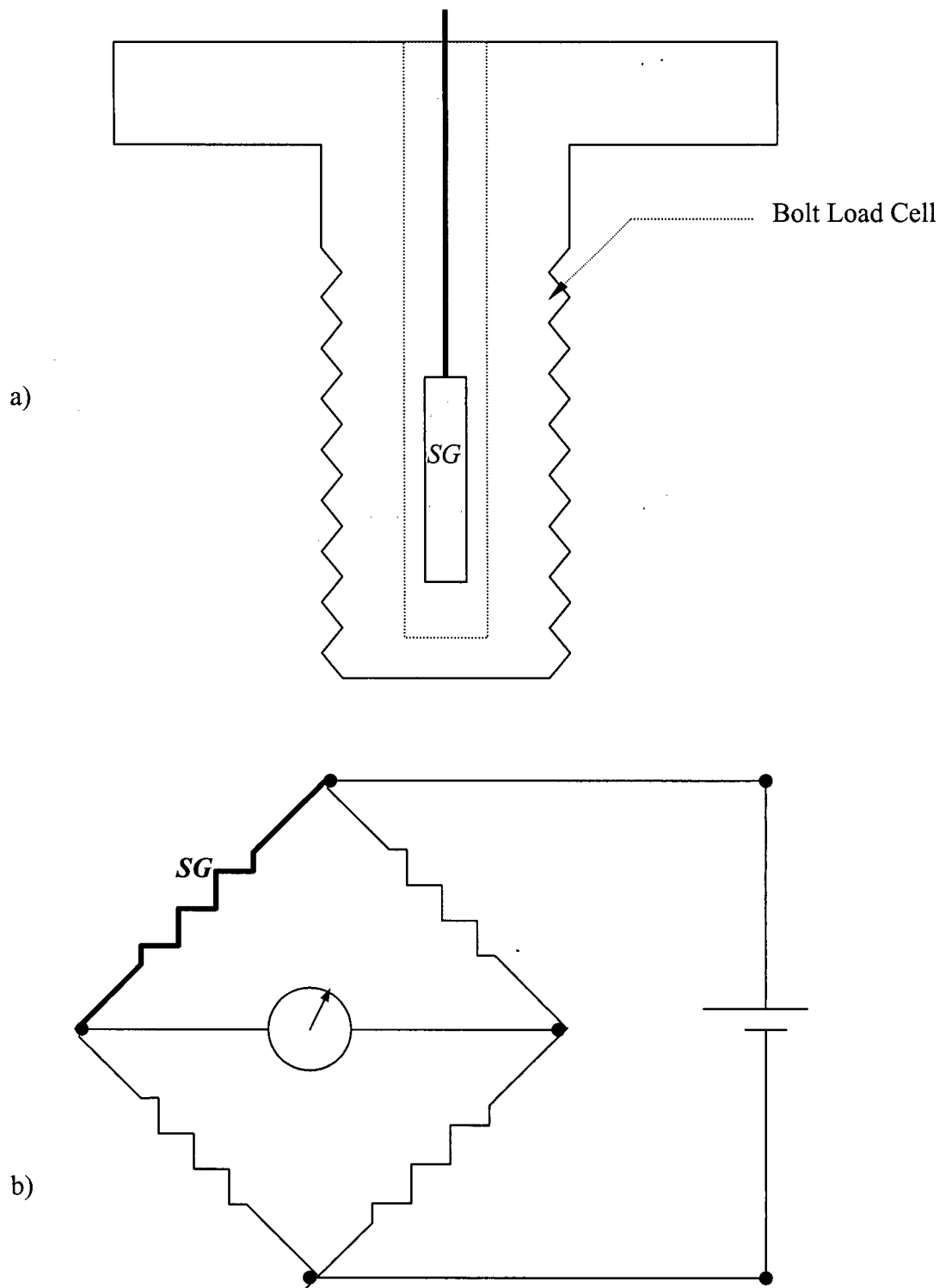
Figure 4.9   Bolt Load Cell a) Schematic Showing Strain Gauge (SG) Embedded
Within the Bolt; b) Circuit Diagram for the "Quarter Bridge"
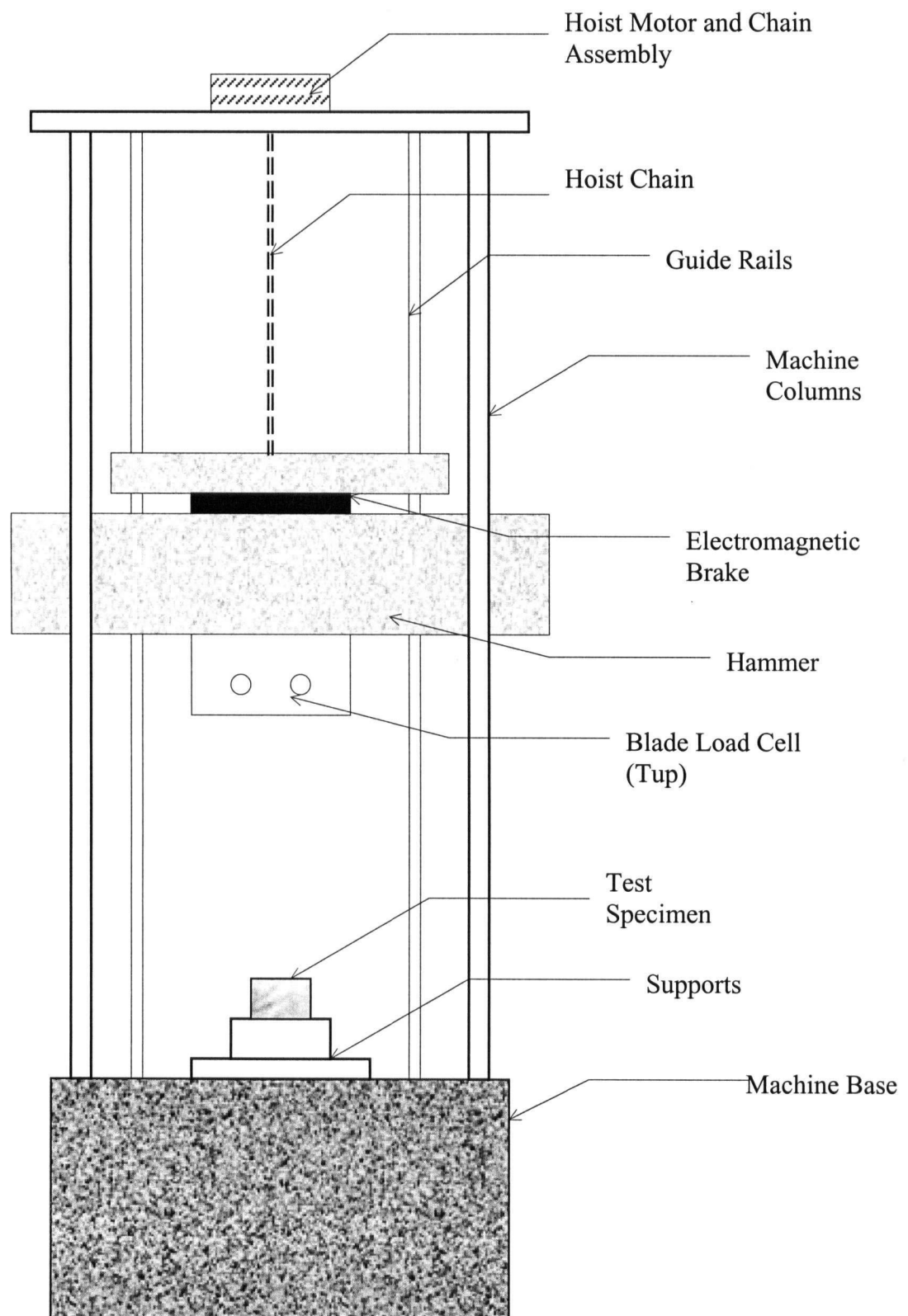
Figure 4.10   Schematic view of the Medium Impact Machines (1,000 J Capacity)

54
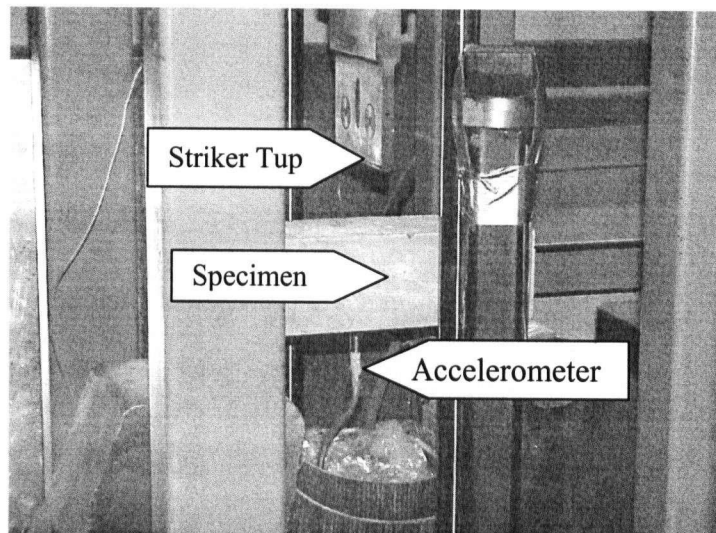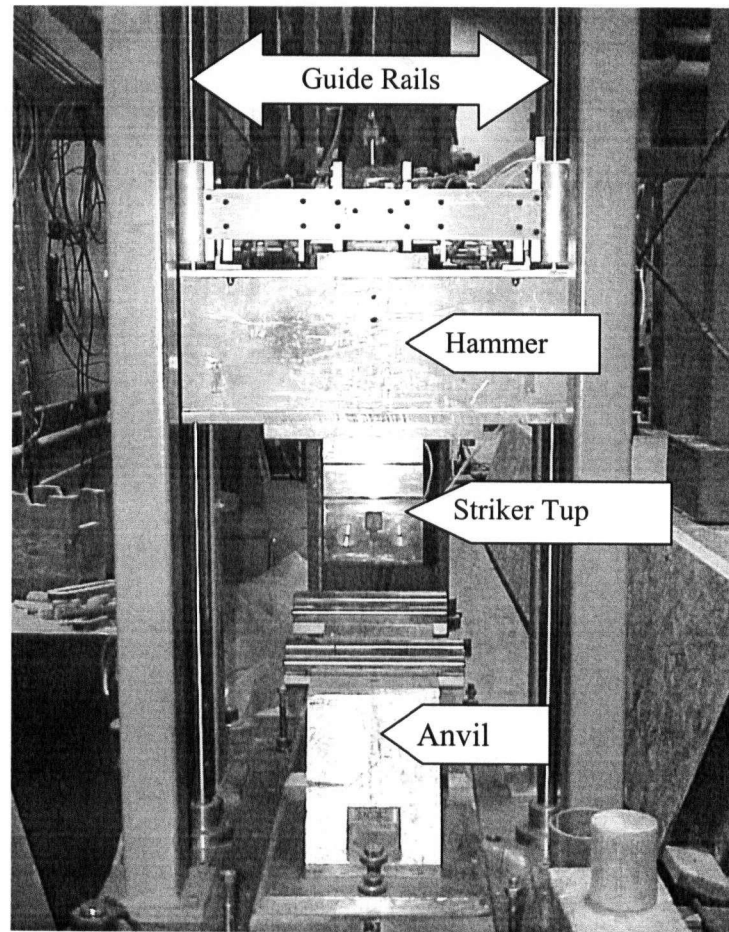
Figure 4.11   a) Drop-Weight Impact Machine with 1,000 J Capacity *(Referred to in this thesis as the MEDIUM MACHINE)*; b) Instrumentation
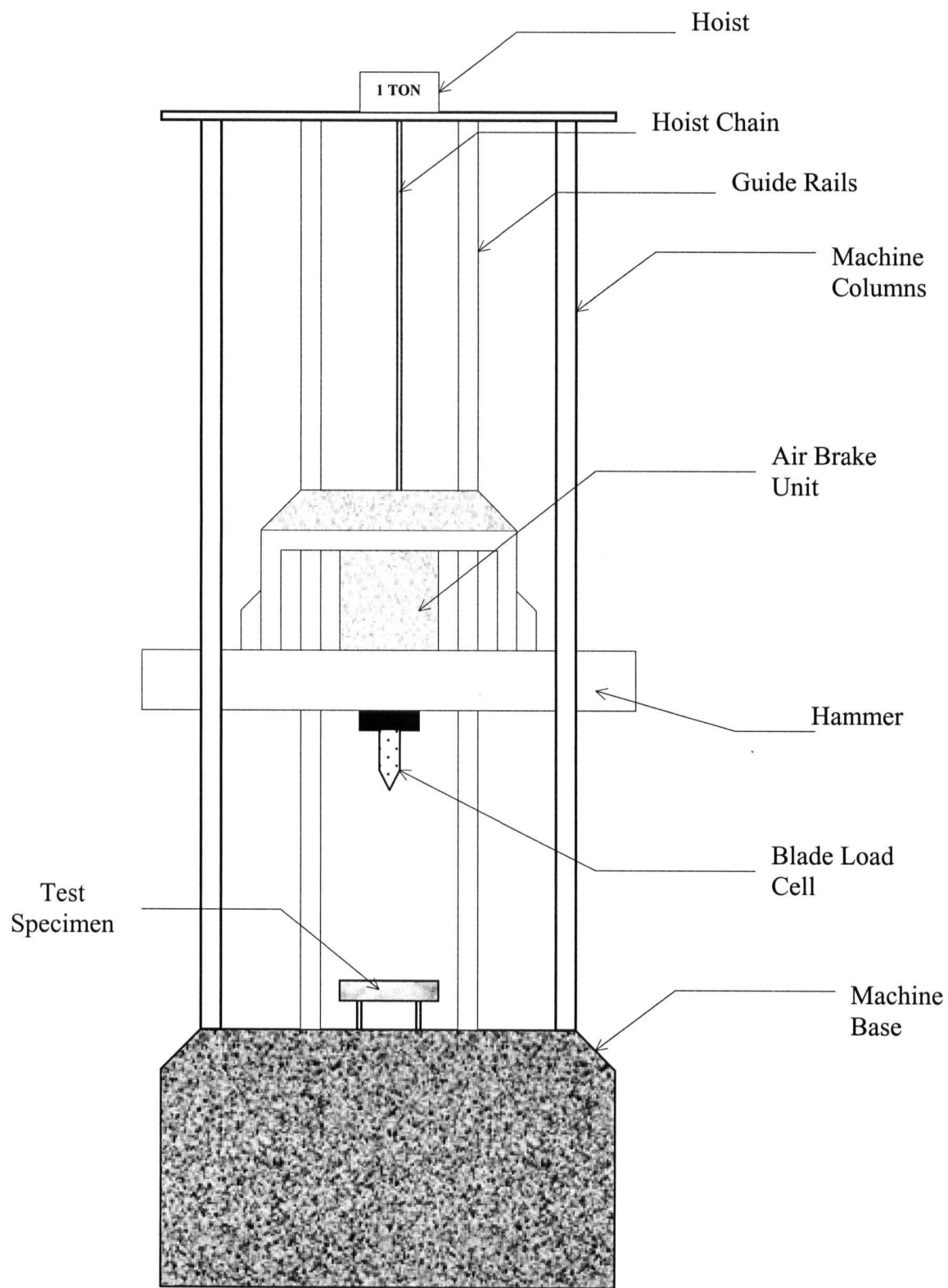
Figure 4.12   Schematic View of the Large Impact Machine (10, 000 J capacity)
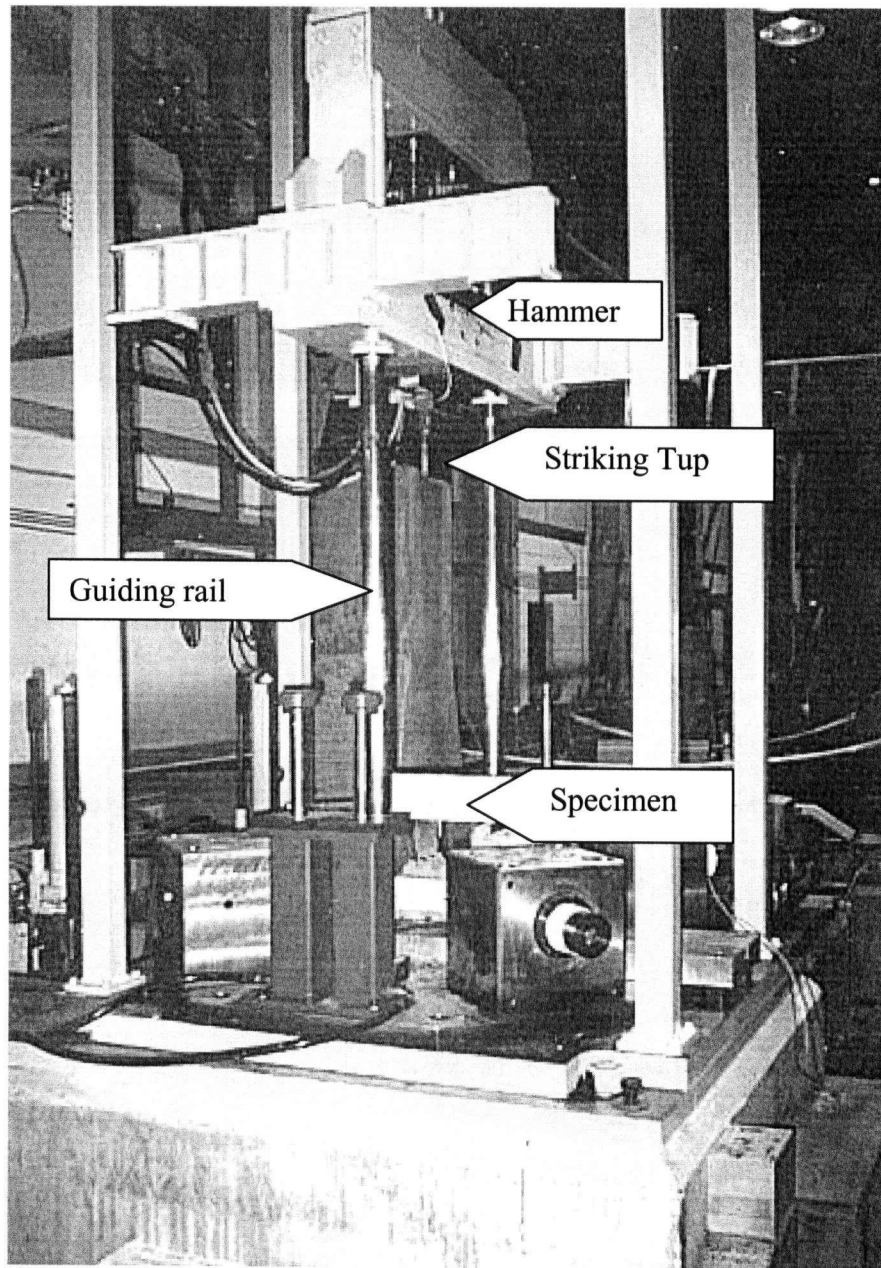
Figure 4.13   Drop-Weight Impact Machine (10,000 J Capacity)
(Referred to in this thesis as the LARGE MACHINE)
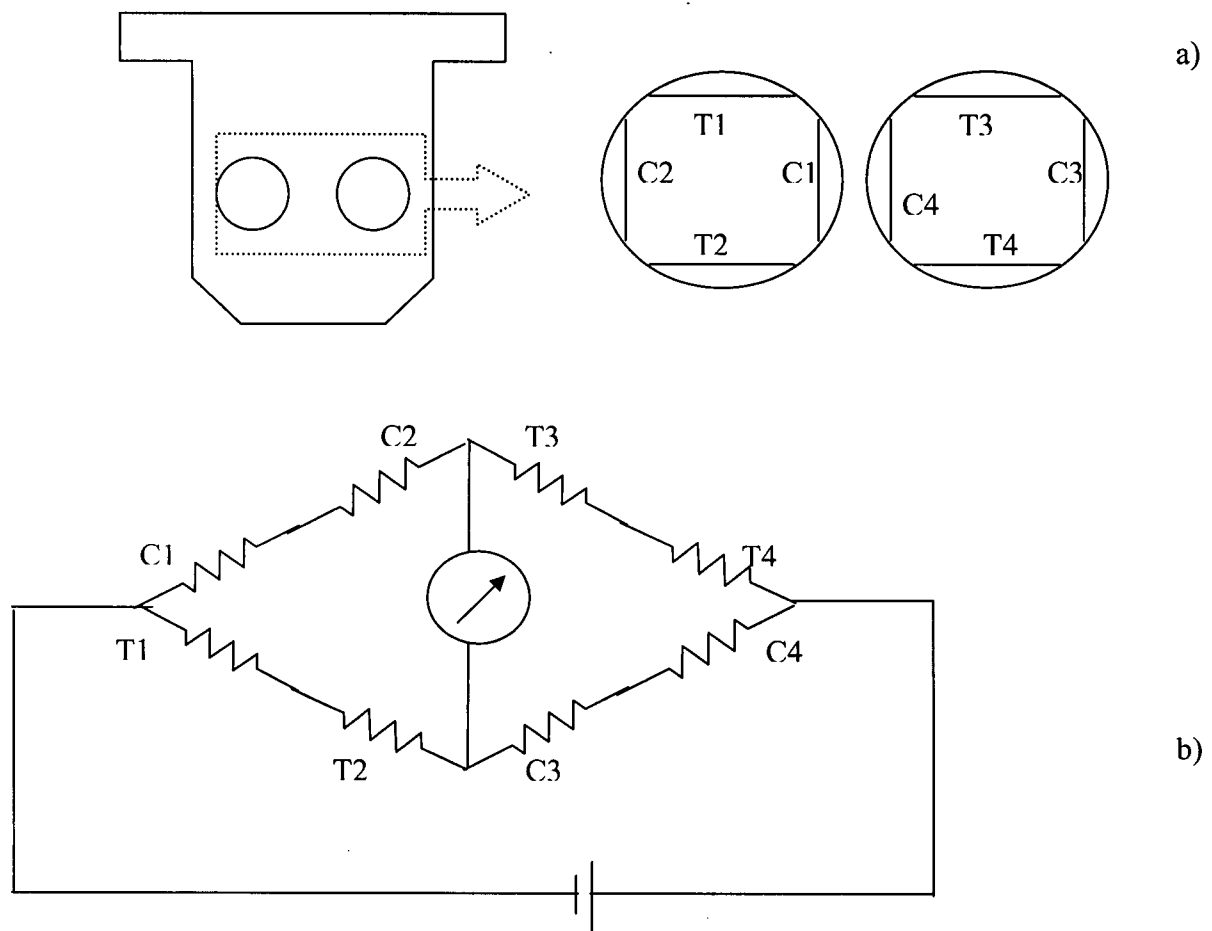
Figure 4.14   6" Blade Load Cell: a) Location of Strain Gauges in Tup; b) Wheatstone
Bridge Circuit

The striking tups used for the testing beams were made of heat-treated carbon steel. Two circular holes, 25 mm in diameter, were machined in the tups as shown in Figure 4.14a. The 8 strain gauges mounted on the inside surface of the two holes were connected to form a Wheatstone Bridge as shown in Figure 4.14b. The circuit is balanced in the "no load" configuration. Although these load cells were employed for impact testing, they were calibrated under quasi-static load to 70 % of their rated limits. The calibration curves were perfectly linear in both ascending and descending cycles. The calibration curves for the three load cells used is this program are provided in Appendix 2.

For all impact tests using the drop-weight machines, an accelerometer in the form of a piezoelectric sensor was employed. This was screwed into mounts which were glued to the specimens prior to testing. With a resonant frequency of 45 kHz and a resolution of 0.01 g ('g' refers to the earth's gravitational acceleration), the accelerometer could read up to $\pm$ 500 g and carried an overload protection of up to 5000 g.

The velocity and displacement histories at the load-point were obtained by integrating the acceleration history with respect to time. If is the acceleration at the load point, $\dot{u}_0(t)$ is the velocity at the load-point and $u_0(t)$ is the displacement at the load-point, then:

$$\dot{u}_0(t) = \int \ddot{u}_0(t).dt$$

...(4.1)

$$u_0(t) = \int \dot{u}_0(t).dt$$

...(4.2)

In Figures 4.15a–c, the Fast Fourier transform of the acceleration time-histories from the three different drop-weight impact machines are plotted in the frequency domain. Filters should be used if the machine vibrations interfere with the natural frequency of the specimen.
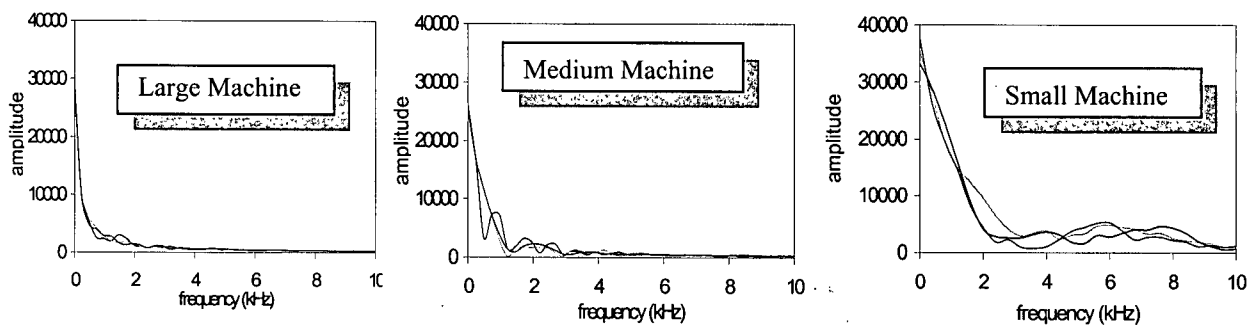
Figure 4.15   Fast Fourier Transforms of the Acceleration–Time Histories for a) Large Machine, b) Medium Machine and c) Small Machine

4.4.2.4 Dynamic Pull-Out Tests

This machine was constructed specifically for dynamic pull-out testing and is shown in Figure 4.16. The specimen is held in the machine such that the top half is stationary while the bottom half is pulled down rapidly by an air-gun. The top half of the specimen is suspended from a dynamic load-cell of 5 kN capacity with a resolution of 0.01 N. The displacement of the specimen during a test, (which is also the COD if the elastic deformation may be ignored) is measured by means of a single Fast LVDT (*FASTAR*™ 1000) fixed to the moving bottom half.
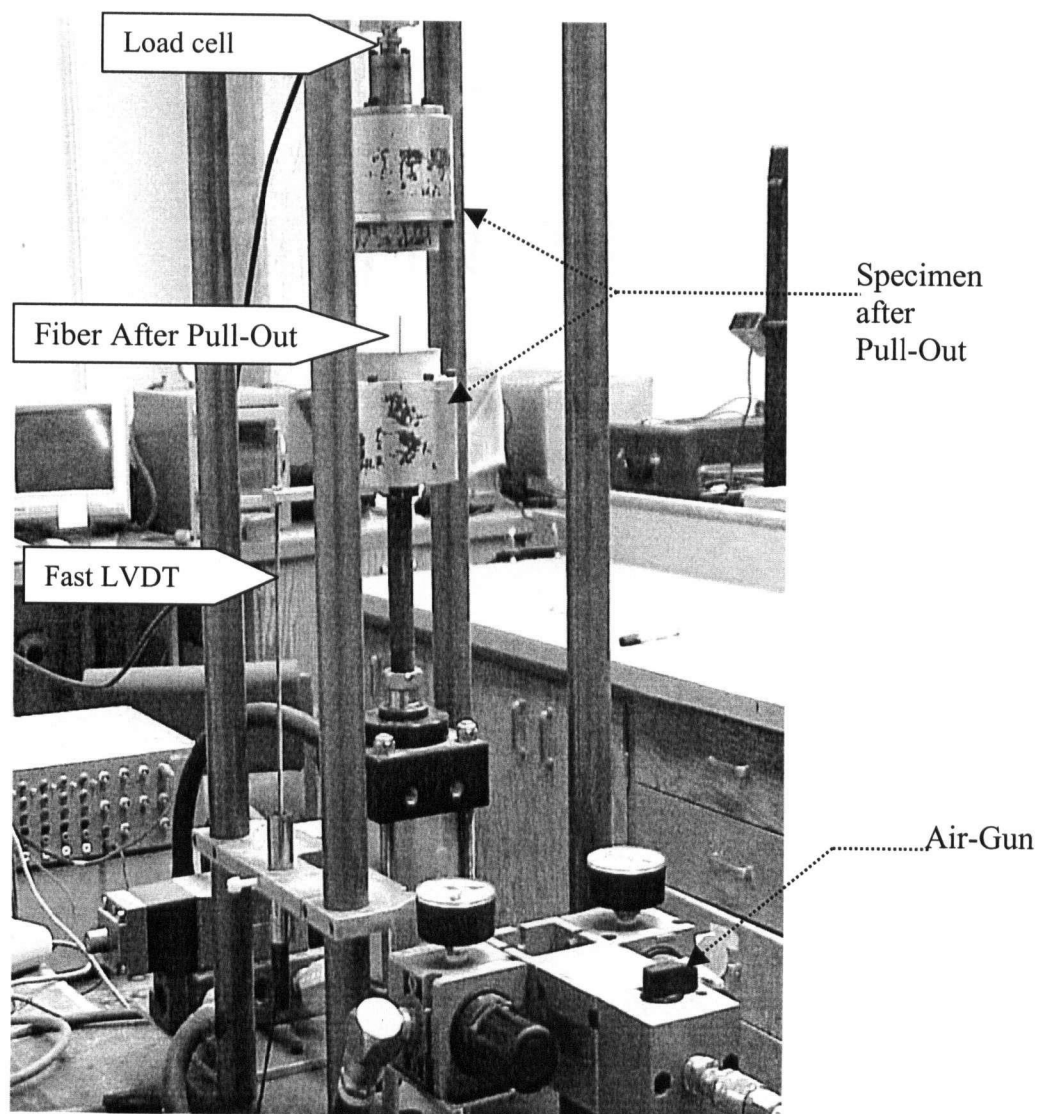
Figure 4.16   Dynamic Pull-Out Testing Machine

The fast LVDT consists of an aluminium core that moves within a coil-wound tube. It can measure rapidly oscillating linear displacement at frequencies of up to 6 kHz because of its very high carrier frequency[1] (112 kHz compared with 2.5 kHz for the typical LVDT used in quasi-static testing). It has a range of 50 mm and 0.001 mm resolution with $\pm$ 0.15% non-linearity. The air-gun could operate at a peak pressure of 0.35 MPa, which generated a pull-out displacement rate (i.e. COD rate) of 3 m/s. At this rate, a complete fiber pull-out took approximately 40 ms. The data acquisition system for dynamic tests recorded input from the load cell and the LVDT at a rate of 20,000 Hz.

4.5   Testing Program

The tests were divided into four series: a) compression and split-tensile testing, b) flexural toughness tests on beams, c) pull-out tests on single-fibers bonded to a cement-based matrix, and d) CDCB specimens subjected to MODE I fracture. Of these, compression and split-tensile tests were done under quasi-static rates only while the rest were conducted under both quasi-static and impact rates of loading.

4.5.1   Compression Tests

Plain and fiber reinforced concrete cylinders were tested under compression in accordance with ASTM C 39-1998. In addition, as appropriate, cylinders were tested in splitting tension as per ASTM C 496-1998.

4.5.2   Flexural Testing

Plain and fiber reinforced concrete beams were subjected to one rate of quasi-static loading and up to 4 rates of impact loading. The different test matrices are shown in Tables 4.6-4.9. Quasi-static tests were conducted as per ASTM C 78-1998 under 4-point loading. The data was analysed in accordance with JSCE SF 4-1984. Impact testing was performed under 3-point bending.

---

[1] The carrier frequency governs the excitation voltage that may be applied in order to acquire data.

Table 4.6   Flexural Testing Program: Plain Concrete (6 Specimens Each)

Mix	Machine	Drop-height	Dimensions (mm x mm x mm)	Span/Depth (mm/mm)
Normal Strength Concrete	Small	200	100 x 100 x 350	300/100
		1000	100 x 100 x 350	300/100
	Medium	200	50 x 50 x 450	150/50
			100 x 100 x 350	300/100
			150 x 150 x 500	450/150
		500	50 x 50 x 450	150/50
			100 x 100 x 350	300/100
			150 x 150 x 500	450/150
		750	50 x 50 x 450	150/50
			100 x 100 x 350	300/100
			150 x 150 x 500	450/150
		1000	50 x 50 x 450	150/50
			100 x 100 x 350	300/100
			150 x 150 x 500	450/150
	Large	20	100 x 100 x 350	300/100
		200	100 x 100 x 350	300/100

Table 4.7   Flexural Testing Program: Effect of fiber length and geometry
(3 Specimens Each)

Mix	Machine	Drop-height	Dimensions (mm x mm x mm)	Span/Depth (mm/mm)
MF1	Large	100	100 x 100 x 350	300/100
MF2				
MF3				
MF4				

Table 4.8   Flexural Testing Program: Steel Fiber Reinforced Concrete
             (6 Specimens Each)

Mix	Machine	Drop-height	Dimensions (mm x mm x mm)	Span/Depth (mm/mm)
SFRC	Medium	200	50 x 50 x 450	150/50
			100 x 100 x 350	300/100
			150 x 150 x 500	450/150
		500	50 x 50 x 450	150/50
			100 x 100 x 350	300/100
			150 x 150 x 500	450/150
		750	50 x 50 x 450	150/50
			100 x 100 x 350	300/100
			150 x 150 x 500	450/150
		1000	50 x 50 x 450	150/50
			100 x 100 x 350	300/100
			150 x 150 x 500	450/150

4.5.3 Pull-out testing

One quasi-static rate and two dynamic rates were investigated. In order to capture the effect of fiber orientation, the fiber was initially inclined at 6 intervals (0°, 15°, 30°, 45°, 60°, 75°) with respect to the load. However, subsequently, it was realised that 4 intervals (0°, 22.5°, 45°, 67.5°) would suffice as shown in Table 4.10. The fibers were embedded to half their lengths. The pressure was delivered by the air-gun at two levels for the impact

Table 4.9   Polypropylene Fiber Reinforced Concrete: Flexural Testing Program (6 specimens each)

Mix	Machine	Drop-height	Dimensions (mm x mm x mm)	Span/Depth (mm/mm)
PFRC	Medium	200	50 x 50 x 450	150/50
			100 x 100 x 350	300/100
			150 x 150 x 500	450/150
		500	50 x 50 x 450	150/50
			100 x 100 x 350	300/100
			150 x 150 x 500	450/150
		750	50 x 50 x 450	150/50
			100 x 100 x 350	300/100
			150 x 150 x 500	450/150
		1000	50 x 50 x 450	150/50
			100 x 100 x 350	300/100
			150 x 150 x 500	450/150

Table 4.10   Pull-Out Testing Program (5 specimens each)

Mix	Fiber	Embedment Length	Inclination (from loading-direction)	COD rate (mm/s)
NSC	F1	25	0°, 15°, 30°, 45°, 60°, 75°	0.033
	F2	15		
	F3	25		
	F4	15		
	F1	25	0°, 22.5°, 45°, 67.5°	2000, 3000
	F2	15		
	F3	25		
	F4	15		
HSC	F1	25	0°	0.033, 2000, 3000
	F2	15		
	F3	25		
	F4	15		

loading viz. 0.20 MPa and 0.35 MPa, corresponding to COD rate of 2000 and 3000 mm/s respectively.

4.5.4   Crack Growth Studies

For quasi-static tests, the load was applied vertically at a cross-arm travel rate of 0.1 mm/min, which resulted in a horizontal opening load (OL), whose magnitude was calculated later by resolving the forces (Figure 4.17). Although the specimens were subjected to a vertical load in addition to the horizontal opening load, the vertical component could be ignored if the angle of the wedge α were kept sufficiently small. Accordingly, an angle of 15° was chosen. In addition, the coefficient of friction between the cantilever arm of the specimen and the wedge was ignored. For small wedge angles, this assumption is valid. However, with an increase in the angle of wedge, the coefficient of friction also increases. In order to record the crack opening displacement, a clip gauge displacement transducer was used as shown in Figure 4.5. The applied load-CMOD data was acquired using a digital data acquisition system running at 5 Hz. For impact testing, the tup (Figure 4.8a) was machined to have an angle of 15°, in order to keep it identical to the wedge angle under quasi-static loading.

Table 4.11   Test Program for Crack Growth Studies (3 Specimens Each)

Mix	Quasi-Static Loading	Impact Loading Drop-Height (mm)	
Plain Concrete			
SFRC-1	Cross-Arm Displacement Rate = 0.00166 mm/s	Small Machine	500, 750, 1000
SFRC-2			
PFRC-1			
PFRC-2			
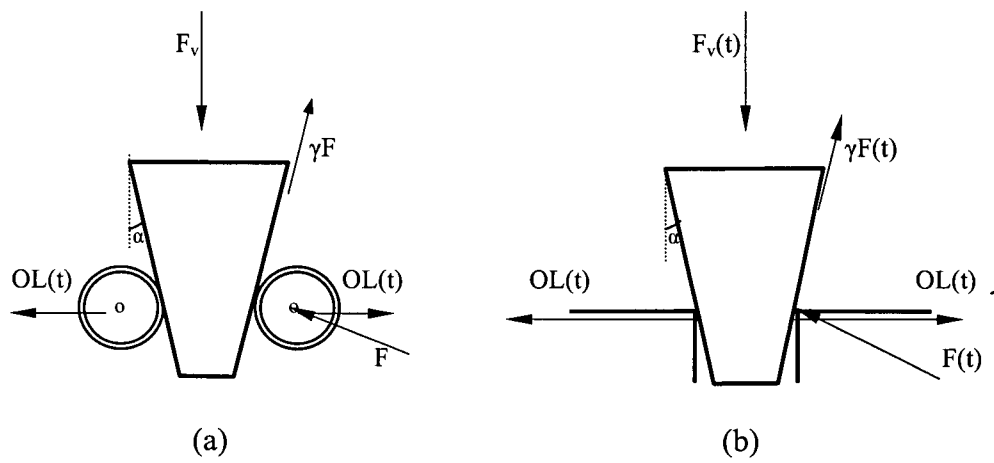
For $\gamma = 0$,

(Static) $OL = F_v/2\tan\alpha$

(Impact) $OL(t) = F_v(t)/2\tan\alpha$

Figure 4.17   Vertical Load Resolved for a CDCB Specimen to Obtain Opening Load under a) Quasi-Static Loading; b) Impact Loading

Chapter 5

IMPACT RESPONSE OF PLAIN CONCRETE BEAMS

5.1 Introduction

Several techniques have been developed to assess the impact response of quasi-brittle materials like concrete. With the lack of a standard system or procedure for impact testing of concrete, a quantitative understanding of the impact resistance of concrete is not possible without an extensive characterization of the parameters involved. This Chapter examines the impact response of plain concrete through a wide-ranging investigation using instrumented drop-weight machines. In particular, machine specific parameters, such as hammer mass and drop-height are investigated, followed by a study of the specimen size-effect on the impact response of plain concrete beams.

Indications are that different machines, which vary widely in size and capacity although employing the same principle (for instance, the drop-hammer), may lead to very different conclusions. Unfortunately, machine/test parameter influences are not understood at all. Wang [136] recorded that a machine carrying a heavier hammer creates a longer pulse, where as varying the drop height leads to a change in load amplitude without affecting the duration of the pulse. In its service life, a concrete member may experience impact loads in a wide range of amplitude and/or duration. Accordingly, it is imperative that a test-program simulates the actual impact situation to assess the material response accurately.

As indicated in section 3.11, all materials exhibit a size-effect and concrete is no exception. An important step towards the standardization of an impact test is the choice of a suitable specimen size. Fracture is a rate-sensitive process, which is to say that the effective fracture properties depend upon the crack growth rate. It follows therefore that the size-effect on the nominal strength of quasi-brittle materials like concrete should be studied in conjunction with their stress-rate sensitivity.

5.2 Machine-Effects

5.2.1 Test Regimes

In order to study the influence of machine characteristics on the impact properties of concrete, plain concrete beams were subjected to flexural impact using three different instrumented drop-weight machines (described in detail in section 4.4.2). To compare the responses, the study was carried out under two broad regimes: 1) Equal hammer-potential energy and 2) Equal hammer-velocity (i.e. drop-height). These regimes are illustrated in Table 5.1.

Table 5.1   Test Regimes for Study of Machine-Effect

Equal Potential Energy		
Machine Type	Drop Height (mm)	Potential energy (J)
Large	20	120
Medium	200	120
Small	1000	120
Equal Drop Height		
Machine Type	Drop Height (mm)	Potential Energy (J)
Large	200	1200
Medium	200	120
Small	200	24

5.2.2 Results

The complete dynamic analysis leading to the inertial load correction P_i (t) is described in detail by Banthia *et al.* [137]. At any instant of time, the acceleration distribution along the length of both plain and fiber reinforced concrete (with nominal fiber dosage) was approximated as linear and symmetric about the mid point (Figure 5.1). Using the recorded mid-span acceleration out-put, the acceleration at any point from $x = 0$ to $x = l/2$ could then be obtained. Thus we have:

$$u(x,t) = \frac{2u_0^b(t)}{l} x \qquad \qquad \ldots(5.1)$$

$$\ddot{u}(x,t) = \frac{2\ddot{u}_0^b(t)}{l}x \qquad \qquad \ldots (5.2)$$

$$\delta u(x,t) = \frac{2\delta u_0^b(t)}{l}x \qquad \qquad \ldots (5.3)$$

where, $u(x,t)$ = deflection at any point x, on the beam at a given time t

$u_0^b(t)$ = mid-span deflection of the beam specimen at any time t

$\ddot{u}(x,t)$ = acceleration at any point x, on the beam at a given time t

$\ddot{u}_0^b(t)$ = measured mid-span acceleration of the beam at any time t

$\delta u(x,t)$ = virtual deflection at any point x, at time t

$\delta u_0^b(t)$ = virtual deflection at mid-span at any time t
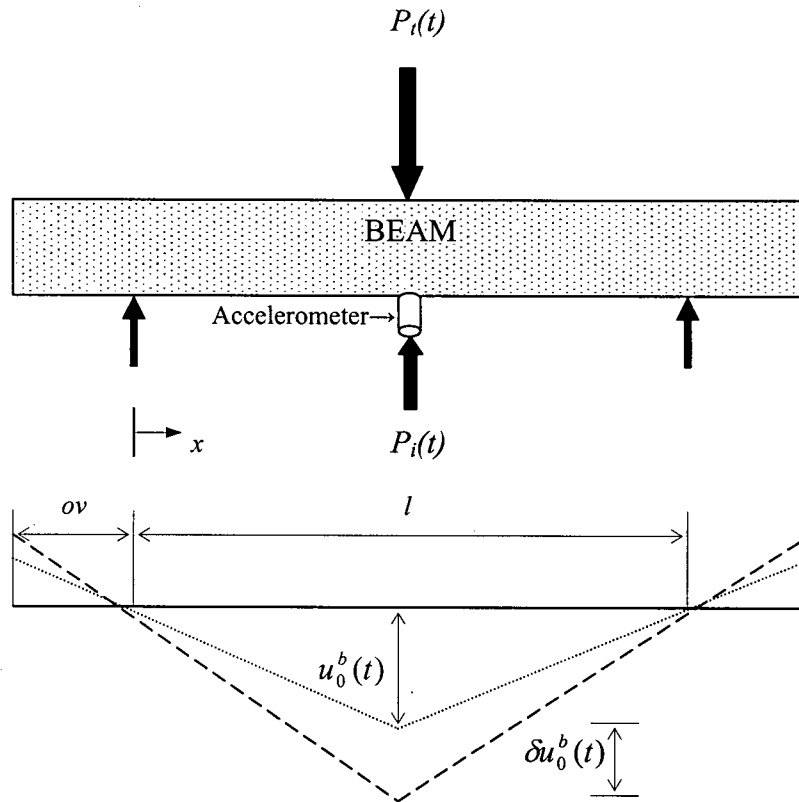
Figure 5.1　The Generalized Inertial Load and Acceleration Distribution for a Plain (or Fiber Reinforced) Concrete Beam

69

The inertial load dI, for the beam segment dx, with acceleration $\ddot{u}(x,t)$ at its center is then given by:

$$dI(x,t) = \rho A \ddot{u}(x,t)dx \qquad \qquad ...(5.4)$$

where, ρ = density of concrete

         A = area of cross-section of the beam

A generalized inertial load at mid-span, $P_i(t)$ may be obtained by using the principle of virtual work. Here, the virtual work done by the distributed inertial load acting over the distributed virtual displacement should be equal to the virtual work done by the generalized inertial load $P_i(t)$, acting over the virtual displacement at the center. Accounting for beam overhang ov, the generalized inertial load is given by::

$$P_i(t)\delta u_0^b = 2 \int_{-ov}^{\frac{l}{2}} \rho A \ddot{u}(x,t)\delta u(x,t)dx \qquad \qquad ...(5.5)$$

where, l = clear-span of the beam

         ov = length of overhang

Substituting Equations (5.2) and (5.3) into Equation (5.5), $P_i(t)$ may be obtained as:

$$P_i(t) = \rho A \ddot{u}_0^b(t)\left[\frac{l}{3} + \frac{8(ov)^3}{3l^2}\right] \qquad \qquad ...(5.6)$$

Once the generalized inertial load is calculated, the true generalized bending load, $P_i(t)$ can be determined by using Equation (5.7):

$$P_b(t) = P_t(t) - P_i(t) \qquad \qquad ...(5.7)$$

where, $P_t(t)$ = tup-load recorded by the load-cell

Figure 5.2 shows the performance of plain concrete under an "equal potential energy" condition and Figure 5.3 shows the performance under the "equal drop height" condition. The quasi-static response is also shown for comparison.
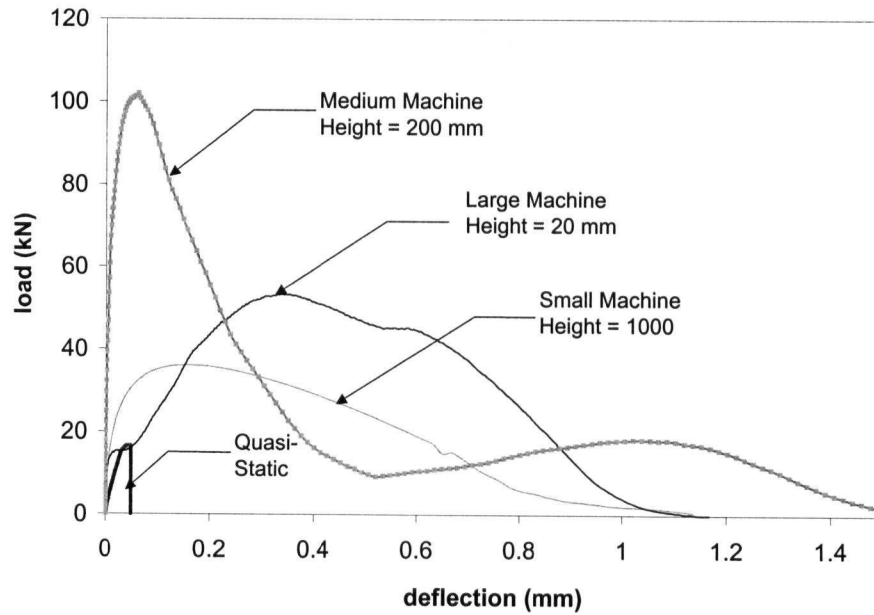
Figure 5.2   Flexural Response of Plain Concrete under Impact at Equal Potential
Energy
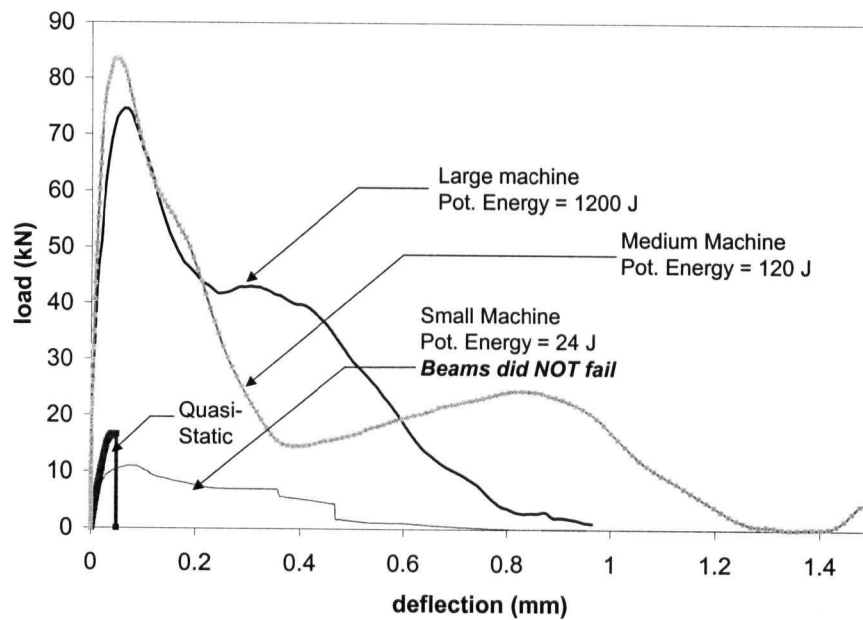
Figure 5.3   Flexural Response of Plain Concrete to Impact through Equal Drop Height

After analysing the data, the inertial correction appeared only for the two larger machines
and these are shown in Figure 5.4. Upon impact, in all but the case for beams in the small
machine during the second testing regime, the event ended with the beams breaking into
two halves.

71
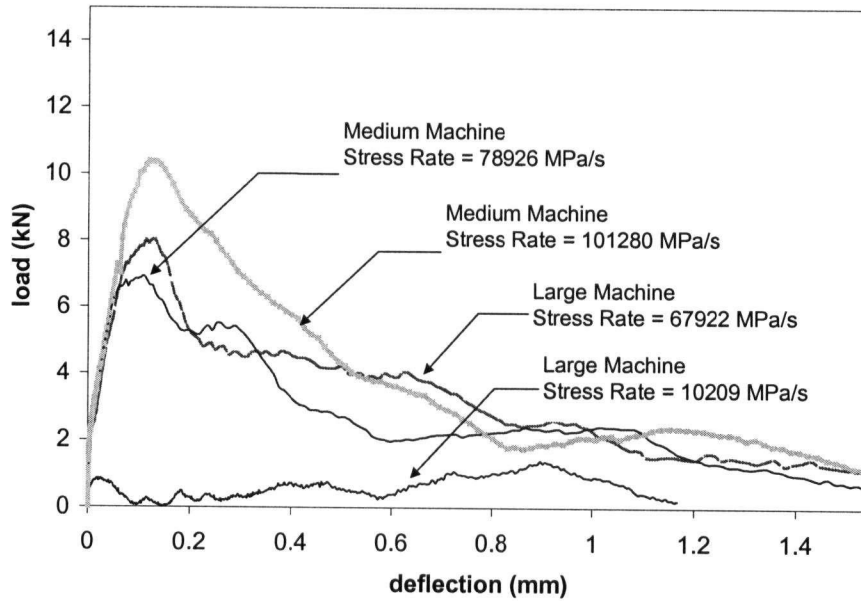
Figure 5.4   Inertial Load Correction for LARGE and MEDIUM Machines

The beam velocity (at mid-span), machine losses, stress rates achieved and the corresponding flexural toughness values are given in Table-5.2.

Table 5.2   Results from the Impact Tests (3 Specimens)

	Equal Potential Energy					
Machine type	Beam Velocity (m/s)		Machine Loss		Stress	Flexural
	Peak	Failure	Peak (%)	Failure (%)	Rate (MPa/s)	Toughness (J)
Large	0.32	0.74	57.67 (8.65)	46.58 (7.73)	1.02E+04	32.41 (5.18)
Medium	0.66	2.09	81.23 (8.2)	52.18 (5.81)	1.01E+05	26.56 (2.39)
Small	1.68	4.41	52.77 (11.08)	54.40 (10.92)	5.59E+04	21.25 (4.03)
	Equal Drop Height					
Machine type	Beam Velocity		Machine Loss		Stress	Flexural
	Peak	Failure	Peak (%)	Failure (%)	Rate (MPa/s)	Toughness (J)
Large	0.69	2.13	80.99 (11.34)	56.68 (8.5)	6.79E+04	28.82 (4.61)
Medium	0.65	1.89	81.96 (9.02)	58.05 (5.75)	7.89E+04	23.35 (2.1)
Small	0.45	0.98	84.60 (7.17)	65.94 (5.98)	1.07E+04	4.42 (0.35) *(beams did not fail)*

The main difference between the static and the dynamic response in either loading regime (Figure 5.2 and 5.3) is the increase in the peak load and fracture energy under impact. This difference may be explained on the basis of fracture mechanics and the concept of sub-critical crack growth. The Griffith theory states that the tip of a crack (or a flaw) in a loaded continuum is a point of stress concentration. Although the nominal stress may be far below the theoretical strength of the material, the stress at the crack tip may well approach this theoretical strength and thus result in failure. The stress at the vicinity of the crack tip is a function of both the nominal stress and the crack geometry. These two parameters may be combined to express crack growth in a brittle material in terms of a single parameter, known as the stress intensity factor, K_I. Failure is said to occur when the stress intensity factor reaches a critical value 'K_{IC}', called the fracture toughness.

The concept of subcritical crack growth implies that a crack of subcritical size can grow through mechanism such as stress- corrosion. So, when the size of the crack reaches the critical size (such that $K_I = K_{IC}$), the crack becomes unstable and failure will occur. Now, subcritical crack growth has been found to be rate-sensitive according to Equation (5.8) (described in Chapter 3 as Equation (3.9)):

$$V = AK_I^n \qquad \qquad ...(5.8)$$

The growth of a subcritical crack occurs at an increasing rate under a constant nominal stress as the crack extends. If the loading is slow, the subcritical flaws have enough time to grow and approach the critical value, thereby causing failure. But if the loading is rapid, there is little or no time for the subcritical crack to grow. Therefore, the member can support momentarily, a higher load, giving the material an apparently high strength. Now, for an ideally brittle material, the energy consumed for unit crack extension is a constant. But concrete is not an ideally brittle material and as such, the propagation of a crack is preceded by a formation of a process zone around the crack tip. The formation of the process zone requires energy and thus, the total energy that must be supplied to enable unstable crack growth is a sum of energies required for crack extension ahead of the crack as well as subcritical cracking in the process zone. Therefore, under impact, the

higher energy requirement in the post peak region of Figures 5.2 and 5.3 is probably a reflection of an increase in the width of the process zone compared to static loading.

5.2.3 Energy Balance

The energy lost to the machine during an event may be derived from the principle of "energy balance" where, at any time during the impact, the energy lost by the hammer should be accounted for following the law of conservation of energy. In order to describe the loss in energy to the machines, an energy balance was performed in accordance with Banthia *et al.* [138]. Briefly, loss in kinetic energy of the hammer ΔE (t) may be written as

$$\Delta E (t) \quad = \quad E_m (t) + E_{KEr} (t) \quad + \quad E_b (t) \qquad \ldots(5.9)$$

where, $\quad \Delta E(t) \quad$ = total energy lost by the hammer

E_m (t) $\quad$ = energy lost to the various machine parts in the form of vibration or elastic energy (i.e. machine losses)

E_{KEr} (t)= rotational kinetic energy of the specimen

E_b (t) $\quad$ = bending energy in the specimen eventually utilized in fracture

Here, $E_m(t)$ represents the energy lost to the machine while the sum of $E_{KEr}(t)$ and $E_b(t)$ represent the energy consumed by the specimen.

Energy Balance at Peak Load

At peak load (t = t_p), the bending energy given by the area under the load-vs.-mid span-displacement plot, comprises of the elastic strain energy, $E_{SE}(t_p)$ and the work of fracture $E_{WOF}(t_p)$:

$$E_b(t_p) \quad = \quad E_{SE}(t_p) \quad + \quad E_{WOF}(t_p) \qquad \ldots(5.10)$$

Energy Balance Just After Failure

At the end of the impact event $(t=t_f)$, once again, the bending energy $E_b(t_f)$ is evaluated as the area under the load-mid span displacement plot. However, since the strain energy can be assumed to be negligible in the broken halves of the beam, all of the energy $E_b(t_f)$ represents the work of fracture, or the fracture energy, $E_{WOF}(t_f)$.
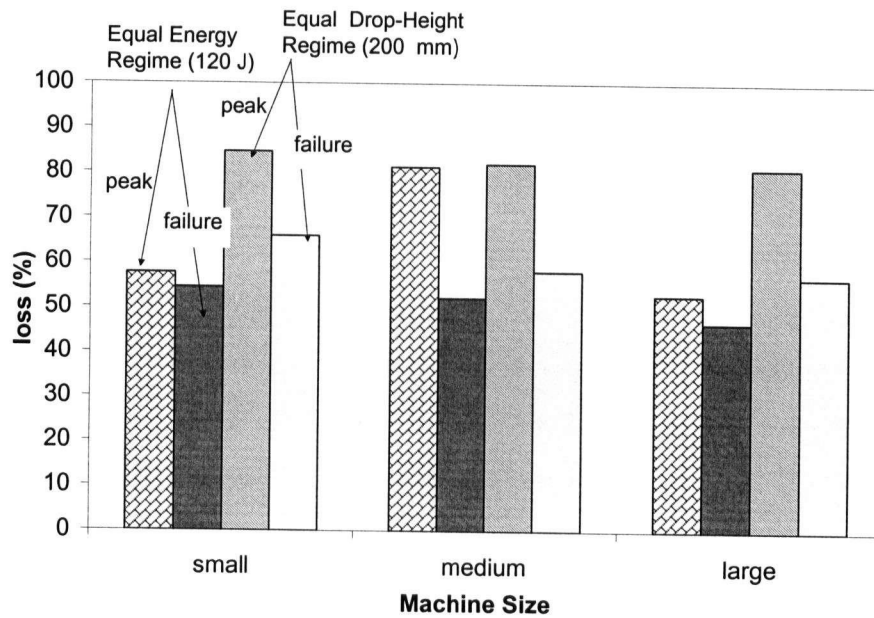
Figure 5.5   Energy Lost to Test Machines

In equation (5.9), $\Delta E(t)$ may be evaluated through the impulse-momentum relationship, while $E_{KEr}(t)$ is obtained from calculating the beam velocity at mid-span. The bending energy, $E_b(t)$ is given by the area under the load vs. mid-span deflection plot. Thus the quantity $E_m(t)$ described as the "machine losses" may now be calculated. Figure 5.5 presents the machine losses as a percentage of the total energy lost by the hammer ($= E_m/\Delta E \times 100$).

As reported by Banthia *et al.* [138], here too the loss of energy to the machine was very high at the point of peak load (~80%), but was considerably less at failure (~50%). For equal drop-heights, the percentage loss in energy at peak load and failure was nearly identical across all machines, provided the specimen fractured. For both regimes, at failure, the larger machine consistently absorbed the least energy as machine losses. Figure 5.6 shows the stress-rate sensitivity of plain concrete (modulus of rupture vs. stress rate), represented by N for the different machines.
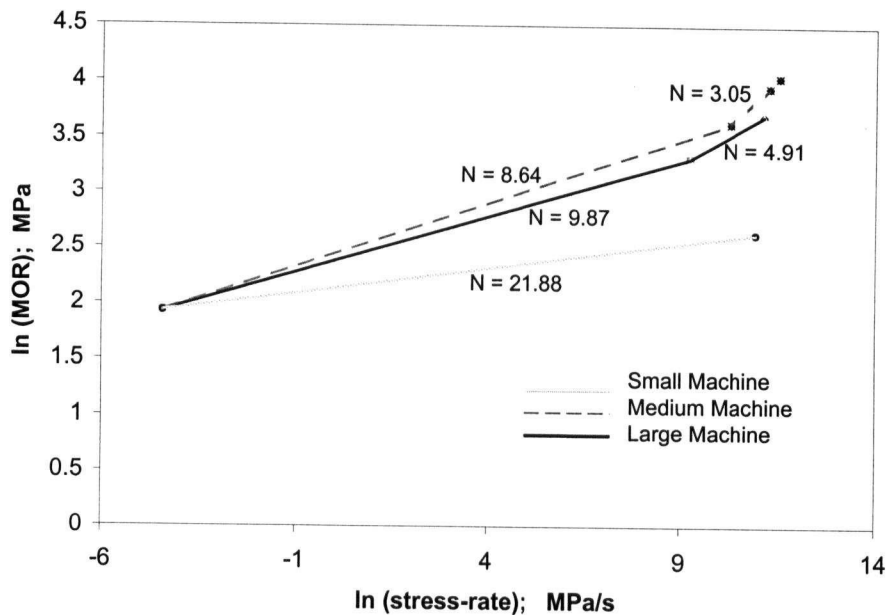
Figure 5.6   Stress-Rate Sensitivity of Plain Concrete under Flexure

For the same material, notice a considerable variation in the perceived sensitivity in Figure 5.6. In terms of energy dissipated, Figure 5.7 shows the effect of stress-rate on the flexural toughness of the beams. Once again, a unique stress-rate sensitivity does not emerge. In fact, while for the two smaller machines, the flexural toughness of concrete is highly stress-rate dependent in the impact range, for the large machine, it appears to be relatively insensitive.
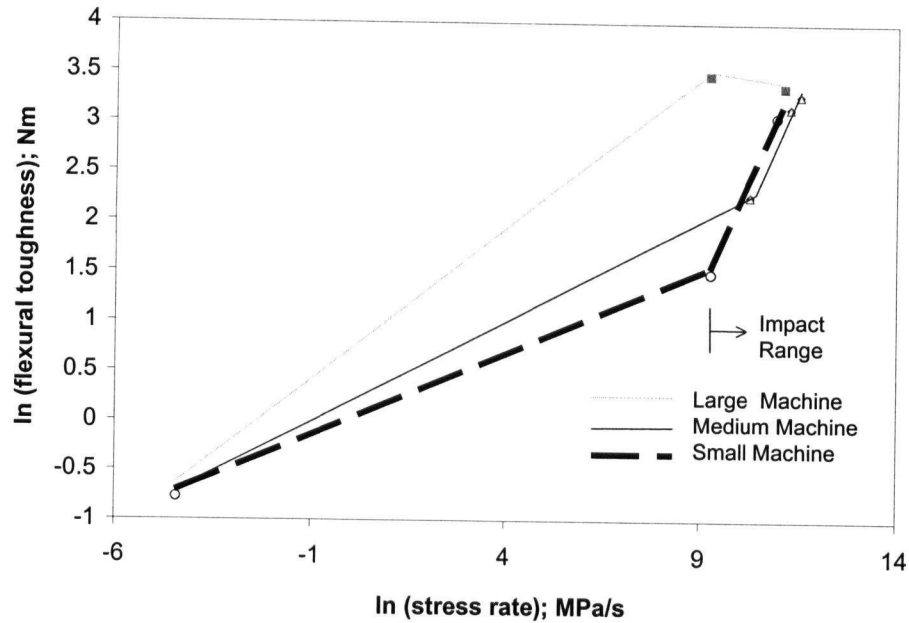
Figure 5.7   Effect of Stress-Rate on the Flexural Toughness of Plain Concrete Beams

In order to explain this phenomenon, one must examine the load-time and deflection-time responses, as shown in Figures 5.8 and 5.9.
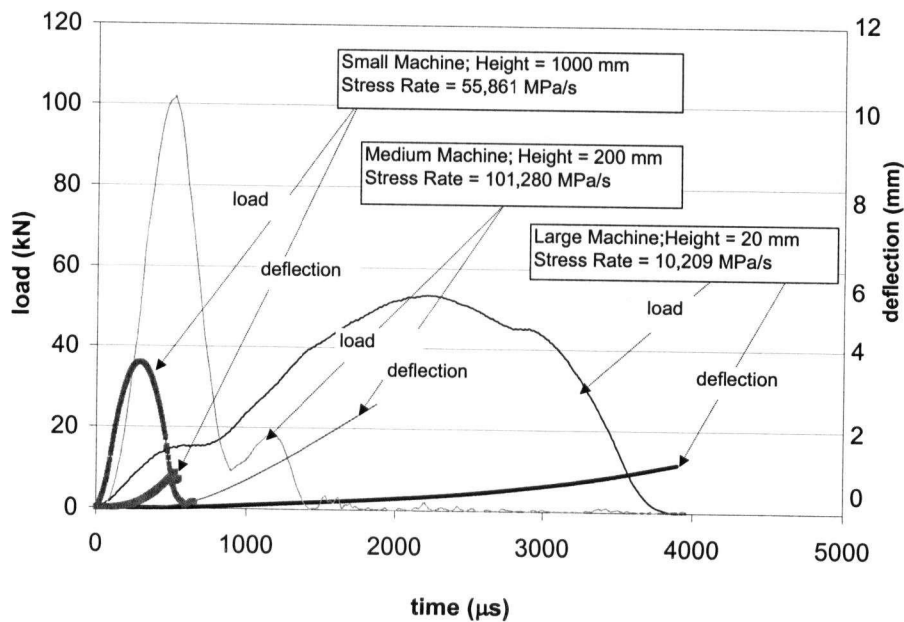
Figure 5.8   Impact Response of Plain Concrete under Equal Potential Energy Regime
               (Time Histories)

It may be seen that since the larger machines carried a heavier hammer, this resulted in an impact pulse of longer duration. The impact pulse was consequently 'flatter' and spread over the period of impact in comparison with those from the smaller machines.
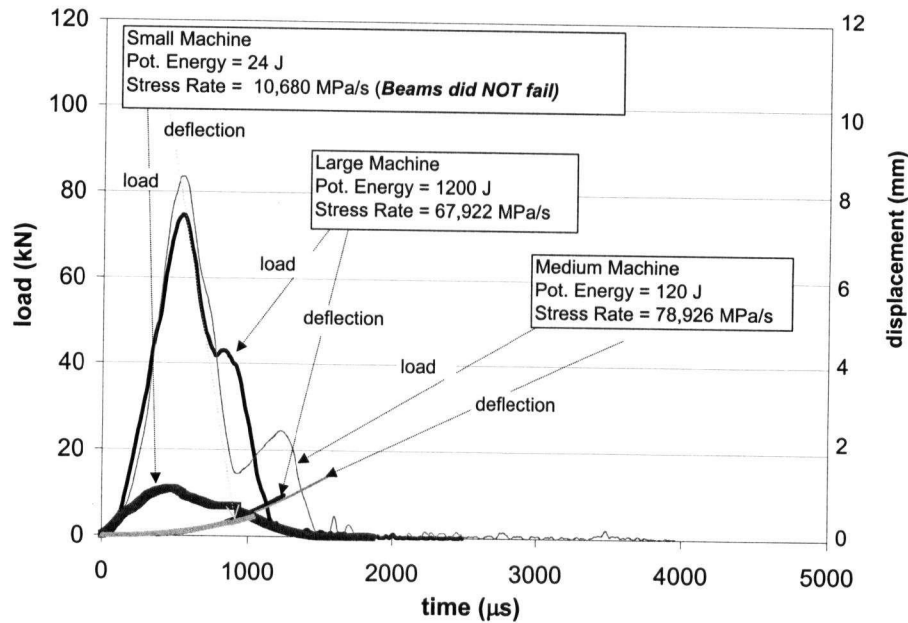
Figure 5.9   Impact Response of Plain Concrete under Equal Drop-Height Regime (Time Histories)

This means that for the larger machines, even at low stress-rates, the transfer momentum and hence the bending energy was high. On the other hand, smaller machines imparted shorter pulses and thus resulted in smaller values of bending energy and hence lower toughness at low stress rates. When the hammer was raised higher, the pulse duration fell universally with all machines, thus resulting in higher stress rates. Note that this drop in the pulse duration was greater for larger machines. Therefore the relative increase in bending energy was always greater with smaller machines (i.e. machines with lighter hammer mass).

5.3   Size effects

5.3.1   Flexural response

Figures 5.10a-d show the flexural response of the plain concrete beams of various sizes under impact from four drop heights. Table 5.3 lists the mechanical properties obtained from these tests. Notice a drop in peak flexural stress for larger beams. Under impact, as seen in the stress-time plots (Figures 5.11a-d), notice that the time to peak load increases
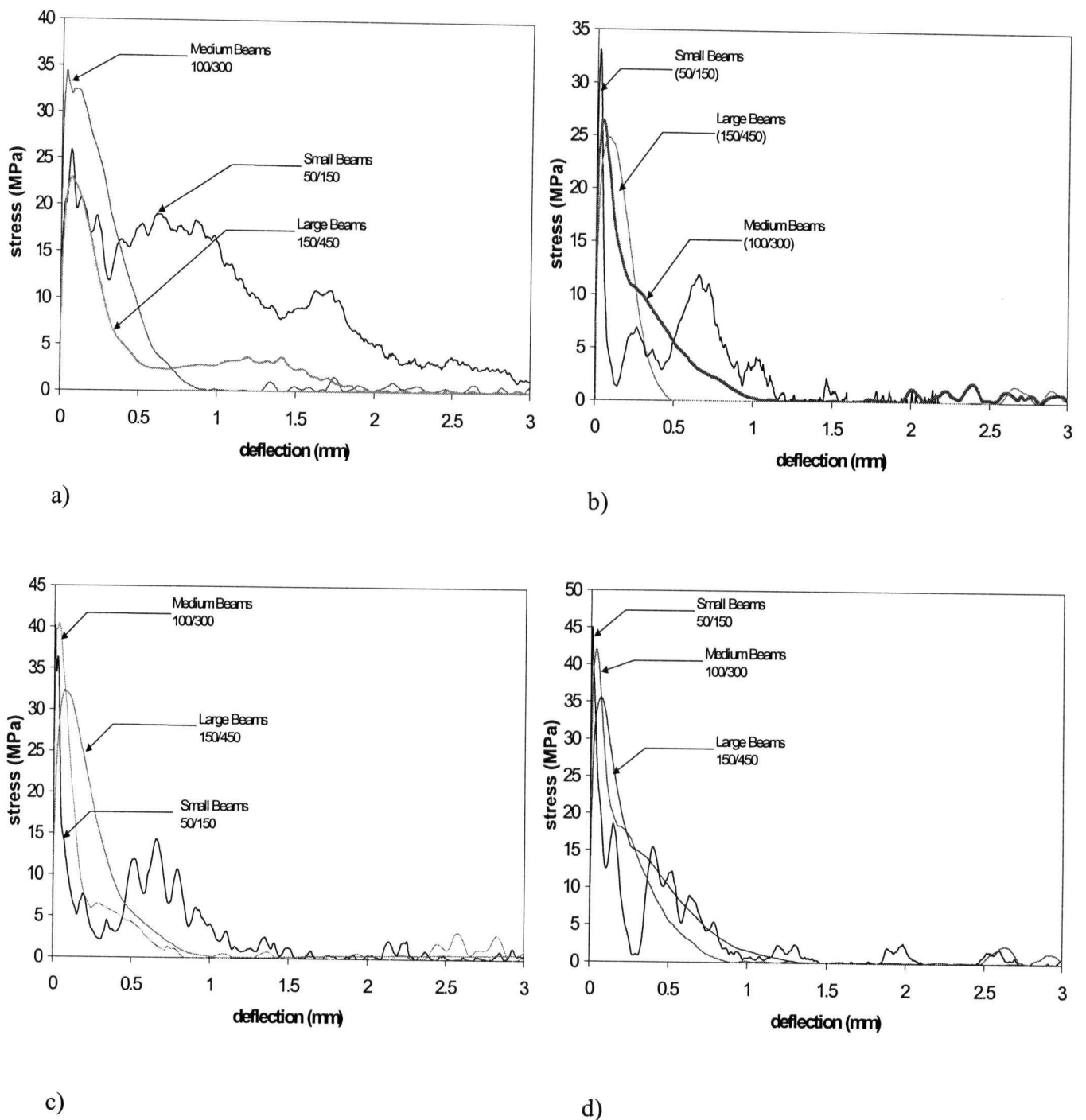
Figure 5.10   Effect of Size on the Impact Response of Plain Concrete Beams under a
Drop-Height of a) 200 mm; b) 500 mm; c) 750 mm & d) 1000 mm
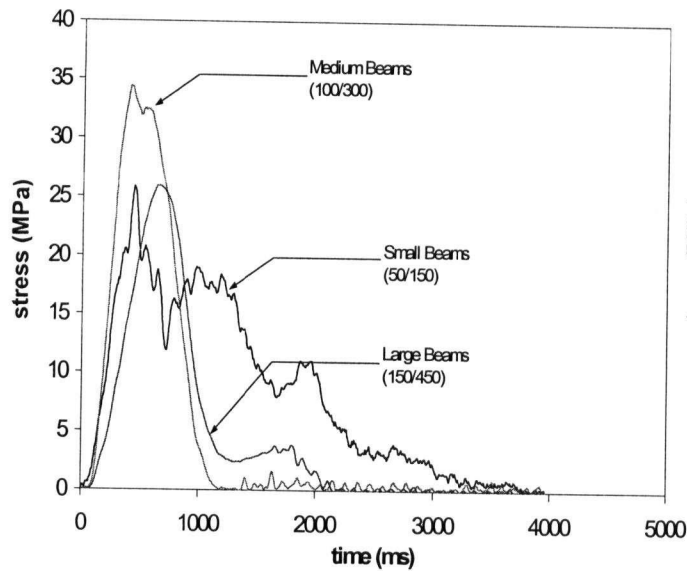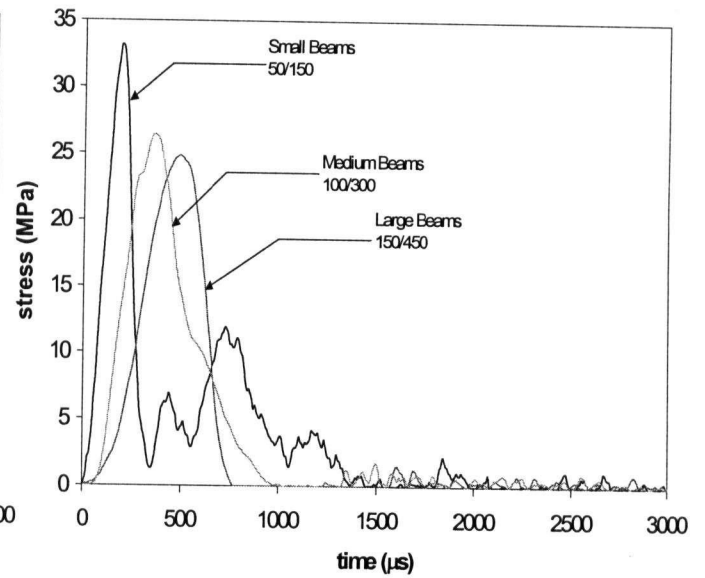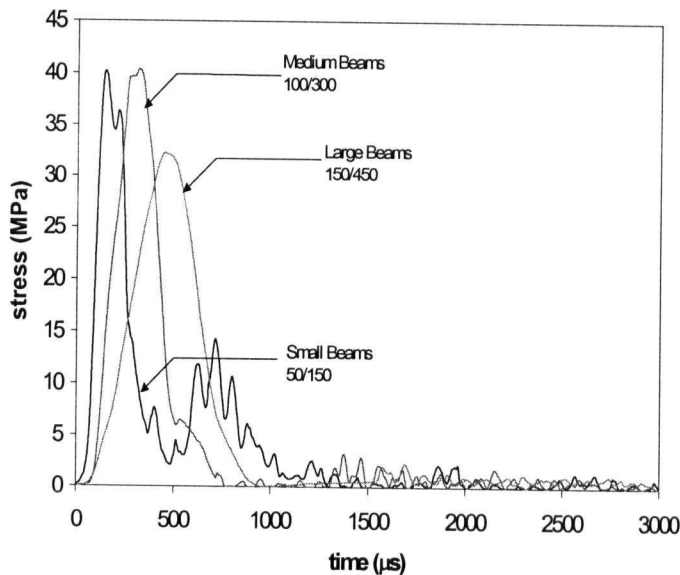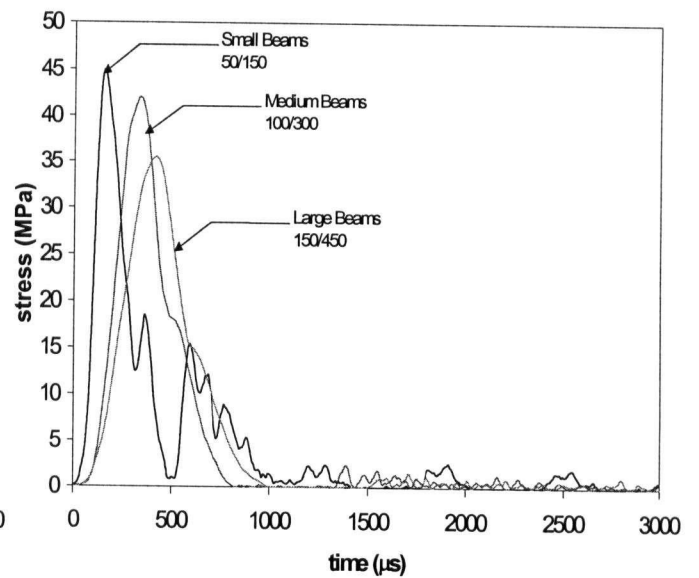
Figure 5.11   Stress-Time Response of Plain Concrete Beams under Impact Loading from a Drop-Height of: a) 200 mm; b) 500 mm; c) 750 mm & d)1000 mm

with specimen size. This means that for identical loading conditions, smaller specimens experience a higher stress-rate, as seen in Figure 5.12. Furthermore, as seen from Table

5.3, the ratio of time to peak varies in proportion to the characteristic specimen size (beam depth). Qian *et al.* [128] have reported a similar trend during projectile impact on composites plates. Each series of impact tests has been analysed to account for the underlying inertial effects. The broken beams were later examined to study the crack path. Figure 5.13 reveals the trend for aggregate fracture. Notice a fall in the proportion of aggregates that fracture with increasing beam size. For the sake of comparison, the quasi-static test data in this section is taken from a previous study by Chen [124].
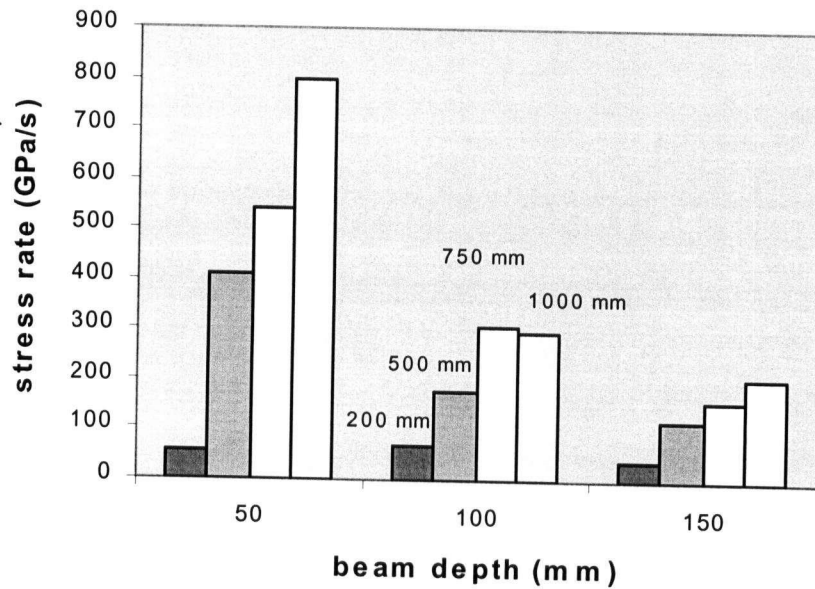
Figure 5.12   Effect of Size on the Apparent Stress-Rate Experienced by Plain Concrete Beams
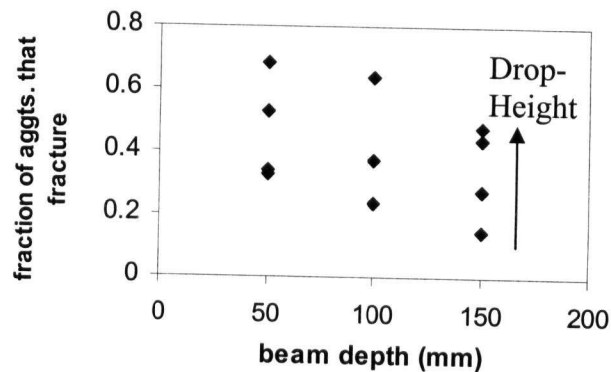
Figure 5.13   Aggregate Fracture after Impact Failure of Plain Concrete Beams

Table 5.3　Results of Impact Testing (6 Specimens)

Beam size	Drop height (mm)	Peak stress (MPa)	t_p time to peak (μs)	Deflection at peak (mm)	Stress rate (MPa/s)
Small	200	25.41 (5.10)	456 (16)	0.065	54.63
	500	32.78 (5.89)	200 (24)	0.017	411.09
	750	39.74 (7.55)	152 (8)	0.005	539.50
	1000	44.98 (9.91)	152 (8)	0.007	794.76
Medium	200	33.12 (3.20)	448 (24)	0.033	69.83
	500	26.35 (2.37)	368 (8)	0.047	174.63
	750	39.68 (4.83)	280 (24)	0.037	308.34
	1000	41.84 (4.39)	344 (16)	0.039	297.62
Large	200	24.75 (1.98)	744 (32)	0.073	40.63
	500	24.78 (2.23)	496 (24)	0.090	121.11
	750	32.30 (3.07)	448 (8)	0.084	160.20
	1000	35.42 (2.88)	424 (8)	0.077	203.33

Table 5.4　Model Parameters to Effect Optimized Curve Fitting (6 Specimens)

Loading type	BSEL		MFSL	
	Bf_u	d_0	f_t	L_{ch}
Quasi-static	5.56	319.39	4.34	21.52
200 mm drop	34.54	226.73	26.60	12.38
500 mm drop	96.59	107.11	52.86	61.59
750 mm drop	139.21	75.36	64.21	92.95
1000 mm drop	152.76	69.82	67.80	99.63
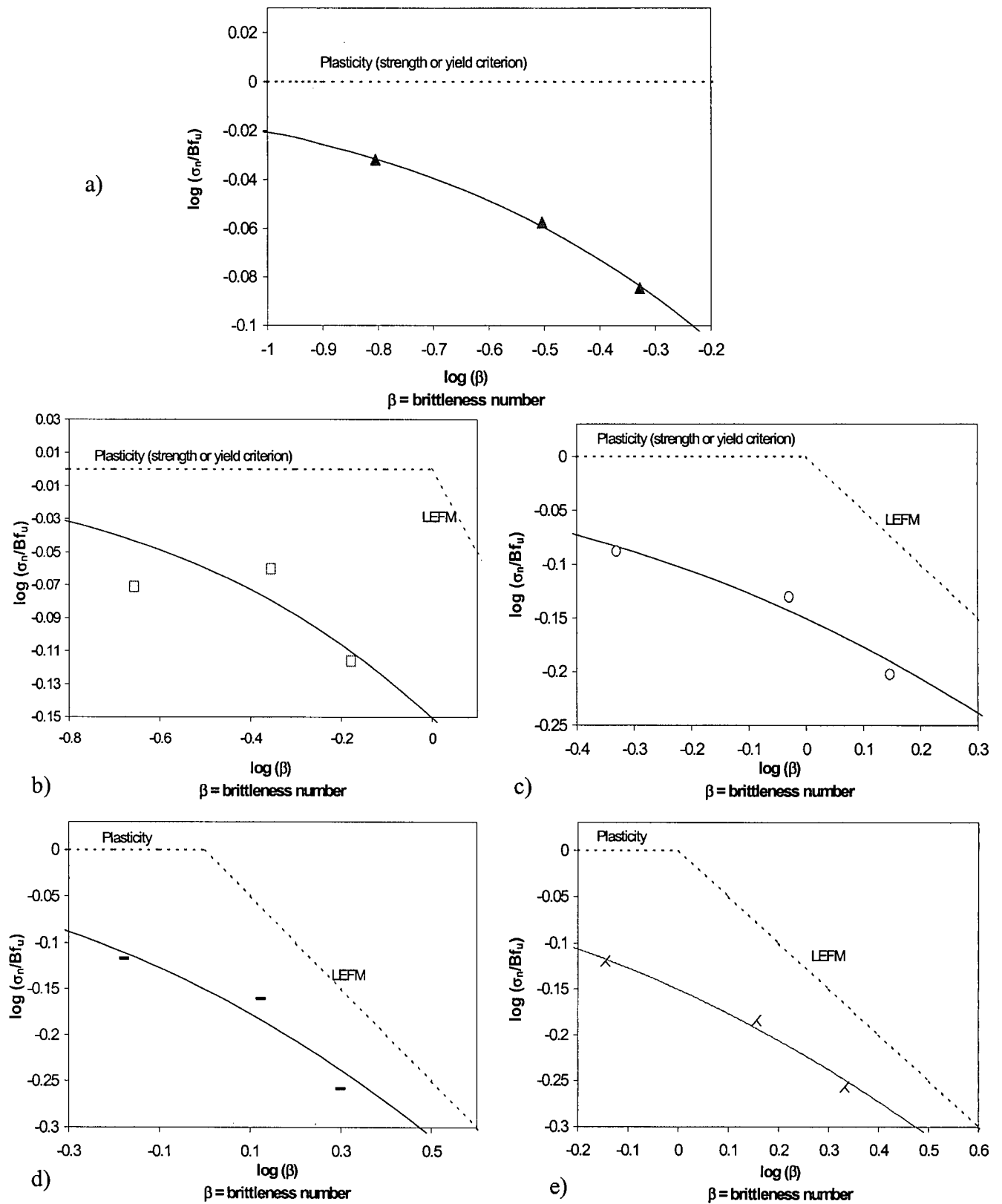
Figure 5.14   Flexural Test Data Fitted According to BSEL: a) Quasi-Static; b) 200 mm

Drop; c) 500 mm Drop; d) 750 mm Drop; e) 1000 mm Drop
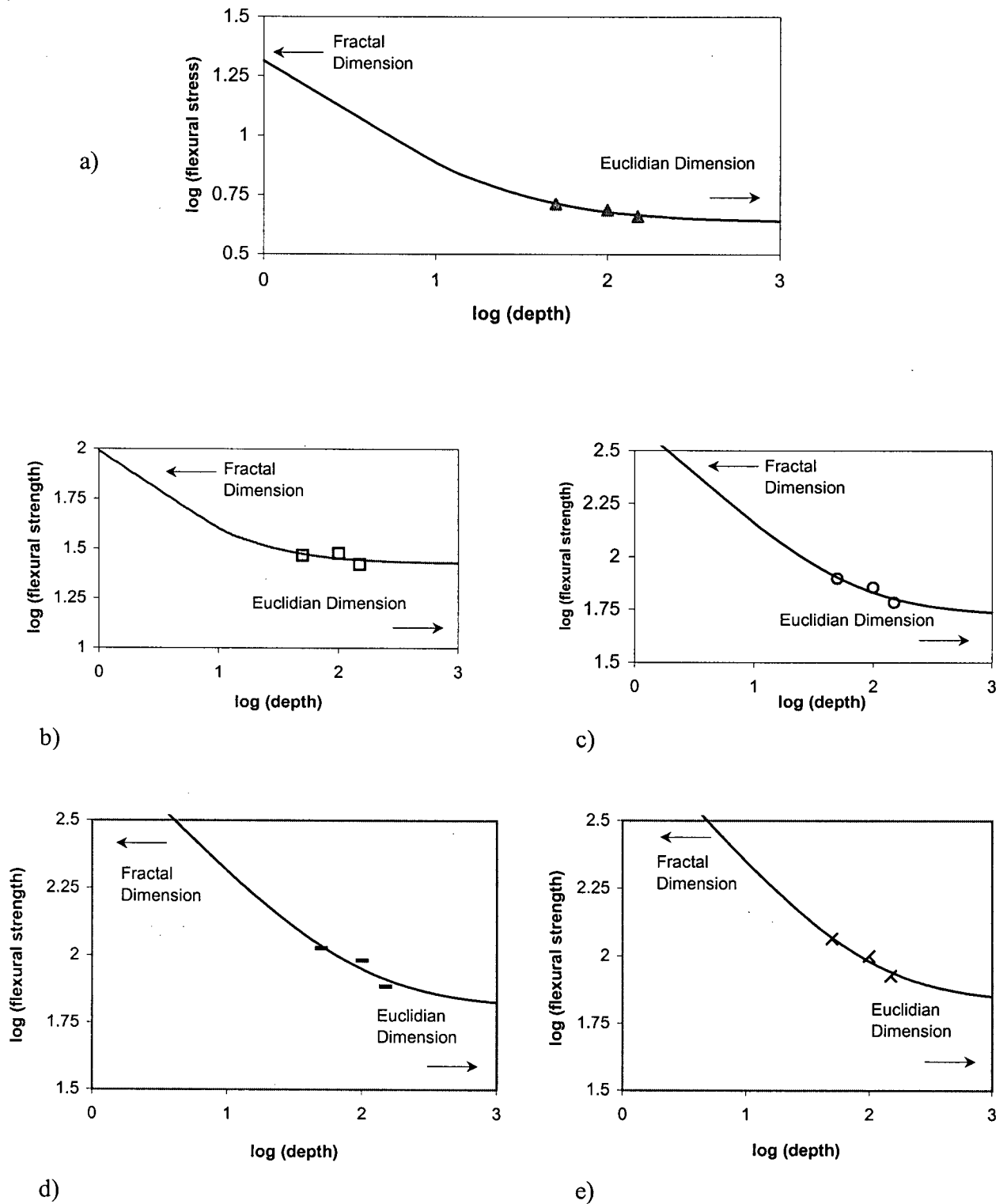
Figure 5.15 Flexural Test Data Fitted According to MFSL: a) Quasi-Static;
b) 200 mm Drop; c) 500 mm Drop; d) 750 mm Drop; e) 1000 mm Drop

84

The data obtained from the impact tests were fitted to Bažant's Size Effect Model [Equation (3.21)] by means of a mathematical software, employing the Levenberg-Marquardt principle [139]. The curves in Figure 5.14a-e are the optimized fits for each loading condition. The optimized values of Bf_u and d_0 are listed in Table 5.4. Similarly, the impact data has been fitted to the Multifractal Scaling Law [Equation (3.22)] in Figure 5.15a-e. As pointed out earlier, both MFSL and SSEL are in complete accordance. Hence, for the purpose of comparison, only BSEL and MFSL are considered in the present study.

5.3.2   Discussion

5.3.2.1 Stress rate sensitivity

The formulation proposed by Nadeau *et al.* [Equation (3.10)] has been adopted in Figure 5.16 to describe the stress rate sensitivity for the beams in this study. Notice that larger beams depict a higher stress rate sensitivity (this corresponds to a lower value for the parameter 'N'). Since larger beams also exhibit a lower apparent strength, the above phenomenon (i.e. a higher sensitivity) is in keeping with the trend observed for all lower strength materials. A case in point is the higher stress rate sensitivity noticed for low strength concrete compared to higher strength concrete.
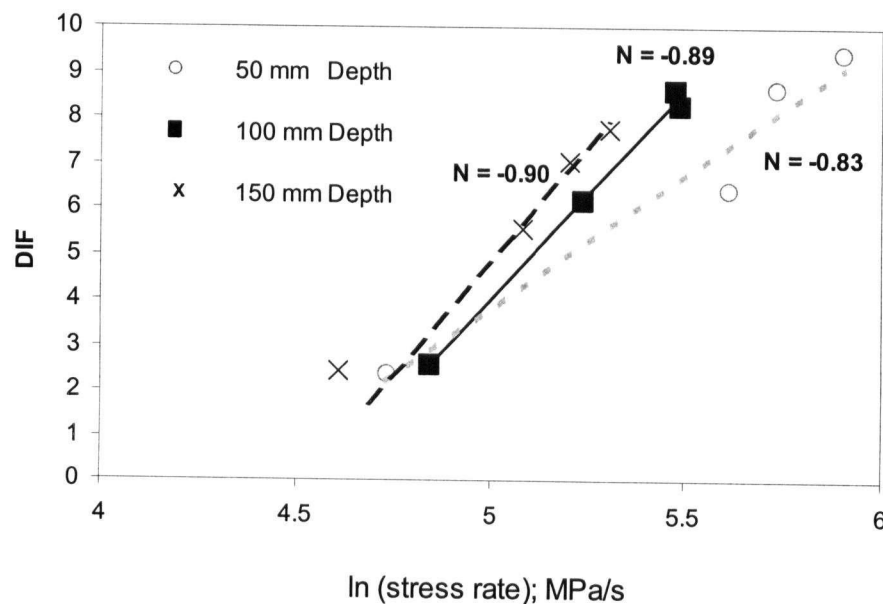
Figure 5.16   Size-Effect on the Stress-Rate Sensitivity of Plain Concrete Beams

Further, the issue of size effects under impact loading is made more difficult by the fact that maintaining an identical stress-rate during impact tests on specimens of varying sizes is impossible. For identical drop heights, larger beams experience lower stress rates, and hence what one notices is a combined influence of size and stress-rate, rather than that of size alone. Therefore, smaller beams depict higher apparent strength due not only to their smaller size but also due to having experienced a higher stress rate. Clearly, one must normalize[1] the test data with respect to constant stress rate in order to observe the true influence of specimen size. In this study, this normalization was carried out on the basis of the stress rate sensitivity plot determined earlier (Figure 5.16).

5.3.2.2 Brittleness and Fracture Energy

As seen in Figures 5.14 and 5.15, for each loading rate, the data can be fitted satisfactorily to either of the two models. A better understanding of the behaviour emerges from Figures 5.17 and 5.18 where, the size effect for various loading rates has been combined into a single plot, according to BSEL and MFSL respectively.
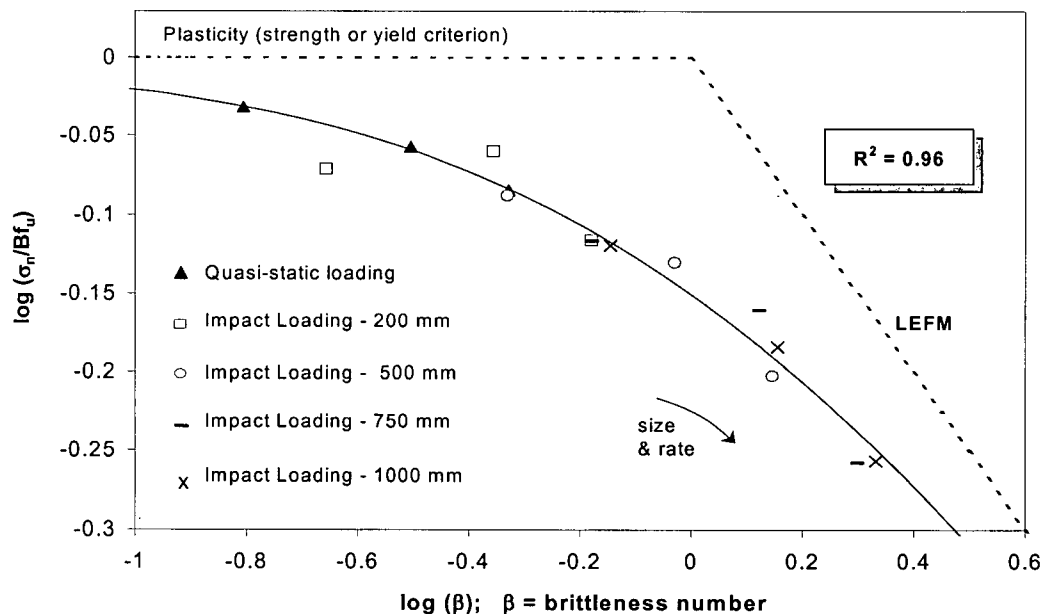
Figure 5.17   Size-Effect on the Flexural Strength of Plain Concrete Beams under Different Loading Rates (Described by BSEL)

---

[1] Morton [127] proposed that under impact loading, scaling requires that the time-to-peak-load be kept constant for all sizes. A similar suggestion is made by Bažant and Gettu [125]. However, it was practically impossible under the present testing conditions. Hence an indirect approach was adopted where by the apparent stress rate was normalized.
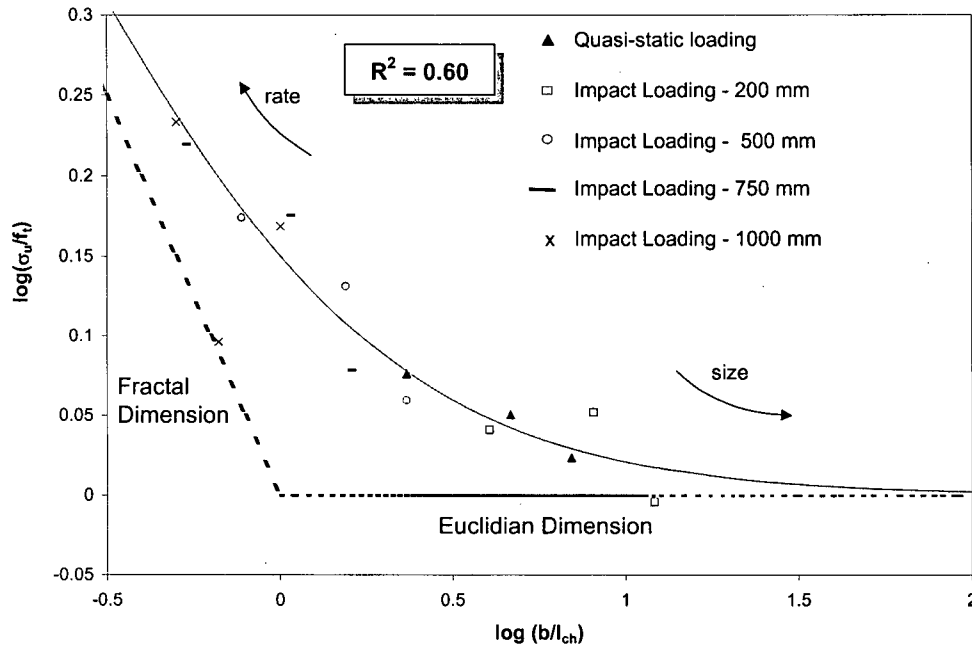
Figure 5.18   Size-Effect on the Flexural Strength of Plain Concrete Beams under Different Loading Rates (Described by MFSL)

The following distinction between the two models emerges from the plots: under MFSL, while an increase in the rate yields a shift towards the LEFM behaviour, an increase in the size results in the nominal strength approaching an asymptote. On the other hand, under BSEL, increase in both size and rate result in a shift towards LEFM behaviour. For the present study, notice that the correlation coefficient (represented by R^2 in Figures 5.17 and 5.18) is significantly higher in the case of Bažant's Size Effect Model, indicating a better fit.

Bažant and Gettu [125] in their study on creep detect size effects with an increasing brittleness under creep rates ($t_p > 10,000$ s). The present study indicates a shift towards brittle behaviour even under impact. This apparent contradiction has been suggested earlier by Wittmann [126] and may be explained as follows: A higher brittleness arises out of a smaller fracture process zone or the localization of the energy dissipation within a smaller area at the crack tip. Under creep, the relaxation of the stresses leads to a lower stress concentration at the crack tip and therefore a smaller process zone. Where as, under impact, the energy dissipation is concentrated within a small area due to inertial effects

(i.e. the material farther from the crack tip does not have time to react). Thus, at both extremes rates of loading (creep and impact), one sees a shift towards higher brittleness. Figure 5.19 shows the relative increase in fracture energy 'G_f' (for different sizes) due to loading rate, where G_{f-I} and G_{f-s} are for the impact and static cases, respectively.
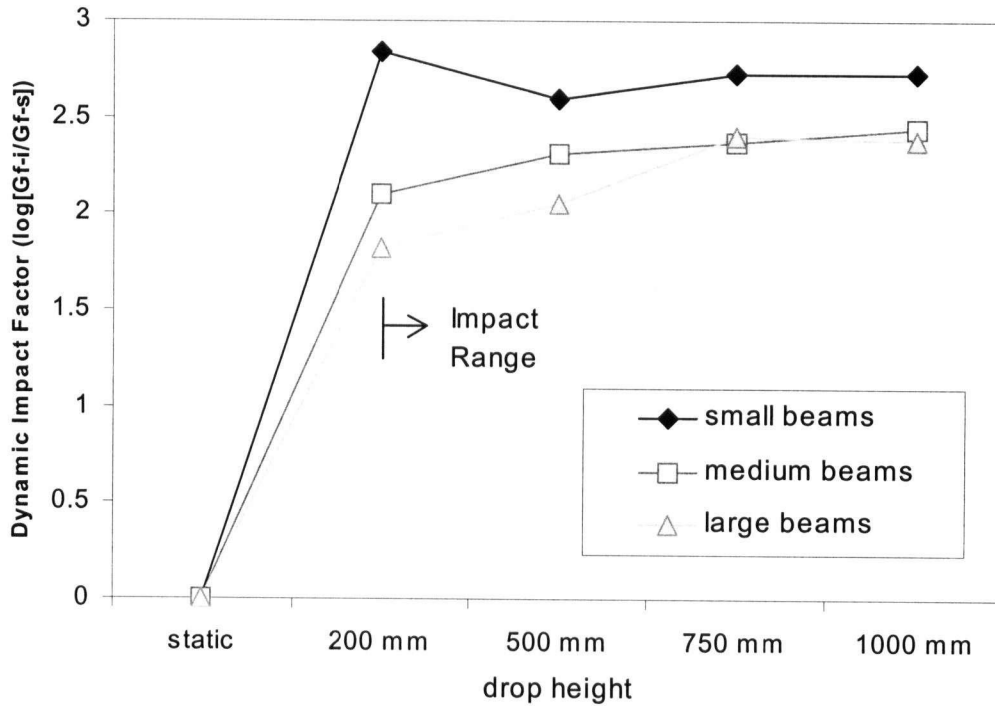
Figure 5.19   Influence of Size and Loading Condition on the Fracture Energy of Plain Concrete Beams

The trend-lines yield the following relationships for the rate sensitivity of 'G_f':

DIF (= G_{fi}/G_{fs}) = 0.4404 ln $\dot{\sigma}$ + 0.1548   (for beams of depth 50 mm)

DIF (= G_{fi}/G_{fs}) = 0.4824 ln $\dot{\sigma}$ - 0.2279   (for beams of depth 100 mm)

DIF (= G_{fi}/G_{fs}) = 0.8499 ln $\dot{\sigma}$ - 2.1249   (for beams of depth 150 mm)

Note that larger specimens exhibit a somewhat higher stress rate sensitivity for G_f in the impact range. This is in keeping with the trends seen under quasi-static rates by Oh and Chung [140]. Given that a higher fraction of aggregates underwent fracture during the failure of smaller beams, as well as the greater time-to-peak stress in the case of larger

88

beams, it is clear that a more tortuous path is taken by the moving crack in the case of larger beams. This resembles the behaviour of low-strength concrete. Therefore, increasing the specimen size appears in many ways analogous to reducing its strength. In the present study, the self-weight of the beams was not considered. Mindess [122] reported that accounting for self-weight yields no size-effect on the fracture energy of plain concrete under quasi-static loading. However, self-weight remains a statically applied load and its part in influencing size-effects is expected to diminish under impact rates of loading. It is fair to say that if the self-weight were considered, the size-effect seen here will diminish somewhat. However, in Figures 5.17 and 5.18, notice that the size-effect is not the same across all drop-heights. This indicates that the size-effect noticed in the present study on impact, is not solely due to a lack of normalizing for the self-weight of the beams.

While higher loading rates and larger specimen size, both result in an increased brittleness, it remains to be seen whether the latter effect (due to size) intensifies/diminishes or even levels off at very large sizes. The range of sizes investigated in this study does not distinguish between BSEL and MFSL (although clearly, they are very different in their predictions). Performing tests on a higher range of sizes should reveal a better understanding of the nature of the size effect. As indicated by Arslan and Ince [114], neural network modeling reveals a behaviour which would support the contention of both MFSL and BSEL, through a smooth transition between them for very large sizes. Clearly, a more physical approach (as opposed to the semi-empirical approaches characterized by the existing size effect laws) will ultimately lead to reliable design tools for impact. Furthermore, it remains to be seen how the amount and the type of fiber reinforcement affect the size-effect under impact loading. These issues are addressed in Chapter 6.

5.4   Conclusions

The following conclusions were drawn on the basis of the results in this Chapter:

1. Energy lost to the machine is greatest at the instant of peak load and is considerably less at failure.

2. Stress-rate sensitivity of MOR and flexural toughness is dependent upon the drop-weight machine used for testing. If the drop-height is maintained, beams that failed experienced similar stress-rates, regardless of machine capacity.

3. Lighter hammers and greater drop heights, both produce shorter pulses. Hence, the choice of a testing machine must reflect practical impact conditions.

4. Size effect in plain concrete has been identified under impact loading, although this study does not account for the self-weight of the specimen. It was found that the stress rate sensitivity of plain concrete is affected by the specimen size. Larger beams exhibit higher stress rate sensitivity for both nominal strength and fracture energy.

5. There is an increase in the time-to-peak for greater specimen sizes. On the other hand, for identical loading conditions, smaller specimens witness higher stress rates.

6. The size effect behaviour of plain concrete under impact is effectively captured by both, Bažant's Size Effect Law and the Multifractal Scaling Law. However, for the data obtained in the present study, a better correlation is achieved through Bažant's Size Effect Law.

7. Impact loading results in an increasingly brittle behaviour and shifts the material response towards LEFM predictions. Increasing the size causes a further shift towards brittle behaviour. This implies that the size effect becomes more pronounced at higher loading rates.

Chapter 6

IMPACT RESPONSE OF FIBER REINFORCED CONCRETE, PART-1: FIBER-MATRIX INTERACTION

6.1   Introduction

Fiber reinforced concrete (FRC) is a composite with at least three distinct phases: the fiber, the cementitious matrix and the fiber-matrix interface. For proper optimization of the composite, a rational understanding of the complex interaction within these three phases and the interrelated micro-mechanical processes is essential.

One may divide the load-displacement response of conventional FRC into two qualitative phases: first, the pre-peak response during which only the relatively weaker and more brittle cement-based matrix undergoes tensile micro-fracturing and second, the post-peak response where fibers bridge fully coalesced matrix cracks and undergo bond-slip processes that consume energy. Clearly, one must consider both regions of response if highly optimized FRCs are desired. While the enhanced resistance to impact of FRC is well known in qualitative terms, there is only limited quantitative data in the literature related to its impact performance [72,141]. This is particularly true in the case of polymeric fibers [76,142].

Based on the research carried out in the field of steel fiber reinforced concrete (SRFC) [143], it is now clear that the primary advantage of adding fibers to the brittle cementitious matrix is derived only after the matrix cracks and the fibers bridging such a crack help transfer the stresses across it. As indicated in section 3.5.2, only limited research has been conducted on the dynamic response of the fiber-matrix bond. In addition, under impact, the different constitutive responses of the steel and polypropylene fibers themselves contribute to their ability to dissipate energy during impact loading of FRC.

In this Chapter, the bond-slip behaviour of fibers pulling out from a concrete matrix is addressed. By means of single-fiber pull-out tests, the following sections examine the effect of fiber material and geometry on its pull-out response. Steel and polypropylene fibers, with widely differing constitutive properties form the basis of this investigation. This Chapter also describes the effect of matrix strength and loading orientation on the fiber bond-slip. The quasi-static response of the four fibers is presented first, followed by their impact response.

6.2   Quasi-Static Pull-Out

Banthia and Trottier [43,44] studied the bond-slip behaviour of steel fibers when bonded to a cement-based matrix and correlated the results with the performance of FRC under static loading.
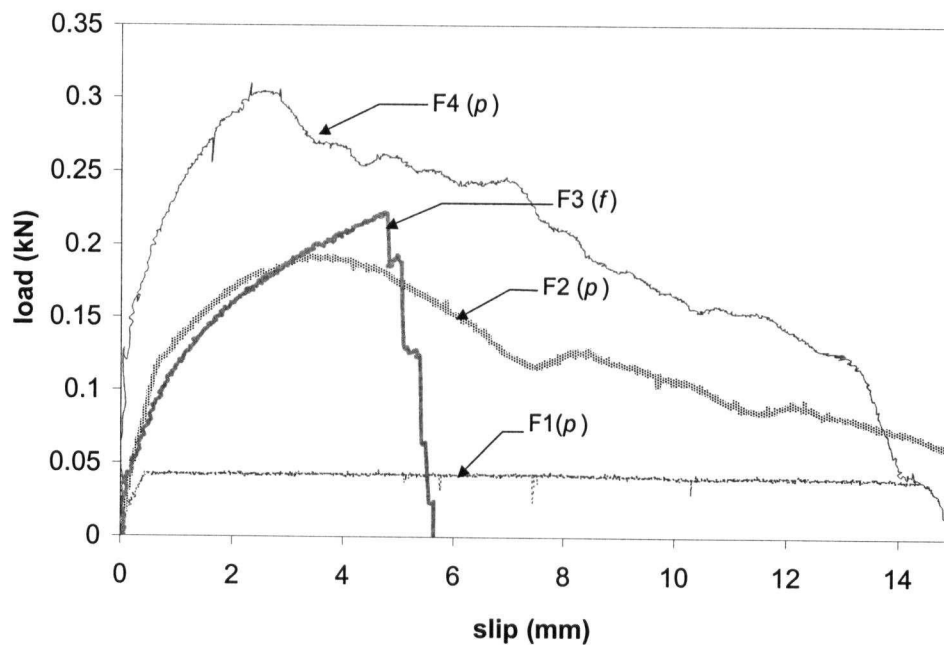
Figure 6.1   Pull-Out Response of Fibers under Quasi-Static Load (0° with Load-Line) from a NSC Matrix (p: Fiber Pull-Out; f: Fiber Fracture)

They demonstrated that fiber geometry, fiber orientation and the strength of the matrix, all influence the bond-slip performance and a more holistic approach is essential to optimize the bond-slip response in an FRC composite. Furthermore, although the link

between the fiber-matrix response and the actual composite performance is often questioned, it has been shown that, by appropriate modeling, and with sufficient regard to variations in fiber orientation and bonded length, fiber-matrix bond-slip information can be useful in predicting the toughness response of a composite [80]. The results presented in this section on quasi-static responses form the basis of comparison with their response under impact loading, presented in the succeeding sections of this Chapter.
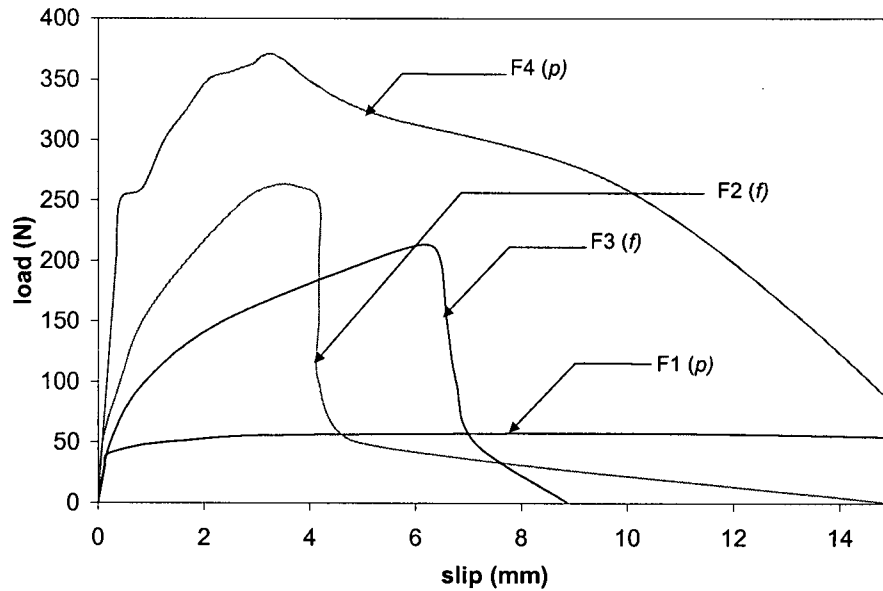
Figure 6.2   Pull-Out Response of Fibers under Quasi-Static Loading (15° with Load-Line) from a NSC Matrix; (*p*: Fiber Pull-Out; *f*: Fiber Fracture)

6.2.1 Normal Strength Concrete Matrix

Representative load-COD (or load-slip) curves from the quasi-static pull-out tests for different fibers are shown in Figures 6.1-6.6 for six different fiber inclinations. These curves were further analyzed and the results are given in Table 6.1. Four fiber types were examined: F1, a straight, undeformed polyolefin fiber (length = 50 mm, ϕ = 1 mm); F2, straight, crimped polypropylene fiber (length = 30 mm, ϕ = 1 mm); F3, straight, crimped polypropylene fiber (length = 50 mm, ϕ = 1 mm) and F4, straight, steel fiber with flattened ends (length = 30 mm, ϕ = 0.70 mm). As seen, the steel fiber (F4) absorbed the

Table 6.1   Pull-Out Response of Fibers under Quasi-Static Rate of Pull-Out (NSC Matrix; COD Rate = 0.03 mm/s)

Fiber	Bonded length (mm)	Failure Mode*		Peak Load (N)		Slip at Peak Load (mm)		Energy to Peak Load (N-m)		Total Pull-Out Energy (N-m)	
		0°	45°	0°	45°	0°	45°	0°	45°	0°	45°
F1	25	P	P	41 (5)	78 (10)	0.49 (0.09)	5.50 (0.24)	0.03 (0.005)	0.18 (0.04)	0.73 (0.18)	1.90 (0.35)
F2	15	P	F	191 (20)	232 (22)	3.70 (0.96)	4.29 (1.10)	0.62 (0.11)	0.53 (0.9)	2.19 (0.55)	0.63 (0.16)
F3	25	F	F	220 (24)	180 (19)	4.79 (1.00)	5.00 (1.00)	1.1 (0.27)	0.52 (0.16)	1.19 (0.21)	0.56 (0.08)
F4	15	P	F	304 (11)	261 (10)	2.64 (0.31)	5.60 (0.65)	0.78 (0.06)	1.16 (0.08)	3.59 (0.45)	1.50 (0.19)

*   P: Pull-Out; F: Fracture

$f'c = 40$ MPa

F1: Straight, Undeformed Polyolefin Fiber (length = 50 mm, ϕ = 1 mm);

F2: Straight, Crimped Polyolefin Fiber (length = 30 mm, ϕ = 1 mm);

F3: Straight, Crimped Polyolefin Fiber (length = 50 mm, ϕ = 1 mm);

F4: Straight, Flattened-End Steel Fiber (length = 30 mm, ϕ = 0.70 mm);
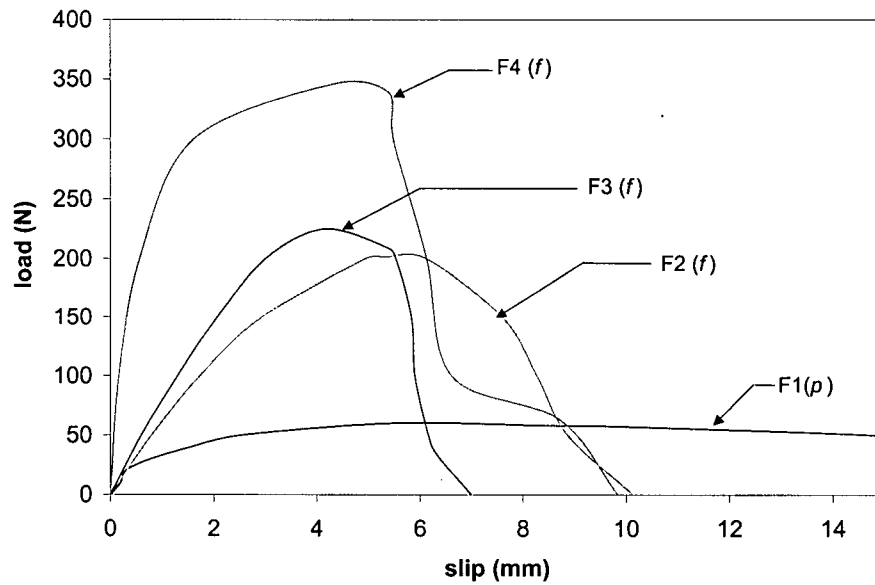
Figure 6.3   Pull-Out Response of Fibers under Quasi-Static Loading (30° with Load-Line) from a NSC Matrix (*p*: Fiber Pull-Out; *f*: Fiber Fracture)
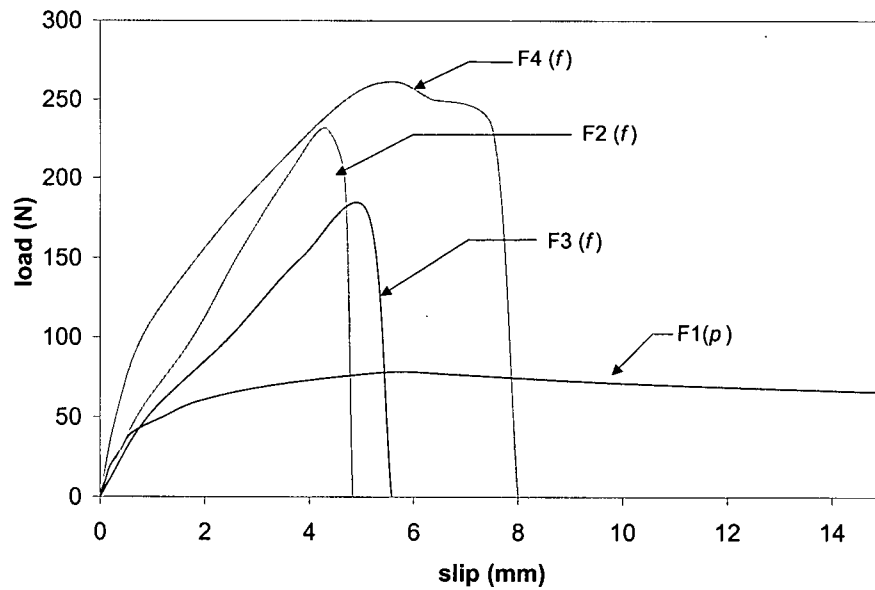
Figure 6.4   Pull-Out Response of Fibers under Quasi-Static Loading (45° with Load-Line) from a NSC Matrix; (*p*: Fiber Pull-Out; *f*: Fiber Fracture)

greatest amount of total energy of all fibers during pull-out. Further, the deformed polypropylene fibers (F2 & F3) carried a far greater peak load than the undeformed polyolefin fiber (F1). This clearly highlights the importance of placing fiber deformations and specifically demonstrates the effectiveness of sinusoidal crimping in enhancing the strength of the fiber-matrix bond. An increase in the energy absorption capacity due to crimping may also be noted.
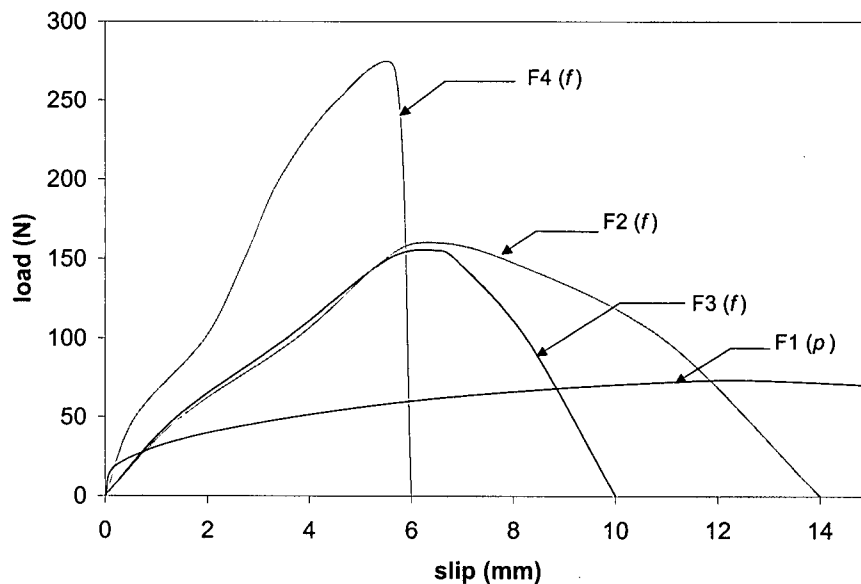
Figure 6.5   Pull-Out Response of Fibers under Quasi-Static Loading (60° with Load-Line) from a NSC Matrix; (p: Fiber Pull-Out; f: Fiber Fracture)

However, there is a limit to the usefulness of this bond improvement through surface deformities. For polymeric fibers, a heavily jagged profile may strengthen the fiber-matrix bond beyond the tensile strength of the polymer material. This will cause a transition in the failure mode from fiber pull-out to fiber fracture, resulting in a drop in the energy dissipation.
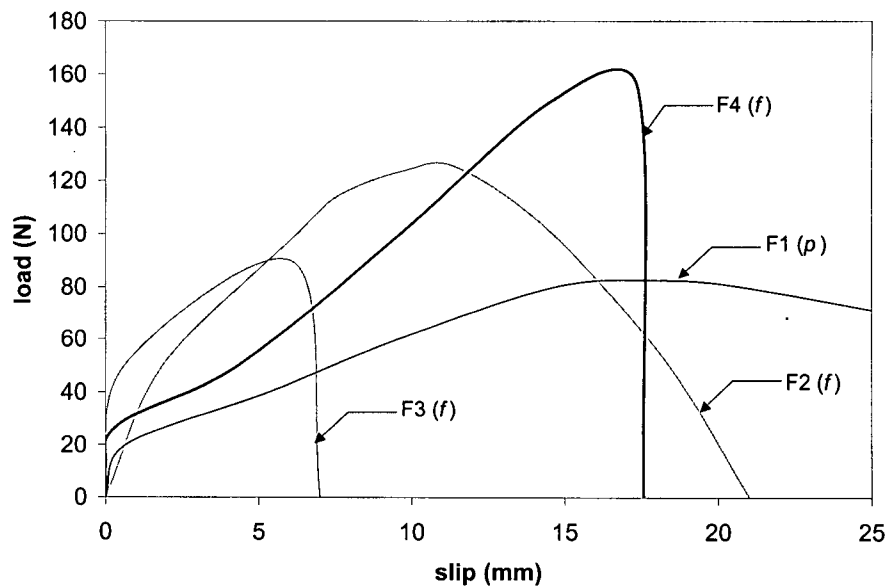
Figure 6.6   Pull-Out Response of Fibers under Quasi-Static Loading (75° with Load-Line) from a NSC Matrix; (*p*: Fiber Pull-Out; *f*: Fiber Fracture)

Under aligned loading, it is clear that bond enhancement through crimping reduces the critical length of the fiber, so that at 50 mm (Fiber F3), the polypropylene fiber appears to have already exceeded the critical length. Consequently, as seen in Figure 6.1, the 50 mm deformed fibers (Fiber F3) fractured during pull-out, while the 30 mm fibers (Fiber F2) pulled-out under aligned loading. Note also that the 50 mm long undeformed fiber F1 pulls-out without fracturing. Clearly, the critical length for the given sinusoidal deformations and fiber dimensions is between 30 and 50 mm for the case of quasi-static pull-out.

Figures 6.7-6.10 illustrate the effect of fiber orientation on its pull-out performance. The orientation indicates the angle, which the fiber makes with the plane of the crack. For the steel fiber F4, there is a benefit accruing from the inclined loading. Because of its higher stiffness, considerable energy is consumed in bending the fiber. Consequently, at smaller inclinations, a higher peak pull-out is registered. This fact has been documented before [43,51]. However, for the relatively softer polymeric fibers, no improvement occurs because not much energy is required to bend these fibers.
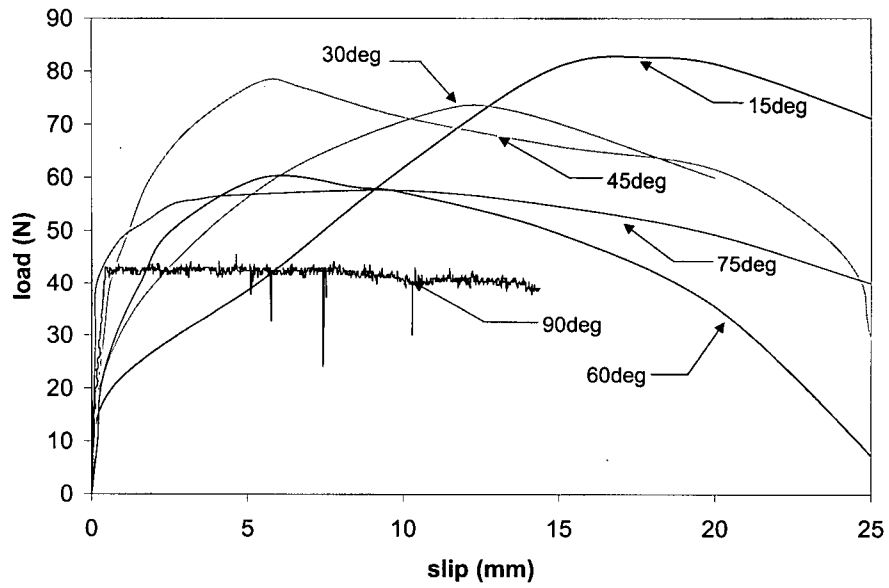
Figure 6.7   Quasi-Static Pull-Out of Fiber F1 (NSC Matrix)
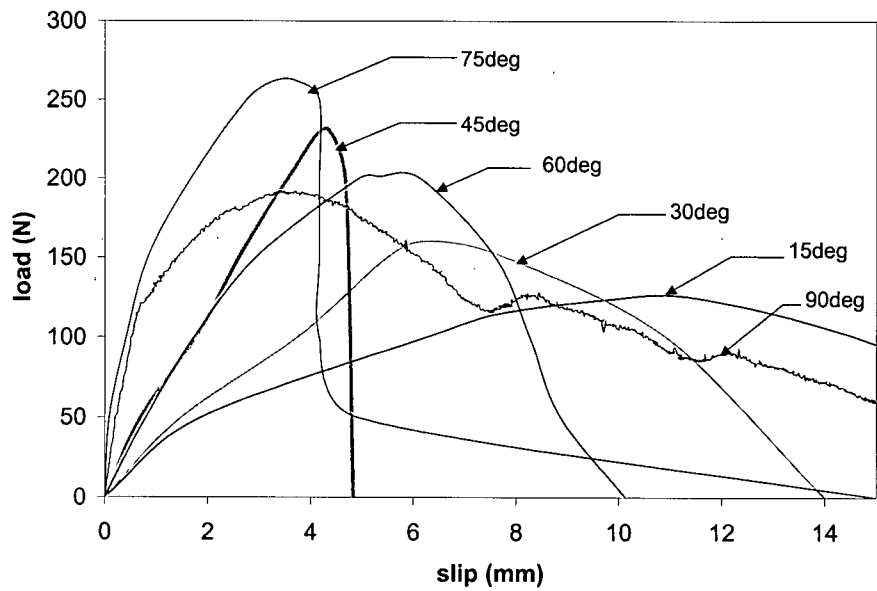
Figure 6.8   Quasi-Static Pull-Out of Fiber F2 (NSC Matrix)
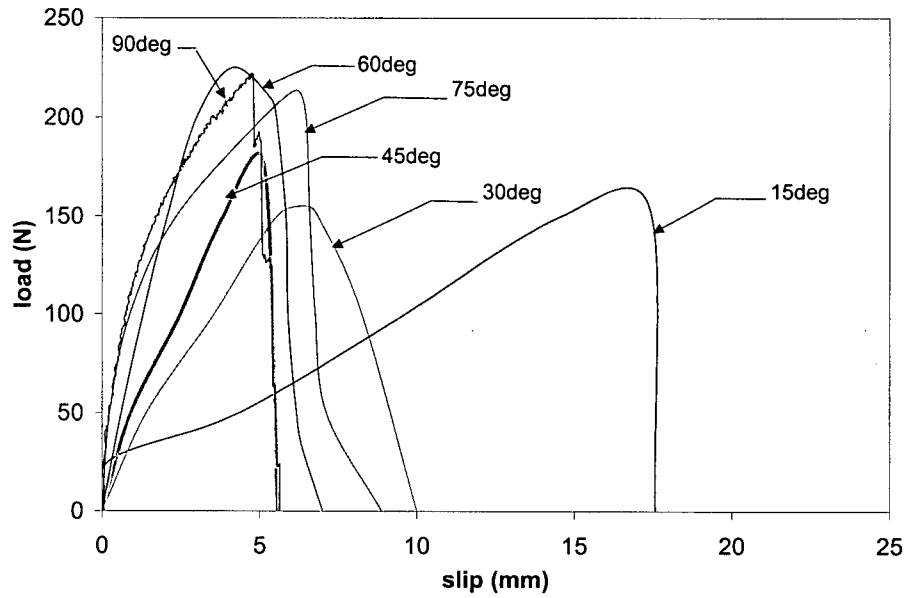
Figure 6.9   Quasi-static pull-out of fiber F3 (NSC matrix)
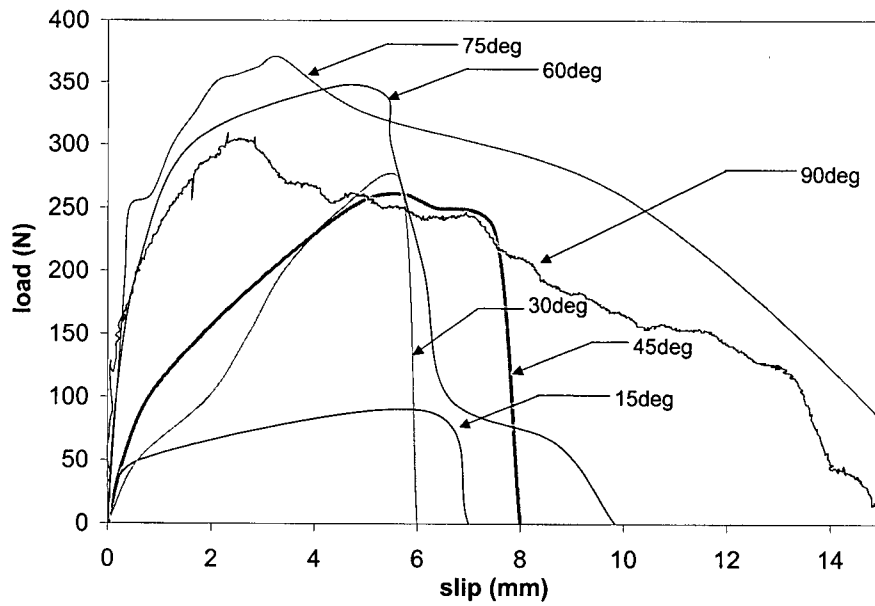
Figure 6.10   Quasi-static pull-out of fiber F4 (NSC matrix)

An interesting switch was noticed at large inclinations:- For the steel fibers, the slip at peak increases proportionately with the angle of inclination without a significant decline in the peak load itself. However, the two deformed polymeric fibers, being composed of a material softer than the surrounding concrete, undergo abrasion at the crack-opening and suffer a premature fracture. There was no change in slip at the instance of peak load for the inclined fibers F2 and F3. However, a considerably lower peak pull-out load was registered by these deformed fibers. On the other hand, for the undeformed polymeric fiber F1, increasing the angle of orientation actually improved its bond-slip performance. The reason is not hard to find: once again, being composed of a softer material, the fiber, when inclined, abrades against the surrounding concrete at the crack opening and, although it pulls out, it undergoes considerable damage compared to its relatively unabraded pull-out during aligned loading. As witnessed in Figure 6.1, the load supported by the undeformed polymeric fiber F1 is not very high to begin with. Therefore, the energy spent in abrading this fiber under inclined loading appears as a higher pull-out load and dissipated energy. Inclining the fibers increases the abrasion for the deformed fibers as well; in fact, the deformities lead to a better anchorage and hence greater abrasion. However, the load supported by the deformed polymeric fibers F2 and F3 even under aligned loading is very close to their ultimate tensile strength, which means the improved bonding arising out of the crimped profile creates fibrillation and localized, successive fracture of these fibrils. Consequently, there is no visible increase in peak load or bond energy.

6.2.2   High Strength Concrete Matrix

Figure 6.11 describes the quasi-static pull-out response (under aligned loading) of the various fibers, from a high-strength concrete matrix (f'_c = 80 MPa). The effect of matrix strength on the bond-slip response of each fiber is evident in Figures 6.12-6.15. The peak pull-out load is higher for the high strength matrix for all the fibers.
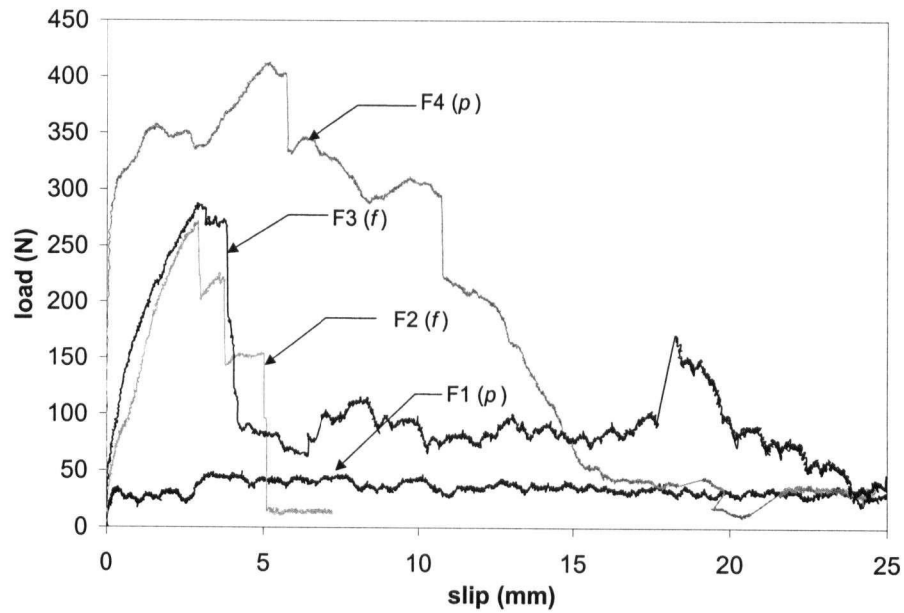
Figure 6.11   Quasi-Static Pull-Out Response of Aligned Fibers from HSC Matrix
(*p*: Fiber Pull-Out; *f*: Fiber Fracture)
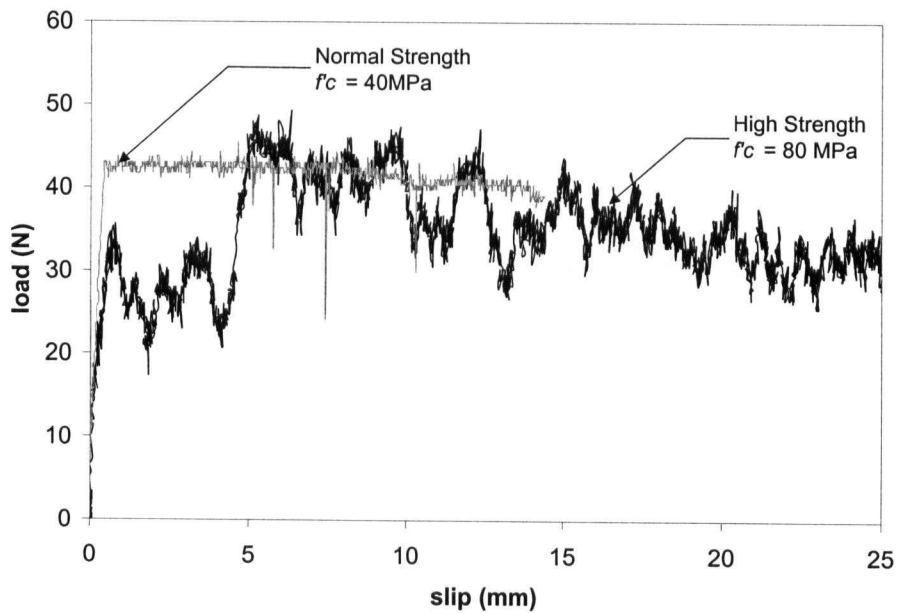
Figure 6.12   Effect of Matrix Strength on Quasi-Static Pull-Out of Aligned Fiber F1
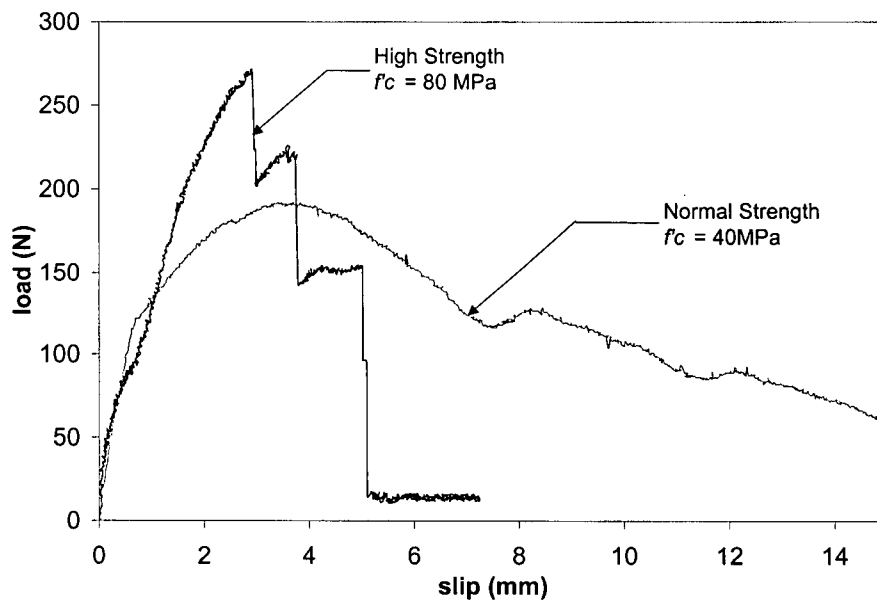
Figure 6.13   Effect of Matrix Strength on Quasi-Static Pull-Out of Aligned Fiber F2
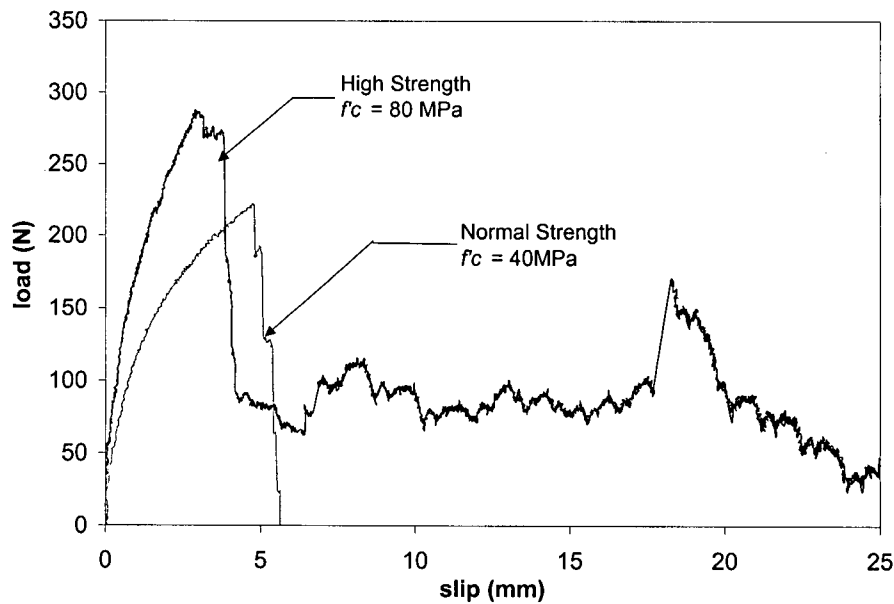
Figure 6.14   Effect of Matrix Strength on Quasi-Static Pull-Out of Aligned Fiber F3

This fact has been illustrated earlier [43,51,144]. A core of concrete takes part in the transfer of load during pull-out. Therefore, when a fiber is deformed, the effect of matrix strength on its pull-out characteristics is more pronounced. Thus, fibers F2, F3 and F4

witness higher jumps in peak pull-out load compared to the undeformed polyolefin fiber F1 in Figure 6.12.
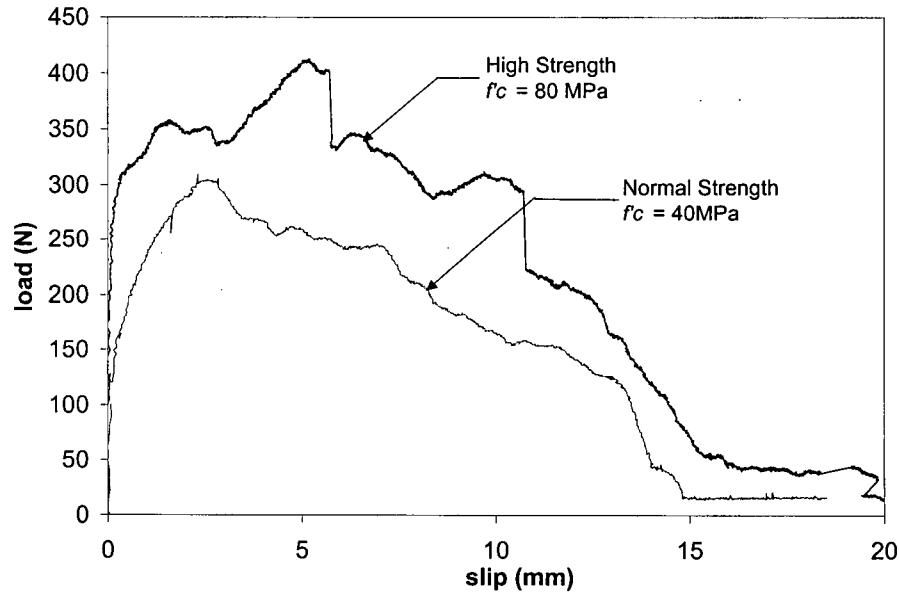
Figure 6.15   Effect of Matrix Strength on Quasi-Static Pull-Out of Aligned Fiber F4

Higher strength matrix induces fracture as the dominant mode of fiber failure. This is best depicted in the case of fiber F2, which pulled out from the normal strength matrix but fractured when pulling out from the high strength matrix. Clearly, higher matrix strength promotes a more brittle bond-slip response. This is emphasized by the reduction in the energy of pull-out in the case of high strength matrix (Table 6.2).

Table 6.2   Quasi-Static Pull-Out Performance of Fibers from High-Strength Matrix

Fiber	Bonded Length (mm)	Failure Mode	Peak Load (N)	Slip at Peak Load (mm)	Energy to Peak Load (N-m)	Total Pull - Out Energy (N-m)
F1	25	P	49 (6)	0.50 (0.10)	0.66 (0.12)	2.33 (0.60)
F2	15	F	276 (29)	2.77 (0.73)	1.04 (0.20)	1.97 (0.50)
F3	25	F*	285 (28)	3.03 (0.65)	1.37 (0.33)	7.45 (1.5)
F4	15	P	407 (24)	5.27 (0.62)	4.2 (0.03)	10.65 (0.70)

*   80% of the fiber fractured

103

6.3   Dynamic Pull-Out

Bond-slip responses of the fibers (F1-F4) under impact rates of crack opening displacement (COD) are presented in this section. By comparing these responses with those under quasi-static loading in section 6.2, it is possible to understand the high stress-rate behaviour of the fiber-matrix interface.
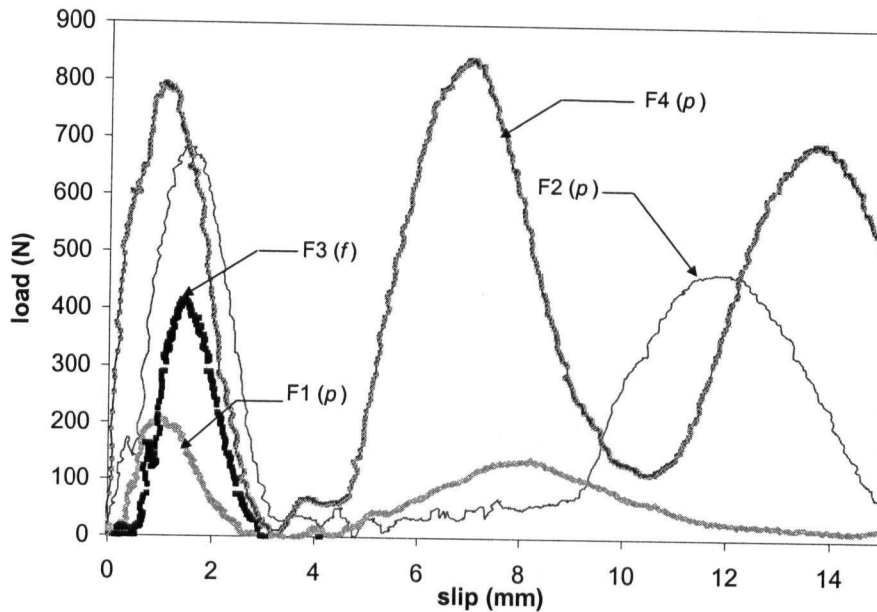
Figure 6.16   Pull-Out Response of Fibers from NSC Matrix under Impact, (COD Rate = 2000 mm/s; 0° with Load-Line); (*p*: Fiber Pull-Out; *f*: Fiber Fracture)

6.3.1   Normal Strength Concrete Matrix

The representative pull-out curves of the four fibers under a dynamic pull-out rate of 2000 mm/s are shown in Figures 6.16-6.19, and those performed at a COD rate of 3000 mm/s are shown in Figures 6.20-6.23. To capture the effect of fiber orientation, the fibers were inclined at four different angles (0°, 22.5°, 45° & 67.5°) with respect to the applied load. Note that both fracture and pull-out modes of failure were noted for the aligned case of Fiber F2 at a COD rate of 3000 mm/s and only the fracture mode is reproduced in Figure 6.20.
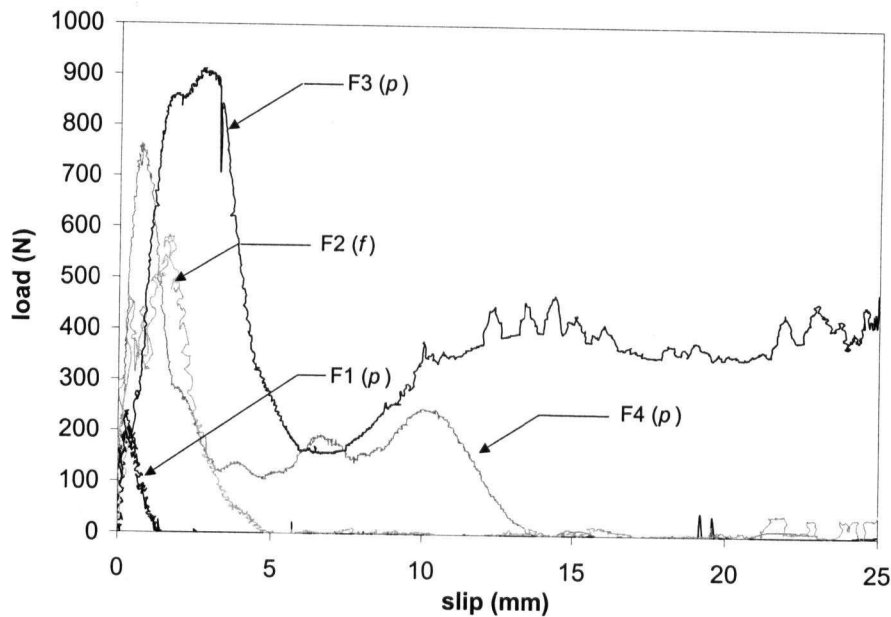
Figure 6.17   Pull-Out Response of Fibers from NSC Matrix under Impact, (COD Rate = 2000 mm/s; 22.5° with Load-Line); (*p*: Fiber Pull-Out; *f*: Fiber Fracture)

At a COD rate of 2000 mm/s, on the other hand, fiber failure modes were no different from those observed in the quasi-static pull-out case. That is to say, while for aligned loading, only the 50 mm crimped polypropylene fiber (F3) fractured, with increasing angle of orientation, all but the undeformed polymeric fiber (F1) underwent fracture during the pull-out process. At a higher rate of 3000 mm/s, a third of the shorter (30 mm) deformed fibers pulled out while the others fractured. A preservation of the fiber pull-out mode for Fiber F2 resulted in a vast improvement in its efficiency as seen in Figure 6.24 (also see Tables 6.3 and 6.4).

Table 6.3   Pull-Out Performance of Fibers from NSC matrix (COD rate = 2000 mm/s); $f'c$ = 40 MPa

Fiber	Bonded Length (mm)	Failure Mode		Peak Load (N)		Slip at Peak Load (mm)		Energy at Peak Load (N-m)		Total Pull-Out Energy (N-m)	
		0°	45°	0°	45°	0°	45°	0°	45°	0°	45°
F1	25	P	P	212 (120)	105 (45)	0.98 (0.16)	1.49 (0.23)	0.26 (0.04)	0.22 (0.03)	1.63 (0.27)	2.73 (0.45)
F2	15	P	F	681 (265)	196 (55)	1.41 (0.49)	1.84 (0.64)	0.75 (0.25)	1.02 (0.35)	3.81 (1.29)	1.97 (0.7)
F3	25	F	F	417 (145)	238 (71)	1.45 (0.47)	2.06 (0.6)	0.41 (0.16)	0.81 (0.29)	0.88 (0.31)	1.79 (0.65)
F4	15	P	P	794 (5)	405 (35)	1.03 (0.12)	3.21 (0.4)	0.78 (0.04)	1.63 (0.1)	7.74 (1.32)	4.5 (0.8)

Table 6.4   Pull-Out Performance of Fibers from NSC matrix (COD rate = 3000 mm/s); $f'c = 40$ MPa

Fiber	Bonded Length (mm)	Failure Mode 0°	Failure Mode 45°	Peak Load (N) 0°	Peak Load (N) 45°	Slip at Peak Load (mm) 0°	Slip at Peak Load (mm) 45°	Energy at Peak Load (N-m) 0°	Energy at Peak Load (N-m) 45°	Total Pull-Out Energy (N-m) 0°	Total Pull-Out Energy (N-m) 45°
F1	25	P	P	290 (89)	136 (40)	0.12 (0.06)	1.7 (0.08)	0.49 (0.20)	0.60 (0.20)	2.45 (0.92)	1.48 (0.55)
F2	15	F	F	726 (217)	535 (160)	0.88 (0.29)	0.52 (0.20)	0.60 (0.19)	0.63 (0.18)	1.09 (0.27)	2.2 (0.54)
		P	-	696 (100)	-	0.57 (0.10)	-	0.54 (0.09)	-	3.09 (0.62)	-
F3	25	F	F	625 (208)	467 (150)	1.03 (0.41)	0.23 (0.09)	0.53 (0.19)	0.54 (0.15)	0.93 (0.37)	2.93 (1.19)
F4	15	P	P	584 (25)	833 (37)	0.48 (0.09)	0.92 (0.16)	0.50 (0.04)	1.22 (0.10)	5.45 (0.45)	6.23 (0.41)
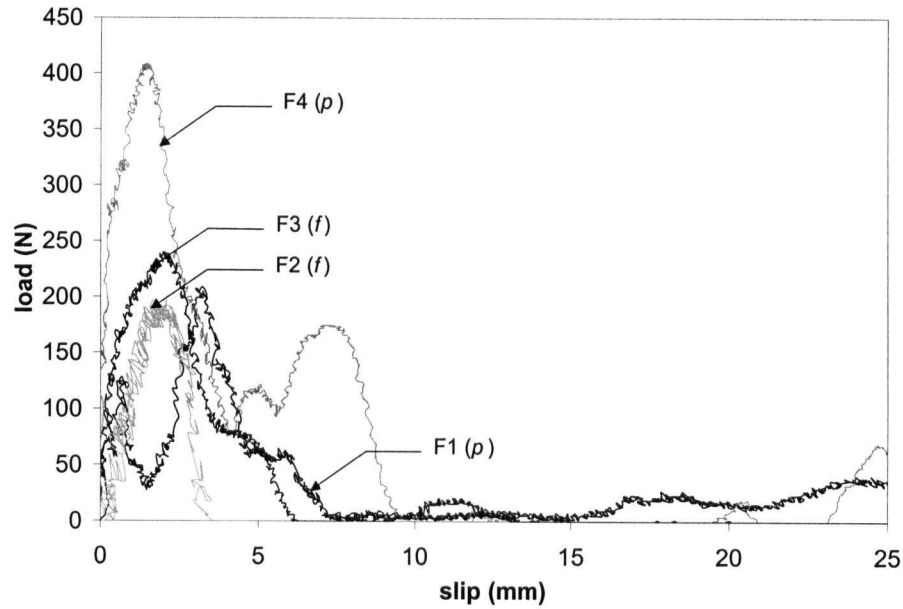
Figure 6.18   Pull-Out Response of Fibers from NSC Matrix under Impact; (COD Rate = 2000 mm/s; 45° with Load-Line); (*p*: Fiber Pull-Out; *f*: Fiber Fracture)
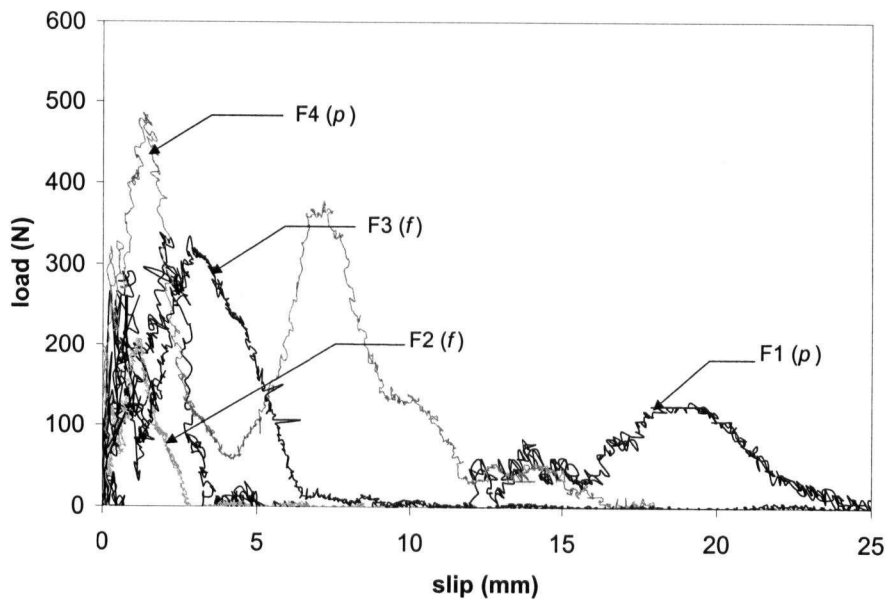
Figure 6.19   Pull-Out Response of Fibers from NSC Matrix under Impact; (COD Rate = 2000 mm/s; 67.5° with Load-Line) (*p*: Fiber Pull-Out; *f*: Fiber Fracture)
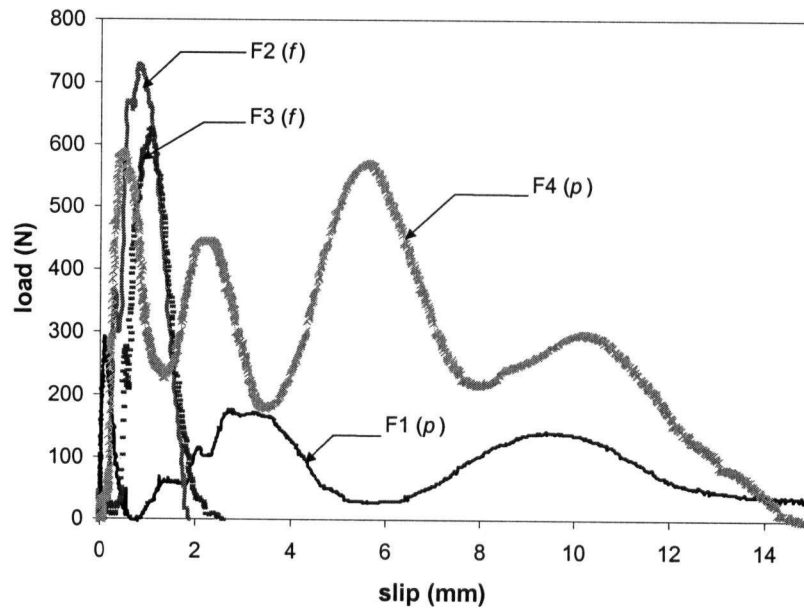
Figure 6.20   Pull-Out Response of Fibers from NSC Matrix under Impact; (COD Rate = 3000 mm/s; 0° with Load-Line); (*p*: Fiber Pull-Out; *f*: Fiber Fracture)
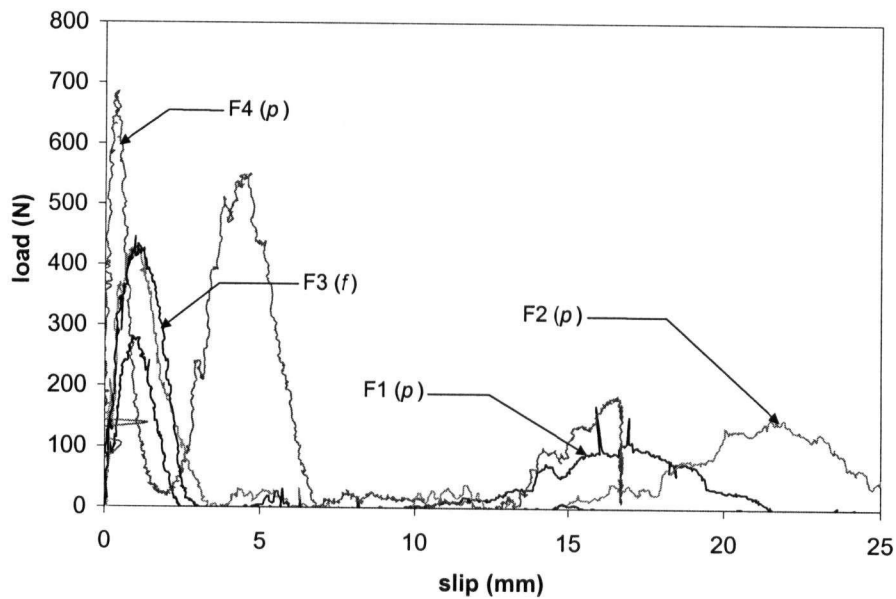
Figure 6.21   Pull-Out Response of Fibers from NSC Matrix under Impact; (COD Rate = 3000 mm/s; 22.5° with Load-Line) (*p*: Fiber Pull-Out; *f*: Fiber Fracture)
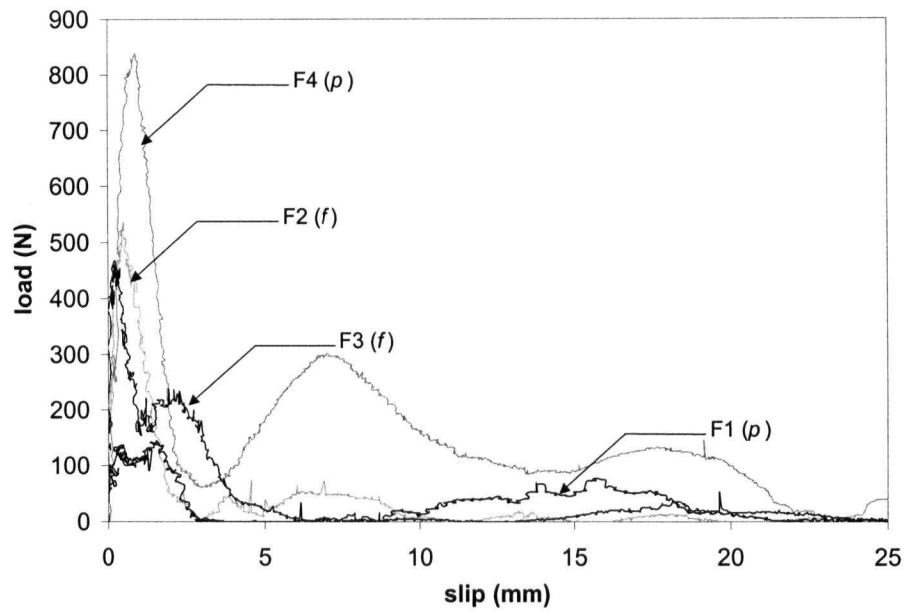
Figure 6.22   Pull-Out Response of Fibers from NSC Matrix under Impact; (COD Rate = 3000 mm/s; 45° with Load-Line); (*p*: Fiber Pull-Out; *f*: Fiber Fracture)
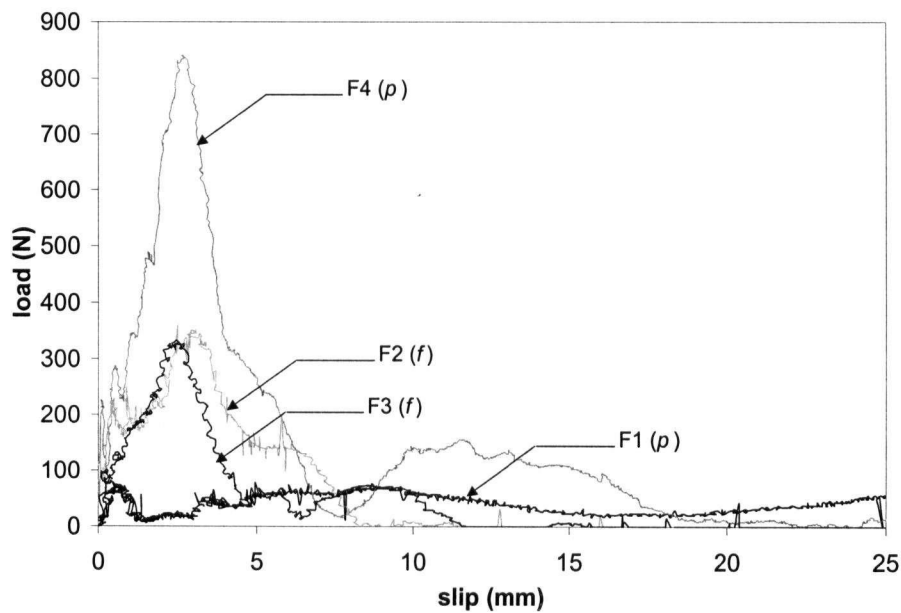
Figure 6.23   Pull-Out Response of Fibers from NSC Matrix under Impact; (COD Rate = 3000 mm/s; 67.5° with Load-Line); (*p*: Fiber Pull-Out; *f*: Fiber Fracture)
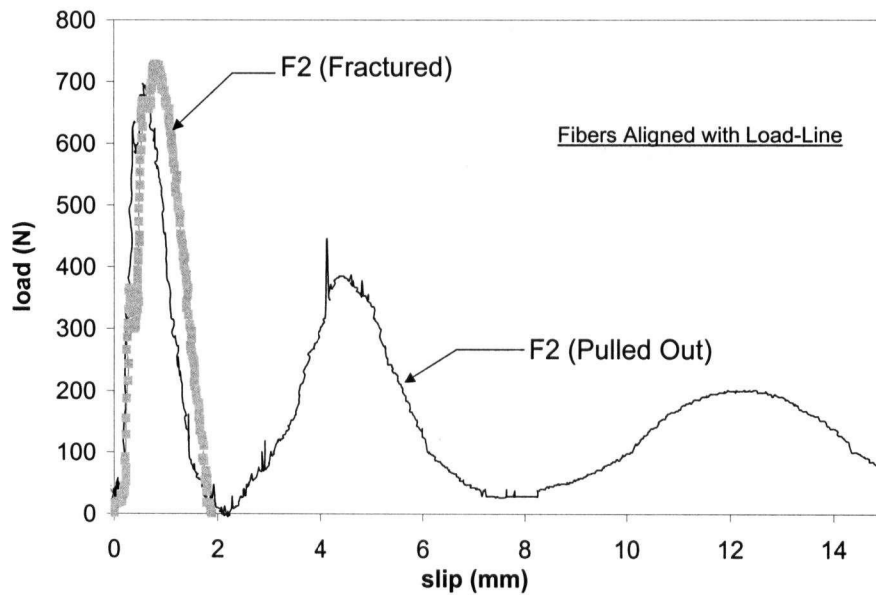
Figure 6.24   Pull-Out Performance of Fiber F2 Showing Different Failure Modes under
Impact at COD Rate = 3000 mm/s (from NSC Matrix)

Figures 6.25-6.28 show the effect of fiber orientation on its pull-out performance under
two rates of impact loading. The slip at peak load increases uniformly for all four fibers
with increase in their inclination to applied load. For polymeric fibers, unlike in the case
of quasi-static loading, the inclined pull-out leads to lower peak loads for both
undeformed (Figure 6.25) and deformed fibers alike (Figures 6.26 and 6.27). This is in
contrast to the quasi-static case where in the undeformed fiber F1 improved with
increasing angle of orientation. A possible explanation is as follows: Under impact
loading, due to the rapidity of the event, no scope for abrasion exists and the undeformed
fiber pulls out relatively intact resulting in lower peaks and pull-out energy.
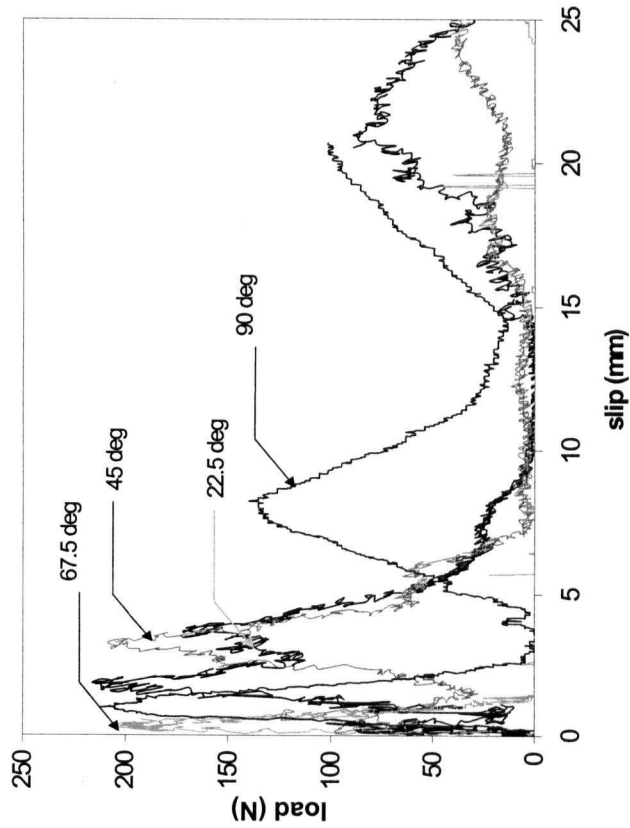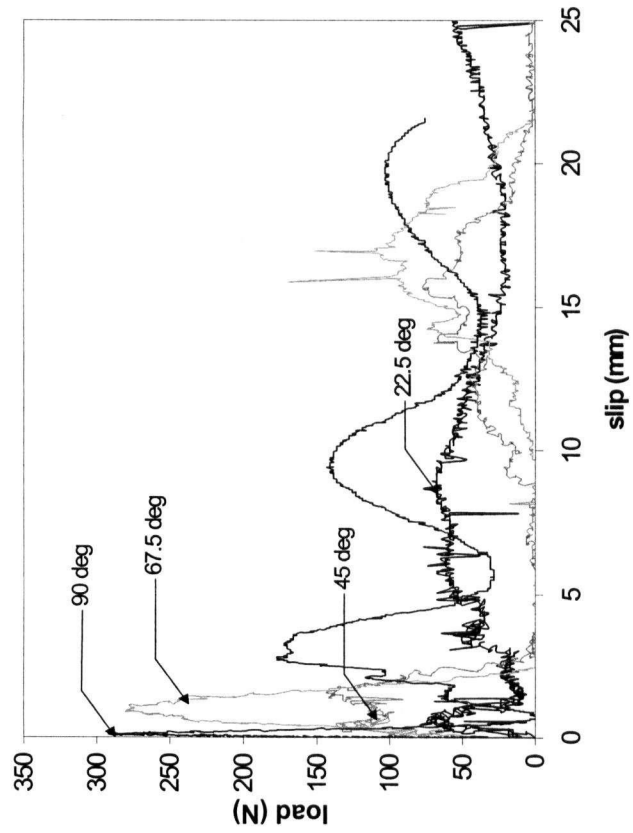
Figure 6.25   Effect of Fiber Inclination on the Pull-Out Response of Fiber F1 under Impact: a) COD Rate = 2000 mm/s;

b) COD Rate = 3000 mm/s

112
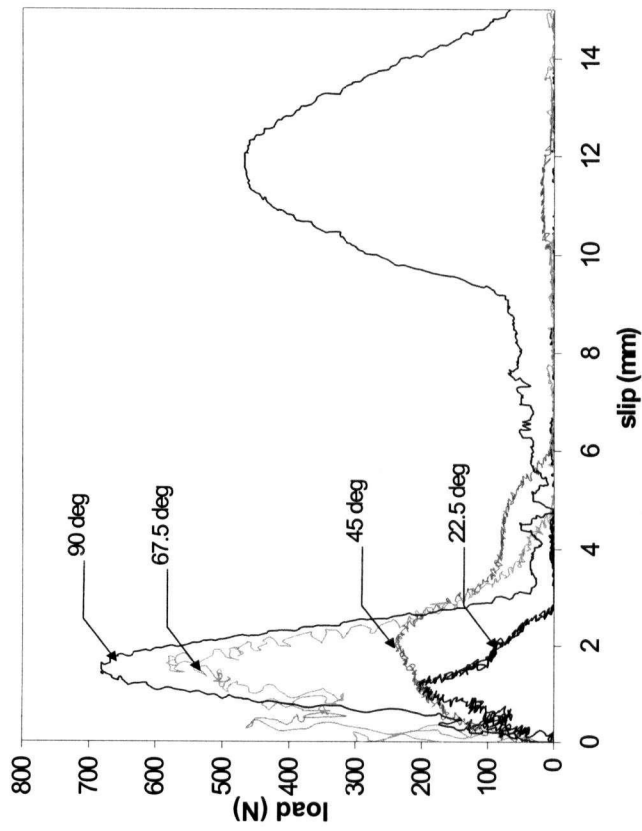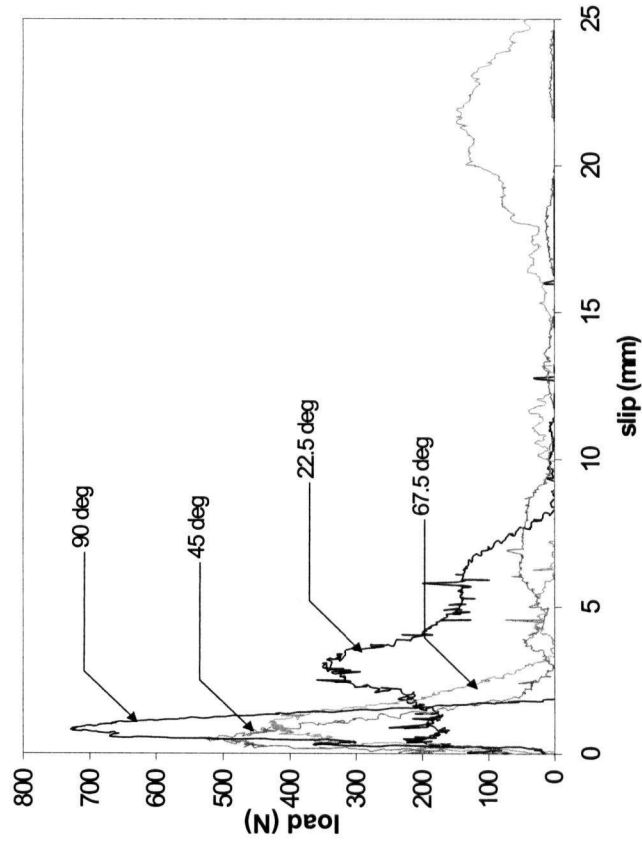
Fiber 6.26   Effect of Fiber Inclination on the Pull-Out Response of Fiber F2 under Impact: a) COD Rate = 2000 mm/s; b) COD Rate = 3000 mm/s
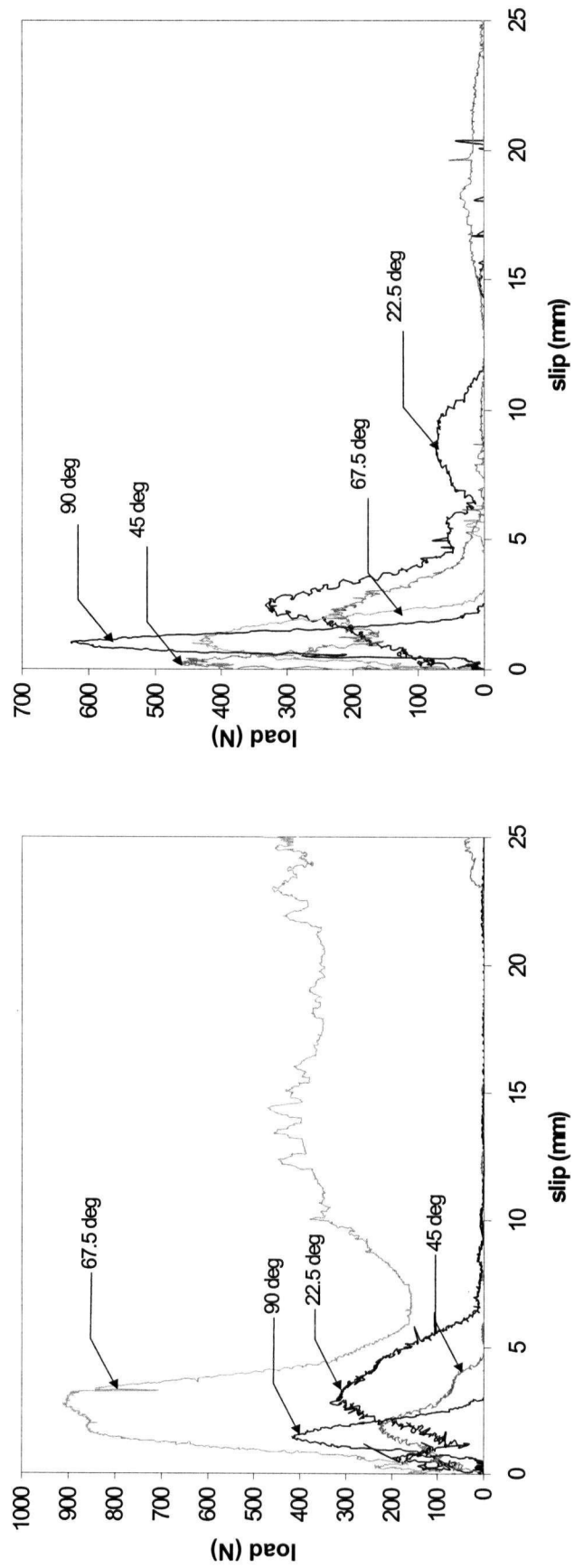
Figure 6.27   Effect of Fiber Inclination on the Pull-Out Response of Fiber F3 under Impact: a) COD Rate = 2000 mm/s;
b) COD Rate = 3000 mm/s

114
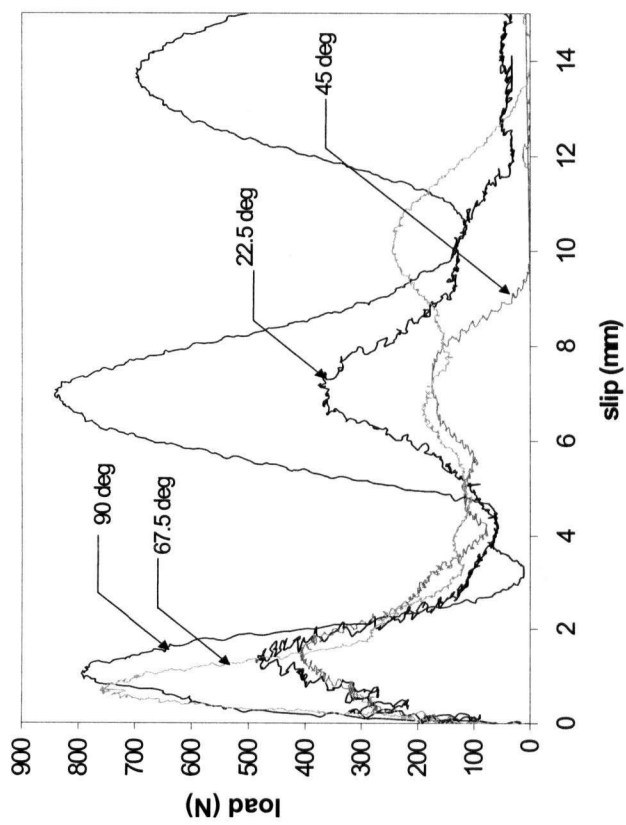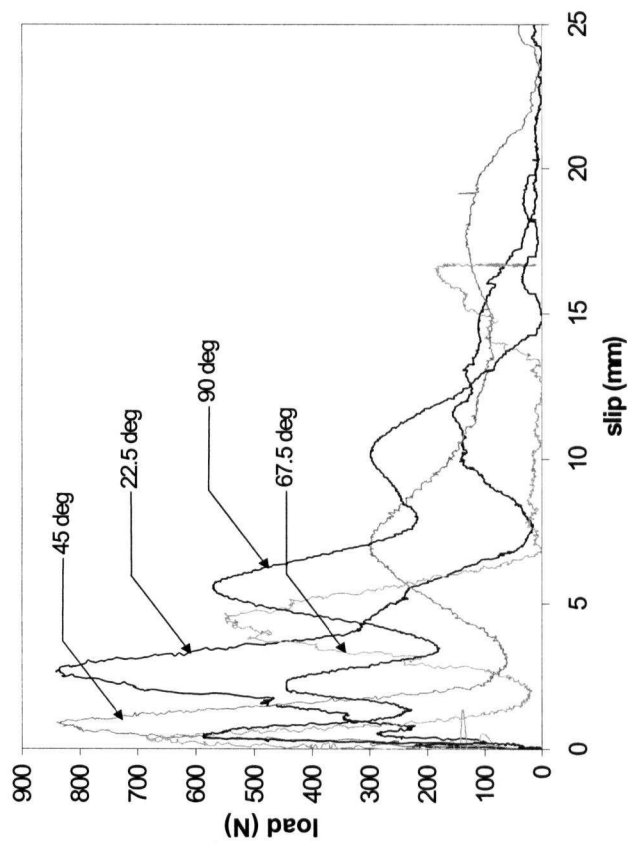
Figure 6.28   Effect of Fiber Inclination on the Pull-Out Response of Fiber F4 under Impact: a) COD Rate = 2000 mm/s;
b) COD Rate = 3000 mm/s

Another difference noted between the two impact responses was the higher number of peaks at higher impact rates, seen clearly in the case of aligned loading (Figures 6.16 and 6.20). It is clear from Tables 6.5 and 6.6 that in terms of energy dissipated both up to the peak load and during the entire event, the deformed polypropylene fibers perform better under impact conditions if the critical length is not exceeded and a fiber pull-out mode is preserved. In absolute terms, however, steel fibers always absorbed greater energy than the rest of the fibers. Due to its higher strain-rate sensitivity, the deformed polypropylene fibers may approach the performance of steel fiber at higher strain rates when a pull-out mode of failure is preserved. Some of these observations are further discussed later.

6.3.2   High Strength Concrete Matrix

Figure 6.29 shows the four fibers pulling out under an impact load (COD rate = 3000 mm/s) from a high strength concrete matrix. As shown in section 6.4.2, it was observed that the two fibers that pulled out namely, the undeformed polymeric fiber F1 and the flat end steel fiber F4, both benefit from a higher strength matrix. Comparing the data from Tables 6.4 and 6.7, one notes that Fibers F1 and F4, both registered a higher peak load in a high strength matrix.
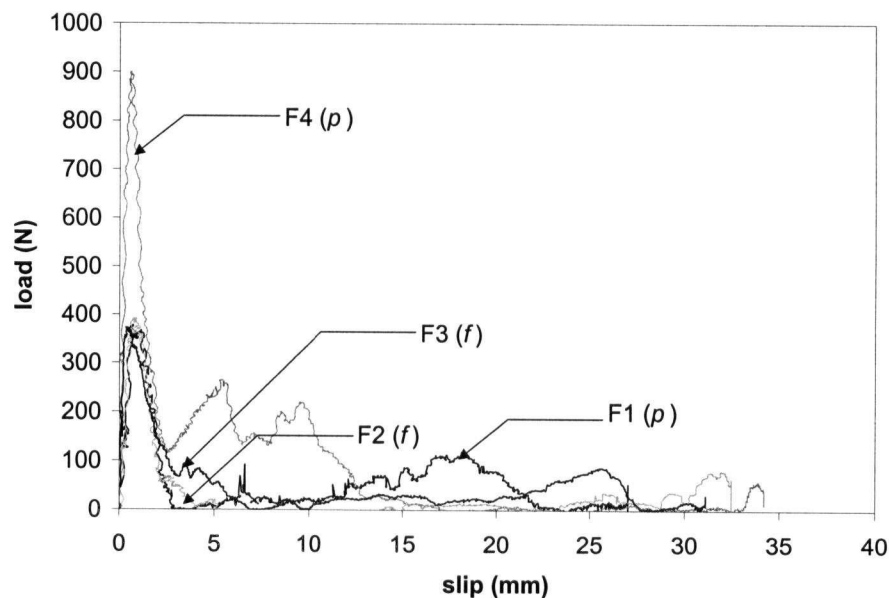
Figure 6.29   Pull-Out Response of Aligned Fibers under Impact; (COD Rate = 3000 mm/s) from HSC Matrix; *p*: Fiber Pull-Out; *f*: Fiber Fracture

Table 6.5   Comparison of Fiber Performance at Various COD Rates (Ratio between impact and static response)

Fiber	Ratio; Impact/Static															
	Peak Load				Slip @ Peak				Energy @ Peak Load				Total Energy			
	3000 mm/s		2000 mm/s		3000 mm/s		2000 mm/s		3000 mm/s		2000 mm/s		3000 mm/s		2000 mm/s	
	0°	45°	0°	45°	0°	45°	0°	45°	0°	45°	0°	45°	0°	45°	0°	45°
F1	7.05	1.74	5.17	5.19	0.25	0.31	2.00	0.27	16.36	3.33	8.56	1.22	3.36	0.78	2.22	1.44
F2	3.64	2.31	3.56	0.84	0.15	0.12	0.38	0.43	0.87	1.18	1.2	1.92	1.41	3.49	1.74	3.13
F3	2.83	2.59	1.90	1.32	0.22	0.05	0.30	0.41	0.48	1.04	0.38	1.56	0.78	5.23	0.74	3.20
F4	1.92	3.19	2.61	0.77	0.18	0.16	0.39	0.57	0.64	1.05	1.00	1.41	1.52	4.15	2.15	3

Table 6.6   Comparison of Fiber Performance at Various COD Rates (Ratio under impact between COD rate of 3000 mm/s to COD rate of 2000 mm/s)

Fiber	Ratio; High rate (3000 mm/s)/Low rate (2000 mm/s)							
	Peak Load		Slip @ Peak		Energy @ Peak Load		Total Energy	
	0°	45°	0°	45°	0°	45°	0°	45°
F1	1.36	0.34	0.12	1.15	1.91	2.73	1.50	0.54
F2	1.02	2.75	0.40	0.28	0.72	0.61	0.81	1.12
F3	1.49	1.96	0.71	0.12	1.28	0.66	1.05	1.63
F4	0.73	4.14	0.47	0.28	0.64	0.74	0.70	1.38

117

Curiously, they attain their peak loads at a marginally higher slip compared to the case of normal strength matrix. On the other hand, the two deformed polymeric fibers F2 and F3 fractured during the test. In contrast to the response from a normal strength matrix, the peak loads for fibers F2 and F3 dropped considerably as seen in Table 6.7.

6.4   Rate Effects

6.4.1   Effect of Fiber Inclination

From the pull out responses of the fibers tested in this program, it appears that for polymeric fibers, a suitable surface deformation such as sinusoidal crimping, is very effective in enhancing the strength of the bond and the energy dissipation capacity during pull out. The issue of poor concrete-polymer bond, may thus have been at least partially addressed by crimping.
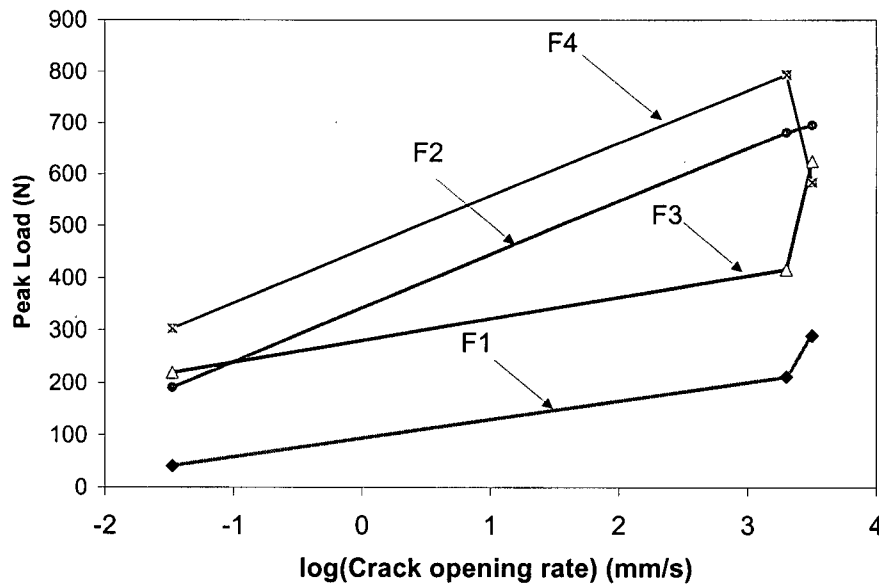
Figure 6.30   Effect of COD Rate on Peak Load (Inclination = 0° with Load-Line)

Table 6.7   Impact Pull-Out Performance of Fibers from High-Strength Matrix
(COD Rate = 3000 mm/s)

Fiber	Bonded Length (mm)	Failure Mode	Peak Load (N)	Slip at Peak Load (mm)	Energy to Peak Load (N-m)	Total Pull - Out Energy (N-m)
F1	25	P	360 (105)	1.06 (0.30)	0.82 (0.32)	2.76 (0.80)
F2	15	F	388 (118)	0.84 (0.36)	0.83 (0.25)	2.42 (0.73)
F3	25	F	365 (120)	0.63 (0.22)	0.56 (0.20)	2.41 (0.80)
F4	15	P	892 (40)	0.74 (0.03)	1.62 (0.07)	6.26 (0.27)

The peak pull-out load is plotted as a function of COD rate in Figure 6.30 for aligned fibers and in Figure 6.31 for fibers inclined at 45°. In general, impact loading resulted in an increase in the peak pull-out load, which is in agreement with previous work [68].
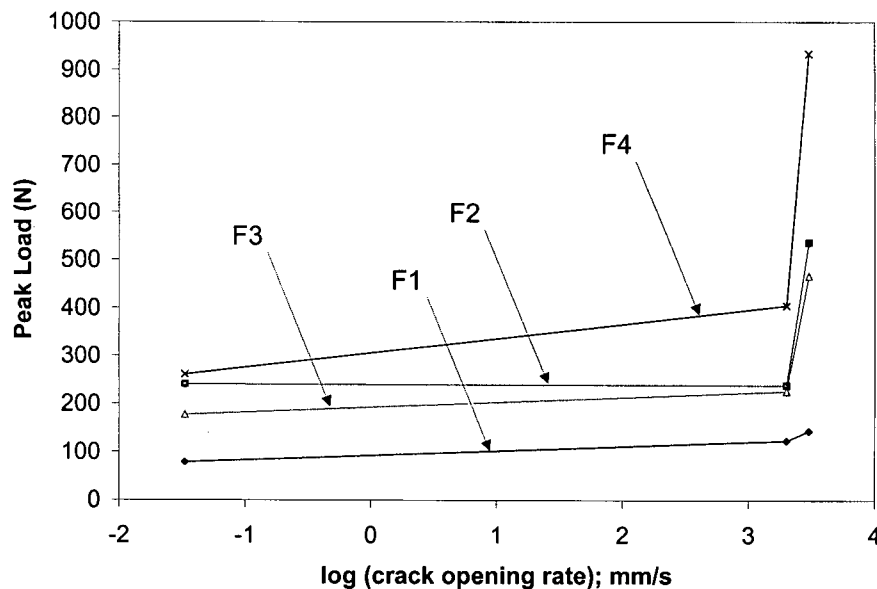
Figure 6.31   Effect of COD Rate on Peak Load (Inclination = 45° with Load-Line)

In the case of the steel fiber F4, however, a decrease in the peak pull-out load with an increase in the COD rate from 2000 mm/s to 3000 mm/s may be noted. This may indicate either a lack of clear dependence of peak load on COD rate for steel fiber, as postulated by Gokoz and Naaman [67], or a change in internal mechanisms in fiber failure beyond

2000 mm/s. The latter may mean, among other things, a premature sacrifice of the flat-ends at a higher rate of COD. This seems plausible for the aligned steel fiber F4.
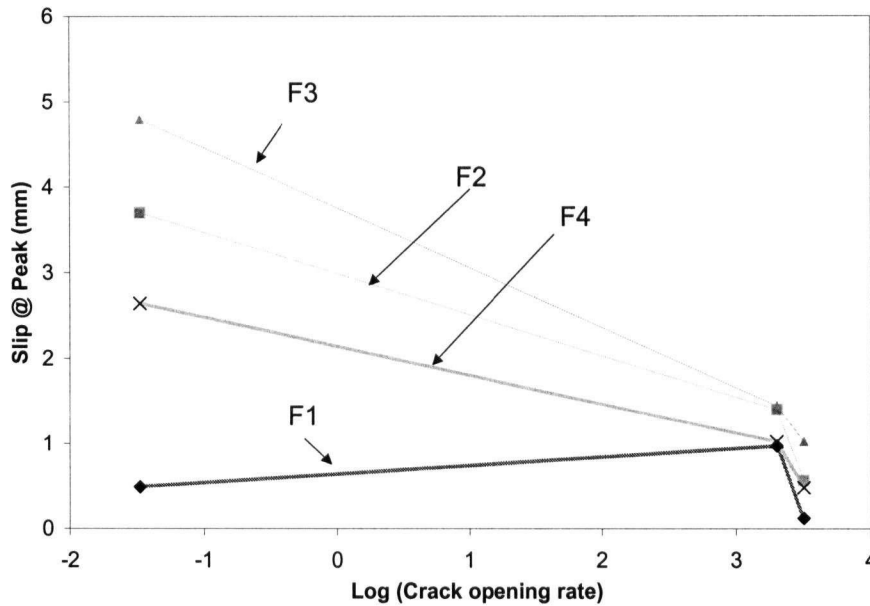
Figure 6.32   Effect of COD Rate on Slip @ Peak Load (Inclination = 0° with Load-Line)

For fibers inclined at 45 degrees, quite a different trend is noticed. At 45° inclination, the peak load for steel fiber F4 increases when COD rates increase from 2000 mm/s to 3000 mm/s. Since the steel fiber straightens out during pull-out, it follows that the flexural strength of steel fibers improves to a greater degree under impact than does the uniaxial tensile strength (in the case of the aligned fibers). In other words, the rate-sensitivity of steel in flexure is higher than that of the aligned steel fiber-matrix bond in concrete. It follows that the observed responses are strongly dependent on the geometry of the steel fiber tested, and a change in the geometry may, in fact, change the trends.

The slip at the peak load for the various fibers is plotted in Figure 6.32 for aligned fibers and in Figure 6.33 for those inclined at 45°. A general reduction in slip with an increase in the rate of load application may be noted. This stiffening in the fiber-matrix bond during the pre-peak stage under impact is of particular significance and advantage for the

polymeric fibers that suffer from a delayed development of the peak-load (see Figure 6.1).
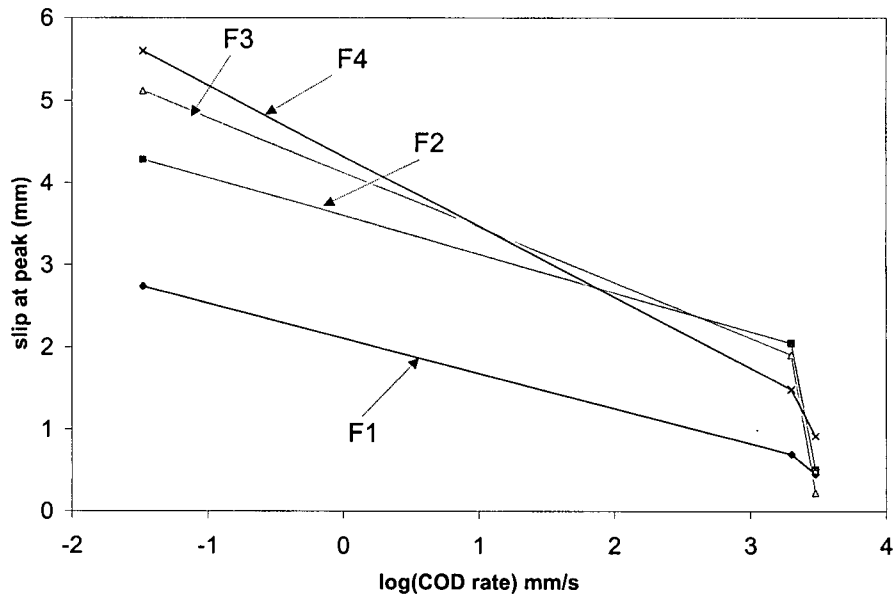
Figure 6.33   Effect of COD Rate on Slip @ Peak Load (Inclination = 45° with Load-Line)

Steel fibers, due to their higher elastic modulus develop their peak loads at much lower crack opening displacements (or fiber slips), and this gives them a definite advantage from a serviceability point of view when large crack widths may not be tolerated. Even though mechanical anchorage may be improved through surface deformations [46,50] or chemical treatment [66], and the fiber may be stressed closer to its ultimate tensile strength, the low stiffness of the polypropylene fiber still means that a higher energy dissipation during pull out does not necessarily translate into higher toughness of the composite at small overall crack openings and displacements. Since serviceability requirements impose a limit on the maximum allowable crack openings, any efficient use of polypropylene fibers requires that the peak loads be attained at smaller crack openings.

From this study, it appears that the fiber-matrix bond in the case of polymeric fibers is greatly stiffened at higher rates of loading, and the slips at peak load may in fact approach those observed in steel fibers. Polypropylene macro-fibers with proper surface

deformities are, therefore, better suited for applications where dynamic loads occur routinely.

Figure 6.34 shows the energy up to first peak, E_{peak} as a function of COD rate under aligned loading while the trend for a fiber inclination of 45° is shown in Figure 6.35. Under aligned conditions, one notices a convergence of polypropylene and steel fibers at higher rates of loading corresponding to impact. This is, as mentioned before, an indication of the stiffening of fiber-matrix bond in the case of deformed polypropylene fibers. But for fibers inclined at 45°, a drop in the E_{peak} was witnessed for all deformed fibers. The reason for this apparent embrittlement is as follows: with the three polymeric fibers, abrasion with the matrix leads to better anchorage with the result that the bond is much stiffer and causes fibrillation. Given that the slips at peak fall uniformly, clearly, the dissipation of energy is not so much through actual slippage but through fibrillation and damage to the fiber.
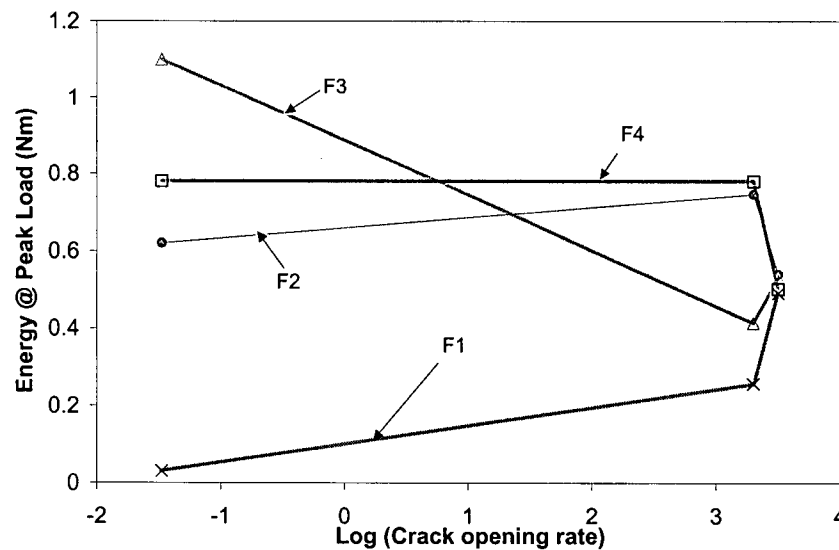
Figure 6.34   Effect of COD Rate on Energy @ Peak Load (Inclination = 0° with Load-Line)

For the steel fiber F4, which as mentioned before straightens out, the bond between concrete and fiber stiffens, as witnessed by the increase in peak load. Under aligned conditions, the weakening of the bond with concrete results in energy dissipation.
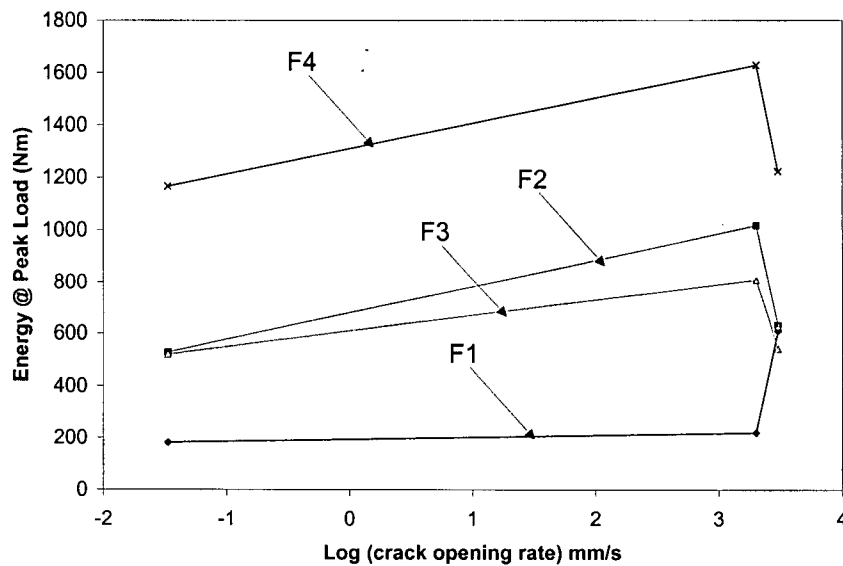
Figure 6.35   Effect of COD Rate on Energy @ Peak Load (Inclination = 45° with Load-Line)

On the other hand, with inclined fibers, the energy is mainly consumed during straightening the fiber. This straightening proceeds beyond the peak-load. So, during the pre-peak phase of a steel fiber, higher peak loads together with smaller slips-at-peak combine to yield lower levels of dissipated energy. In this phase, we witness the role of the rate-sensitivity of steel in uniaxial tension, which is much less than rate-sensitivity of the fiber-matrix bond, or even the rate-sensitivity of steel in flexure. The pre-peak response under lower COD rates is flatter than at the COD rate of 3000 mm/s. Consequently, energy to peak load drops at the highest rate. However, impact at this rate also induces multiple peaks during pull-out resulting in a large increase in total energy dissipation.

Figure 6.36 and 6.37 show the effect of rate on the total energy absorbed (for the case of aligned loading and fiber orientation of 45°, respectively). It is a function of the mode of fiber failure and hence depends upon whether they pulled-out completely or fractured. As mentioned earlier, the mode of failure for some deformed polypropylene fibers changed from pull-out to fracture at higher pull out rates, this significantly reduced their capacity

to dissipate energy. While one does not see a clear trend in Figure 6.36, a fact previously reported [68], it is clear that if a deformed polymeric fiber preserves its pull-out mode of failure during an increase in loading rate, then its energy absorption capacity may in fact approach that of steel.
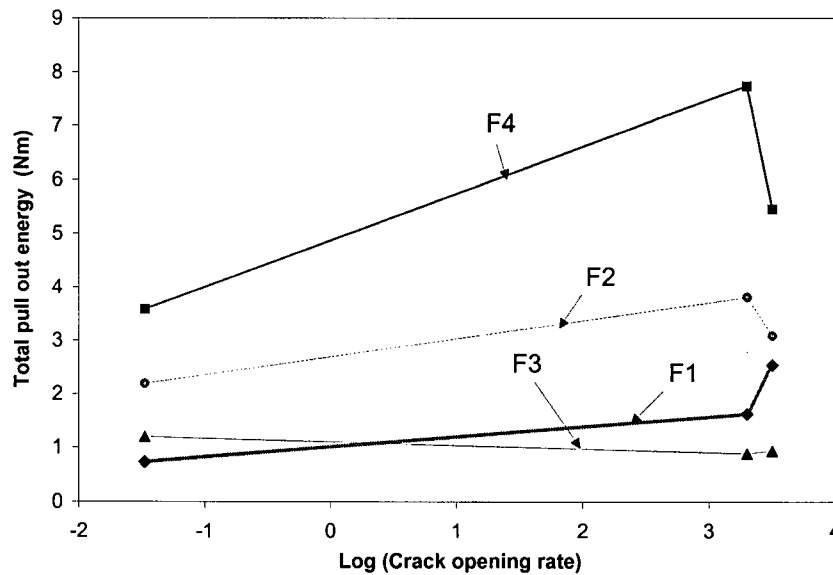
Figure 6.36   Effect of COD Rate on Total Energy (Inclination = 0° with Load-Line)
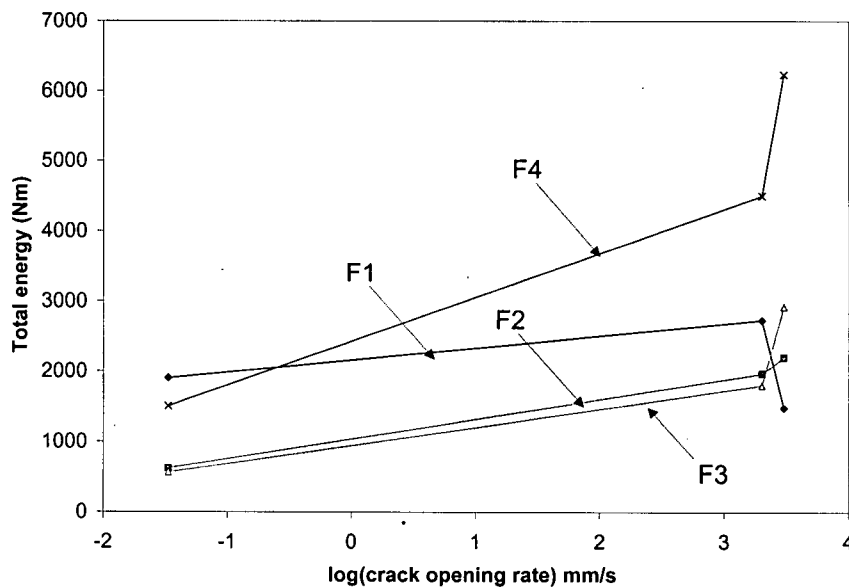
Figure 6.37   Effect of COD Rate on Total Energy (Inclination = 45° with Load-Line)

124

6.4.2 Effect of Matrix Strength

Figures 6.38-6.41 depict the effect of matrix strength on the pull-out of the four fibers under different loading rates. A clear distinction emerges between those fibers that pulled out (Fibers F1 and F4) and those that fractured (fibers F2 and F3) under impact loading.
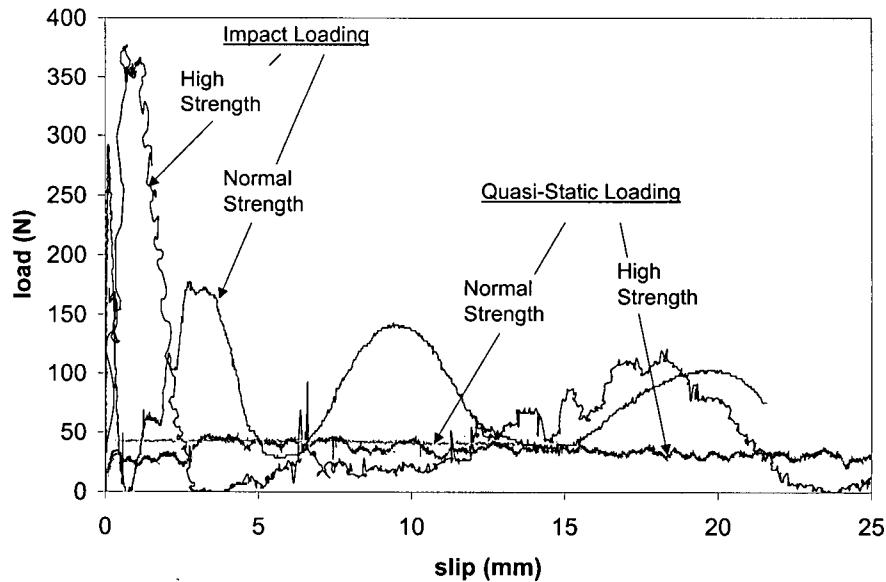
Figure 6.38   Effect of Matrix Strength on the Pull-Out Response of Fiber F1
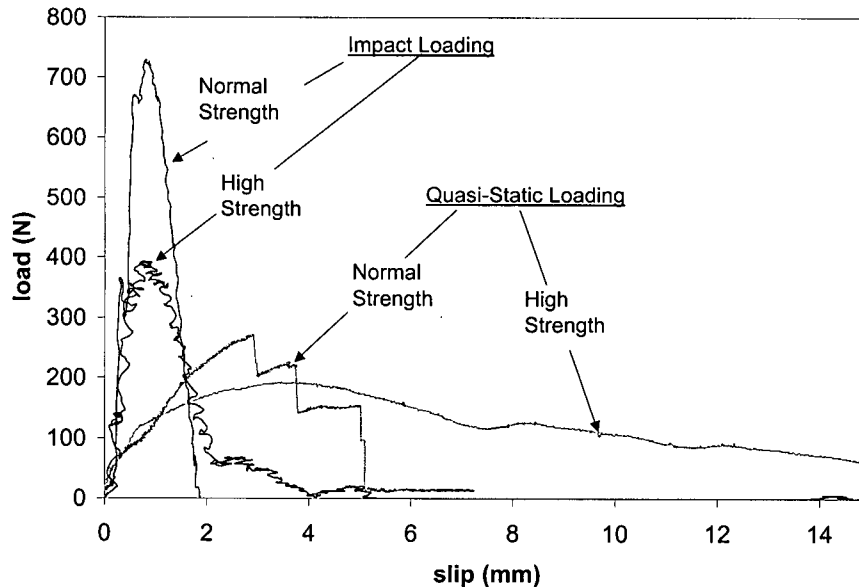
Figure 6.39   Effect of Matrix Strength on the Pull-Out Response of Fiber F2
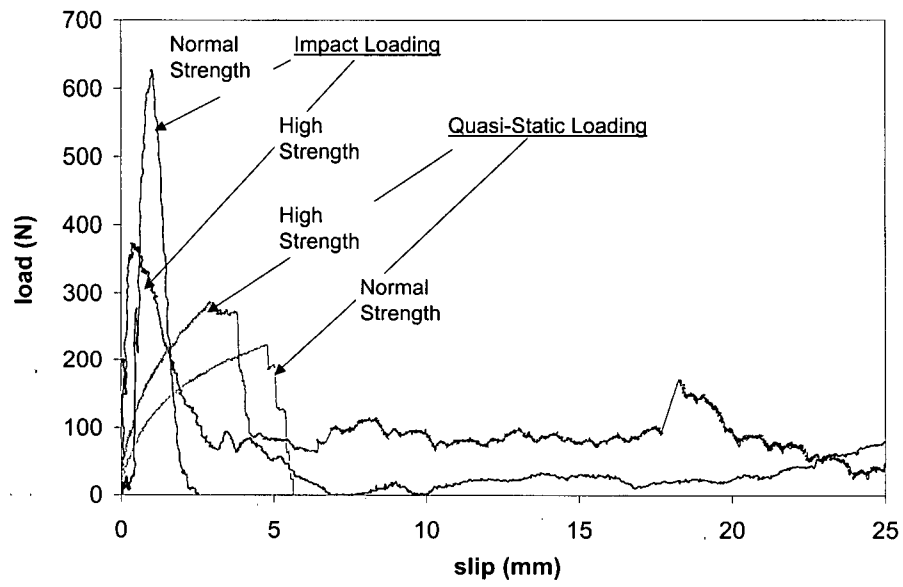
Figure 6.40   Effect of Matrix Strength on the Pull-Out Response of Fiber F3
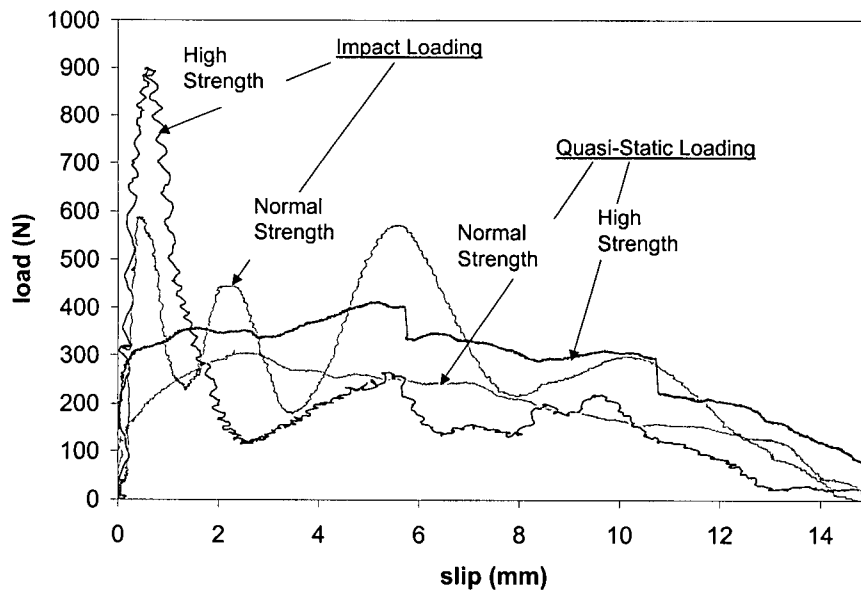
Figure 6.41   Effect of Matrix Strength on the Pull-Out Response of Fiber F4

126

Whereas increasing the matrix strength led to higher peak loads at smaller slips for Fibers F1 & F4, Fibers F2 & F3 do not follow a similar trend. Under quasi-static loading, increasing the matrix strength helps increase the peak pull-out load for the deformed polymeric fibers but under impact, the higher matrix strength appears to be detrimental to their performance. Clearly, the benefit from a higher strength matrix may be realized only if a pull-out mode of fiber response be maintained. However, the energy of pull-out drops across all fiber types when the matrix has a higher strength. This indicates that as expected, the higher strength matrix does lead to an increasingly brittle behaviour for the fibers.

6.4.3   Mode of fiber failure

Scanning electron micrographs of fibers after pull-out show the extent of damage that occurred in the deformed polypropylene and steel fibers during pull-out at the different rates of loading. While polypropylene fibers have extensive fibrillation and even longitudinal splitting (Figures 6.42 a-d), steel fibers sacrificed their flat ends (Figure 6.42 e & f). It appears, however, that the damage is not related to the loading rate. Wang *et al.* [50] also observed fibrillation on quasi-statically pulled out polymer fibers and found it to be proportional to the length of fiber pulling out from the matrix. As polymeric fibers have a lower modulus of elasticity than the cement-based matrix, they reasoned that during pull out, the contact points in the matrix act as indenters that abrade the fiber surface. Synthetic fibers are highly oriented structures composed of long chain molecules aligned with the fiber axis. Due to such microstructure, the fiber debris is not necessarily separated from the fiber and hence results in peeling and fibrillation. Gokoz and Naaman [67] did not notice any resistance in polypropylene fibers at the instant of final pull out from the matrix. Conceivably, the abrasive action resulting in fibrillation is likely to offer frictional resistance even at later stages of final pull-out. In this research program, a finite pull out load was registered for all polymeric fibers at the instant of their final exit from the matrix.
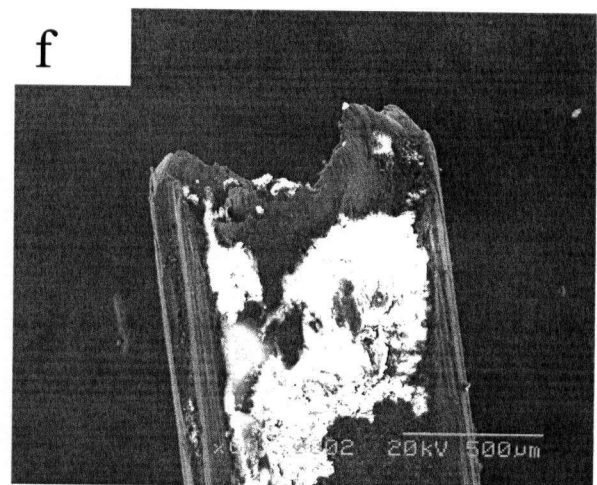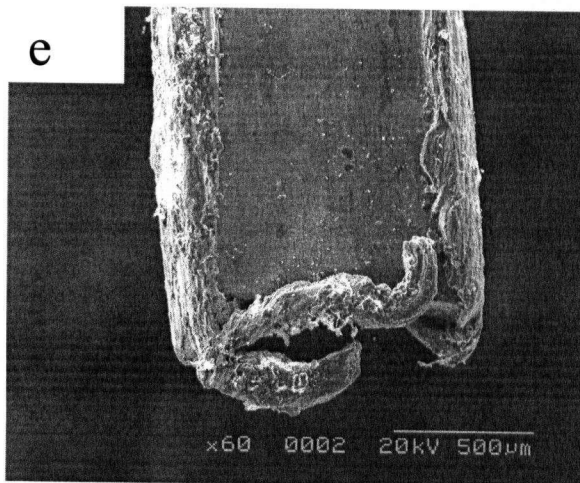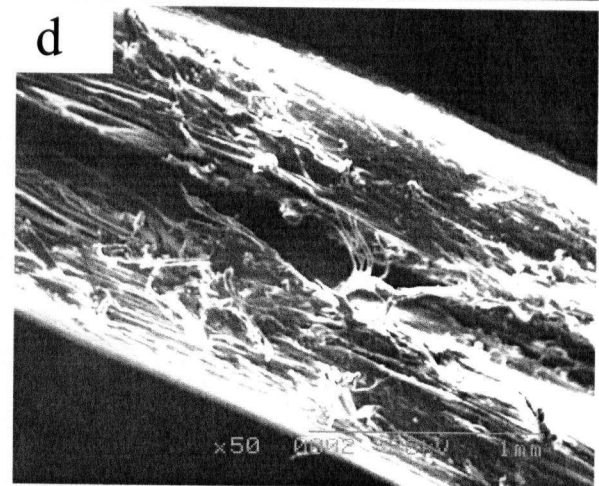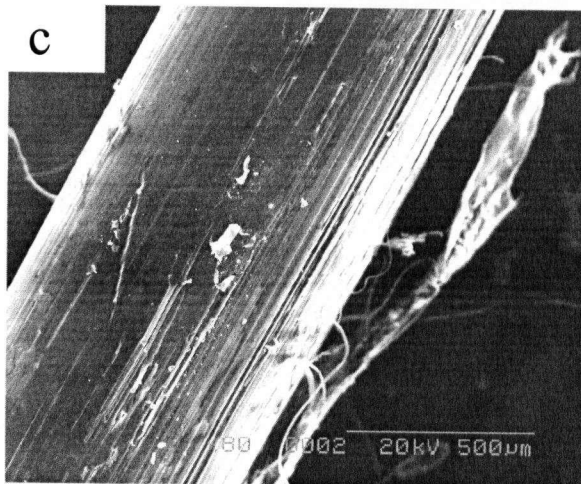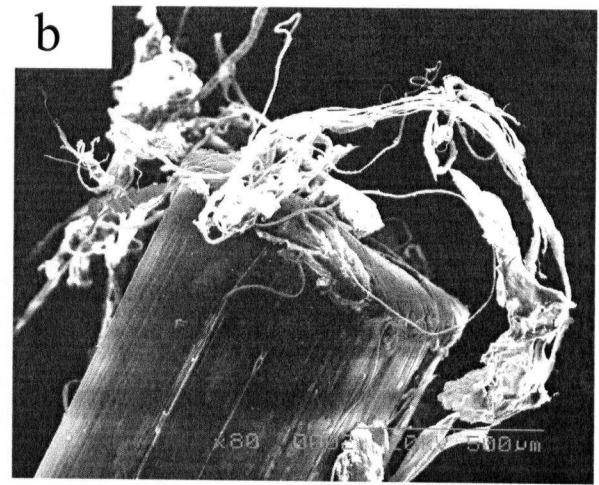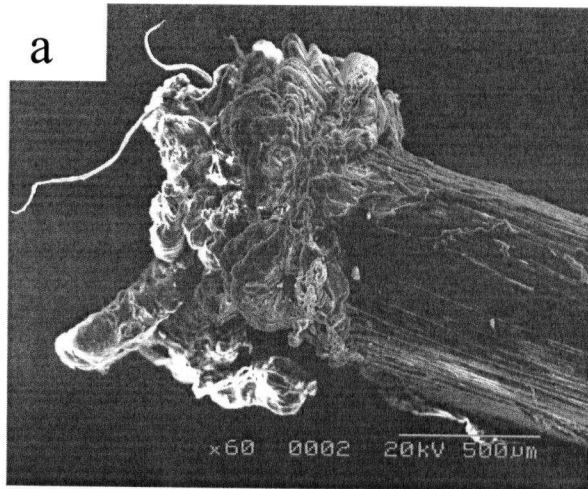
(Previous Page)

Figure 6.42   SEM Micrographs Showing Extent of Damage to the Fibers during Quasi-Static and Impact Pull-Out Loading: Fibrillation at the Ends of F2 a) Static Loading, b) Impact Loading; Fibrillation and Split Along the Length of F2 under c) Static Loading and d) Impact Loads; Loss of Flat Ends in F4 under e) Static Loading & f) Impact Loading.

6.5   Conclusions

1. The number of peaks in the pull-out load vs. Crack Opening Displacement (COD) curve increases with an increase in the rate of loading. The peak pull-out load increases with an increase in the loading rate. Due to its superior flexural rigidity and a higher modulus, inclined steel fibers depicted vastly improved peak loads under impact loading.

2. The COD associated with the peak pull-out load decreases with an increase in the COD rate. This results in a stiffening of the bond under high rates of loading, and is of specific advantage to low modulus polymeric fibers.

3. The energy absorbed to peak pull-out load increases with an increase in the loading rate if the mode of fiber failure is preserved. Steel fiber was once again an exception where the energy absorption was seen to decrease at very high rates of pull-out even when the fiber failure mode remained one of 'complete' pull-out at static as well as dynamic rates.

4. For deformed polymeric fibers, if a pull-out mode of failure may be preserved, the performance of deformed polypropylene fibers may approach that of the steel fibers both on the basis of energy absorbed to the peak load and on the basis of the total pull-out energy.

129

5. SEM observations show that both static and impact loading may cause similar damage to the fibers tested. While polypropylene fibers showed fibrillation and splitting, steel fibers lost their flat ends during pull-out.

Chapter 7

IMPACT RESPONSE OF FIBER REINFORCED CONCRETE, PART-2: FLEXURAL TOUGHNESS

7.1 Introduction

As discussed before, the role of fibers in a quasi-brittle matrix lies in dissipating energy beyond the instance of matrix cracking through processes that result in pull-out or fracture. The bond-slip response reported in Chapter 6 refers to the fiber-matrix interaction at the level of their interface. It was established in Chapter 6 that this interaction is highly rate sensitive. In this Chapter, beams reinforced with steel and polymeric fibers (from among those investigated in the previous Chapter) are assessed for flexural toughness under quasi-static and impact loading. There is very limited data pertaining to the response of concrete having polypropylene fibers as structural[1] reinforcement. An attempt is made to correlate the fiber-matrix bond-slip information generated in Chapter 6 to the flexural toughness response reported here. This is followed by a detailed study of the toughening capacity of steel and polypropylene fiber reinforced concrete under increasing stress-rates. Finally, the issue of specimen size-effect on the impact response of FRC is addressed.

7.2 Quasi-Static Loading

Quasi-static tests were conducted on concrete beams (normal strength ~ 40 MPa) reinforced with fibers (F1, F2, F3, F4) at a dosage rate of 0.75 % volume fraction. Although the quasi-static flexural toughness tests were conducted as per ASTM C 1018, the analysis on the resulting load-displacement curves was performed as per the JSCE SF-4 recommendation. The ASTM C1018 analysis technique involves locating the exact point of 'first crack' on the load-deflection curve, and this is never possible [145]. To illustrate this point, some magnified pre-peak portions of the quasi-static curves are

---

[1] The term "structural" refers to those fibers whose intended role is the ability to dissipate energy during the crack development in the hardened concrete matrix. This is as opposed to those fibers which may be added to modify the rheology, control shrinkage cracks, effect electrical conduction etc.

shown in Figure 7.1. Notice the non-linear nature of the curve up to the peak load, and the clear lack of a well-defined first crack point. In the JSCE SF-4 technique, instead of locating the first crack, the overall energy absorption up to a large deflection of 2 mm (span/150) is calculated and designated as the Flexural Toughness Factor. This quantity has the units of stress and it indicates qualitatively, the post-cracking residual strength of the material when loaded to an arbitrary deflection of span/150. The analysis as per the JSCE SF-4 procedure is not tied to the conditions at the so-called 'first crack'. As is well known [145], during such a test, the specimen supports settle in the direction of load application, and concrete crushing occurs at the load points. In order to eliminate these extraneous specimen deflections, a "Japanese yoke" was installed around the specimens as shown in Figure 4.4. With such an arrangement, only the net deflection of the neutral axis is measured which relates well with the theoretical deflection arising from bending and shear in the specimen. The total theoretical deflection, δ including flexure and shear is given by:

$$\delta = \left(\frac{23 P l^3}{1296\, EI} \right) \times \left\{ 1 + \frac{216\, d^2 (1 + \mu)}{1151^2} \right\} \qquad \ldots(7.1)$$

$$\Uparrow \qquad\qquad \Uparrow$$

(flexure)　　　　　(shear)

where, δ　　= deflection of the beam

P　　= applied load

EI　　= beam flexural rigidity

l　　= beam span

D　　= depth of the beam section, and

μ = Poisson's ratio for the material of the beam.

During a test, both the applied load and the specimen deflection in the direction of the applied load were measured. The deflections were measured by two linear variable displacement transducers (LVDTs) placed on either side of the specimen, results from which were averaged and recorded as beam displacement.
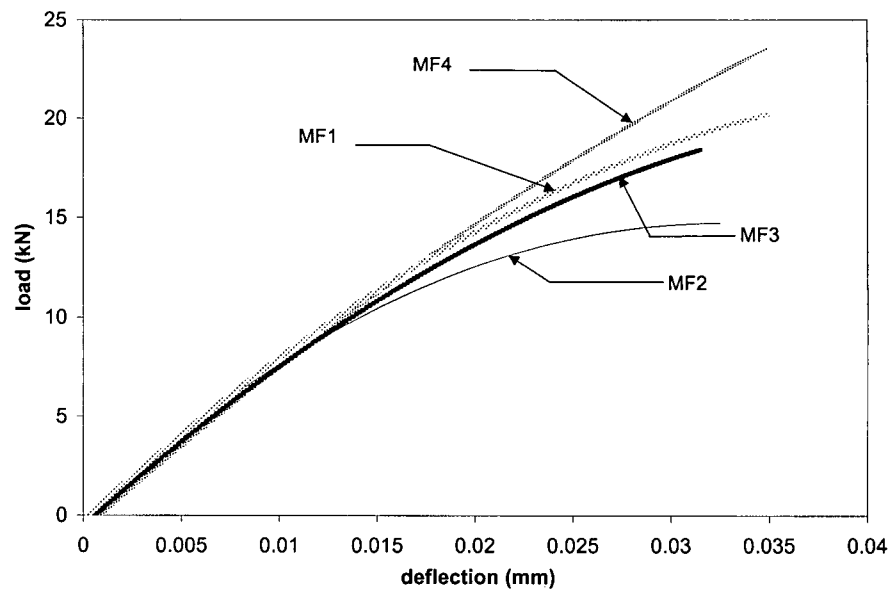
Figure 7.1   Pre-Peak Flexural Response of FRC Beams (Note Non-Linearity in Curves)

Representative quasi-static load-deflection curves for beams reinforced with the four fiber types are shown in Figure 7.2. Notice the superior load-displacement response of the steel fiber reinforced concrete beams over concrete reinforced with polymeric fibers. Of the three polymeric fibers investigated, the 50 mm deformed polypropylene fiber (F3) was clearly the most effective. Notice also that under quasi-static loading, while the steel fibers are mobilized to resist crack opening at very small deflections, beams reinforced with polymer fibers exhibit considerable instability at the instant of peak load and the cracks had to open wider for the fibers to carry stresses beyond matrix cracking. A suitable length and surface deformation, as in the case of Fiber F3, resulted in an eventual increase in the load, but only at very large deflections and crack openings.
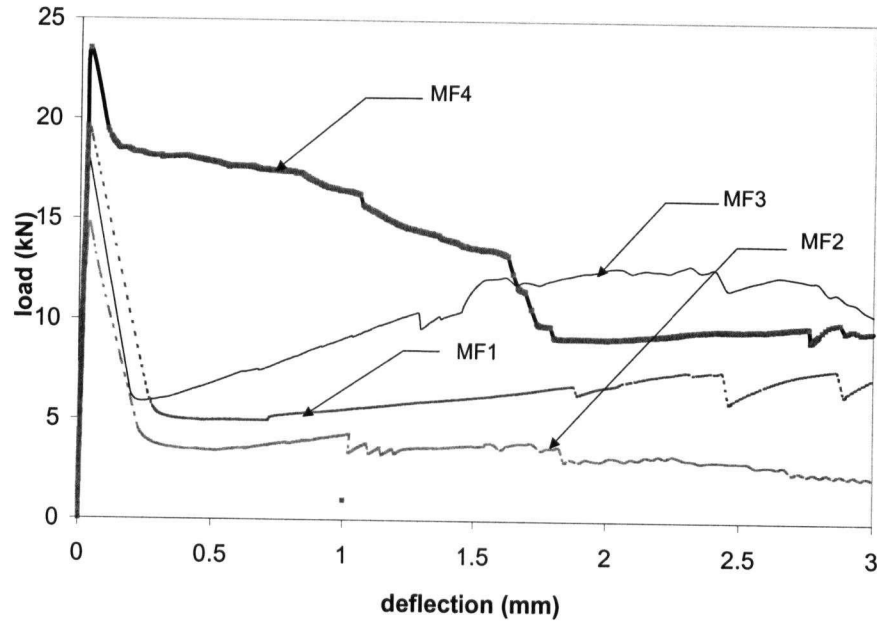
Figure 7.2   Flexural Response of FRC Mixes (MF1-MF4) under Quasi-Static Loading

7.3   Impact Loading

7.3.1   Effect of Fiber Length and Fiber Geometry

In this section, the flexural response of FRC beams reinforced with the four fiber types F1, F2, F3, F4, are assessed for toughness, which is subsequently correlated with their bond-slip response from the previous Chapter. Accordingly, these beams were subjected
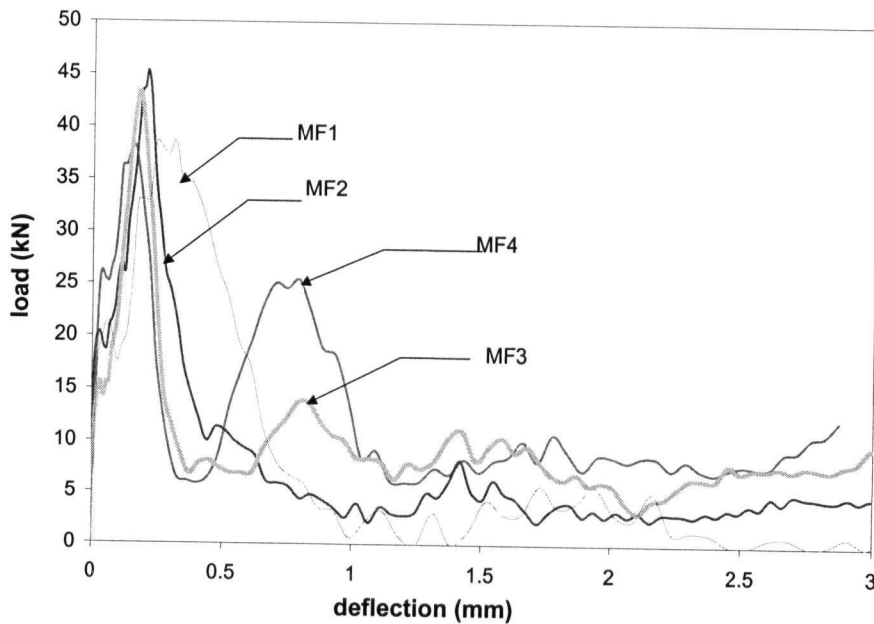
Figure 7.3   Flexural Response of FRC Mixes (MF1-MF4) under Impact Loading

134

to impact from a height of 100 mm in the large machine giving an incident impact energy of 600 J. Representative load-deflection curves under impact conditions for beams reinforced with the four fibers are shown in Figure 7.3. Notice the irregular and "wavy" nature of the curves as compared to the static curves of Figure 7.2. Notice also that while the first peak in the curve occurred at more or less the same value of load, the differences emerged only in the later part where either a second peak occurred (mixes with Fibers F3 and F4) or did not occur (mixes with Fibers F1 and F2). The differences also emerged in the level of load the specimens supported after the first peak, or if applicable, after the second peak. While the Fibers F1 and F2 supported minimal loads beyond the first peak, Fibers F3 and F4 both supported a large load after the second peak.

Figures 7.2 and 7.3 are further analyzed in Table 7.1 where flexural strength, fracture energy to 2 mm displacement and the flexural toughness factors under static and impact conditions are reported. Worth noting in Table 7.1 are the various ratios under the two stress rates. Notice first, the increase in the flexural strength for all mixes under impact, and second, the increase in the fracture energies under impact in the case of the polymeric fibers. Finally, notice the decrease in the fracture energy under impact loading for the mix reinforced with steel fiber (MF4).

For illustrative purposes, in Figures 7.4a & b, the quasi-static responses of mixes MF3 and MF4 are compared with their impact responses. Notice the very different responses of materials under two rates of loading. Notice also that the beams supported a larger peak load under impact than under quasi-static loading. In the case of mix having polymeric fiber F3 (MF3), notice that the load carrying capacity at large displacements actually exceeded that of steel fiber reinforced beams (MF4).

As mentioned earlier the large impact machine was employed with a drop-height of 100 mm, which resulted in an impact energy of 600 J. At this drop height, the dynamic flexural toughness factor drops below the static value in the case of the steel fiber F4. This clearly indicates that the inherent stress-rate sensitivity of the fiber

Table 7.1   Static and Impact Results for Fiber Reinforced Concrete Beams[2]

Mix no.	Incident energy (for Impact)	$f'c$ (MPa)	Flexural Strength			JSCE Fracture Energy[3]			JSCE SF4 FTF[4]		
			Static (MPa)	Impact (MPa)	Ratio (Impact/ Static)	Static (Joules)	Impact (Joules)	Ratio (Impact/ Static)	Static (MPa)	Impact (MPa)	Ratio (Impact/ Static)
MF1	1.33 E4	38	4.50 (0.60)	11.79 (1.45)	2.62	11.62 (1.54)	14.68 (1.80)	1.26	1.74 (0.23)	2.20 (0.27)	1.26
MF2	1.55 E4	40	5.70 (0.70)	13.35 (1.90)	2.34	7.56 (0.80)	16.30 (2.31)	2.12	1.13 (0.12)	2.40 (0.34)	2.12
MF3	1.61 E4	43	5.40 (0.60)	12.60 (1.76)	2.3	16.12 (1.74)	16.96 (2.13)	1.05	2.41 (0.26)	2.54 (0.32)	1.05
MF4	1.29 E4	43	6.90 (0.30)	10.50 (1.66)	1.52	26.25 (0.94)	20.98 (1.87)	0.79	3.93 (0.14)	3.14 (0.28)	0.79

[2] Plain concrete mix was not cast in this series.
[3] From area under the load-deflection curve computed to a deflection of span/150 = 2 mm.
[4] Flexural Toughness Factor.
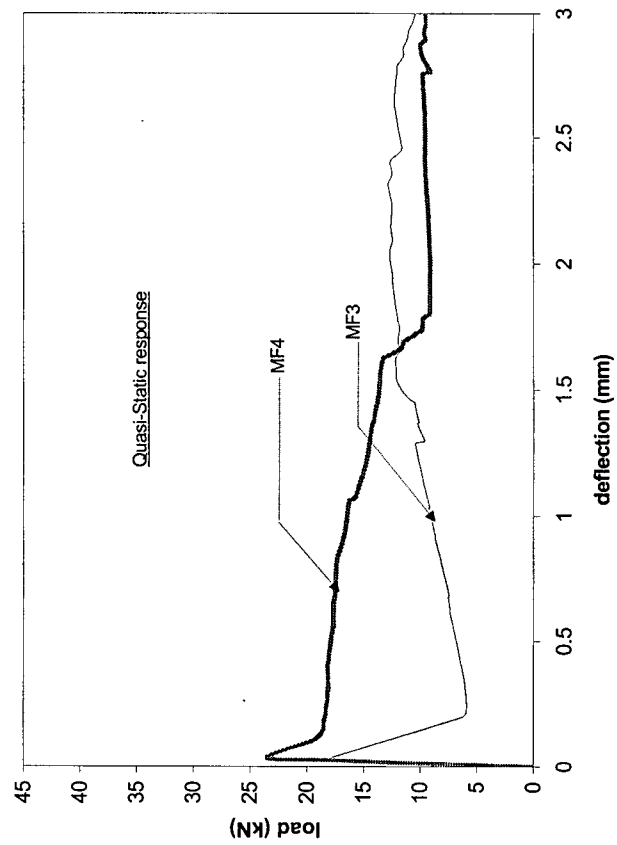
a)
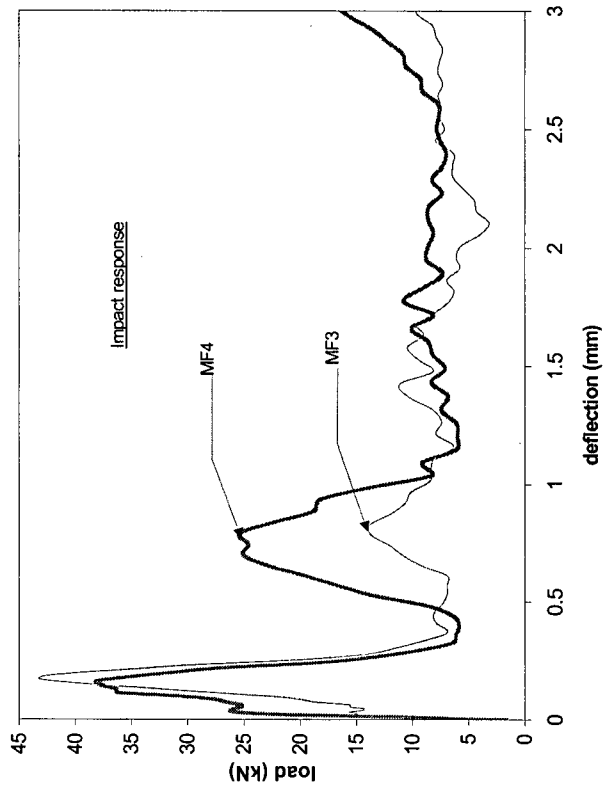
b)

Figure 7.4   Flexural Response of FRC Beams of MF3 (Reinforced with Crimped Polypropylene Fiber F3) and MF4 (Reinforced with Steel Fiber F4) under: a) Quasi-Static Loading and b) Impact Loading

137

material is working in favour of the polymeric fibers (especially the deformed ones) while it works against the steel fiber. Thus, the rest of the impact testing was conducted with the medium machine which, due to its lower capacity (a tenth of the large machine), was capable of investigating the whole range of intermediate rates.

7.3.2 Comparison with the Bond-Slip Response

In this section some comparisons are made between the observed flexural toughness responses of beams with the bond-slip responses reported in sections 6.2 and 6.3. In Figure 7.5, the fractured surfaces of the beams tested under impact loading are shown for the four fibers. No fiber fractures could be noted, and the same applied to the static loading case. In Figure 7.6a and b, the pull-out responses for the two fibers F3 and F4 are compared with the flexural toughness responses under static loading. The comparison for the same two fibers under impact loading is carried out in Figures 7.7a and b.

When one considers the static pull-out responses (Figure 7.6), it is clear that, compared to the steel fibers, the polymeric fibers get mobilized only at large crack openings. This is a major drawback of such low modulus fibers, and translates into a stress-transfer capability in concrete only at large matrix cracks when the serviceability conditions may already have been exceeded. While a suitable deformation or geometry improves the peak pull out load carrying capacity in such polymeric fibers, this peak load is attained only at large slips. Steel fibers on the other hand, due to their high material modulus, get mobilized at small crack widths and hence are able to carry greater loads immediately after matrix cracking. These tests are well predicted from the pull-out tests.

Further, as seen in the pull-out tests, beam tests indicate that the low modulus polymeric fibers benefit significantly from an increase in the rate of loading. They were shown to exhibit bond-stiffening during pull-out such that peak loads are attained at relatively small values of crack openings, and this applies also to beam tests. Under impact, therefore, a suitably deformed polymeric fiber may perform as well as steel fibers as was seen here.
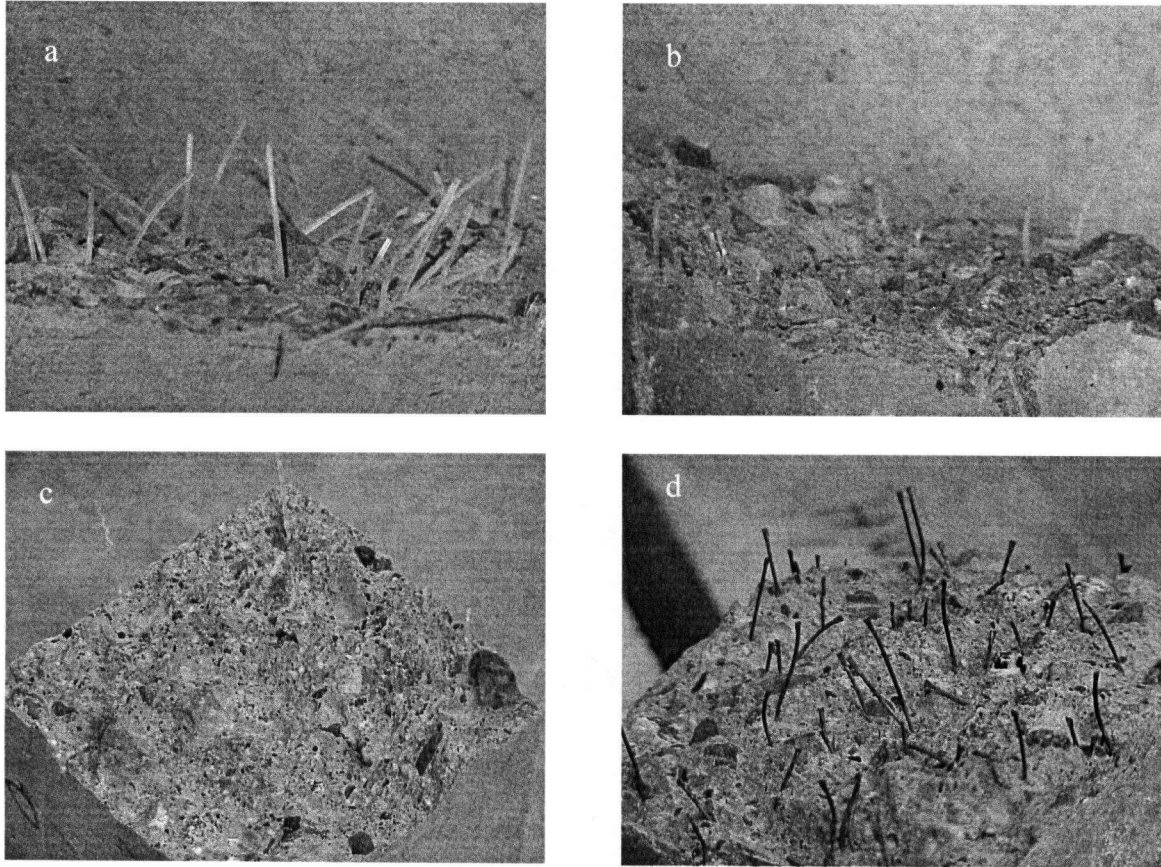
Figure 7.5   Fracture Surface of Beams: a) MF1; b) MF2; c) MF3 and d) MF4.
                Note Fiber-Pull-Out in all Cases

Some inconsistencies between the pull-out results and toughness test results must also be pointed out. Previous work [76] reported that fibers fractured at very high impact loading rates indicating a transition in the failure mode at higher strain rates. Ansari and Navalurkar [92] have also reported a fiber fracture mode of failure in the steel FRC beams tested under impact.
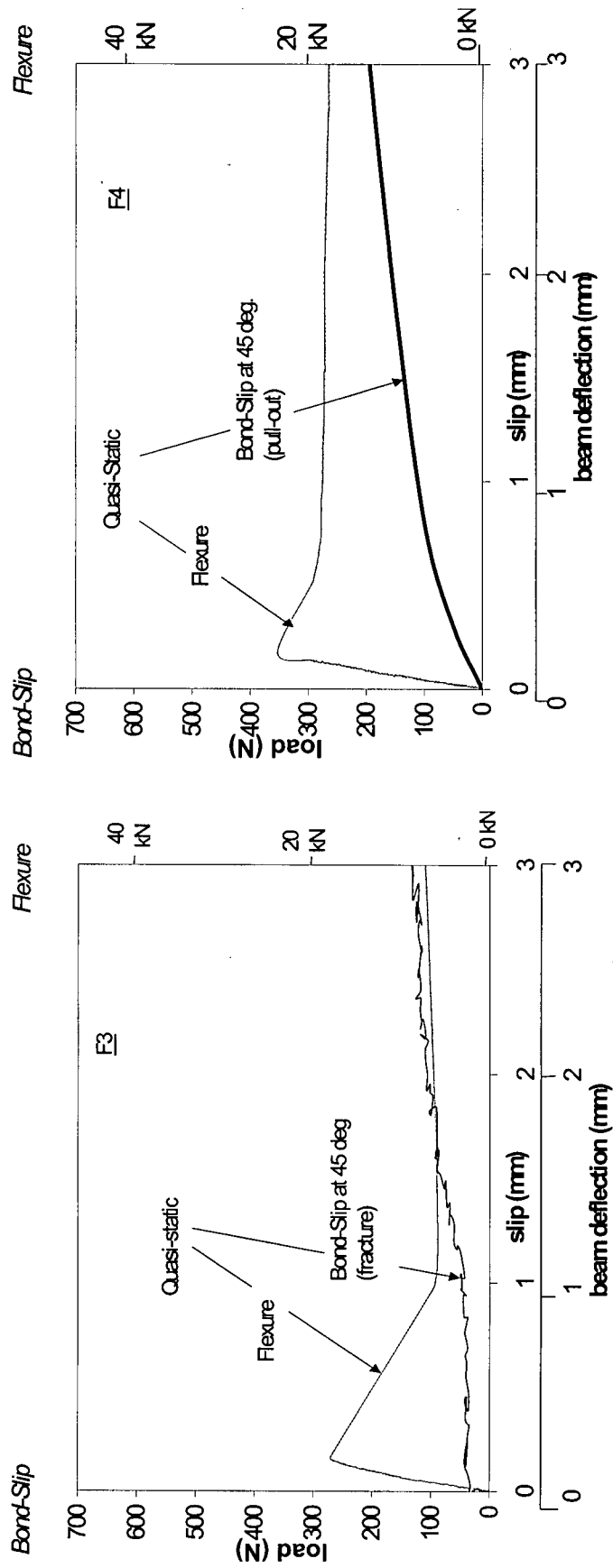
a)

b)

Figure 7.6   Comparison of Single-Fiber Pull-Out Response and Flexural Toughness Response under Quasi-Static Loading for
a) Fiber F3 and b) Fiber F4. (Note that the Bond-Slip Response is Shown for the Fiber Inclined at 45° to the Load-Line)
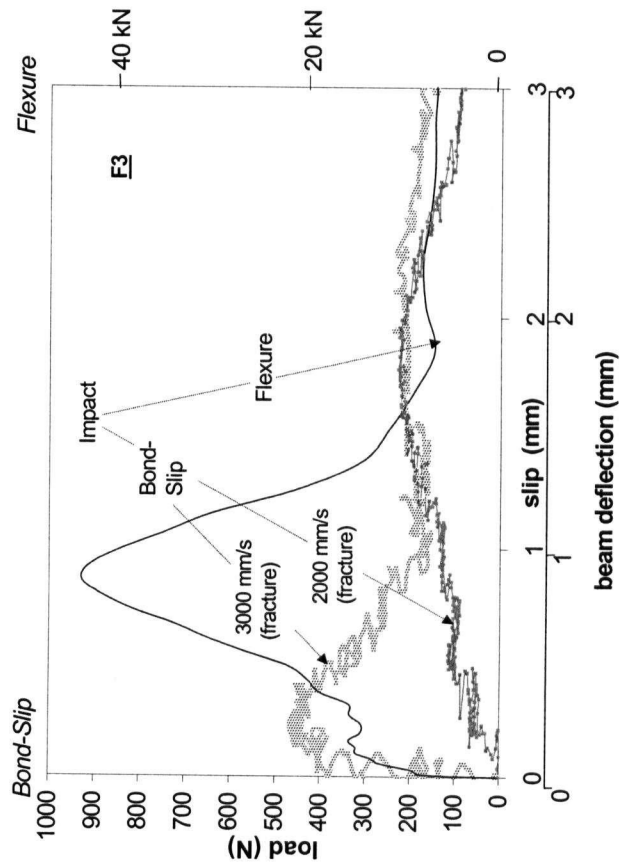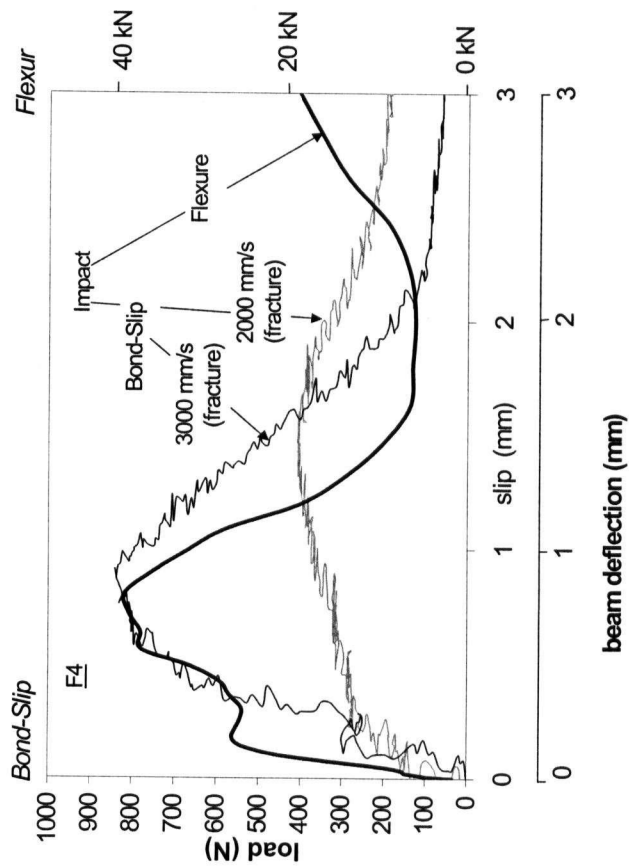
Figure 7.7   Comparison of Single-Fiber Pull-Out Response and Iimpact Loading for a) Fiber
F3 and b) Fiber F4. (Note that the Bond-Slip Response is Shown for the Fiber Inclined at 45° to the Load-Line)

141

In this study, surprisingly, Fiber F3, which fractured at all rates of loading during pull-out tests showed a complete pull-out in the beam tests. Consequently, while this fiber demonstrated a poor response in pull-out tests, its response in toughness tests was far superior to the other polymeric fibers, and in fact, approached that of the steel fiber. Similarly, for Fiber F2, while a possibility of transition from complete fiber pull-out to fiber fracture was noted in the pull-out tests, such a change was not seen in the flexural tests. Likewise, while steel fibers sacrificed their flat ends during pull out under all rates of loading, fractured surfaces revealed that steel fibers did not lose their flat-ends during failure of beams in flexure.

In a previous study with steel fiber and quasi-static loading, Banthia and Trottier [44] observed a good correlation, at least qualitatively between pull-out and flexural responses for a given fiber. In Figure 7.6, bond-slip and flexural responses of fibers F3 and F4 are compared under quasi-static loading. To account for random fiber orientation, bond-slip responses for fibers inclined at 45° are shown. The polymeric Fiber F3 is mobilized at a later slip value and this is reflected in the higher instability in its flexural response. Under impact, the flexural responses for the same two fibers are compared with their bond-slip behaviour in Figure 7.7 under two rates of pull-out. Clearly, the polymeric fiber F3 experiences a significant improvement in bond-slip stiffness which is reflected in terms of toughness values comparable to steel Fiber F4. However, for the steel fiber, under impact, failure occurred through fracture, and this accounts for the drop in its flexural toughness vis-à-vis its response under static loading.

7.3.3 Effect of Fiber Material

As indicated previously, the Medium Machine was used in order to investigate the response of fiber reinforced concrete to impact loads, where the height of hammer drop was varied. In impact tests conducted with the Large Machine, steel fiber reinforced concrete registered a drop in their flexural toughness. The Medium Machine was chosen in favour of the Large Machine as it allowed for investigating material response over an intermediate range of stress-rate. Consequent to the results of tests conducted on the four fiber types (and described in sections 6.2-6.3), two fiber types were studied further in

142

order to investigate the effect of fiber material on the impact performance of FRC in flexure. These were the flat-end steel fiber and the crimped polypropylene fiber, both 30 mm in length. Fiber reinforced beams in three span/depth sizes (150 mm/50 mm, 300 mm/100 mm, 450 mm/150 mm), were examined under impact loading from four drop-heights. This section describes the performance of each individual beam size.

Small Beams (150 mm/ 50 mm)

Figures 7.8a and b depict the flexural response of small beams under various drop-heights. Notice an increase in flexural strength (MOR) with an increase in the drop height for both composites. Fiber fractures for both steel and polypropylene fibers were evident upon inspecting the broken halves of the beams. Notice also that as the drop-height increased, the peak loads occurred at lower deflections in the case of PFRC (Table 7.2). This suggests, once again, a stiffening response for PFRC over that of SFRC especially at large drop-heights.

Medium Beams (300 mm/100 mm)

Figures 7.9a and b show the flexural response under various drop heights for medium size SFRC and PFRC beams, respectively. Once again, note a clear increase in the MOR with an increase in the height of hammer drop (or the stress-rate). The dominant mode of fiber failure in SFRC was fiber pull-out with very few fibers fracturing. However in PFRC, equal instances of both fiber pull-out and fiber fracture were observed. It is seen in Table 7.2 that the deflection at MOR is higher for PFRC at low drop-heights, but with an increase in the drop-height, the response of PFRC becomes stiffer and the MOR was attained at smaller values of deflection. Indeed, the values of deflection for PFRC at higher drop-heights were similar in value to that for SFRC at higher drop-heights.

Large Beams (450 mm/150 mm)

The flexural response of large size beams is presented in Figures 7.10a and b for SFRC and PFRC respectively. As with the small and medium size beams, the MOR increases with the drop-height. The deflection at corresponding to MOR is uniformly lower for PFRC beams than the SFRC beams. Also, upon inspecting the broken

Table 7.2　　　　Impact Response of FRC Beams Tested with the Medium Machine

(6 Specimens)

Mix	Size	Drop-Height (mm)	MOR (MPa)	δ_{peak} (mm)	FTF (MPa)
Sfrc	Small	200	38 (6)	0.39 (0.08)	8 (1.50)
		500	43 (8)	1.32 (0.24)	29 (0.65)
		750	56 (4)	1.14 (0.21)	44 (0.91)
		1000	60 (11)	0.93 (0.22)	47 (0.82)
	Medium	200	29 (3)	0.39 (0.05)	10 (0.12)
		500	33 (5)	0.39 (0.03)	25 (0.32)
		750	38 (3)	0.64 (0.09)	30 (0.33)
		1000	51 (7)	0.50 (0.06)	37 (0.40)
	Large	200	16 (2)	0.62 (0.10)	3.5 (0.40)
		500	24 (3)	0.90 (0.10))	17 (0.18)
		750	30 (3)	0.93 (0.09)	22 (0.25)
		1000	33 (4)	1.06 (0.15)	27 (0.23)
PFRC	Small	200	23 (5)	0.10 (0.03)	6 (1)
		500	37 (7)	1.55 (0.2)	25 (5.53)
		750	45 (4)	1.03 (0.15)	36 (6)
		1000	58 (7)	0.79 (0.90)	47 (8.71)
	Medium	200	31 (4)	0.14 (0.02)	4.5 (6.23)
		500	24 (4)	1.54 (0.25)	18 (2.21)
		750	35 (3)	0.49 (0.07)	28 (3.45)
		1000	43 (6)	0.65 (0.07)	38 (4.75)
	Large	200	22 (3)	0.19 (0.01)	2.2 (0.23)
		500	23 (3)	0.64 (0.05)	16 (0.14)
		750	27 (2)	0.56 (0.06)	21 (0.18)
		1000	31 (5)	0.75 (0.06)	26 (0.30)
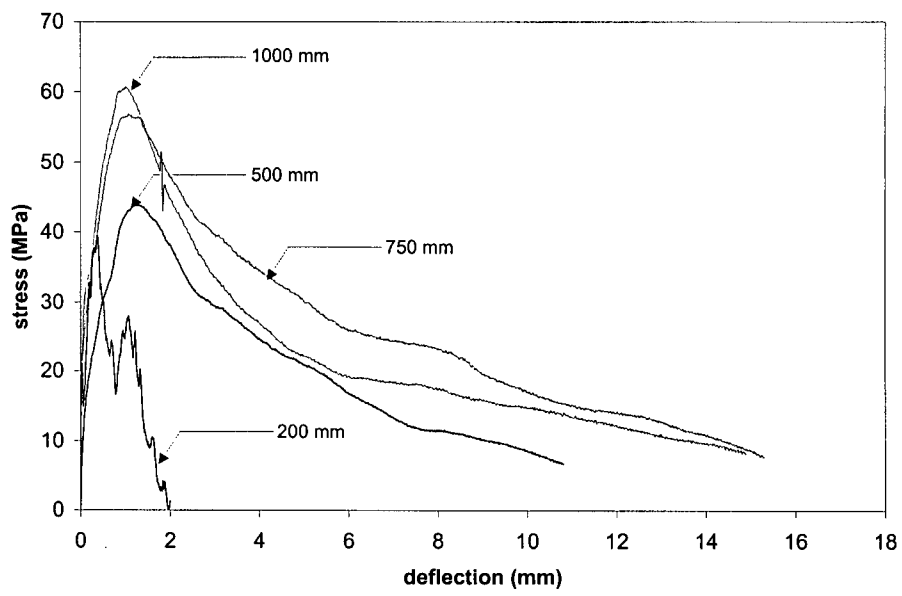
a)
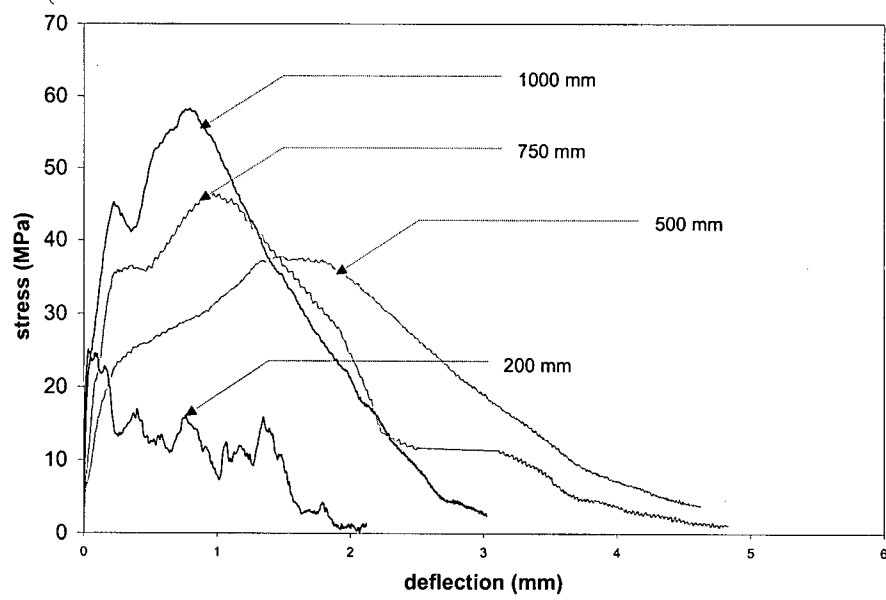
b)

Figure 7.8   Impact Response of Small Size Beams Made with a) SFRC and b) PFRC
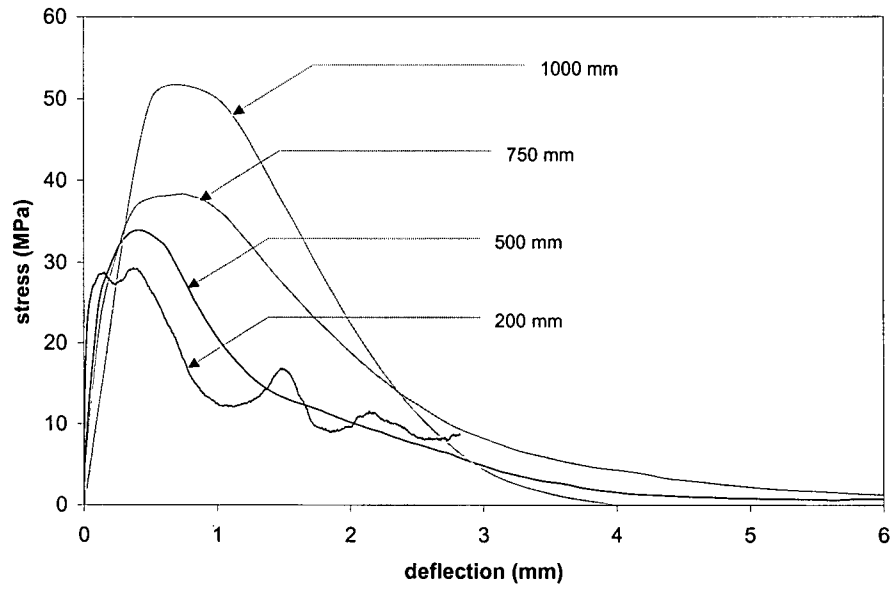
a)
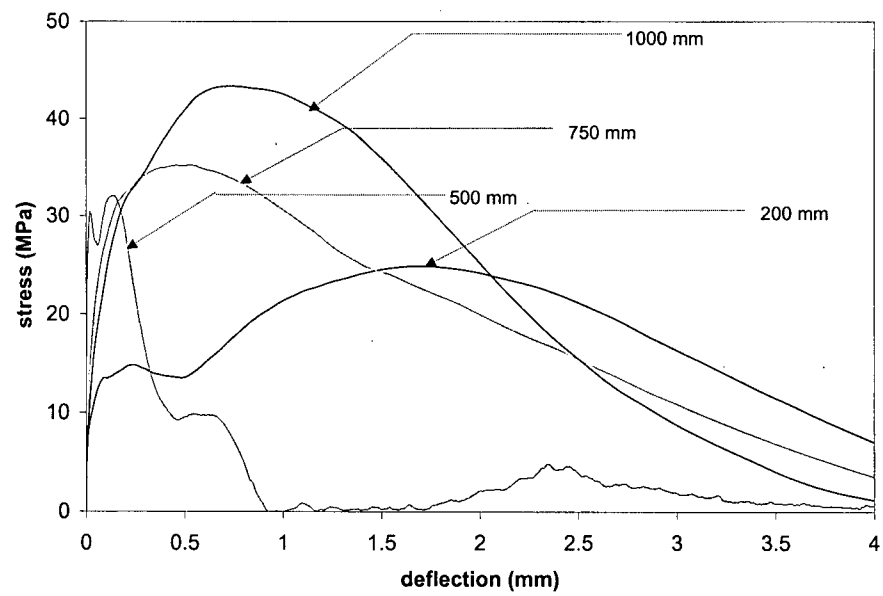
b)

Figure 7.9   Impact Response of Medium Size Beams Made with a) SFRC and b) PFRC

specimens, it was evident that all steel fibers pulled out while some polypropylene fibers fractured.
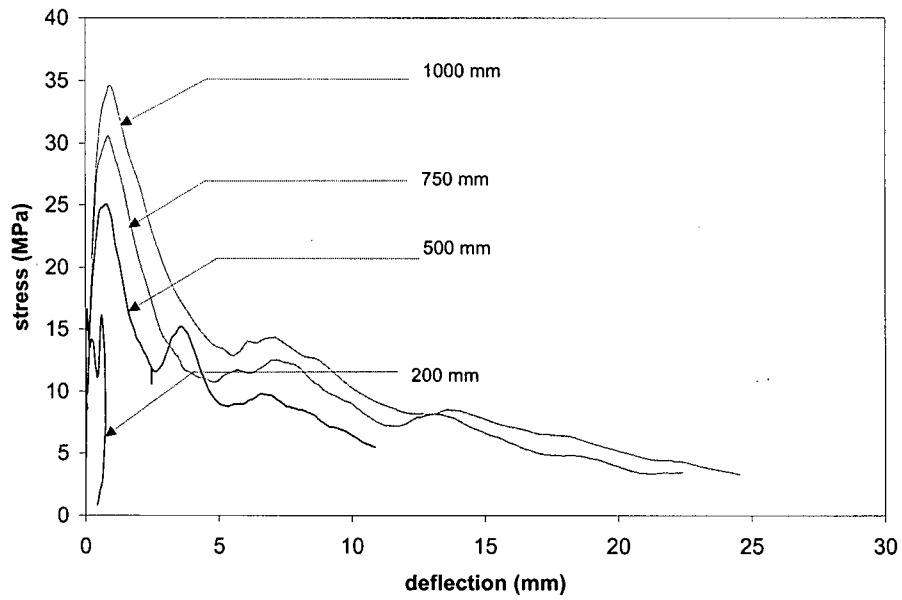
a)
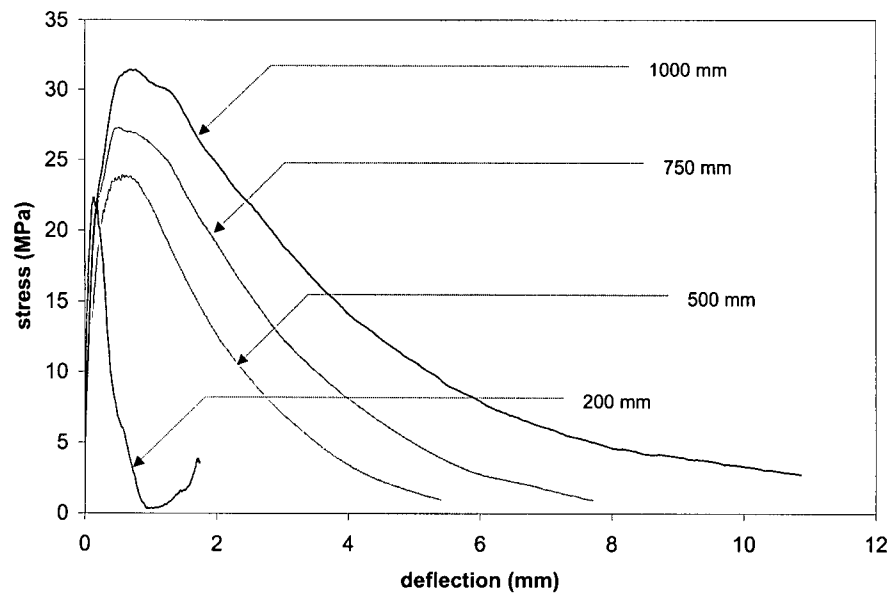
b)

Figure 7.10   Impact Response of Large Size Beams Made with a) SFRC and b) PFRC

7.4 Stress-Rate Sensitivity

7.4.1 Effect of Fiber Length and Geometry

From the load-displacement responses in Figures 7.2 and 7.3, it appears that fiber reinforcement is highly effective in both quasi-static and impact conditions in improving the absorption of energy. However, between the two types of fibers tested—steel and polymeric—the nature of responses is very different. Comparing the three polymeric fibers with the steel fiber, one notes that the polymeric fibers "catch-up" with the steel fiber F4 under impact. Specifically, this is seen through the diminished difference between the two fiber types under impact loading. This is further illustrated in Figure 7.11, where the energy absorption of the various polymeric fibers is reported as a percentage of that absorbed by the steel fiber (F4) at two rates of loading. Notice that the response of polymeric fibers improves significantly under impact loading, and the longer of the two deformed polymeric fibers (F3), absorbed nearly 80% of the energy absorbed by steel.
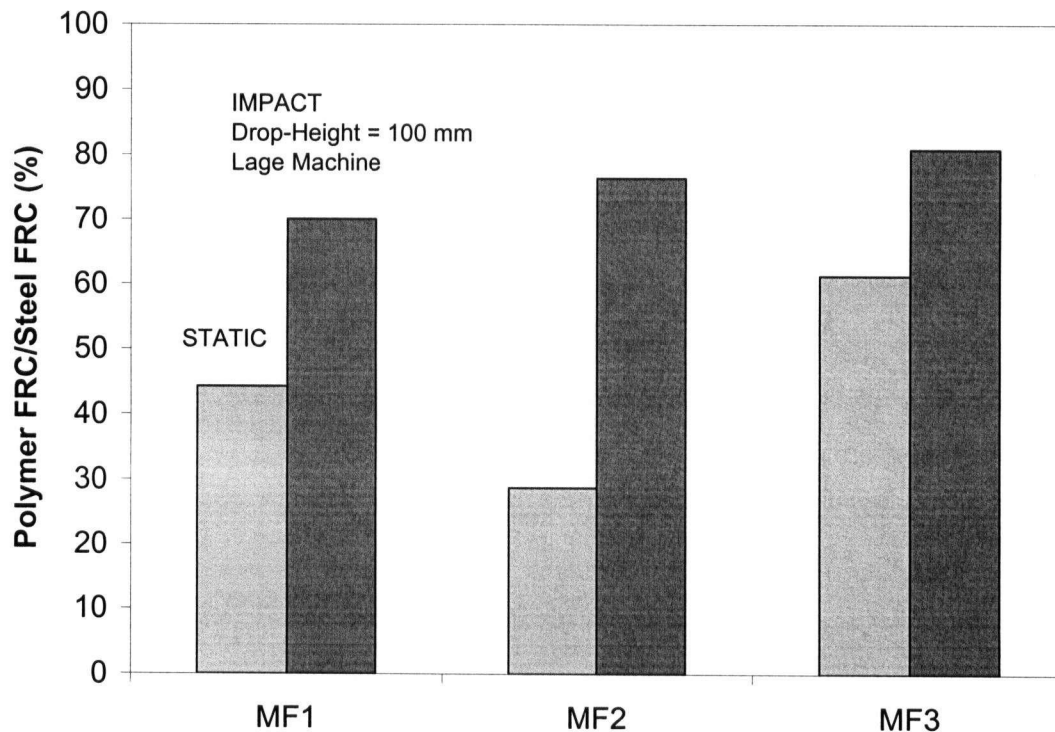
Figure 7.11   Fracture Energy Dissipated by Polymeric Fibers (F1, F2, F3) Compared with that by Steel Fibers (F4)

Further in Figure 7.12, the flexural toughness factors under impact loading are compared with those under static loading as a ratio.
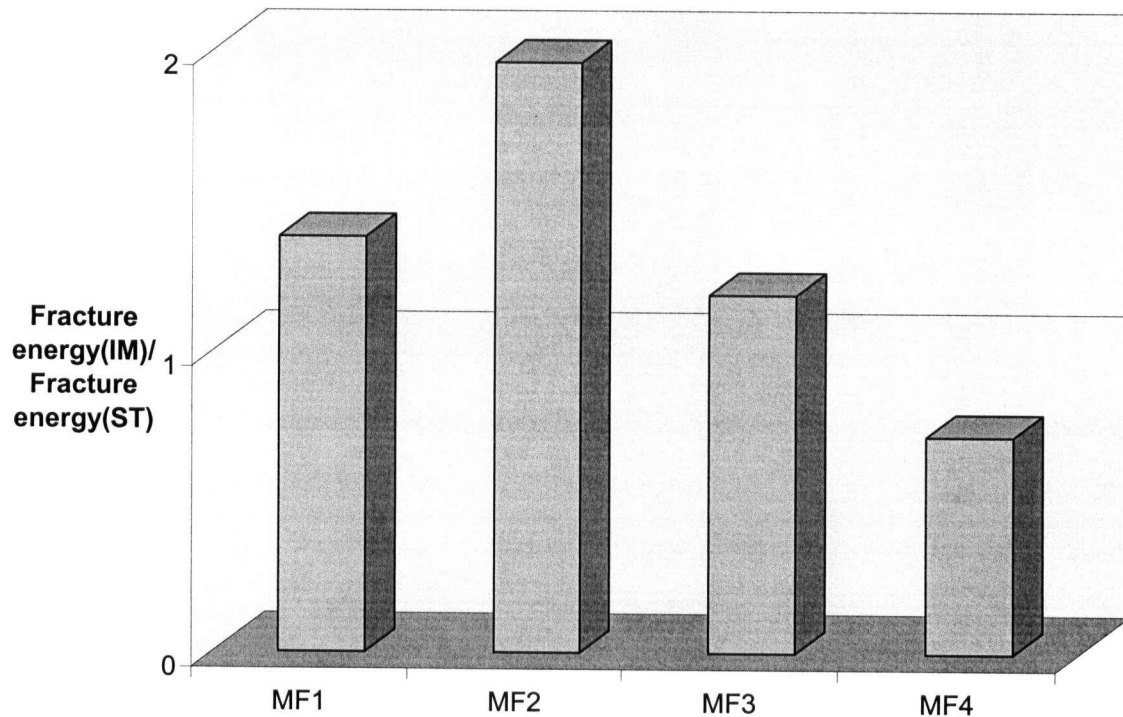
Figure 7.12   Ratio of JSCE FTF Values under Static (ST) and Impact Loading (IM)

Notice an increase in this ratio for the three polymeric fibers (F1, F2, and F3), but a decrease in this ratio for the steel fiber. In other words, while the concrete with polymeric fibers absorbed a greater amount of energy under impact loading as compared to static loading, steel fiber reinforced concrete absorbed less energy under impact. This observation is not generally supported in the literature [72,76,146] and hence applies specifically to the geometry of the fiber, strength and type of the matrix, method of placement and the rate of load application employed in this study. Much further research remains to be done in order to clearly understand the influence of stress rates, placement technique and strength of the matrix on the ability of these composites to absorb energy.

7.4.2 Effect of Fiber Material

7.4.2.1 Flexural Strength

It is clear from Table 7.1 and Figures 7.2-7.4, that under impact loading an increase in the flexural strength may be expected. This has been previously reported [17,20,72]. Using the formulation developed by Nadeau *et* al. [101] the stress-rate sensitivity of flexural strength for all the mixes investigated may be described. Such a comparison is made in Figure 7.13 for plain and fiber reinforced concrete (SFRC and PFRC). A 10-fold increase is noticed in the flexural strength and values as high have been reported before [76]. It is significant to note that based on the parameter 'N', plain concrete appears to be more sensitive than FRC. Further, there does not seem to be an influence of fiber type in Figure 7.13, but the curve shows the so called 'knee' at higher rates of loading as reported before. The point of greater interest, however, is the influence of stress-rate on the energy absorption capability or flexural toughness.
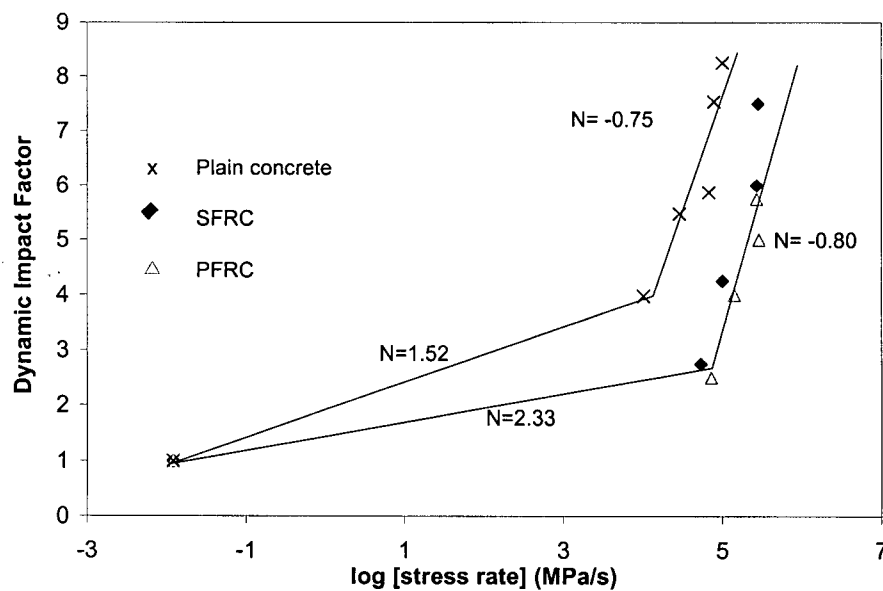
Figure 7.13   Stress-Rate Sensitivity of Plain and Fiber Reinforced Concrete under Flexure

7.4.2.2 Flexural Toughness

The flexural toughness of the fiber reinforced specimens tested in this program reveals an interesting trend. As expected, steel fiber reinforcement provided a higher toughness than

150

the polypropylene fiber reinforcement under quasi-static rates. Unlike with the Large Machine, Figure (7.12), as the stress rate was increased by increasing the hammer drop height, steel fiber reinforced concrete depicted a continual increase in its energy absorption capacity. Polypropylene fiber reinforced concrete on the other hand, demonstrated an increase in the energy absorption capacity with an increase in the stress rate, and in fact, surpassed the toughness of the steel fiber reinforced concrete at very high rates at a drop-height of 1000 mm (Figure 7.14).
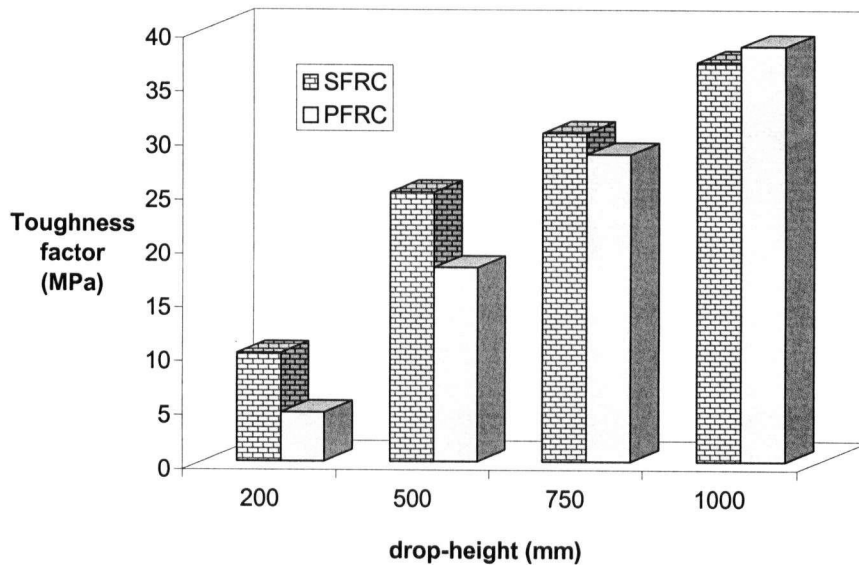
Figure 7.14   Flexural toughness of FRC beams (Medium Size) reinforced with fibers.

Clearly, this "switch" between the steel and polypropylene fibers under very high stress rate arises from their different constitutive responses, stress rate sensitivities and bonding characteristics. Studies on strain rate sensitivity of steel [34] and polypropylene [35] indicate that while steel undergoes an increase of about 20 % in its strength when the strain rate is increased from 10^{-4} to 10^2, polypropylene experiences an increase of nearly 300 % in the same range. The modulus also follows a similar trend, and polypropylene depicts a much stiffer response under impact loading. Note that the results presented in Figure 7.14 were conducted in the Medium Machine, while those shown in Figure 7.12 were performed with the Large Machine. Figure 7.14 shows an increase in the FTF value for SFRC for a drop-height of 1000 mm ($\approx$ 600 J), where as in Figure 7.12, under identical condition of incident energy, but from a drop-height of only 100 mm, a drop in

151

FTF values was registered for SFRC. Thus, the effect of the impact machine is clear from Figures 7.12 and 7.14. Once again, as with plain concrete, it is evident that maintaining a condition of identical impact energy is not enough to standardize impact tests.

7.5   Size Effect

In section 5.3 plain concrete beams of three different sizes were investigated under impact. The influence of specimen size on the FRC performance under impact loading has received little attention in literature. This section examines the effect of specimen size on the dynamic flexural strength and toughness of FRC. In particular, the influence of fiber type (steel vs. polypropylene) and stress-rate (induced by different drop-heights) are addressed.

7.5.1   Flexural Response of FRC

The response of SFRC for three beam sizes under impact loading is shown in Figures 7.15-7.18 for drop-heights of 200 mm, 500 mm, 750 mm and 1000 mm, respectively. As seen for plain concrete (in Chapter 5), the flexural strength increases as the beam dimensions decrease. Generally, the MOR is attained at lower deflection for larger specimens.

The response of PFRC for three beam sizes under impact loading is shown in Figures 17-20 for drop-heights of 200 mm, 500 mm, 750 mm and 1000 mm, respectively. As seen for plain concrete and SFRC, the flexural strength increases as the beam dimensions decrease. Further, as seen in the case of plain concrete and SFRC, the MOR is attained at lower deflection for larger specimens. As an exception, the medium size beams in both mixes failed at lower deflections and, especially so at higher drop-heights (Figures 7.16-7.18 and 7.20-7.22).

7.5.2   Comparing Steel Fiber and Polypropylene Fiber Reinforced Concrete

Both steel and polypropylene fibers used for investigating size-effects of FRC were 30 mm long. Where as both large beams and medium beams allowed for a random 3-D orientation of fibers (being 150 mm and 100 mm respectively in depth, their minimum
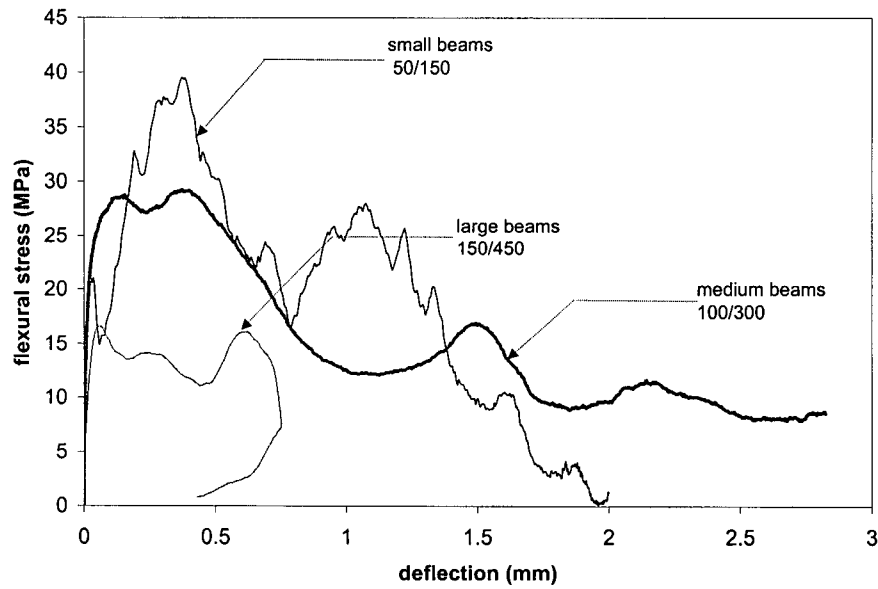
Figure 7.15   Flexural Response of Three Sizes of SFRC Beams under Impact Loading
(Drop-Height = 200 mm)
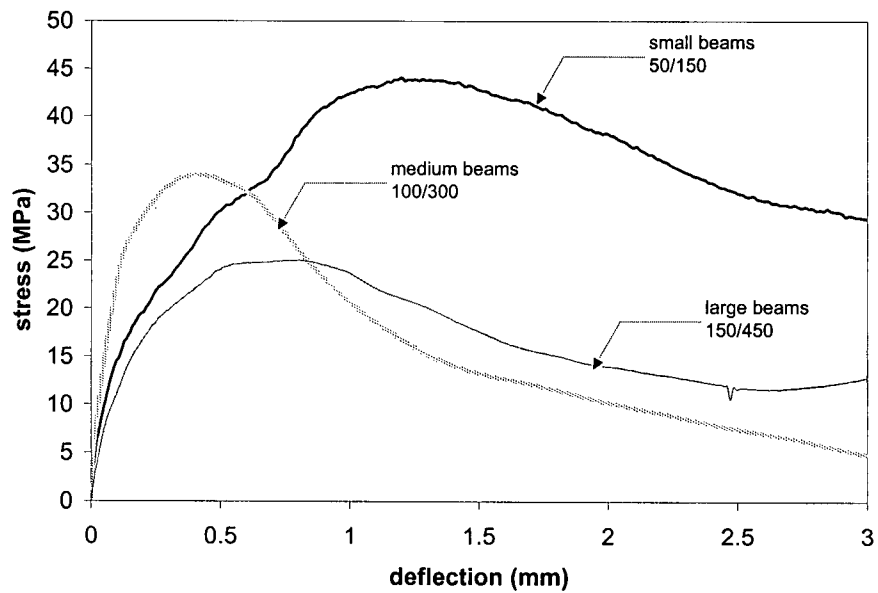
Figure 7.16   Flexural Response of Three Sizes of SFRC Beams under Impact Loading
(Drop-Height = 500 mm)

153
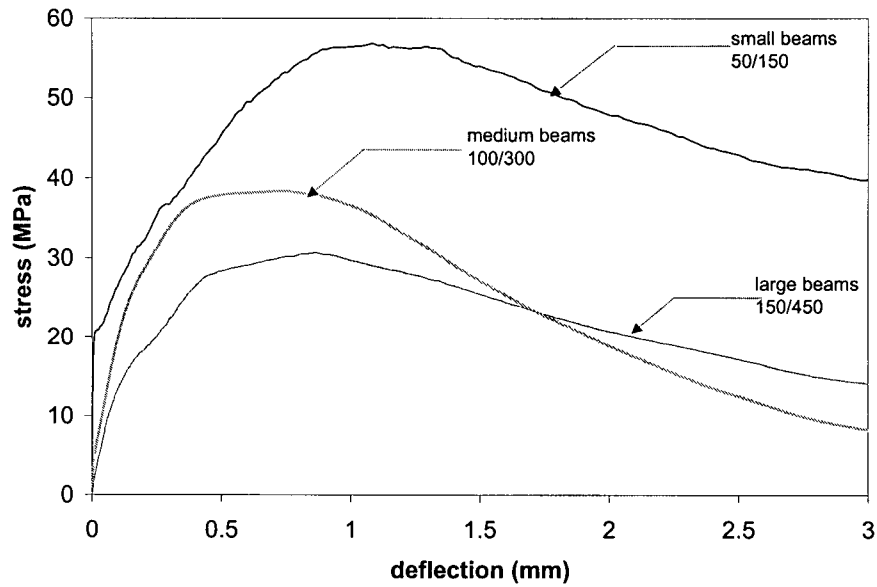
Figure 7.17   Flexural Response of Three Sizes of SFRC Beams under Impact Loading
(Drop-Height = 750 mm)
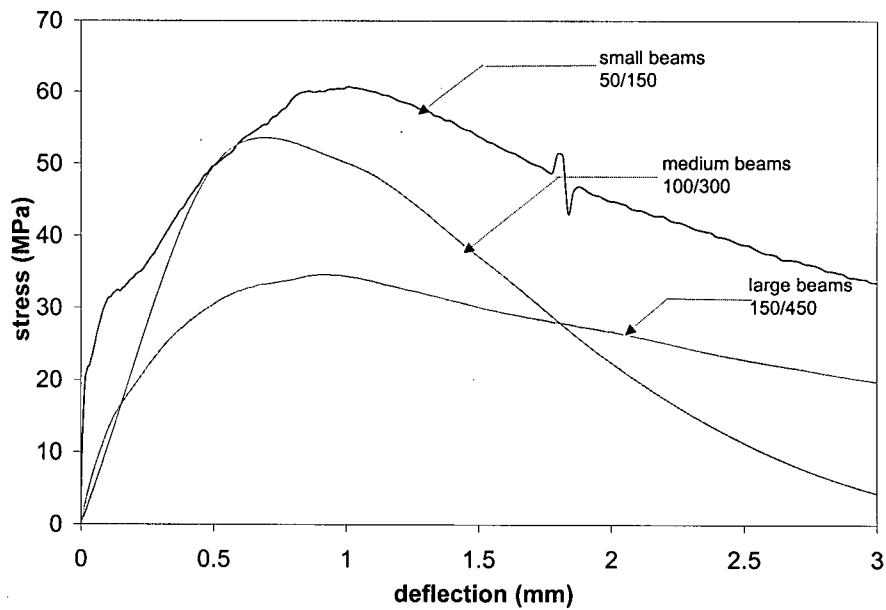
Figure 7.18   Flexural Response of Three Sizes of SFRC Beams under Impact Loading
(Drop-Height = 1000 mm)

154
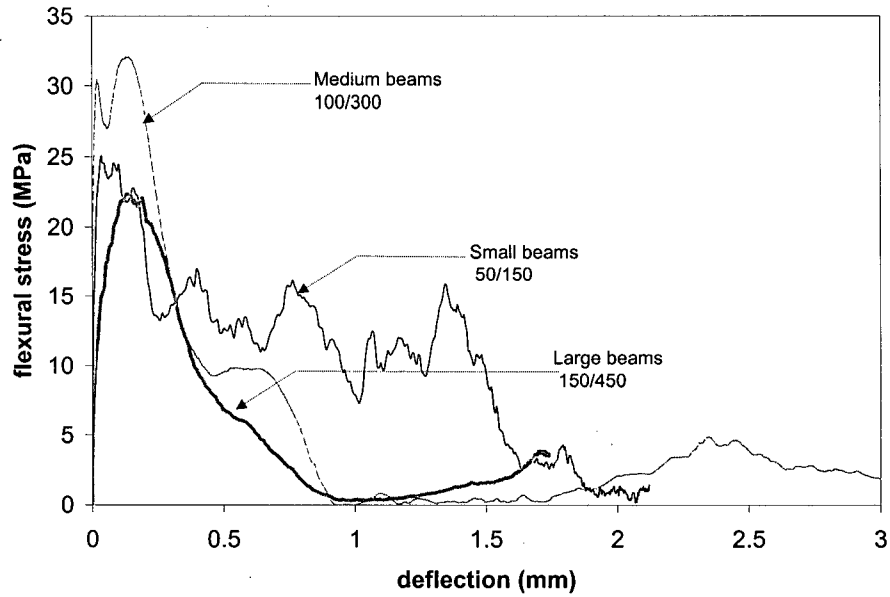
Figure 7.19   Flexural Response of Three Sizes of PFRC Beams under Impact Loading
(Drop-Height = 200 mm)
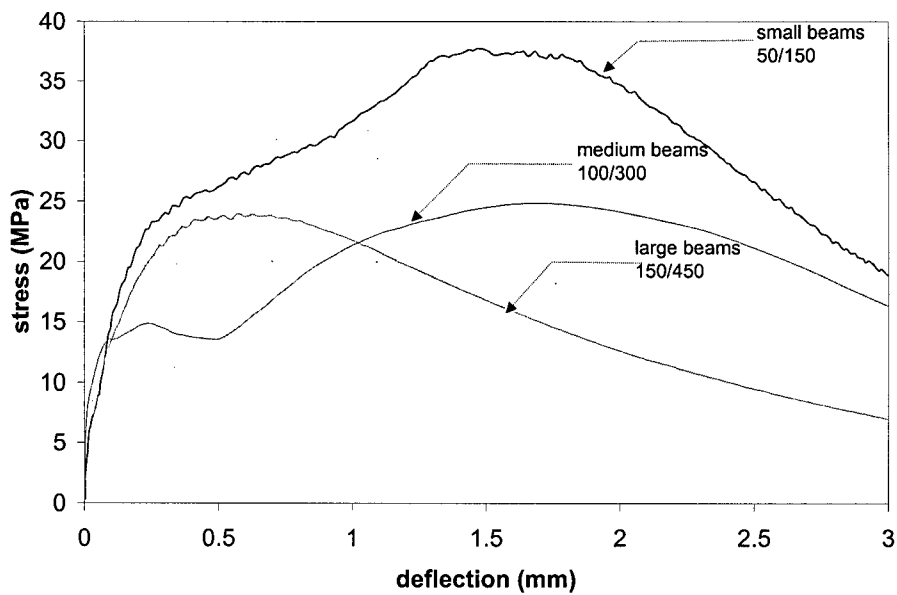
Figure 7.20   Flexural Response of Three Sizes of PFRC Beams under Impact Loading
(Drop-Height = 500 mm)

155
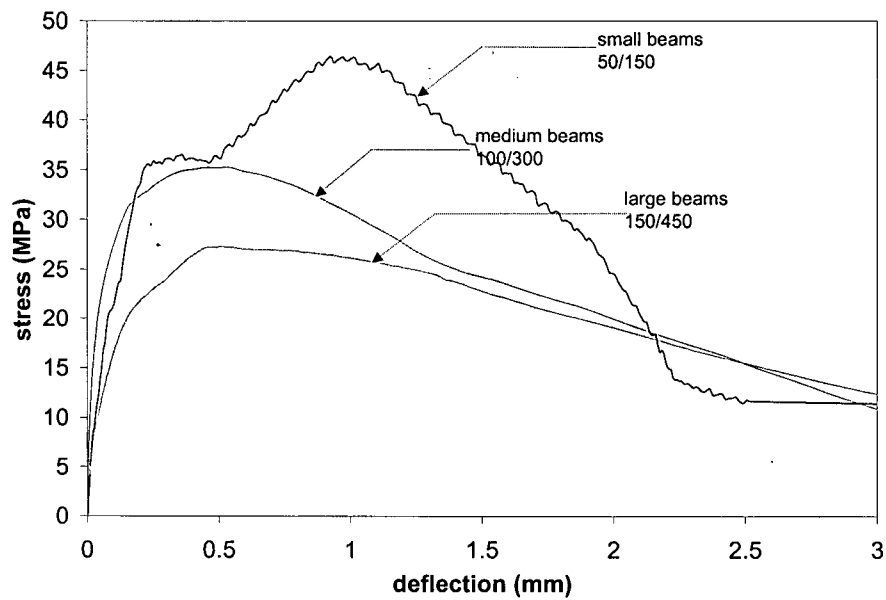
Figure 7.21 Flexural Response of Three Sizes of PFRC Beams under Impact Loading (Drop-Height = 750 mm)
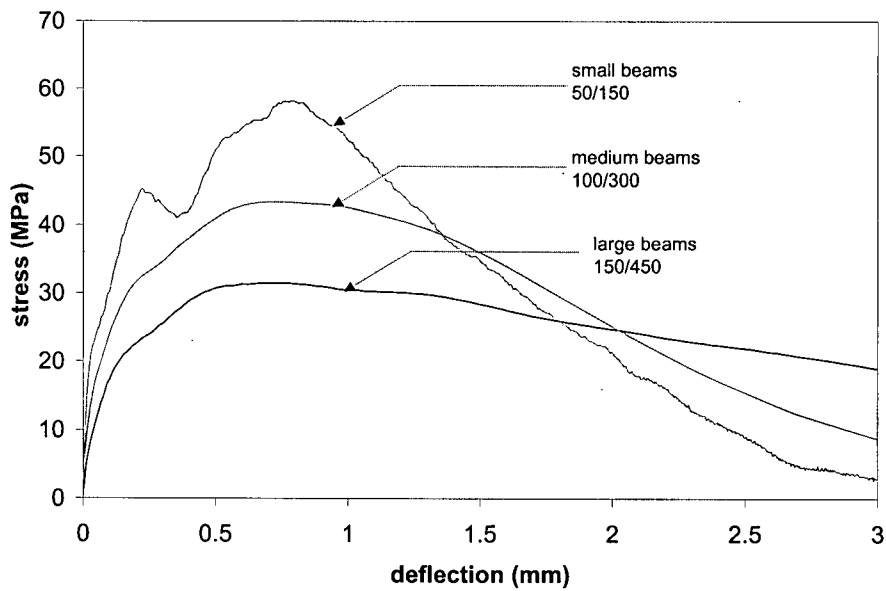
Figure 7.22 Flexural Response of Three Sizes of PFRC Beams under Impact Loading (Drop-Height = 1000 mm)

dimension is over three times the length of the fibers), the size of the small beams (minimum dimension = 50 mm) is less than twice the fiber length and hence it promotes a predominantly 1-D fiber orientation (i.e. most fibers tend to be aligned in the direction of tensile forces generated during flexure). Therefore, it is recognized that the interpretation of the size-effect in this test series is sure to be skewed by the preferential orientation of fibers within the small beams.

7.5.3 Effect of Variable Stress-Rates

It was seen in section 5.3.2.1 that beams of different size do not experience the same stress-rate even though the incident energy remains the same. As with the plain concrete beams, the flexural strength of the FRC beams were normalized for the rate-effect by using the stress-rate sensitivity plot of Figure 7.13. However, it is not clear whether the flexural toughness and toughness factors ought to be normalized as well, and if so, how.

For both steel and polypropylene fiber reinforced concrete, an increase in the specimen size resulted in a decrease in the JSCE flexural toughness factor under impact loading. This was true for all drop-heights investigated in this study as shown in Figure 7.23. It is contrary to the findings of Chen [124] whose results on SFRC under quasi-static loading do not yield a significant size effect on flexural toughness factor based on JSCE values for SFRC beams. One possible reason for this could be the increasingly linear elastic nature of the fracture process under impact compared to the non-linear, micro-fracturing response of FRC under quasi-static loading. Under quasi-static loading, Li et al. [123] have indicated that the size-effect diminishes with the introduction of the fibers since crack-bridging is vastly improved and the MOR is much less dependent upon matrix properties.

While the effect of short discreet fiber reinforcement on existing scaling laws is yet to be determined, Bažant and Planas [147] have shown that for conventionally reinforced concrete, the steel rebars have the effect of decreasing the brittleness number. That is to say, the size-effect law predicts a shift toward the plasticity limit, which means that the size-effect on the diagonal shear strength diminishes with increasing volume fraction of

shear reinforcement. One may infer from their observation that for fiber reinforced concrete as well, under quasi-static loading, the fibers result in reducing the size-effect. However, in the present study on FRC under impact loading, no such reduction in the size-effect on the MOR was witnessed. Notice in Figure 7.23 that the extent of size effect on the JSCE flexural toughness factor increases with an increase in the hammer drop-height for both types of fiber reinforcement. As in the case of plain concrete, here too, the self-weight of the beams was not considered as it is always static in nature.
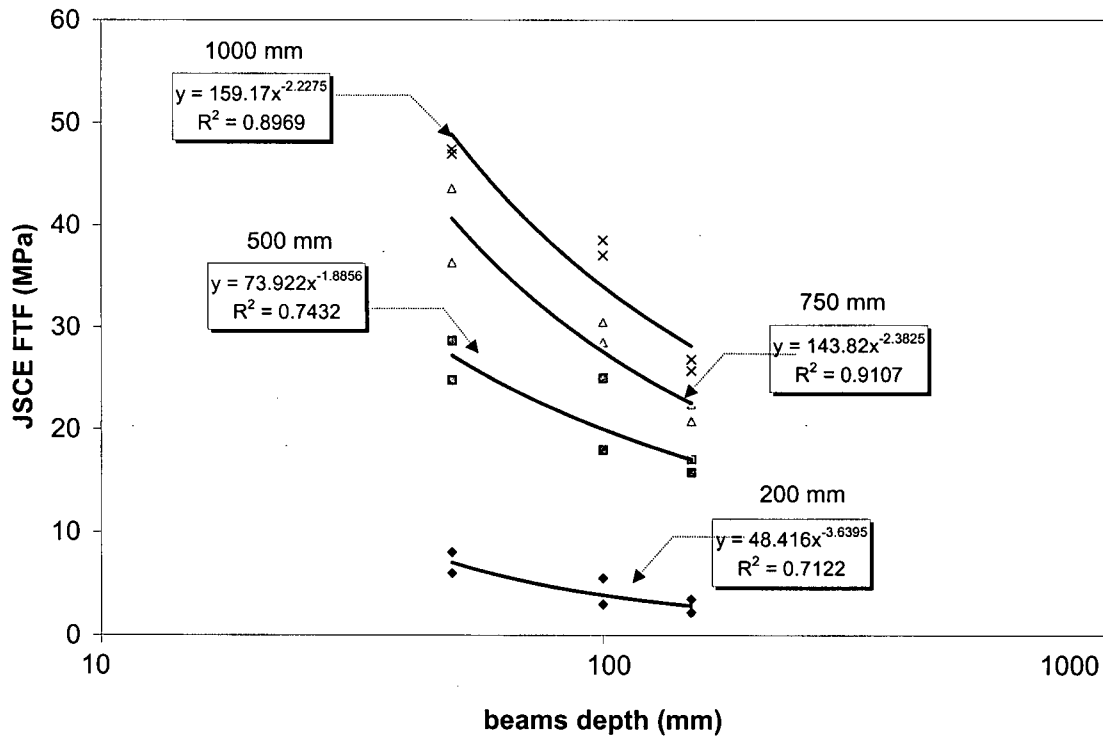
Figure 7.23   Size-Effect on the Flexural Toughness of FRC under Impact loading

It was highlighted in section 7.4.2.2 that under impact loading, the performance of polypropylene fibers improves, so that under high drop-heights, the flexural toughness factor of PFRC is in fact higher than that of SFRC. Figures 7.24a-c depict the effect of increasing drop-height on the JSCE FTF for small, medium and large beams, respectively. Across all sizes, the ability of the polypropylene fiber to catch up with the steel fiber is evident. It also appears that smaller sizes (here, the small and medium sized beams) favour this "switch" between the response of SFRC and PFRC under impact.

158
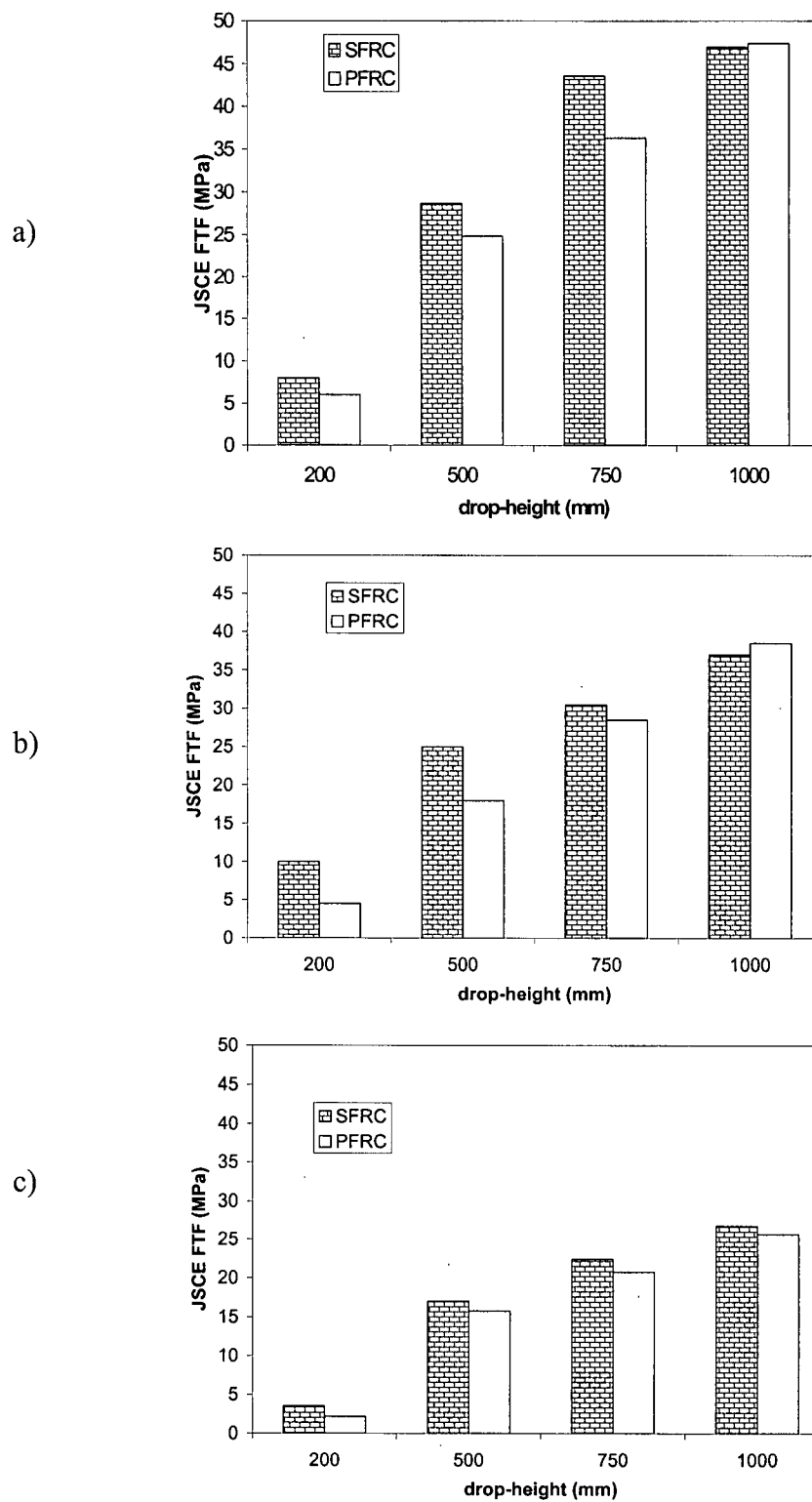
Figure 7.24   JSCE FTF Values for SFRC and PFRC Beams: a) Small Size; b) Medium Size; c) Large Size

Assuming this is also due to the preferred fiber alignment in smaller specimens, it emerges that polypropylene fiber reinforcement should be recommended for two dimensional structural applications subjected to impact.

7.6   Conclusions

The following conclusions may be drawn from the study presented in this chapter:

1. The flexural strength of fiber reinforced concrete regardless of fiber type and geometry is higher under impact loading than under quasi-static loading. The toughness or energy absorption capacity is also higher under impact. But, this improvement under impact is more pronounced in the case of the polymeric fiber reinforced concrete (regardless of fiber length or geometry) than with steel fiber reinforced concrete.

2. The flexural behaviour of FRC may be qualitatively correlated to the bond-slip response of single-fibers reported in Chapter 6, after giving due regard to the randomness of fiber orientation.

3. Fractured surfaces of the specimens reveal that fiber pull-out was a predominant mode of failure for all fibers under both quasi-static and impact rates of loading. This is in disagreement with the pull-out tests of Chapter 6, where the deformed polymeric fibers had fractured under some conditions of static loading. However, a higher degree of fiber fracture was witnessed with a decrease in specimen size. This suggests that the nature of fiber failure in a composite is intimately governed by fiber orientation and grouping effects— issues, which are not captured by single-fiber pull-out tests.

4. Crimped polypropylene fiber is less effective than steel fiber at quasi-static rates of loading. However, at higher stress rates, it performed better than the steel fiber. This "switch" in the behaviour of FRC is attributed to the greater strain rate sensitivity of polypropylene vis á vis steel.

5. Machine effect is reflected in the impact response of fiber reinforced concrete. For the same incident impact energy from two different machines, the flexural toughness of polypropylene fiber reinforced concrete surpassed that of steel fiber reinforced concrete on a machine with a lighter hammer mass.

6. The effect of specimen size is evident on the flexural strength of FRC similar to that seen for plain concrete in Chapter 5. While previous studies at quasi-static loading rates yield no significant size-effect on toughness factors, in this study, both types of FRC exhibit significant size-effect under impact loading. Further, under impact loading, increasing the drop-height amplifies the size-effect, which suggests that the size-effect on the mechanical properties of FRC increases at higher rates of loading.

Chapter 8

CRACK GROWTH RESISTANCE OF FIBER-REINFORCED CONCRETE UNDER IMPACT LOADING

8.1 Introduction

Load rate effects on the fracture of plain concrete have been investigated quite extensively in recent decades [148,149,22,89,94,95]. However, relatively limited studies address the effect of impact loading on the fundamental fracture properties of fiber reinforced concrete [21,92,93]. The study of dynamic fracture of concrete necessitates the design of suitable experimental apparatus together with appropriate analytical methods to capture the fundamental fracture mechanical parameters. The objectives of the work presented here were, on the one hand, to develop a test technique for crack growth studies of cement based composites under dynamic loading, and on the other hand, to assess the effect of fiber type and dosage upon the fracture properties of fiber reinforced concrete. The configuration and instrumentation of a drop-weight impact machine for studying dynamic crack growth is detailed in Chapter 4. This Chapter describes the dynamic analysis required to obtain the fracture parameters of the material and to assess the stress-rate sensitive nature, if any, of these parameters for FRC.

8.2 Analysis

Consider the Contoured Double Cantilevered Beam (CDCB) specimen shown in Figure 4.2. Suppose this CDCB specimen is subjected to a time-dependent impulsive loading. A rapidly growing crack has a non-negligible velocity associated with it, which means that the effective crack length is changing with the applied load. Since, for the case of impact loading, the applied load is varying with time, the effective crack length at a given instant of time depends upon both the instantaneous load and the rate of change of this load. The method adopted here involves transforming the time-dependent event to an equivalent time-independent event (by applying d'Alembert's principle) so that the problem reduces to one of statically applied loading.

162

8.2.1 Static Analysis

The crack growth resistance under quasi-static conditions has been derived in detail by Banthia and Genois [150]. This section follows their approach, which utilizes the compliance method.

8.2.1.1 Evaluating the Crack Growth Resistance (K_R)

The expression for the compliance of the CDCB specimen may be obtained by using the strength-of-materials approach. Consider a rectangular double cantilever beam (DCB). If one assumes that one arm of the DCB is a simple cantilever beam (Figure 8.1) with a constant section B x H and a length a, equal to the crack length existing in the specimen, the compliance 'C' of the specimen is given by:

$$C = \frac{2\Delta}{P} = \frac{CMOD}{P}$$

$$= \frac{24}{EB} \int_0^a \frac{x^2}{H^3} dx + \frac{6(1+v)}{EB} \int_0^a \frac{1}{H} dx \qquad \ldots(8.1)$$
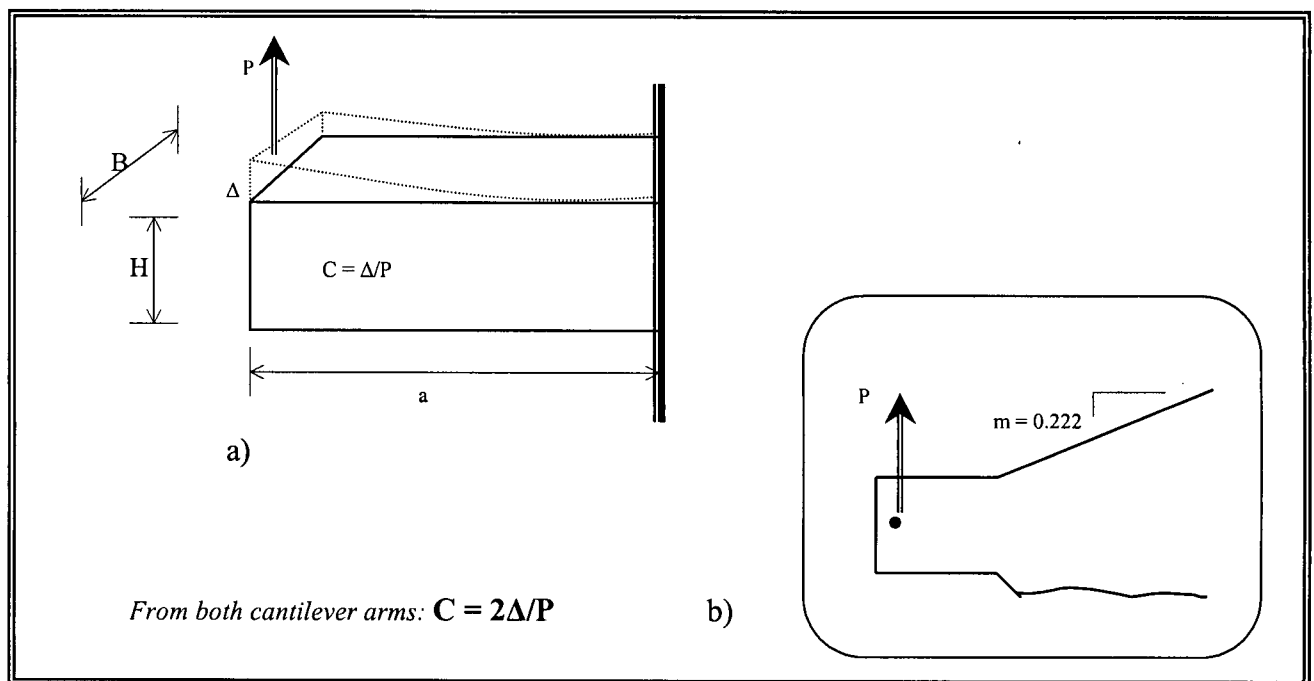
Figure 8.1   a) Determination of Compliance with a Rectangular DCB Specimen

b) One Arm of the CDCB Specimen

The first term on the right hand side of Equation (8.1) illustrates the contribution from the bending deformation while the second term accounts for the shear deformation. For a CDCB specimen, the constant height 'H' in Equation (8.1) corresponds to the mean height 'H_c' so that,

$$H_c = \frac{H_0 + H_a}{2} \quad ; \quad H_a = H_0 + ma$$

Therefore,

$$H_c = H_0 + \frac{ma}{2} \qquad \qquad \qquad ...(8.2)$$

The additional deflection due to the rotation of the assumed "built-in" end of the cantilever beam is accounted for by using a longer crack length in the calculation of the compliance term due to the bending deformation. Using a rectangular DCB, Mostovoy *et al.* [151] established that the rotational effect may be accounted for by assuming a crack length equal to ($a + 0.6H$).

Assuming $v = 0.2$, the expression for the compliance from equation (8.1) as a function of crack length may now be written as

$$C_{th} = \frac{24}{EB} \left\{ \frac{(a + 0.6H_c)^3}{3H_c^{\,3}} + \frac{0.3a}{H_c} \right\} \qquad \qquad ...(8.3)$$
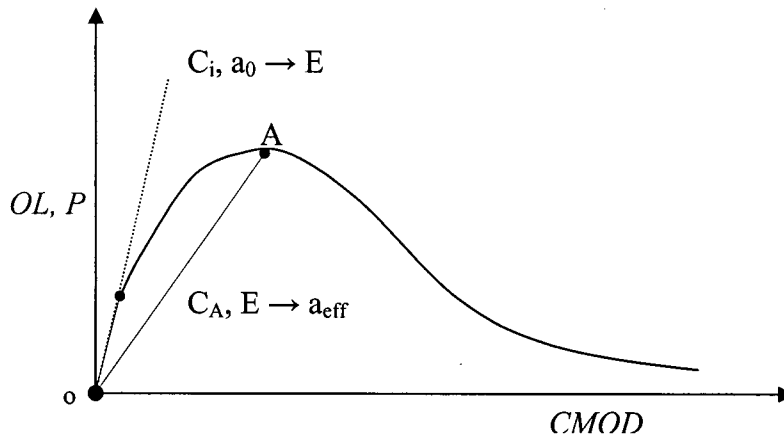
Figure 8.2   Typical Opening Load vs. CMOD Curve Obtained from a Quasi-Static CDCB Test

164

8.2.1.2 Evaluating the Effective Crack Length

The elastic modulus of the material 'E' is calculated using the initial compliance 'C_i' obtained from the experimental opening load 'P' vs. CMOD plot (as in Figure 8.2) and the initial crack length 'a_0'. The initial compliance may now be written as

$$C_i = \frac{CMOD}{P} \quad \Big\} \text{ at the first non-linearity point (BOP)} \qquad \ldots(8.4)$$

Using equation (8.4),

$$E = \frac{24}{C_i B}\left\{ \frac{(a+0.6H_c)^3}{3H_c^{\,3}} + \frac{0.3a}{H_c} \right\} \qquad \ldots(8.5)$$

Beyond the Bending Over Point (BOP), sub-critical crack growth occurs, which manifests itself as an increase in compliance. The elastically equivalent crack length corresponding to this increase is usually referred to as the effective crack length 'a_{eff}'.

The compliance of the specimen at any point A in the non-linear region of the plot is obtained after ignoring permanent deformations. This experimentally evaluated compliance is given by:

$$C_{exp} = \frac{CMOD_A}{OL_A} \qquad \ldots(8.6)$$

The effective crack length is now obtained by equating the theoretical and experimental values of compliance,

$$C_{th} = C_{exp} \qquad \ldots(8.7)$$

8.2.1.3 Stress Intensity Factor at the Crack Tip

The Mode I stress intensity factor (K_I) is calculated using the LEFM equation for a CDCB specimen, which is based on the derivation by Srawley and Gross [152]. This equation is

$$K_I^2 = \frac{P^2}{B^2 H_a^3}\eta^2\left(a^2 + 1.4aH_a + 0.5H_a^2\right) \qquad \ldots(8.8)$$

where, $\eta = 3.1$ for a slope of $m = 0.222$ and H_a is the beam height at a distance 'a' from the point of loading.

It should be noted that in Equation (8.8), B^2, one of the parameters represented by 'B^2' holds for the beam height 'B', while the other represents the crack width 'b'. In the present set-up, the specimen contains a side-groove along the mid-plane, which requires that one of the dimensions indicated by 'B' in equation (8.8) be replaced by 'b', the crack width. Also, to account for the crack growth, the crack length must be updated to the effective crack length, 'a_{eff}'. So that, the stress intensity factor may now be calculated in its final form as:

$$K_I^2 = \frac{9.6P^2}{BbH_{a_{eff}}^3}\left(a_{eff}^2 + 1.4a_{eff}H_{a_{eff}} + 0.5H_{a_{eff}}^2\right) \qquad \ldots(8.9)$$

8.2.1 Dynamic Analysis

Inertial Effects under Impact Loading

As discussed in significant detail before, the dynamic nature of loading under impact induces inertial effects, which are included in the load recorded by the load-cell. As a rule, if the time required to increase the magnitude of the applied load from zero to the maximum value is less than half of the natural period of the structure, then the formation of stress waves due to the inertia effect should be considered as significant. As shown in section 8.3, the natural time period of the CDCB specimen was 150 ms, while the peak loads even for the lowest drop-height (500 mm) were attained in the range of 0.5-1 ms. Since our interest lies only in the true stressing load experienced by the specimen, the

inertial force must be eliminated from the recorded load. Further, during the fracture of a CDCB specimen, the crack length is itself a function of the instantaneous compliance, which in its turn depends upon the true stressing load. Therefore, for the sake of performing the inertial correction, we may divide the event into two phases viz., 1) prior to cracking and 2) after cracking.

8.2.2.1 Phase 1: Uncracked Cantilever

Consider the cantilever beam in Figure 8.3. The beam flexes under the time-dependent load '$P(t)$' (as in Figure 8.3b) such that the following single-degree-of-motion equation may be formed:

$$M \frac{d^2 u(x,t)}{dt^2} + P_b(t) = P_t(t) \qquad \qquad ...(8.10)$$

where,

$P_i(t)$ = Inertial correction

$P_b(t)$ = True stressing load

M = mass of the flexing portion of the cantilever beam

$u(x,t)$ = transverse deflection along the length of the cantilever beam

In other words, equation (8.10) represents the d'Alembert equation of dynamic equilibrium:

$$P_b(t) = P_t(t) - P_i(t)$$

Assuming the deflection '$u(x,t)$' in equation (8.10) to be composed of a generalized coordinate '$z(t)$' and the shape function '$\psi(x)$', we may express the generalized inertial force as:

$$P_i(t) = \overset{*}{M} \frac{d^2 z(t)}{dt^2} \qquad \qquad ...(8.11)$$
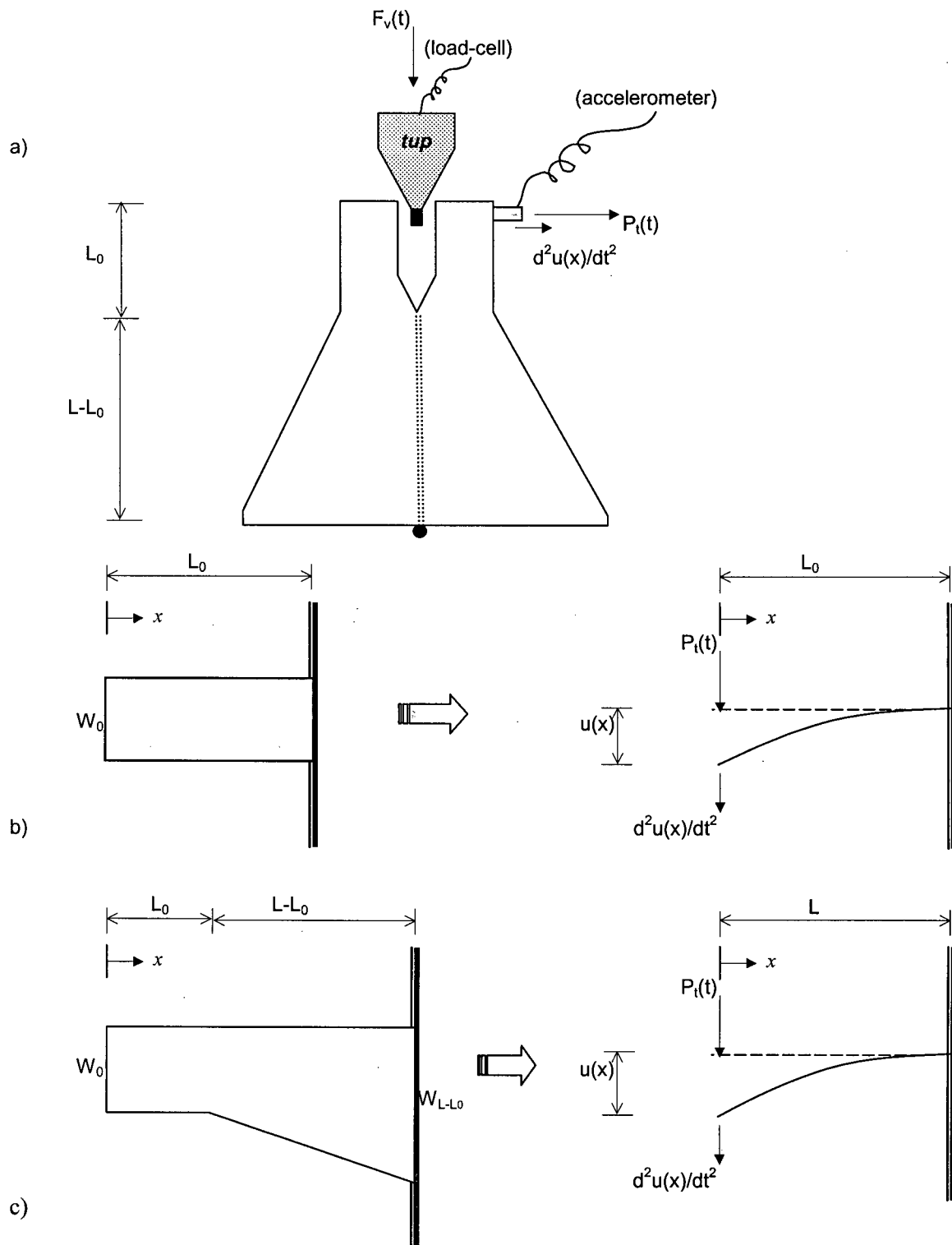
Figure 8.3   a) Wedge loading on a CDCB specimen under impact; b) Uncracked
            Cantilever; c) Cracked Cantilever

where, $\overset{*}{M}$ is the generalized mass [153] given by

$$\overset{*}{M} = \int_0^L \mu(x)\{\psi(x)\}^2 dx \qquad \qquad ...(8.12)$$

where, $\mu(x)$ = mass distribution per unit length of the cantilever beam.

The generalized coordinate $z(t)$, which is the displacement history at the load-point may be obtained by integrating the accelerometer data with respect to time. Thus, if the acceleration history at the free end of the cantilever is $\ddot{z}(t)$, the velocity $\dot{z}(t)$ and the displacement histories are evaluated as:

$$\dot{z}(t) = \int \ddot{z}(t)dt$$

$$z(t) = \int \dot{z}(t)dt$$

Note that the displacement history $z(t)$ represents the crack mouth opening displacement response (CMOD).

Considerable simplification is possible in the above treatment of the inertial force if a simple mathematical function be chosen to describe the shape function of the beam. Existing literature [30,154] indicates that indeed a simple function such as a linear profile may be used to describe the shape function of plain and fiber reinforced concrete beams. Referring to Figure 8.3b, it is seen that for a unit displacement of the free end of the cantilever beam, a linear shape function may be formulated as:

$$\psi(x) = \left(1 - \frac{x}{L}\right) \qquad \qquad ...(8.13)$$

Further, for the cantilever in Figure 8.3b, $\mu(x) = \rho W_0 T$, (where 'T' is the thickness of the beam). Equation (8.12) may now be simplified to yield the generalized mass as:

$$\overset{\bullet}{M} = \rho W_0 T \left[\frac{L}{3} \right] \qquad \qquad \ldots(8.14)$$

and thus the inertial force *before* the onset of cracking is given by

$$P_{iu}(t) = \rho W_0 T \left[\frac{L}{3} \right] \ddot{z}(t) \qquad \qquad \ldots(8.15)$$

8.2.2.2 Phase 2: Cracked Cantilever

Once the crack initiates, the shape function remains as described in equation (8.13), but the mass distribution per unit length of the beam must be modified to include the contoured profile of the cantilever beam and the updated effective crack length. Accordingly, from Figure 8.3c,

$$\mu(x) = \rho \left[W_0 + (W_L - W_0) \frac{x}{L} \right] T \qquad \qquad \ldots(8.16)$$

The generalized mass may be obtained by substituting the value for '$\psi(x)$' and '$\mu(x)$' from equations (8.13) and (8.16) respectively, into equation (8.12) to yield:

$$\overset{\bullet}{M} = \rho T \left[\frac{W_0}{4} + \frac{W_L}{12} \right] L \qquad \qquad \ldots(8.17)$$

Hence, the inertial force for the post-cracking phase of the CDCB specimen is given by:

$$P_{ic}(t) = \rho T \left[\frac{W_0}{4} + \frac{W_L}{12} \right] L \ddot{z}(t) \qquad \qquad \ldots(8.18)$$

The true stressing load $P(t)$ at any instant 't', as found from equation (8.15) or (8.18) is substituted for the opening load OL_A in equation (8.6) in order to obtain the effective crack length and the stress intensity factor under impact loading.

Appendix 1 describes the steps involved in the evaluation of the instantaneous '$a_{eff}(t)$' and '$K_R(t)$' values by considering the inertial correction under impact loading.
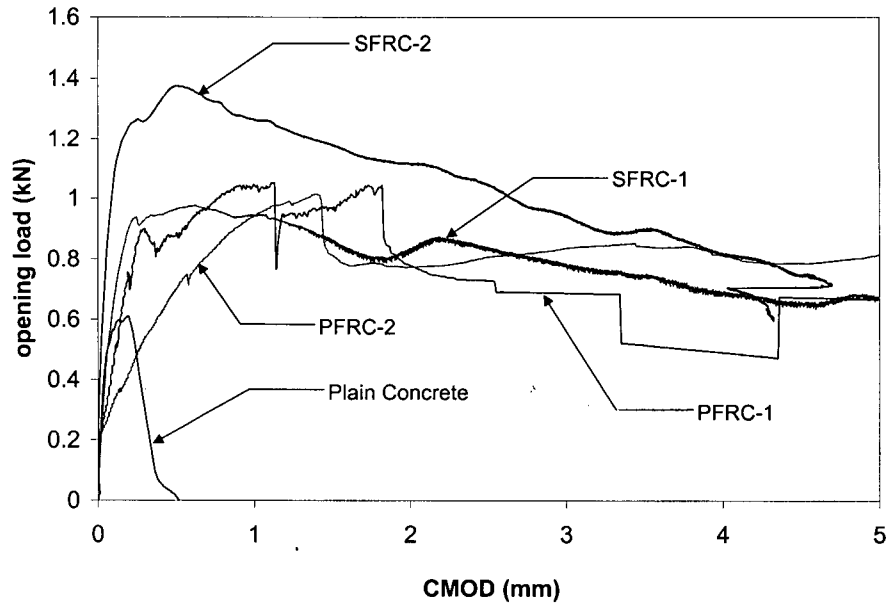
Figure 8.4a   Opening Load vs. CMOD Plot under Quasi-Static Loading
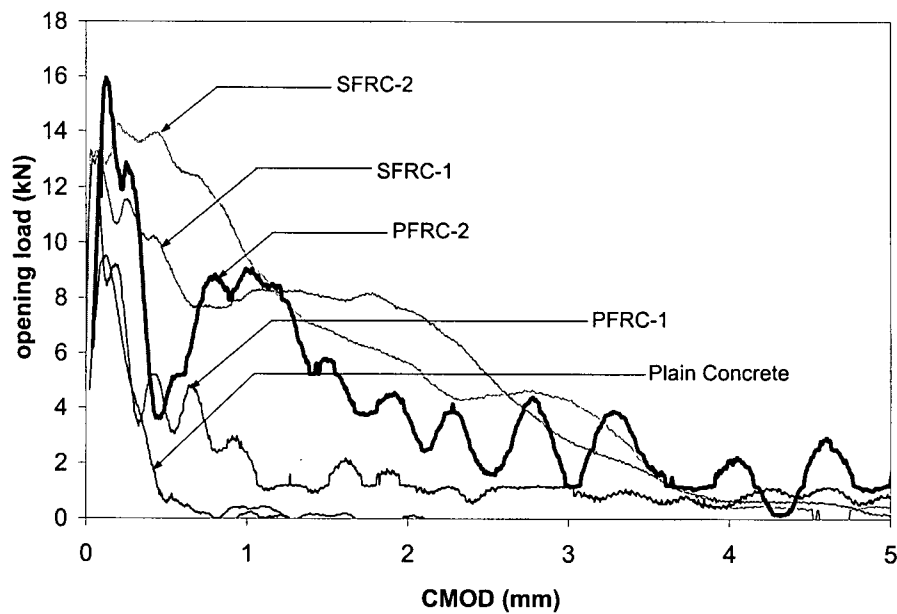
Figure 8.4b   Opening Load vs. CMOD Plot under Impact Loading (500 mm Drop)

8.3 K_R-Curves

Figure 8.4a shows the experimental opening load vs. CMOD plots (corrected for inertial effect) for plain and fiber reinforced mixes under quasi-static loading and those under
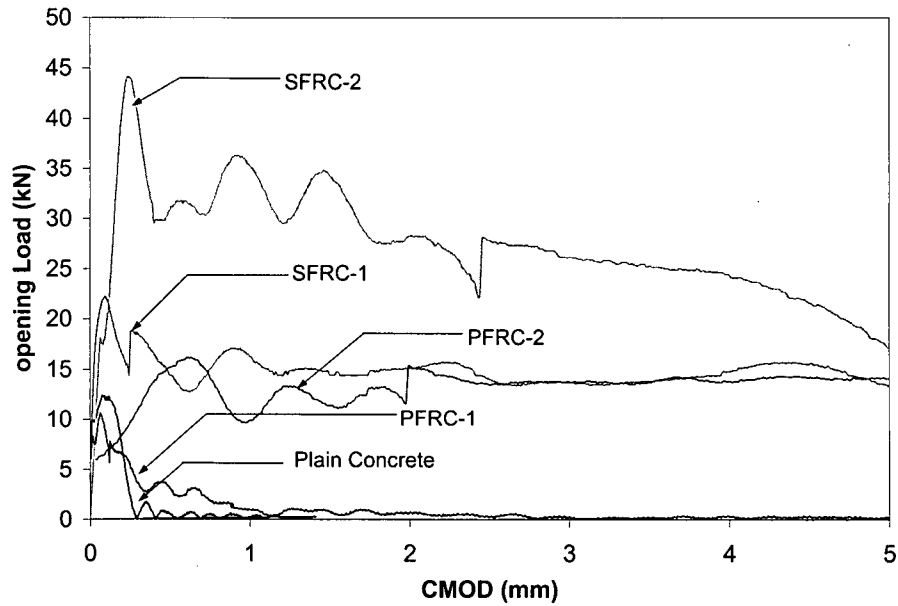
Figure 8.4c   Opening Load vs. CMOD Plot under Impact Loading (750 mm Drop)
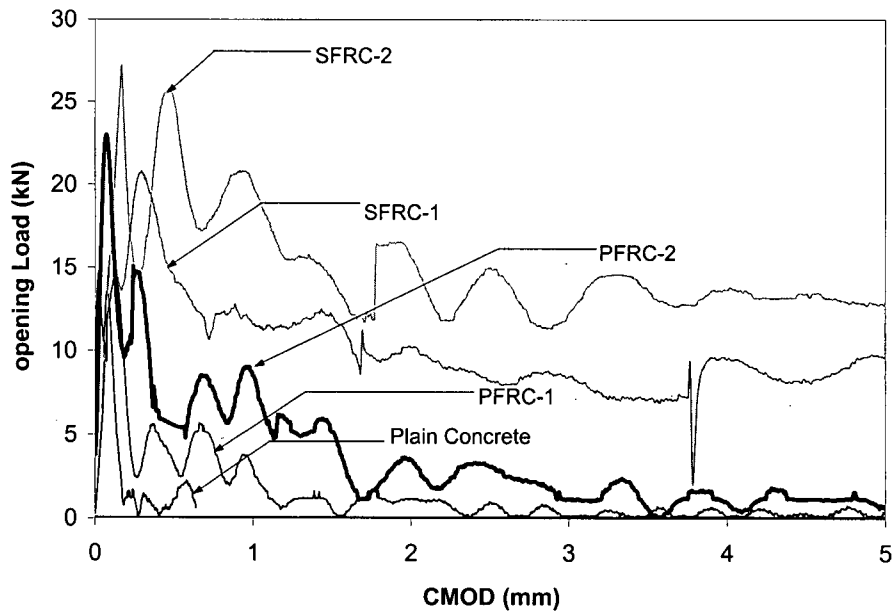
Figure 8.4d   Opening Load vs. CMOD Plot under Impact Loading (1000 mm Drop)

impact loading are shown in Figures 8.4b, c and d, respectively, for drop-heights of 500 mm, 750 mm and 1000 mm.

Notice that the peak loads in these tests increases both with an increase in the fiber volume fraction and with an increase in the rate of loading. The raw load histories as recorded by the tup (and resolved in the direction of flexure of the CDCB arms) are shown in Figures 8.5a-c for drop heights of 500 mm-1000 mm.
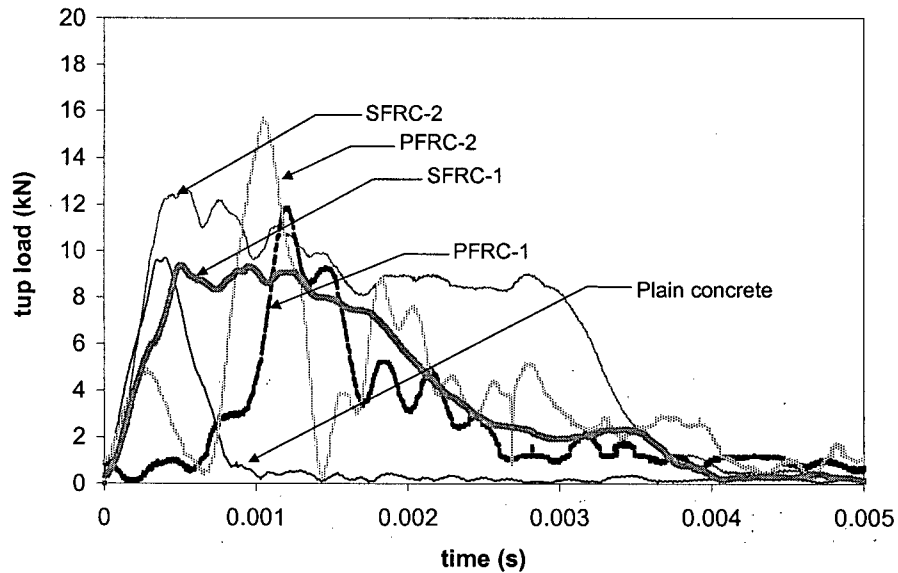
Figure 8.5a   Tup load Time-Histories for Various Mixes under Impact (500 mm Drop)
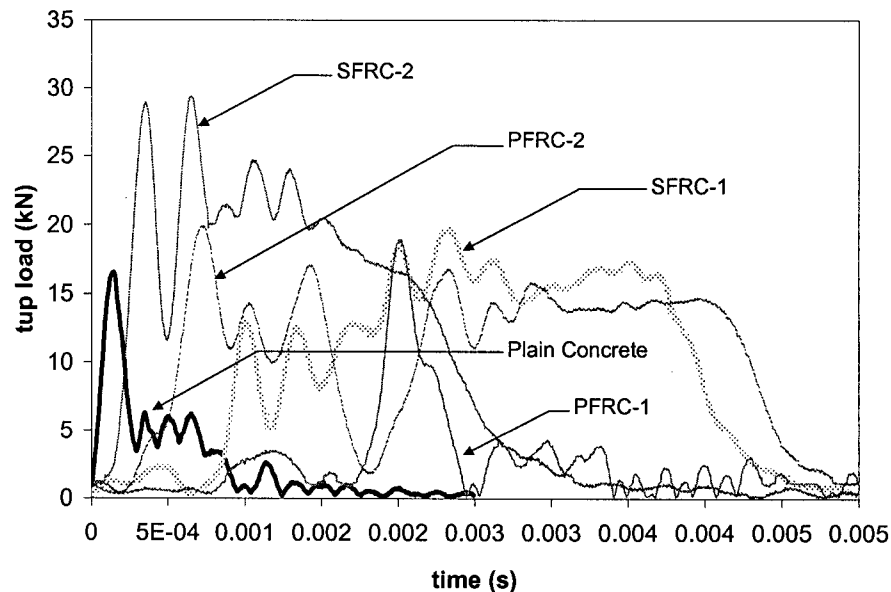
Figure 8.5b   Tup Load Time-Histories for Various Mixes under Impact (750 mm Drop)

173
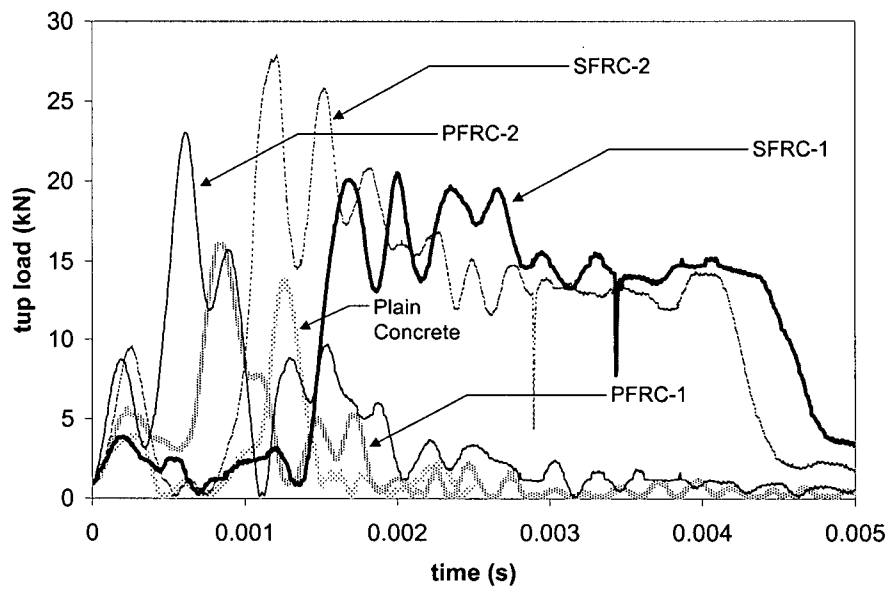
Figure 8.5c   Tup Load Time-Histories for Various Mixes under Impact (1000 mm Drop)

Notice that the time to first peak is less than 0.5 ms in the case of plain concrete and varies between 0.5 and 1 ms for FRC specimens.
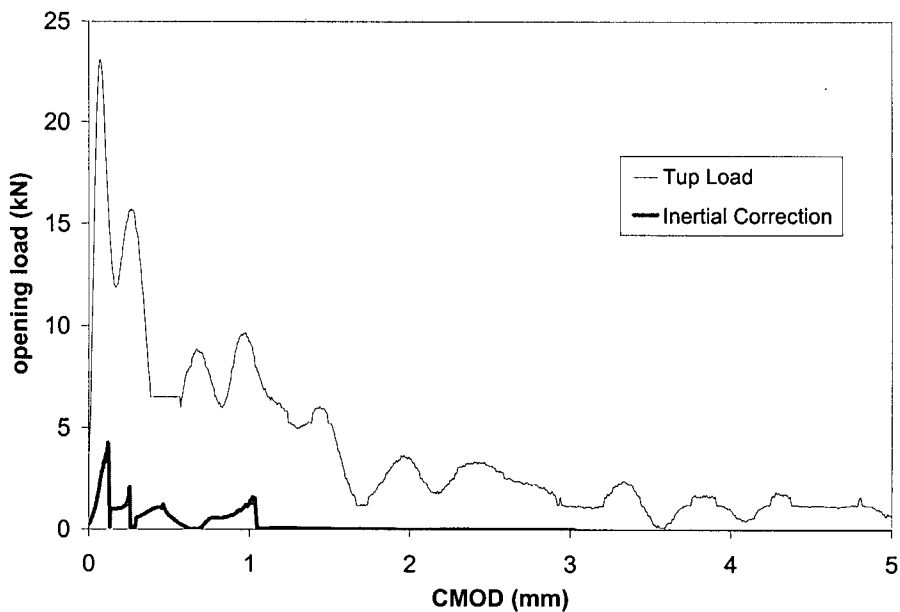
Figure 8.6   Inertial correction in the drop-weight impact loading of PFRC-2 CDCB

Since this value is less than the natural time-period 'τ_n' for the CDCB specimens (~150 ms, calculated as $\tau_n = 2\pi \sqrt{\dfrac{m}{k}}$, where 'm' & 'k' are the mass and stiffness, respectively of the CDCD), the inertial correction was applied to the curves in Figure 8.4 based on the analysis scheme presented in section 8.2.2. A sample case in shown in Figure 8.6. Note that the inertial component is about 25 % of the tup load, which emphasizes once again the importance of the inertial correction. It was noted that while the inertial correction was appreciable in the case of plain concrete and PFRC mixes, it was negligible in the case of SFRC mixes. Following this, the opening load-CMOD plots were analyzed to obtain the crack growth resistance (K_R) curves and the same are shown in Figures 8.7a-d for the four load cases.
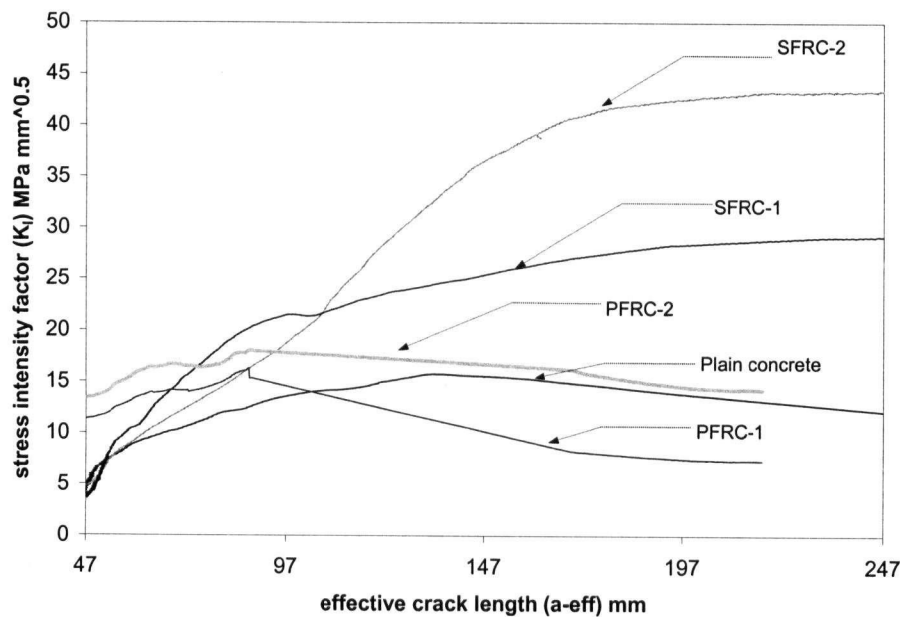
Figure 8.7a   Crack Growth Resistance for Various Mixes under Quasi-Static Loading

8.3.1 Effect of Fiber Type and Dosage

K_R curves for the quasi-static case are shown in Figure 8.7a while those for impact loading are shown in Figures 8.7b-d. Consider the quasi-static case shown in Figure 8.7a. Notice that for plain concrete, the K_R-curve descends rather rapidly, where as for the two PFRC mixes, this descent is delayed to a larger value of effective crack length (a_{eff}), and

for the SFRC mixes, this descent starts still later i.e. at a value of a_{eff} larger than the actual specimen length (and hence outside the graph shown). An explanation of this behaviour is as follows:
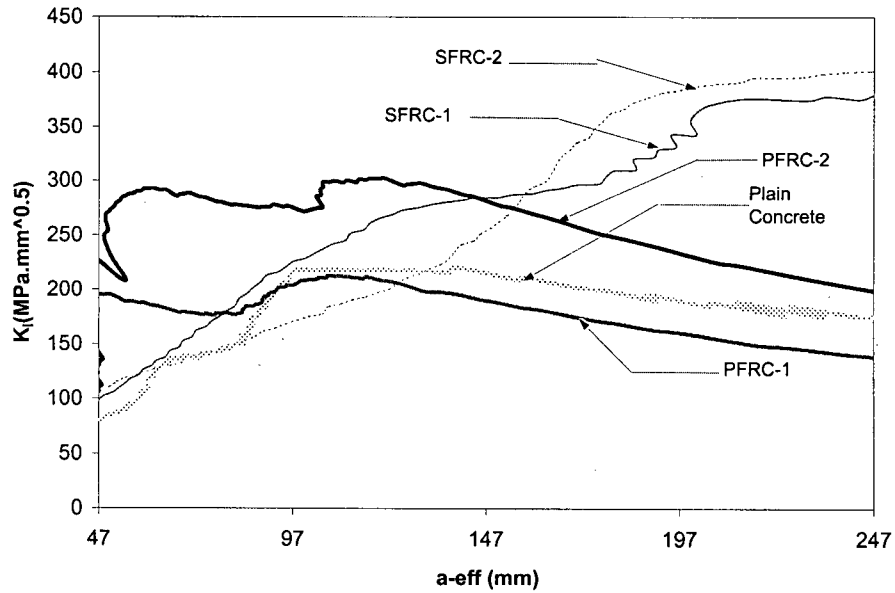
Figure 8.7b   Crack Growth Resistance of the Mixes under Impact Loading (500 mm Drop)
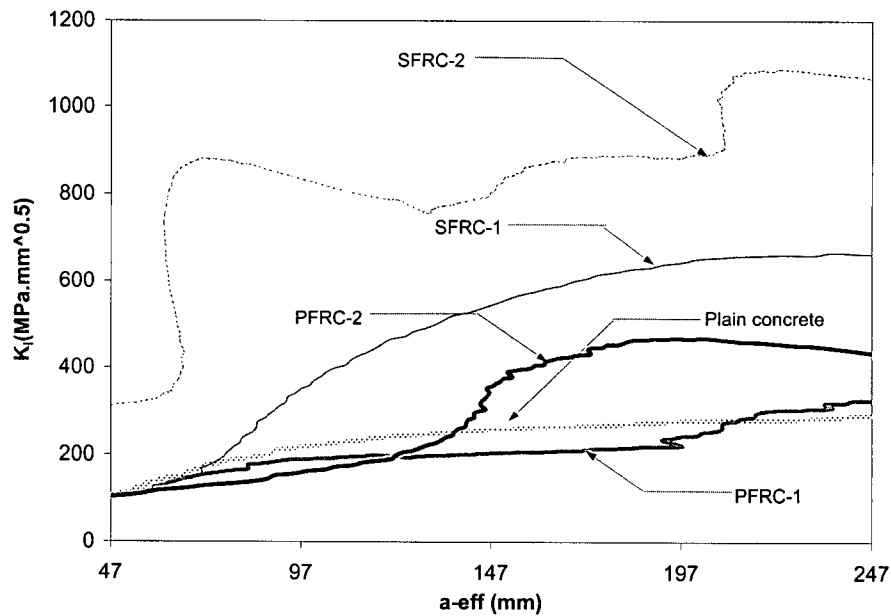
Figure 8.7c   Crack Growth Resistance of the Mixes under Impact Loading (750 mm Drop)
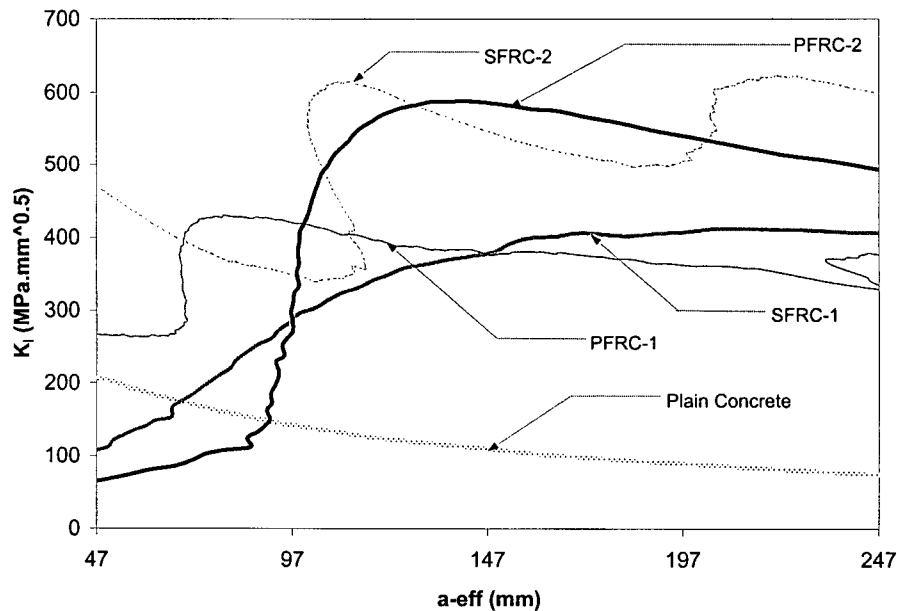
Figure 8.7d   Crack Growth Resistance of the Mixes under Impact (1000 mm Drop)

The crack profile and bridging is shown schematically for the cases of plain concrete, PFRC and SFRC in Figures 8.8a, b and c. For the purpose of distinguishing between these three mixes, only the contribution from fibers to the process of crack-bridging is considered, although clearly, an element of bridging arises through aggregate interlocking as well. The outcome of the analysis presented in section 8.2 is an effective crack length, which corresponds to the load-CMOD response. However, the effective crack tip is by no means the actual crack tip for those materials which are not Griffith (or perfectly brittle) materials.

In Figure 8.8a, plain concrete is idealized as a perfectly brittle material and this helps us concentrate only on the effect of fibers. A crack of CMOD 'w' bears an angle 'θ' with the initial plane of the crack surface (just prior to cracking) as shown.
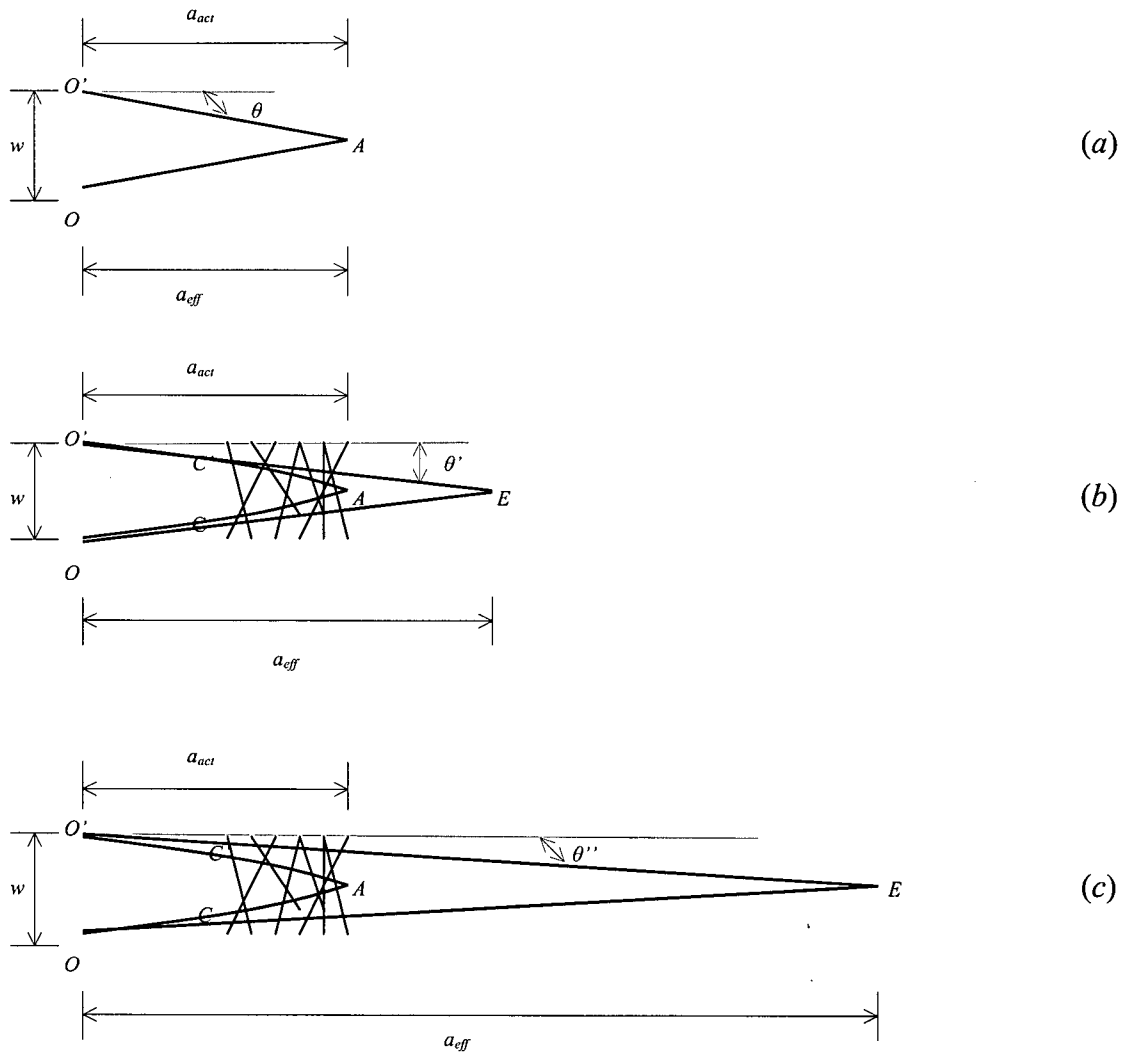
Figure 8.8   Crack profiles under quasi-static loading for a) Plain concrete;
               b) Polymeric FRC and c) Steel FRC

An analysis on the basis of section 8.2 leads to $a_{eff} = a_{act}$, where a_{act} is the length of the actual crack. On introducing polypropylene fibers, some degree of crack bridging develops within the system so that for PFRC, the crack profile is different from that of plain concrete and is shown in Figure 8.8b. Consider that the progress of the actual crack is the same as before (i.e. as in plain concrete; Figure 8.8a). Due to the presence of fibers, the length of the material along OA (and O'A) is no longer traction-free, which means

178

that there exists a crack-closing pressure along some distance CA (and C'A). This pressure causes the crack surface to curve (concave inward) as shown by arcs OCA (and O'C'A) in Figure 8.8b. When analyzing such a crack, the effective length OE, is an outcome of the intersecting tangents OE and O'E to the arcs OCA and O'C'A respectively, at the crack mouth. 'E' is therefore, the tip of the effective Griffith crack. This means that the angle made by the crack face with its original uncracked profile reduces from θ to θ'. Thus, the material can now sustain an additional amount of energy which will account for the difference in the profile corresponding to $\Delta\theta = \theta - \theta$'.

Table 8.1   Dynamic Fracture Properties (3 Specimens)

Mix Description	Peak Load (kN)				Fracture Toughness (MPa√m)			
	QS	0.5 m	0.75 m	1.0 m	QS	0.5 m	0.75 m	1.0 m
Plain Concrete	0.61 (0.15)	9.48 (2.27)	12.45 (2.84)	13.71 (3.56)	0.50 (0.13)	7.06 (1.85)	18.67 (4.58)	7.02 (1.85)
SFRC 1	0.98 (0.13)	13 (1.95)	22.23 (3.33)	20.08 (3.01)	0.95 (0.17)	12.78 (2.01)	20.98 (3.15)	13.48 (2.02)
SFRC 2	1.47 (0.29)	14.24 (2.9)	36.35 (7.30)	27 (6.02)	1.37 (0.28)	13.41 (2.58)	35.28 (7.03)	19.68 (4.01)
PFRC 1	0.78 (0.12)	11.78 (1.83)	10.62 (1.63)	14.63 (2.19)	0.52 (.081)	6.70 (1.10)	10.31 (1.56)	13.03 (6.51)
PFRC 2	1.01 (0.22)	15.82 (4.76)	16.2 (4.78)	22.98 (6.98)	0.57 (0.17)	9.53 (2.86)	14.81 (4.44)	18.60 (5.62)

If the fibers are stiff and have better bonding with the matrix (as in the case of steel fibers), the crack-closing pressure is higher and the curvature of the crack surface increases further. This results in a further reduction of the angle between the crack surface with its original state at the crack mouth to θ''. Thus, the energy demand is even higher for SFRC than PFRC in the quasi-static case. Increasing the fiber dosage increases the concavity by enhancing the fiber bridging capacity in the material. This pushes the

energy demand even higher as reflected by a general increase in fracture toughness (K_{IC}) values for both types of FRC across all types of loading (Table 8.1).

Consider the bond-slip response reported in section 6.2.1. For the case for fibers inclined at 45° with the load-line (Figure 6.4), and using the model proposed by Armelin and Banthia [80], we may arrive at an estimate for actual crack length in the case of each type of FRC. In their model, the load supported by fibers Q, is shown to be proportional to the bond-stiffness of the fibers E_P as obtained from a pull-out test (Figure 3.7):

$$Q \propto E_P \qquad \text{...(8.19)}$$

$$Q \propto V_f \qquad \text{...(8.20)}$$

so that, $\qquad Q \propto E_P V_f \qquad \text{...(8.21)}$

Once the crack initiates, an increase in the applied load may be withstood only through a corresponding increase in the number of fibers being mobilized. In its quest for mobilizing more fibers, the crack proceeds yielding the actual crack length a_{act} in Figure 8.8. That is, the actual crack length is proportional to the number of fibers required. Since volume fraction of fibers determines their number at a cross-section, we have:

$$a_{act} \propto V_f \qquad \text{...(8.22)}$$

i.e. $\qquad Q \propto a_{act} \qquad \text{...(8.23)}$

From Equations (8.21) and (8.23), we may write:

$$Q \propto E_P a_{act} \qquad \text{...(8.24)}$$

or, $\qquad a_{act} \propto Q/E_P \qquad \text{...(8.25)}$

which means that the actual crack length a_{act} is directly proportional to the applied load Q and inversely proportional to the bond stiffness as obtained from the single fiber pull-out test. Further, for the same matrix strength, the load to be carried by the fibers immediately after first-crack is the same, regardless of fiber type. For Fibers F2 and F4, if

the bond stiffness is E_{Pp} and E_{Ps} respectively, one obtains from Figure 6.4, E_{Ps} is nearly equal to 2.5 E_{Pp}. That is, for identical volume fraction, the actual crack length in the case of PFRC is over twice that for SFRC. In the present work, cracks in all the impacted PFRC specimens reached the length of the CDCB while only those for the SFRC specimens impacted from 1000 mm reached their full length.

8.3.2 Effect of Drop-Height

The effect of increasing drop-height on the K_R-curve for plain concrete is shown in Figure 8.9a. Note that while the K_R-curve initially rises with crack extension for the three lower rates of loading, a decaying K_R-curve is obtained for the drop-height of 1000 mm. This implies that the crack became unstable immediately upon impact indicating an early onset of brittle behaviour. For SFRC mixes, a similar trend was observed: an early onset of brittleness occurred in the case of the drop-height of 1000 mm compared to rising K_R-curves under drop-height of 500 mm and 750 mm (Figure 8.9b and c). On the other hand, for PFRC mixes, as seen in Figure 8.9d and e, we obtain a rising K_R-curve under all rates of loading.
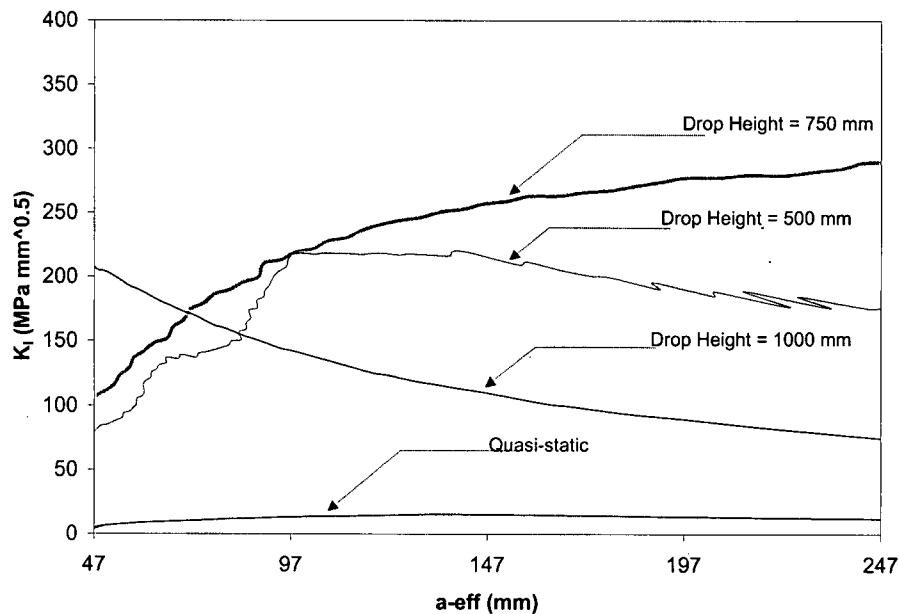
Figure 8.9a   Effect of drop-height on the crack growth resistance of plain concrete

181
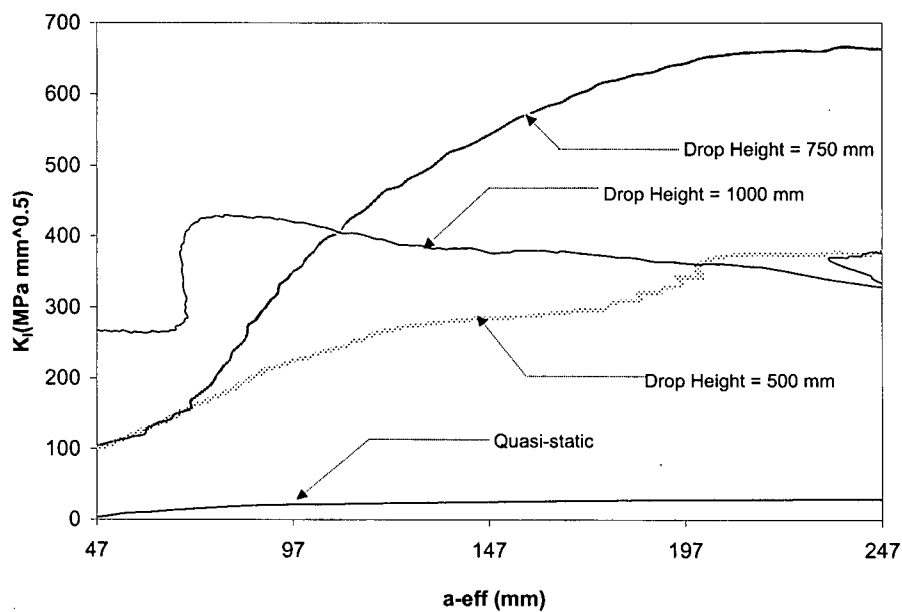
Figure 8.9b   Effect of Drop-Height on the Crack Growth Resistance of SFRC-1
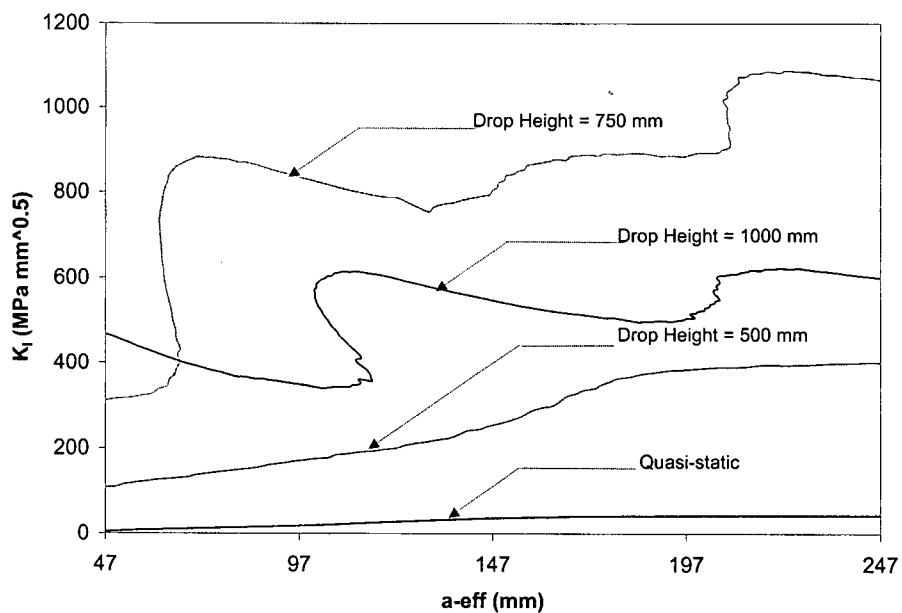
Figure 8.9c   Effect of Drop-Height on the Crack Growth Resistance of SFRC-2

182
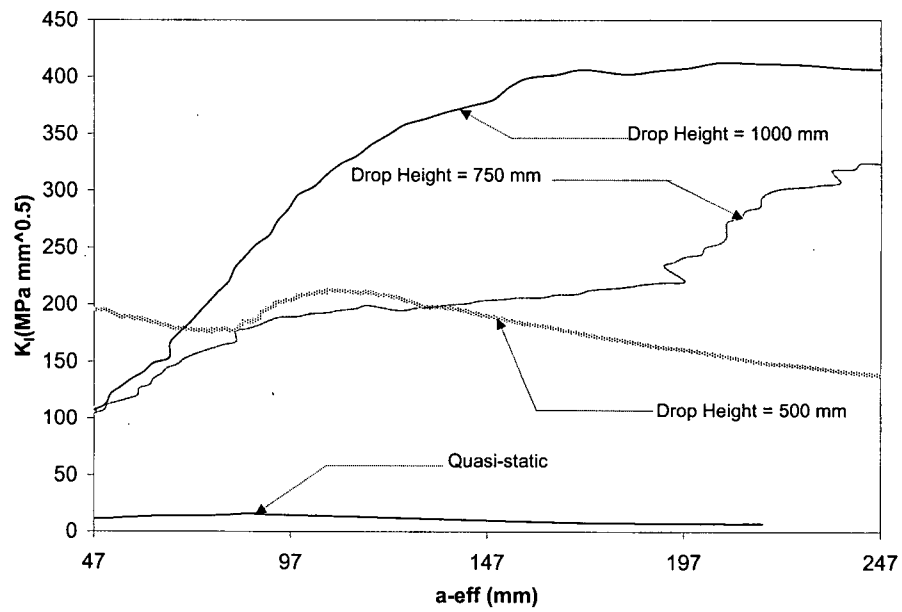
Figure 8.9d   Effect of Drop-Height on the Crack Growth Resistance of PFRC-1
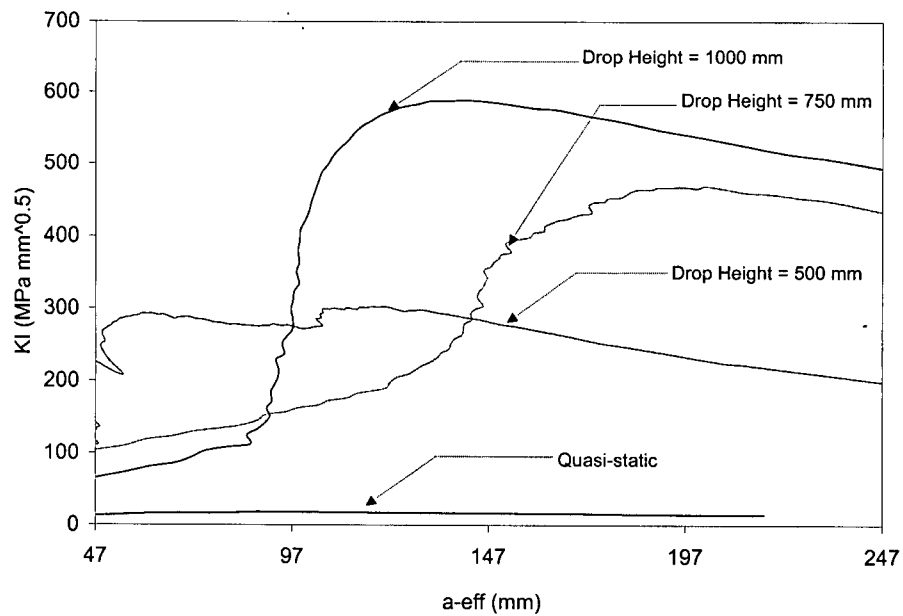
Figure 8.9e   Effect of Drop-Height on the Crack Growth Resistance of PFRC-2

8.4   Effective Crack Velocity

The effective crack extension histories are shown in Figures 8.10a-e for the five mixes investigated. As reported elsewhere [21], initially the crack extends slowly, but propagates very rapidly as the specimen approaches failure.
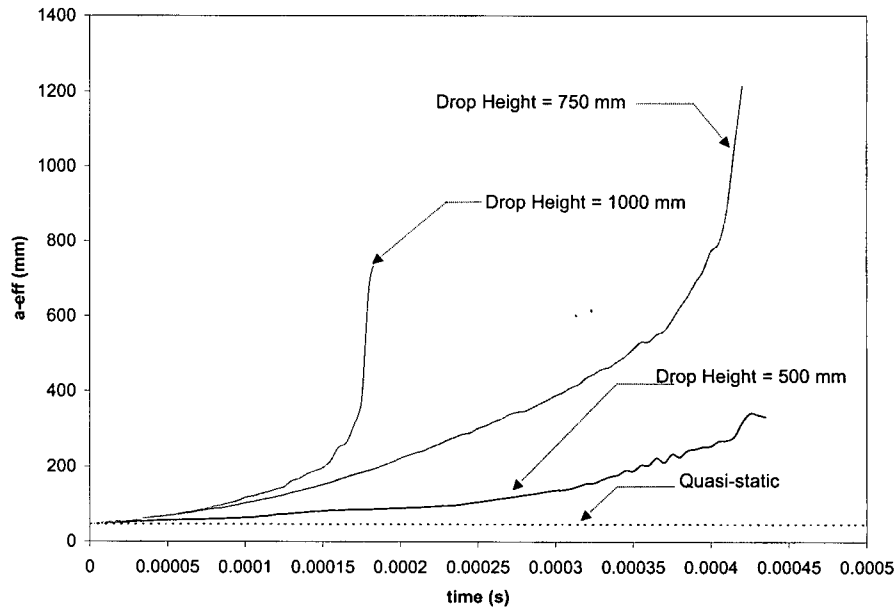
Figure 8.10a   Progress of Effective Crack Length 'a_{eff}' in Plain Concrete
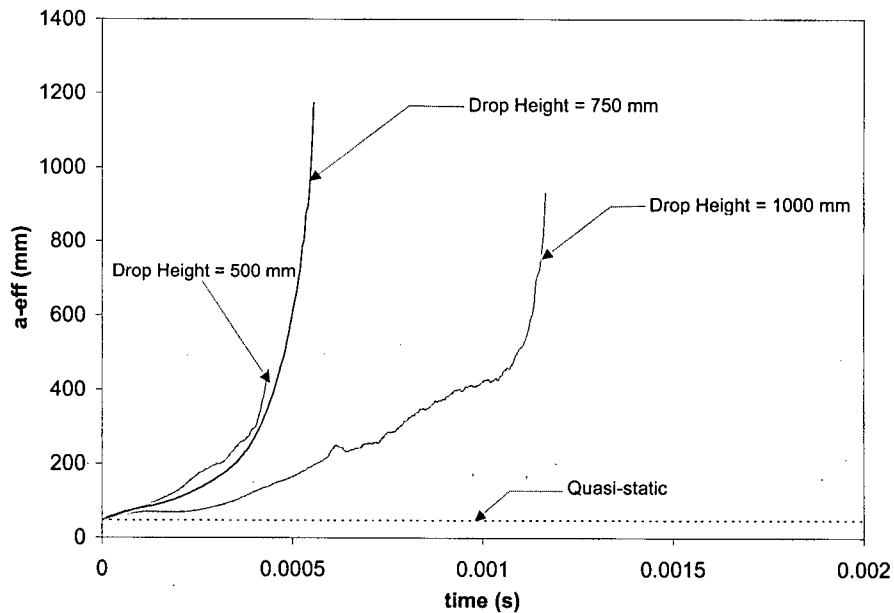
Figure 8.10b   Progress of Effective Crack Length 'a_{eff}' in SFRC-1

184
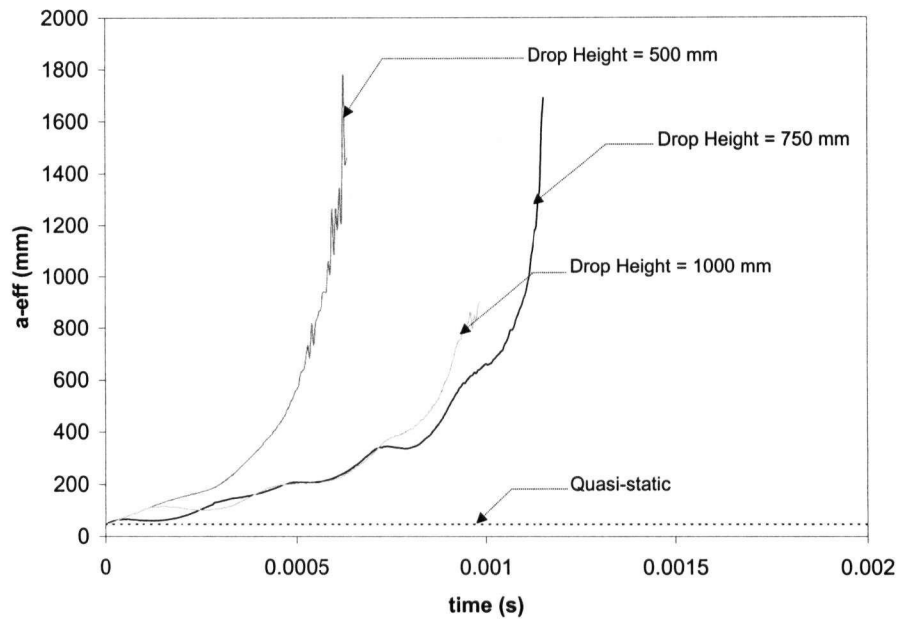
Figure 8.10c   Progress of Effective Crack Length 'a_{eff}' in SFRC-2
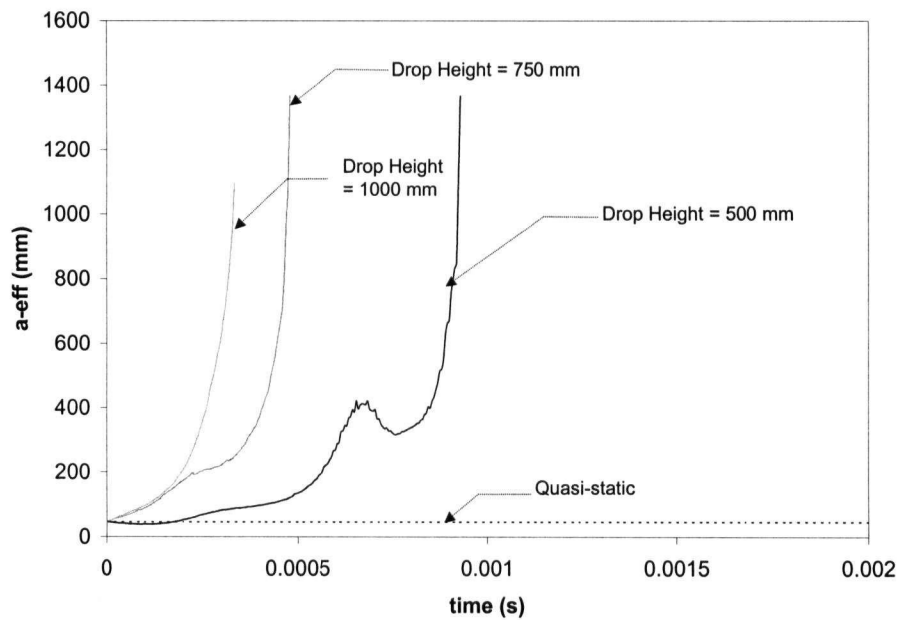
Figure 8.10d   Progress of Effective Crack Length 'a_{eff}' in PFRC-1

One outstanding aspect seen from these plots is the nature of crack extension for SFRC (Figures 8.10b & c). Notice that increasing the drop-height has the effect of delaying the crack extension, i.e. higher impact rates resulted in lower crack velocities. However, for both plain concrete and the PFRC mixes, a higher drop-height leads to faster crack extension. Note that in Figure 8.10, the effective crack length is represented and not the

185

actual crack length. This difference in response of SFRC mixes from those of plain concrete and PFRC mixes may be explained as follows. For SFRC mixes, the steel fibers pulled-out and did not fracture even under impact from very high drop-heights. On the other hand, in the PFRC mixes, some polypropylene fibers underwent fracture even as others pulled-out. At a given extent of crack, steel fibers were quite capable of withstanding the applied load, where as for plain concrete and PFRC, the crack extended in search of new crack bridging agents (aggregates in the former and polypropylene fibers in the latter).
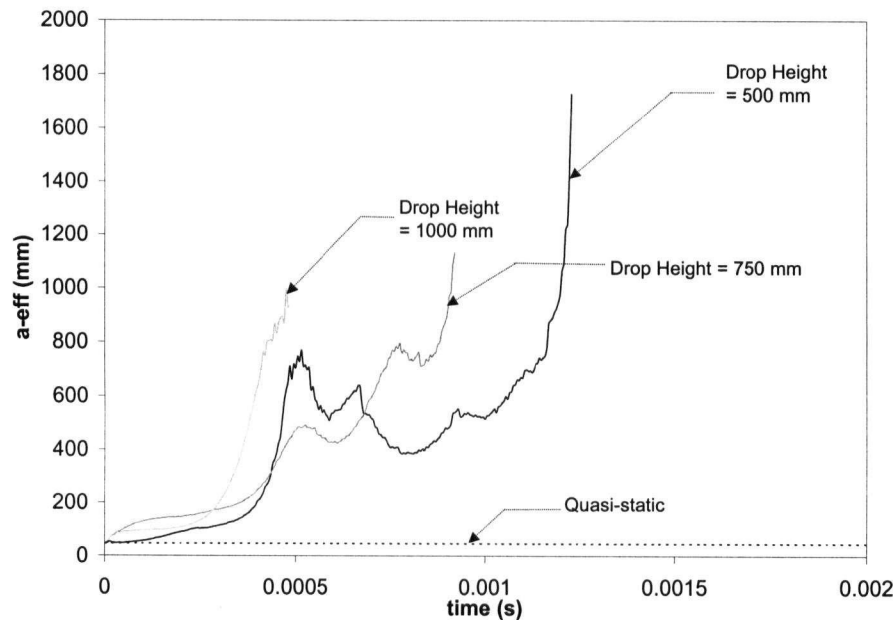
Figure 8.10e   Progress of Effective Crack Length 'a_{eff}' in PFRC-2

8.5   Fracture Toughness

Fracture toughness 'K_{IC}' for all five mixes under the four loading conditions are reported in Table 8.1. Note that for both plain concrete and SFRC, the highest drop-height of 1000 mm resulted in a fall in the value of 'K_{IC}'. On the other hand, for PFRC, the fracture toughness increased all the way under the impact conditions investigated in this study. Increasing the fiber content had a uniform effect of increasing 'K_{IC}', regardless of fiber type. As a result, the fracture toughness of PFRC catches up with that of SFRC at the drop-height of 1000 mm. This is identical to the trend observed for JSCE flexural toughness factors for the SFRC and PFRC mixes as reported in section 7.4.2.2.

186

8.6   Mode of Fiber Failure

Figures 8.11 and 8.12 describe the CDCB specimens made with SFRC and PFRC respectively, after fracture. The broken specimens revealed that for steel fibers, the mode of failure was entirely through fiber pull-out (Figure 8.11a-d). On the other hand, for polypropylene fibers, failure was through a mix of fiber pull-out and fiber fracture (Figure 8.12a-d).
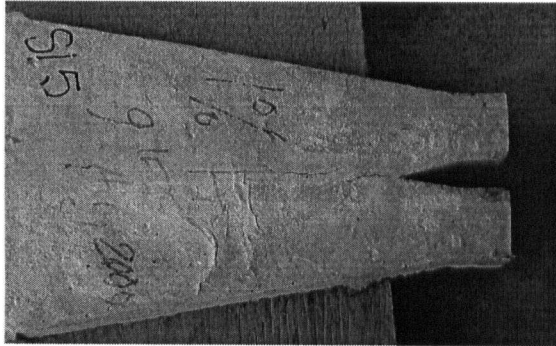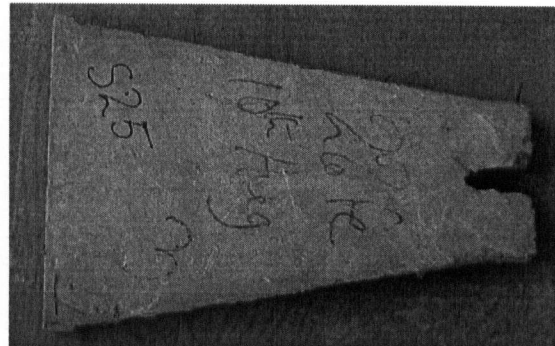
SFRC-1; 500 mm Impact   SFRC-2; 500 mm Impact
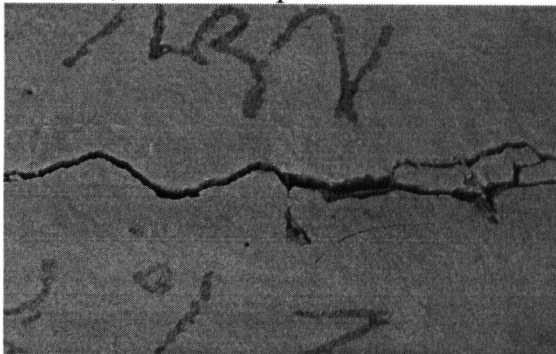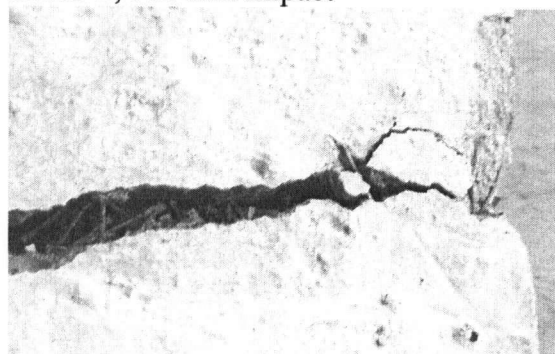
SFRC-1; 750 mm Impact   SFRC-2; 750 mm Impact
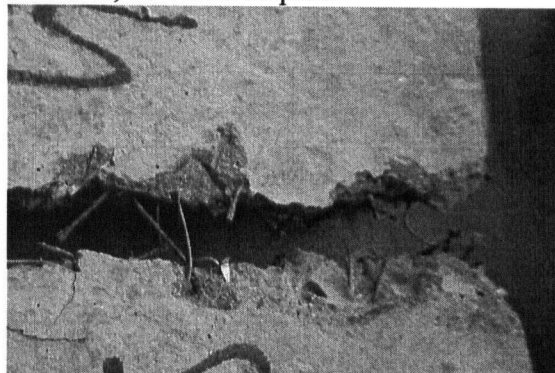
SFRC-1; 1000 mm Impact   SFRC-2; 1000 mm Impact

Figure 8.11   Broken Specimens of Steel Fiber Reinforced Concrete under Impact Loading, showing Fiber Pull-Out
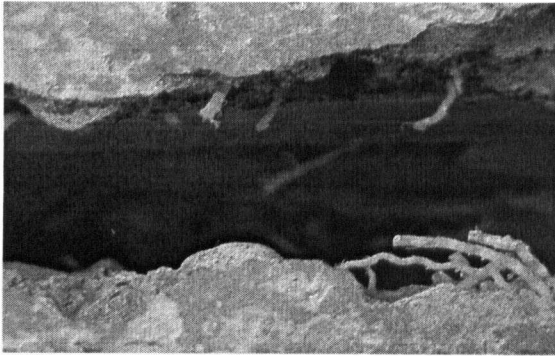
PFRC-1; 500 mm Impact

PFRC-2; 500 mm Impact
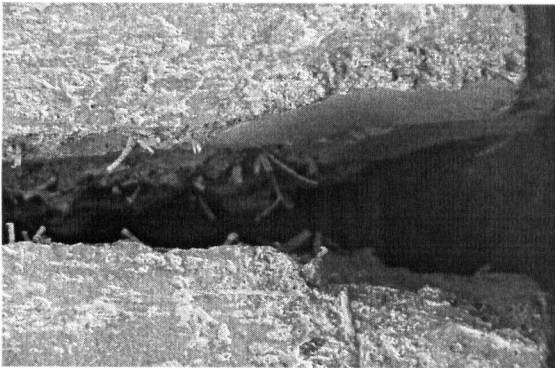
PFRC-1; 750 mm Impact
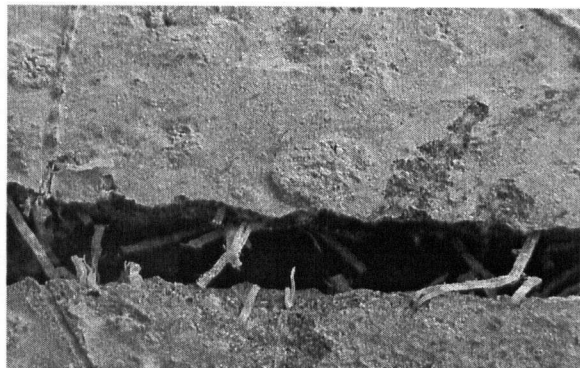
PFRC-2; 750 mm Impact
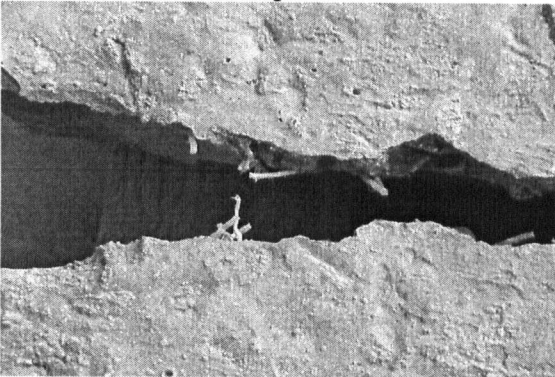
PFRC-1; 1000 mm Impact
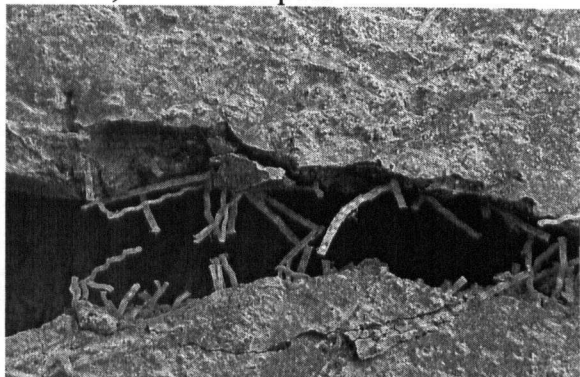
PFRC-2; 1000 mm Impact

Figure 8.12   Broken Specimens of Polypropylene Fiber Reinforced Concrete under Various Impact Drop Heights. Note Mixed Mode of Fiber Failure (Fiber Pull-Out and Fiber Fracture).

Recall that a similar change in the failure mode was witnessed during the bond-slip tests described in section 6.4.3 where the polymeric fiber F2 underwent a transition from fiber pull-out to fiber fracture as the rate of slip increased.

8.7   Stress-Rate Sensitivity

The stress-rate sensitivity of flexural strength and fracture toughness is shown in Figures 8.13a-e for the five mixes investigated. The stress-rate in these plots was calculated based on the stress carried at the fixed end of the cantilever. This implies that regardless of fibers bridging the crack along its length, the analysis was based on the representation of the two cantilever arms as traction free crack surfaces. This assumption could quite possibly lead to rather inordinately high values of flexural strength.

The stress-rate sensitivity plots indicate the dynamic impact factor for the strength and fracture toughness of the five mixes. For plain concrete, the rate sensitivity of fracture toughness was higher than that for strength. This trend is similar to the observations of Du et al. [148], who reported that between peak load and 'K_{IC}', an early rise in the value of 'K_{IC}' emerged under increasing strain-rate. However, with the introduction of fibers, no trend was witnessed in the present work. The PFRC mixes depict lower stress-rate sensitivity for 'K_{IC}' vis-à-vis flexural strength and the same is noted for SFRC with 1 % steel fibers. However, for SFRC with 2 % fiber content, a transition in the rate sensitivities for strength and fracture toughness is noted. It is quite possible that this discrepancy is due to the geometry of the specimen; since steel fibers have a tendency to "ball up" (to a degree far greater than the polypropylene fibers), problems with dispersion were encountered, which may therefore have resulted in reducing the fiber content at certain section so that the data relates to an SFRC mix containing fibers at a lower volume fraction than originally designed (i.e. less than 2%).
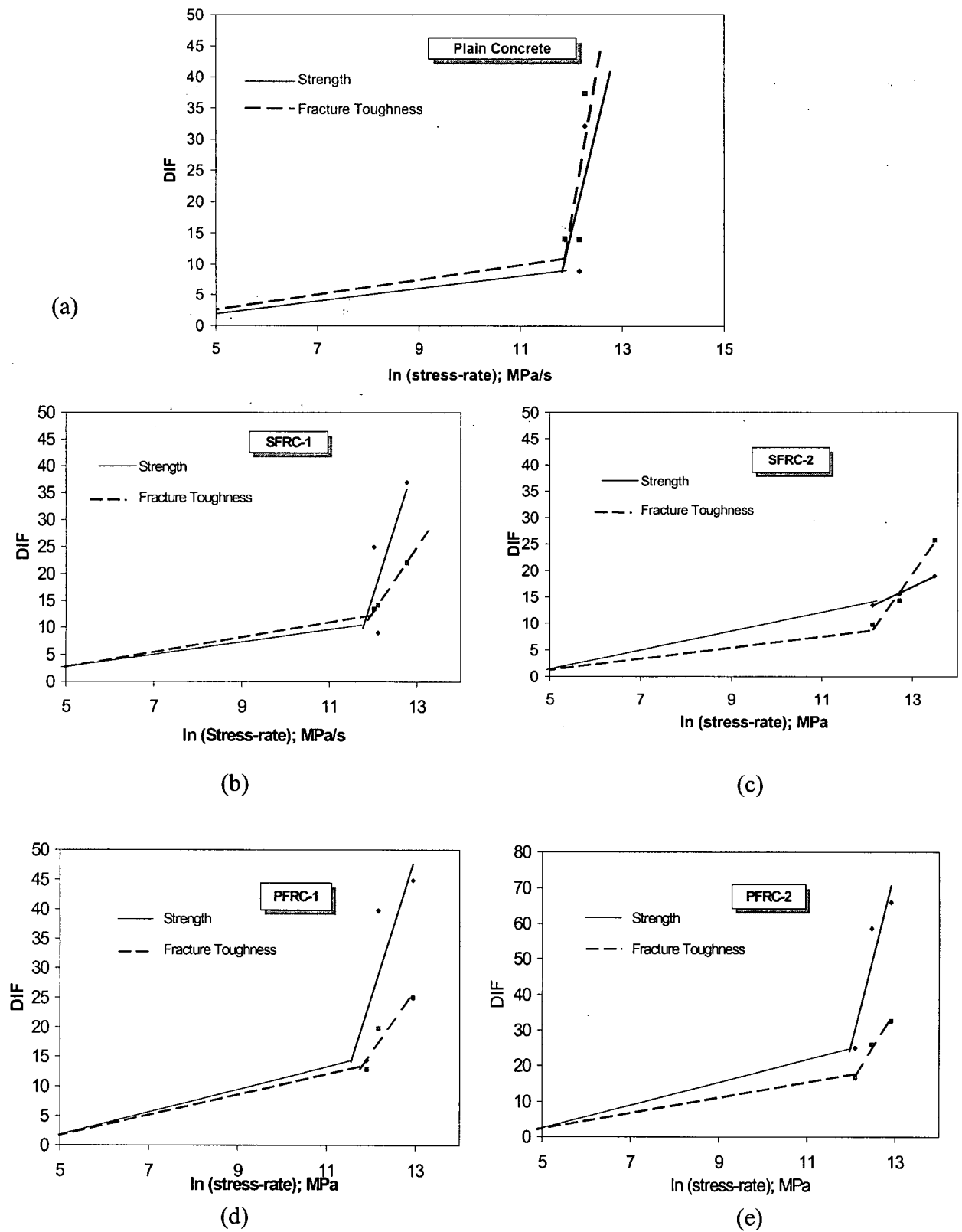
Figure 8.13   Stress-Rate Sensitivity of Fracture Mechanical Properties for a) Plain Concrete; b) SFRC-1; c) SFRC-2; d) PFRC-1 & e) PFRC-2.

190

8.8 Comparison with Previous Work

It emerges that fracture mechanical assessment of cement-based composites is very much dependent on the geometry of the specimen. With (Single Edge Notched Beam) SENB specimens, Banthia and Sheng [137] found an increasing crack growth resistance with higher dosage of steel fibers (Figure 8.14). However, they were not able to distinguish between plain concrete and FRC.
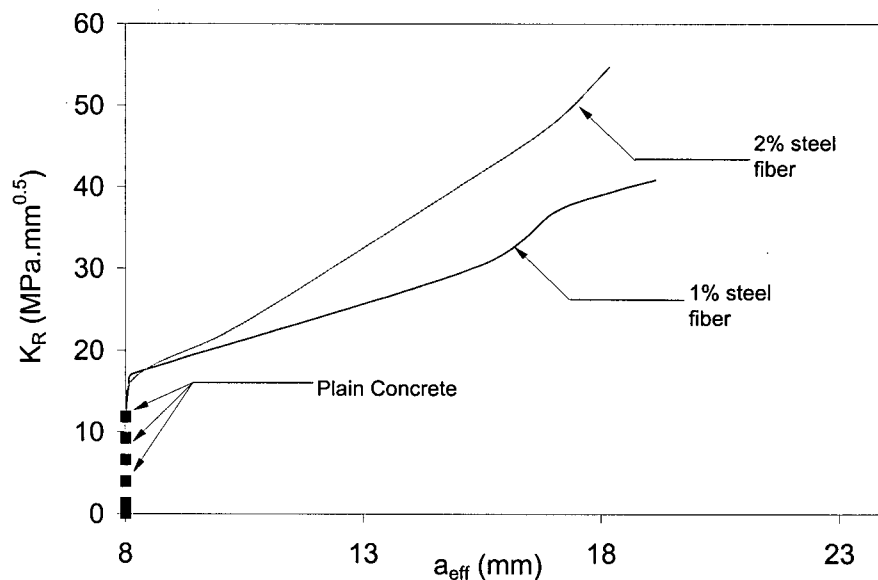
Figure 8.14 K_R-Curves for Steel Fiber Reinforced Composites [137]

Under impact loading, using SENB specimens, Sukontasukkul et al. [93] noticed an increase in the value for nominal strength for both plain concrete and FRC, with an increase in the notch/depth ratio. This increase in strength reflects the size-effect for concrete. They also reported an increase in the dynamic fracture toughness (K_{ID}) for both plain concrete and FRC with an increase in the notch/depth ratio. It implies an increase in the fracture toughness (i.e. a drop in the brittleness) for smaller specimen sizes. However, as reported in Chapter 5, a unanimous view on this matter does not emerge from the present program. For instance, while BSEL predicts an increase in the brittleness for larger sizes, MFSL suggests otherwise.

191

Yon *et al.* [94] observed that the strength and fracture toughness of plain concrete are both rate sensitive. Fracture toughness of plain concrete was more rate sensitive than strength, as seen in this program. However, for FRC, in this program, fracture toughness was seen to be less rate sensitive than strength (Figure 8.13b,d,e).

8.9   Conclusions

The following conclusions may be drawn from this study:

1. An instrumented drop-weight impact machine was successfully employed to monitor crack growth and assess the stress-rate sensitivity of the fracture properties of plain and fiber reinforced concrete. An analytical scheme was developed to derive the dynamic fracture parameters after considering inertial effects.

2. The time to first peak (or first oscillation) was found to be substantially lower than the first natural time period for the CDCB specimen. However, while the inertial correction was found to be significant in the case of plain concrete and polymeric FRC specimens, it appeared to be negligible in the case of SFRC specimens.

3. The stress intensity factor (K_I) depicts stress rate sensitivity under increasing drop heights. The fracture toughness (K_{IC}) increases with an increase in the drop-height. Fiber reinforcement increases the crack growth resistance.

4. While steel fibers are more efficient than polypropylene fibers in improving crack growth resistance, PFRC mixes depict an enhanced fracture toughness at higher drop-heights while an opposite trend was observed for steel fiber reinforced concrete.

192

5. Fracture toughness was found to be more stress-rate sensitive than flexural strength, for plain concrete. This was in keeping with previous studies reported in the literature. However, the trend was mostly reversed in the case of FRC specimens.

Chapter 9

<u>ULTRA-HIGH STRENGTH CEMENT-BASED COMPOSITE</u>
<u>UNDER IMPACT LOADING</u>

9.1   Introduction

Recent world events have clearly highlighted the need for structures of military and strategic importance to withstand severe impact and explosive loads. Very high stress-rates occur during such dynamic loading and, a large amount of energy is suddenly imparted to the structure. To resist such vigorous loading, the material of the structure must possess enough strength at high stress-rate and be tough enough to maintain integrity without shattering and collapse. This Chapter describes an ultra-high performance steel fiber reinforced cement composite with a compressive strength in excess of 150 MPa, which was investigated for its impact response. Direct comparisons are made with conventional normal strength fiber reinforced concrete.

9.2   Compact Reinforced Composite

Compact reinforced composite (CRC) is a special type of ultra high strength concrete reinforced with up to 6% by volume of steel fiber. Developed by Aalborg Portland, it is characterized by a low water/binder ratio, high silica fume content and absence of any coarse aggregate [132]. CRC, as a result, has a very high compressive strength (150-400 MPa) and a high toughness. At the microstructural level, CRC has large amounts (~50 %) of unhydrated cement grains, which in turn, reinforce and stiffen the granular skeleton of the hydrating material [155]. With an exceptionally dense microstructure and virtually inexistent bleed channels, CRC is also expected to be highly durable [156], resist an ingress of deleterious fluids and possess a far greater resistance to attack by physical and chemical agents than any conventional high-strength concrete. With large amounts of silica fume and a complete absence of coarse aggregates, CRC, which is strictly speaking a fiber reinforced mortar, undergoes large autogenous shrinkage at early ages but this is known to subside within the first 10 days [132].

While CRC has been promoted primarily for pre-cast applications in slender structures, its ultra high strength and very high toughness make it potentially very suitable for structures that need to resist impact, shock and explosive loading. These include gas tanks, nuclear reactor containment shields, defence shelters and bunkers, heavy-duty runways, crash barriers and structures of military and strategic importance designed to withstand explosive blasts and attacks with missiles and projectiles.

9.3   Materials

The mix proportions for CRC investigated in this study are given in Table 9.1. For CRC, a white Portland cement containing 66.9 % C_3S, 19.2 % C_2S, 4.35 % C_3A and 1 % C_4AF was used along with silica fume (SF, 24 % by weight of cement). A dry superplasticizer (SP) of condensed naphthalene sulphonate type was used to achieve workability. Typically, the amount of superplasticizer (in the form of a powder) varies between 1 – 4 % by weight of the cementitious components (in this case, "cement + silica fume"). The mix contained 4 mm maximum particle size quartz sand as aggregate and 12 mm long, 0.4 mm diameter steel fiber at a volume fraction of 6 %.

Table 9.1   Mix Proportions for CRC

Composite	Ingredient, kg/m³						
	Cement	Water	SF[1]	SP[2]	Quartz Sand		Fiber (Vf)
					Size Range	Qnty.	
CRC	750	150	179	21	0-0.25 mm	189	457
					0.25- 1 mm	383	
					1-4 mm	613	

1   Silica fume

2   Superplasticizer

A specialized mixing technique was adopted for CRC. Cement, silica fume, sand and superplasticizer were first mixed in a pan mixer for 2 minutes followed by addition of the entire mix water (w/[c+sf] = 0.16). The material was then allowed to mix for another 6 minutes, a somewhat longer time, but required to allow the dry superplasticizer to fully

plasticize the mix. The fibers were then introduced gradually to ensure maximum dispersion. Slump test was carried out both before and after fiber addition. Figures 9.1 and 9.2 show the slump of fresh CRC before and after the addition of 6 % steel fibers. A slump of 200 mm before fiber addition dropped to about 120 mm after fiber addition, which was quite adequate for proper workability. A fiber volume fraction of 6%, however, also appears to be the limit; mixes with higher volume fractions of 9 and 12 % have been found to be highly unworkable [131].
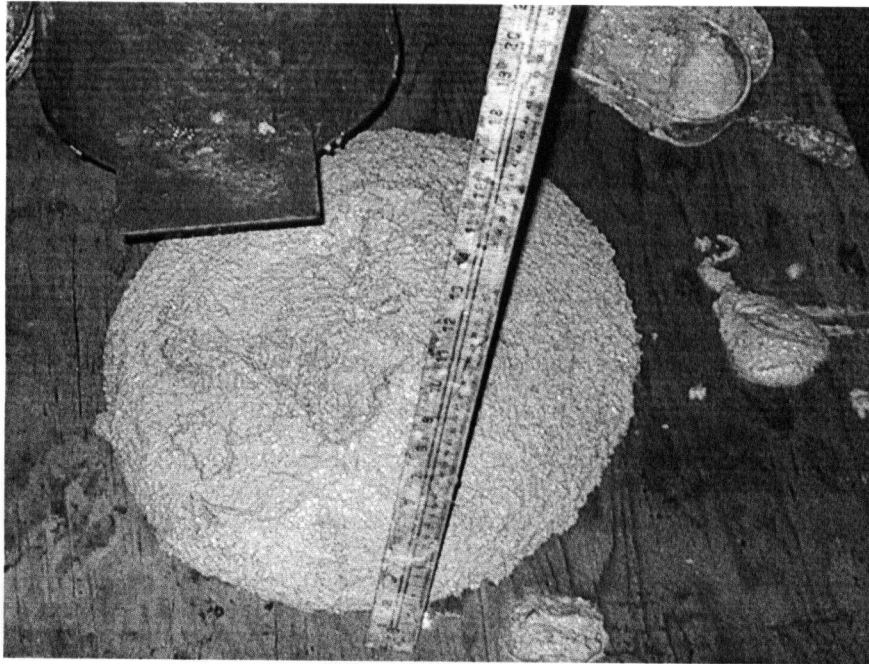
Figure 9.1   Slump Test on CRC Mix *without* Steel Fibers

A with CRC, two conventional fiber reinforced concrete mixes were also investigated with steel (SFRC) and macro-polypropylene fiber (PFRC). The mix design and details of the individual components for the two conventional FRC mixes are given in section 4.2.2.
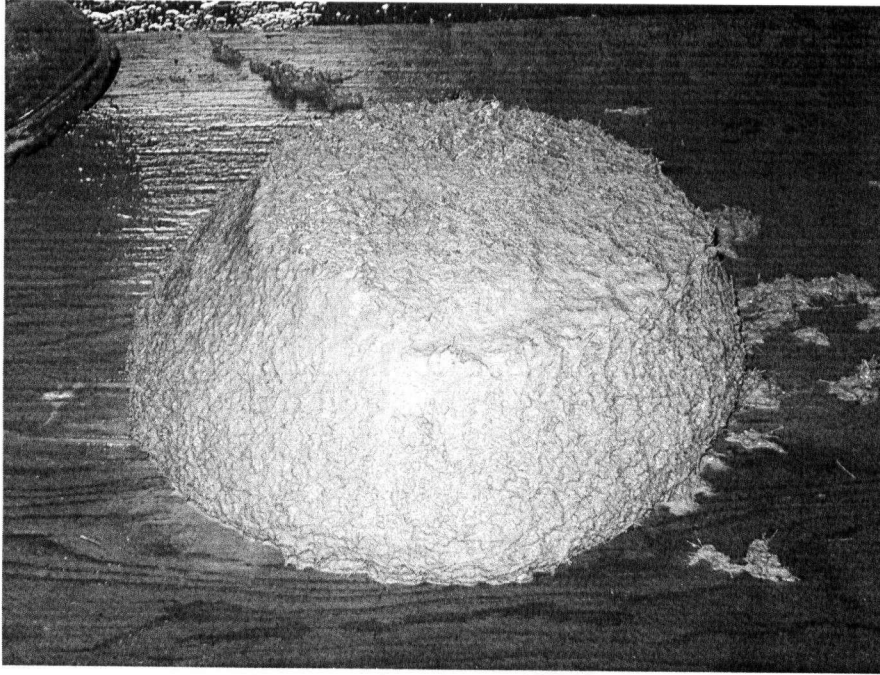
Figure 9.2   Slump Test on CRC Mix *with* 6% Steel Fiber

The test specimens were in the form of cylinders (50 mmϕ x 100 mm height) for compression and splitting tension and beams (100 mm x 100 mm x 350 mm) for determining flexural toughness. Smaller compression cylinders for CRC were chosen primarily out of necessity, as the ultra high strength of CRC required a testing machine of excessive capacity unavailable in the lab. This was, however, not seen as a serious issue given that CRC has no large aggregate and contains fiber of shorter 12 mm length.

9.4 Results and Discussion

9.4.1 Quasi-Static Loading

Results from the quasi-static tests are given in Table 9.2. Notice that a very high splitting tensile strength of 20 MPa was measured for CRC. Compressive strength values indicate that CRC is about 5 times stronger than conventional FRC (SFRC and PFRC). In the same context, CRC also possesses nearly three times higher flexural strength.
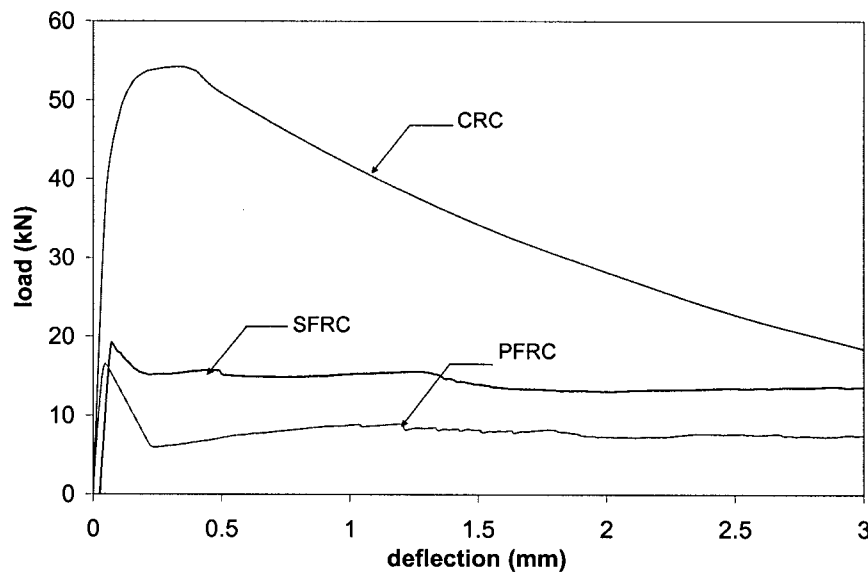
Figure 9.3   Flexural Response Under Quasi-Static Loading

Flexural load displacement plots (ASTM C1018) under quasi-static loading for CRC and FRC beams are shown in Figure 9.3. Notice that for CRC, a synergy between the high performance matrix and a high volume fraction of steel fibers translates into both a higher first crack strength and a remarkably higher ultimate strength. The post-crack toughness is also much greater than conventional FRCs. Between the two conventional FRCs investigated, as expected, SFRC is seen to be tougher than PFRC, due primarily to the greater stiffness of steel fiber over polypropylene fiber.

Table 9.2   Quasi-Static Test Data

Mix	Compressive Strength, MPa	Splitting Tensile Strength	Flexural Strength (MPa)	Flexural Toughness	
				Total Toughness (J)	Toughness Factor (MPa)
CRC	192 MPa (33)	20 MPa (3)	15.90 (2.60)	69.20 (9.62)	10.38 (1.44)
SFRC	43 MPa (7)	-	6 (1.10)	29.40 (1.87)	4.41 (0.28)
PFRC	40 MPa (6)	-	5.40 (0.85)	16.80 (2.27)	2.52 (0.34)

9.4.2   Impact Tests

Results of impact tests are given in Table 9.3 where some of the results of quasi-static testing are reproduced for comparison purposes. The load-displacement responses of CRC, SFRC and PFRC to impact loading are plotted, respectively, in Figures 9.4a, b and c for the four drop heights.
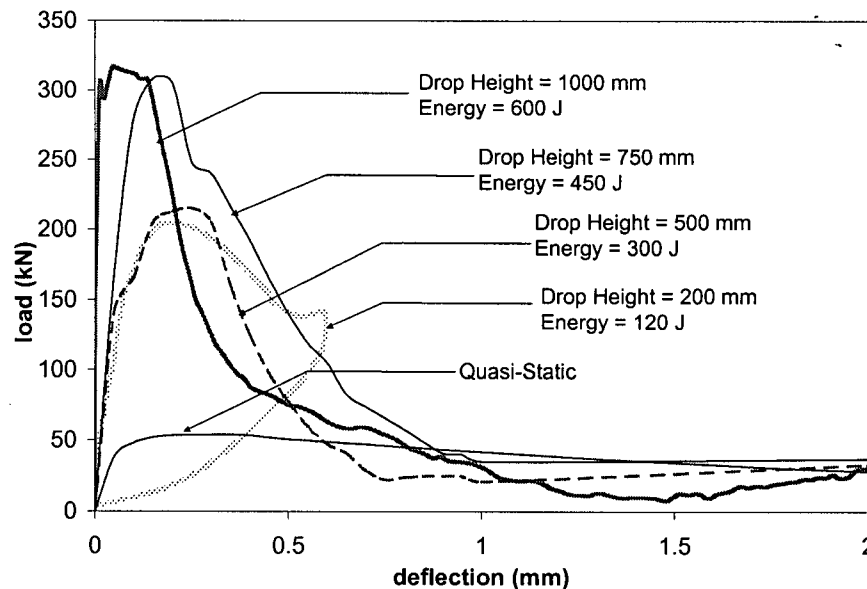
Figure 9.4a   Impact Response of CRC under Flexural Loading

In these plots, results from quasi-static testes are also included. Notice that for all three composites, CRC, SFRC and PFRC, the peak loads (and hence the flexural strengths) increased as the height of hammer drop was increased. Further, with an increase in the height

199

of hammer drop, the peak loads, in general, also occurred at smaller displacements. Thus, all three composites depicted a stiffer response at higher drop heights indicating an increase in the elastic modulus of the material with an increase in the applied stress-rate.
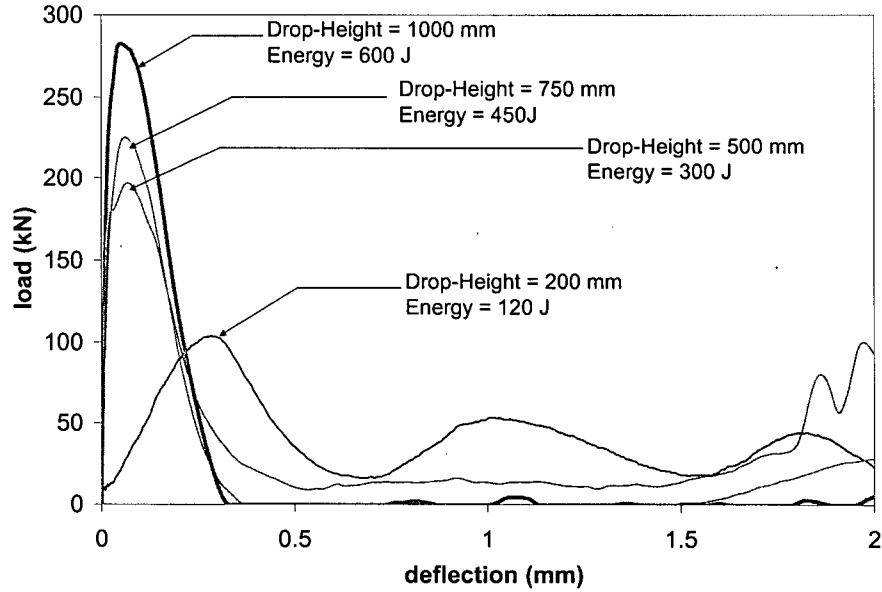
Figure 9.4b   Impact Response of SFRC under Flexural Loading
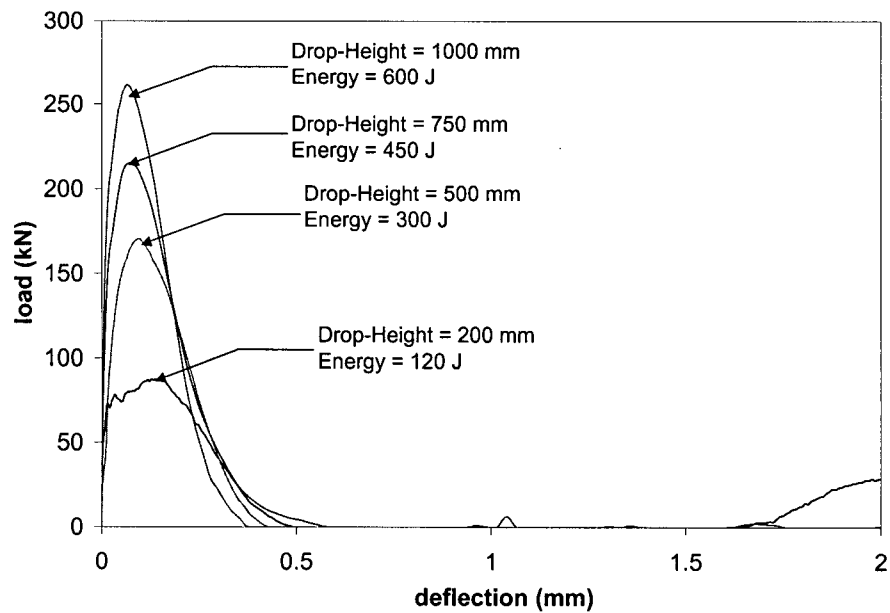
Figure 9.4c   Impact Response of PFRC under Flexural Loading

The load-displacement plots were analyzed as per the JSCE SF-4 technique and the *total toughness* values (to a mid-span deflection of span/150) and the *flexural toughness factors* 'FTF' (calculated by converting total toughness values to equivalent post-crack strength) are given in Table 9.3. The JSCE FTF values are compared for all mixes under different loading rates in Figure 9.5.
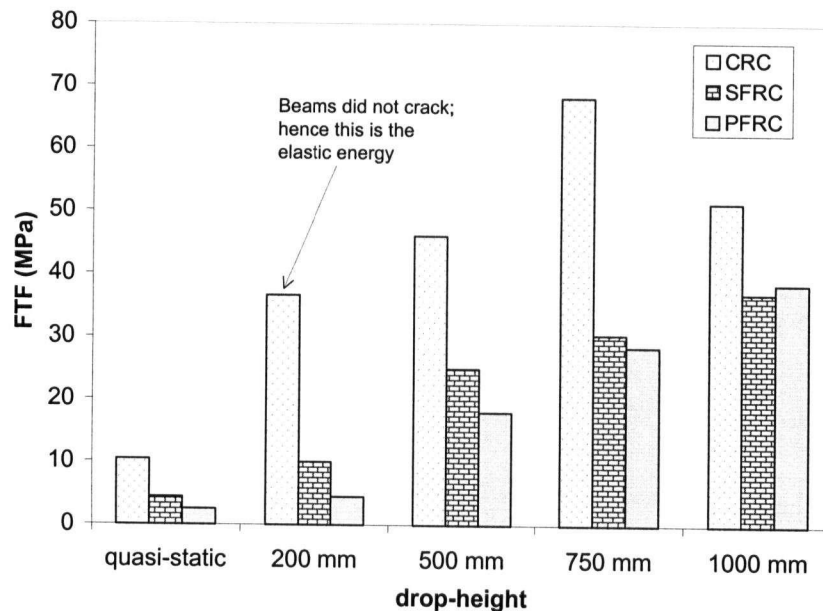
Figure 9.5   JSCE Flexural Toughness Factors for CRC and FRC

Notice the very high impact resistance of CRC over conventional FRC. As mentioned in section 7.4.2.2, note the gradual decrease in gap between the energy absorption capacity of SFRC and PFRC in the same impact range. However, CRC appears to reach an optimum in terms of increase in its flexural toughness with drop-height. Perhaps, this is reflective of its brittleness arising from its ultra-high strength.

A general notion of the stress rate sensitivity may be obtained from the formulation proposed by Nadeau *et al.* (equation (3.10)). This is shown in Figure 9.6 where flexural strength of CRC is compared with that of plain and fiber reinforced normal-strength concrete as a function of stress-rate. Note that CRC is less sensitive to stress-rate than traditional normal strength FRC, and that a steep rise in the stress-rate sensitivity (*knee* in the curve, point D) in the case of CRC occurs at a higher value of applied stress-rate than for normal strength FRC.

This observation is in accordance with findings of Bentur *et al.* [18] and Ross [13], but contrary to the findings of Bischoff and Perry [133] who reported higher stress-rate sensitivity for higher strength concrete in compression. Ross [13] explains that lower strength or lower modulus materials have a lower limiting crack velocity resulting in smaller *facture process zones* (fpz) ahead of a propagating crack. This results in an apparently higher strength at a given strain rate. Since this effect is seen at all strain rates, overall, the apparent stress-rate sensitivity for lower strength materials is higher than that for their high strength counterpart.
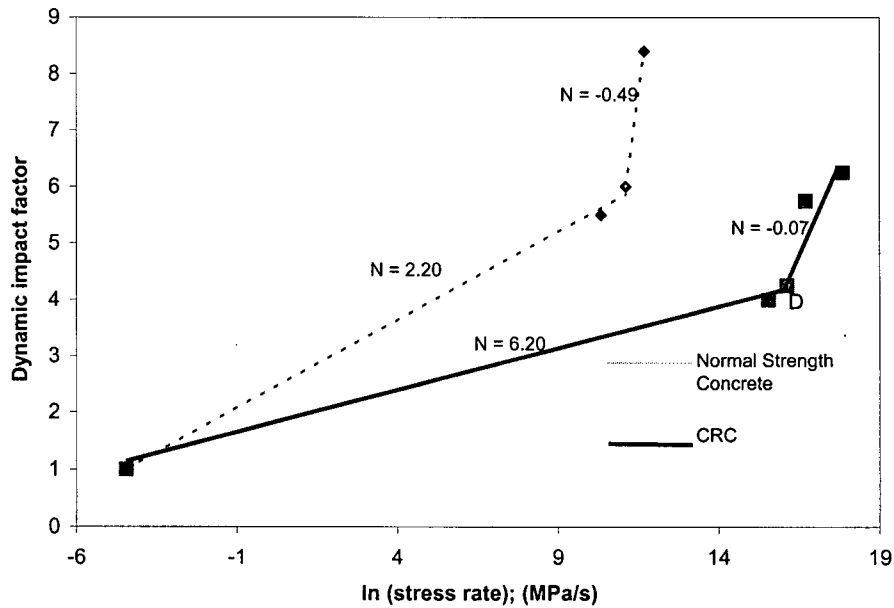
Figure 9.6   Stress-Rate Sensitivity of CRC and FRC
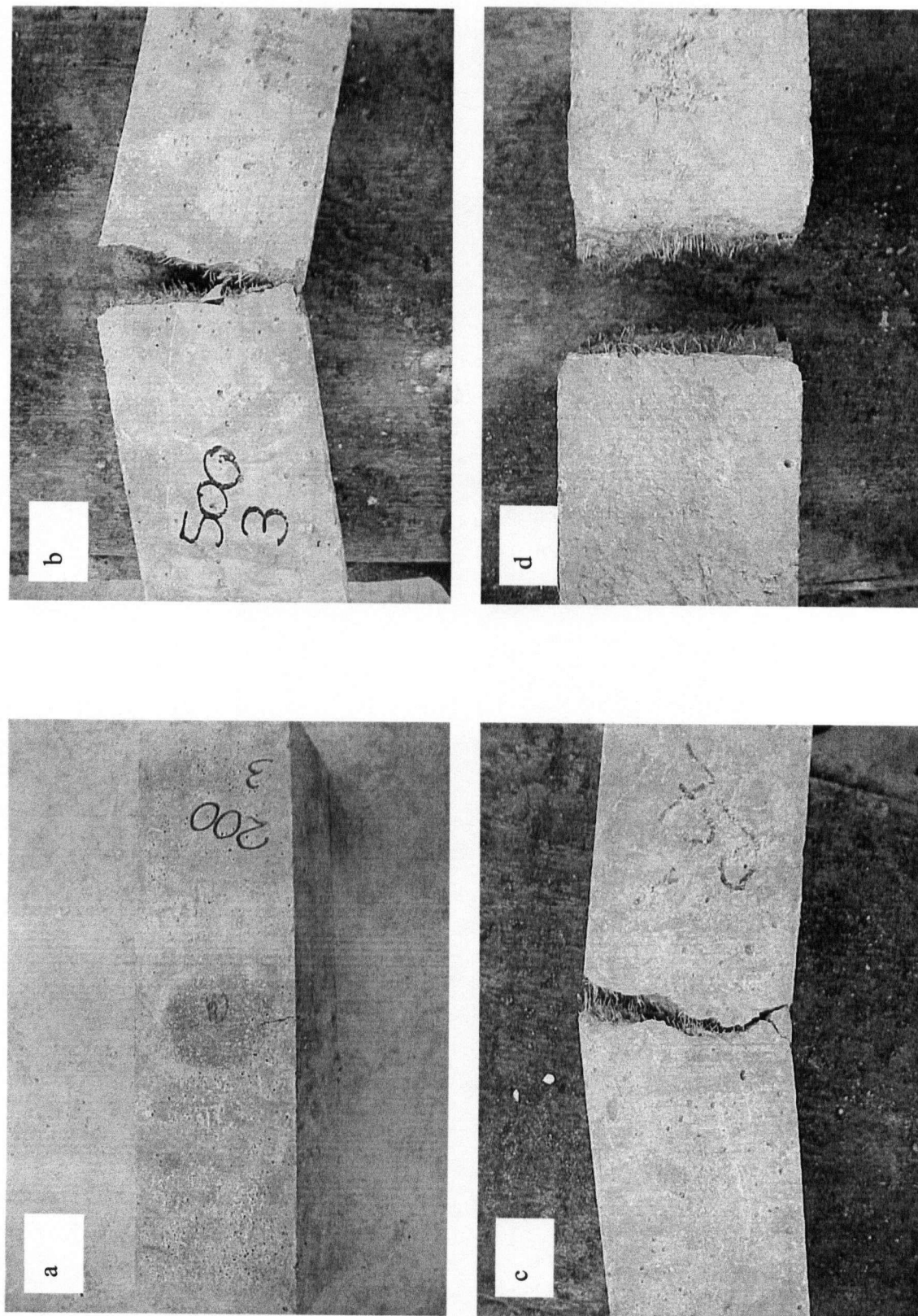
Figure 9.7   Failure of CRC Beams under Impact Loading at Drop-Heights of: a) 200 mm, b) 500 mm, c) 750 mm & d) 1000 mm

203

Table 9.3   Impact Responses of CRC, SFRC & PFRC in Flexure

Composite	QUASI-STATIC TESTS			IMPACT TESTS					Impact factor	
	Peak Load (kN)	Total Toughness (J)	Toughness Factor (MPa)	Drop Height	Peak Load (kN)	Total Toughness (J)	Toughness factor (MPa)		Peak load	Toughness factor
CRC	53 (7)	69.2 (9.6)	10.38 (1.44)	200 mm	205 (36)	244 (23)	36.5 (3.4)		3.87	3.51
				500 mm	215 (32)	305 (29)	48.7 (4.6)		4.06	4.67
				750 mm	308 (25)	450 (46)	69.5 (7.1)		5.81	6.69
				1000 mm	317 (36)	342 (33)	51.2 (4.9)		5.98	4.93
SFRC	20 (4)	29.4 (1.9)	4.41 (0.28)	200 mm	103 (10)	82.2 (11.5)	18.50 (2.6)		5.15	4.19
				500 mm	194 (18)	76.2 (10.6)	17.15 (2.4)		9.49	3.88
				750 mm	222 (33)	46.6 (6.7)	10.49 (1.5)		11.1	2.37
				1000 mm	278 (39)	47.2 (7.1)	10.62 (1.6)		13.9	2.40
PFRC	18 (3)	16.8 (2.3)	2.52 (0.34)	200 mm	88 (11)	30.1 (4.6)	6.77 (1.0)		4.88	2.69
				500 mm	169 (10)	35.3 (5.3)	7.94 (1.2)		9.37	2.97
				750 mm	212 (19)	38.7 (5.8)	8.71 (1.3)		11.66	3.46
				1000 mm	262 (35)	56.2 (7.9)	12.65 (1.8)		14.55	5.01

The impact behaviour of CRC highlights several interesting features (Figures 9.5 and 9.6). As expected from high strength concrete, CRC exhibits a less sensitive behaviour to stress rate. However, because of its high strength and high fiber content, the material is also capable of dissipating greater amounts of energy up to very large stress-rates as seen in Figure 9.6. One notes that while SFRC is increasingly brittle under impact loading, CRC initially improves with impact loading and becomes brittle only at a very large drop height. Figures 9.7a-d show representative CRC specimens after impact. All the beams experienced fiber pull-out mode of failure. Notice that the beams did not fracture completely at lower drop heights and broke apart in two halves only at a drop height of 1000 mm when there also occurred a corresponding decrease in the flexural toughness (see Figure 9.5). It indicates that in spite of being an ultra-high strength material the onset of brittleness is delayed to a high value of stress-rate. This is a desirable attribute of CRC, and it widens the range of its application in structures experiencing blast and impact loading. Dancygier and Yankelevsky [157] and Luo *et al.* [158] reported similar observations for high strength concrete.

9.5   Conclusions

The following conclusions may be drawn from this Chapter:

1. Compact reinforced composite (CRC) is an ultra high performance concrete with compressive strength above 150 MPa and splitting tensile strength around 20 MPa. It is also a highly energy absorbing material with its toughness over three times that of conventional fiber reinforced concrete with steel or polymeric fibers.

2. The flexural strength of CRC is higher under impact loading than under quasi-static loading. CRC is, however, less stress rate sensitive than conventional normal strength fiber reinforced concrete. The material shows characteristic signs of a high-strength composite as evident from the delayed onset of high stress-rate behaviour (bilinear response).

3. Under impact, CRC is capable of dissipating much higher energy compared to conventional fiber reinforced concrete with polymeric or steel fiber. This is an

evidence of the synergy witnessed between a high strength matrix and a high volume fraction of steel fiber. Therefore, CRC emerges as a highly recommended material for structures subjected to blast or impact loading.

Chapter 10

CONCLUSIONS

The principal conclusions that may be drawn on the basis of this study are as follows:

A. Impact test results on plain and fiber reinforced concrete are highly machine dependent.

- Perceived Stress-rate sensitivity of concrete is highly dependent upon the machine parameters under which it is established.

- Heavier hammers generate longer (and flatter) pulses for a given constant incident energy while greater drop-heights generate shorter (and sharper) pulses.

- It is better to maintain the drop-height as the fixed test parameter for standardized testing as this will yield comparable data across machines of widely different capacity.

- For the same incident impact energy, impact response with machines of different mass can be in contrast to one another. The flexural toughness of polypropylene fiber reinforced concrete was lower than that of steel fiber reinforced concrete for a heavier hammer. On the other hand, with a lighter hammer but a larger drop-height, polypropylene fiber reinforced concrete exhibited superior flexural toughness.

B. Plain and fiber reinforced concrete exhibit size-effects under impact loading, and the effect intensifies with an increase in the stress-rate.

- For identical loading conditions, smaller specimens experience an apparently greater stress-rate. A proper analysis of the response of FRC to impact loading must therefore involve the normalization for the applied stress-rate.

- If the self-weight of the specimen is ignored, the stress-rate sensitivity of the flexural strength of plain concrete is seen to be affected by specimen size. Larger

beams exhibit a greater stress-rate sensitivity for both nominal strength and fracture energy.

- Impact loading results in a progressively smaller characteristic length of FRC. Increasing the specimen size causes a further shift towards smaller characteristic lengths (and thus, a rise in the brittleness number). This implies that the size effect amplifies at higher loading rates.

- For both steel and polypropylene fiber reinforced concrete, an evaluation of flexural toughness factor (as per JSCE SF4-1984), reveals a size effect under impact loading. This is in sharp contrast to the case of quasi-static loading, where no significant size-effect has been reported. Further more, under impact loading, with increasing drop-height, the size effect on toughness factors was seen to become more pronounced.

C. Polymeric fibers exhibit greater efficiency under impact loading.

- Crimped polypropylene fibers are less effective than flattened-end steel fibers under quasi-static rates of loading. However, upon increasing the rate of fiber slippage (brought about by higher rates of crack opening displacement), a stiffer response from polymeric fibers is witnessed. This manifests itself in the form of higher peak loads and smaller slips, at the peak load. In most cases that were investigated, the slip-at-peak converged across all fiber types as the stress-rate was increased.

- Impact loading of single, deformed, polypropylene fibers resulted in a transition in the failure mode from pull-out to fracture. Maintaining a pull-out mode of fiber failure results in an increase in the dissipated energy at higher rates of slippage.

- From crack growth studies on Contoured Double Cantilever Beam (CDCB) specimens, it was seen that fracture toughness (K_{IC}) of PFRC as derived from K_R-Curves improves relative to that of SFRC with increasing drop-height of impact. This improvement is sometimes accompanied by a shift in fiber failure mode from fiber pull-out to fiber fracture.

- The flexural toughness of SFRC (with flattened-end steel fibers) was significantly higher than that of PFRC (with crimped polypropylene fibers) under quasi-static

conditions. However, with an increase in the drop-height of impact, this gap steadily narrowed, with the result that for the particular case of drop-height equal to 1000 mm, PFRC was observed to be tougher than SFRC.

D. Compact Reinforced Composite (CRC), combines an ultra-high strength matrix with high steel fiber volume fraction to produce a superior impact resistant material.

- Although it contains 6% steel fibers, CRC yielded a satisfactory slump and posed no difficulty in casting.

- CRC, like other high-strength composites is less stress-rate sensitive than normal strength concrete. However, with its ultra-high strength and a high fiber content, CRC dissipates three to four times more energy than conventional FRC.

Chapter 11

RECOMMENDATIONS FOR FUTURE WORK

On the basis of the work reported in this thesis, the following recommendations are made for conducting future work in this area:

1. The fibers investigated in this program were limited to commercially available geometries. Clearly, they have not been optimized for impact loading. The bond stiffening witnessed in this study highlights the importance of exploring new geometries, which will ensure an efficient pull-out response. This is especially required of steel fibers to avoid fiber fractures at high stress-rates.

2. In the absence of a standard method for testing cement-based composites under impact, extending the scope of the work reported in Chapters 5 and 7 should lead to a standardized technique for testing and characterization of FRC under impact. This will involve specifying both machine parameters (machine capacity, hammer mass and drop-height) and specimen related parameters (shape, size, mix variables, etc.) to achieve uniformity in the results across laboratories. Also, care must be taken to maintain a similitude between the stress-rates experienced by the fiber-matrix system under the test-environment with that existing in the field.

3. In line with the results reported in Chapters 6 and 7, further investigations of the fiber-matrix bond and related fiber reinforced concrete will lead to a predictive modeling of this material under flexural impact. From the stand-point of the end-user, such models will eventually lead to design methodologies for applications in high stress-rate environments.

4. While fibers are proven to be effective under quasi-static shear, their utility under impact loading has never been investigated and promises to be a very attractive

alternative to existing methods of reinforcement with stirrups. Such a study should distinguish between steel and polymeric fibers and produce design suggestions in conjunction with recommendations for flexure as proposed in (1) above.

5. Efforts must be made to study the stress-rate sensitivity of fiber reinforced concrete under very high strain-rates ($> 10^2$) as well as under low temperatures (< 0 °C). The data generated will be useful in specialized applications such as for military requirement, where engineered high-performance products like CRC are most likely to be applied.

6. The impact response of FRC under uniaxial tension, lateral confinement and under mixed-modes needs further investigation. The use of FRP wraps and sprayed FRP coatings in retrofitting existing plain concrete and FRC members has come of age. Understanding the response of FRC in the presence of FRP wraps and coatings will help advance the knowledge and use of this very innovative material.

7. While the benefit from fibers in dynamic-crack bridging has been effectively established in this report (Chapter 8), little is known about the role of two-or-more fibers in the same matrix, especially, in arresting sub-critical crack growth, the fiber-fiber interaction and the possible synergy. While there exists limited data on the improved fiber efficiency through such "hybrid" mixes under quasi-static loading, no such data is available on their role under impact. With a wide variety of fibers available now, hybridized FRC systems offer a tremendous scope for study in the near future.

8. The data generated in this study agrees well with both Bažant's Size Effect Law and the Multifractal Scaling Law. It is clear that specimen size-effect should be addressed based on physical explanations rather than the currently existing empirical formulations.

9. The hydrophobic nature of polypropylene is often cited to explain the issue of poor bonding in a cement-based matrix. However, recent advances in polymer science have led to surface coatings, which use hydrophilic polymers to coat both polymeric and steel fibers. While such coated fibers have been used to modify the fresh concrete rheology, their performance in bridging cracks is yet to be studied. Use of surface coated fibers promises a tremendous potential in both quasi-static and impact regimes.

10. The present work dealt with only fiber reinforced cement composites. The impact performance of structural fibers in the presence of conventional reinforcement, especially against shear remains to be understood.

It is hoped that the present work, in conjunction with future studies will help further our understanding of the material science of fiber reinforced cement-based composites. In the words of the experimental biologist Abraham Trembley (1710-1784), "We must allow Nature to be explained by Nature and not by our own views".

Appendix 1

STEPS INVOLVED IN DETERMINING THE DYNAMIC FRACTURE TOUGHNESS OF A CDCB SPECIMEN

The following steps outline the derivation of fracture toughness values from dynamic crack growth testing of a CDCB specimen in an instrumented drop-weight impact machine as described in Chapter 8.

Step 1. Upon testing a CDCB specimen, obtain the tup load-time history '$F_v(t)$' and the acceleration-time history '$\ddot{z}(t)$'.

Step 2. Resolve the tup-load to obtain the opening load in the cantilever arm '$OL(t)$'. This is the component of the tup-load and is as yet not corrected for the inertial effect. Hence, it is not necessarily the actual stressing load.

Step 3. Obtain the displacement of one arm of the CDCB by integrating the acceleration history twice with respect to time. Double this value to obtain the crack mouth opening displacement $CMOD(t)$.

Step 4. Apply the inertial correction using equation (8.15), with acceleration $\ddot{z}(t)$ from Step 1 above. This yields the corrected stressing load for the uncracked condition in an arm of the CDCB, '$OL^u(t)$'.

Step 5. Plot $OL^u(t)$ vs. $CMOD(t)$ for the entire test. Identify the bending-over-point (BOP), which signifies the onset of cracking. Let this correspond to time t_c.

Step 6. Consider the $OL^u(t)$ and $CMOD(t)$ data beyond time $t = t_c$. Solve for 'a_{eff}' using equation (8.7) while simultaneously applying the inertial correction on $OL^u(t)$ at each time-step using equation (8.18). The solution process at each time-step is iterative and should proceed until equation (8.7) is satisfied.

Step 7. The corrected value for opening load '$OL^c(t)$' will now correspond to the case of cracked cantilevers of the CDCB. Obtain '$a_{eff}(t)$' to yield '$K_I(t)$' using equation (8.9).

Step 8. Plot $K_I(t)$ vs. $a_{eff}(t)$, and obtain the dynamic crack growth resistance for the CDCB under test.

Step 9. Read the maximum value of K_I as the fracture toughness in MODE I for the CDCB, K_{IC}.

Appendix 2

Calibration Charts for Load Cells

4" Blade Load Cell for the Small Impact Machine

$y = 1.2506x - 0.0728$

$R^2 = 0.9883$

Dec. 4th 2000
Calibrated on INSTRON machine
Rate = 0.25 mm/min
Excitation = 6 V
Gain = 1000

voltage (V)

load (kN)
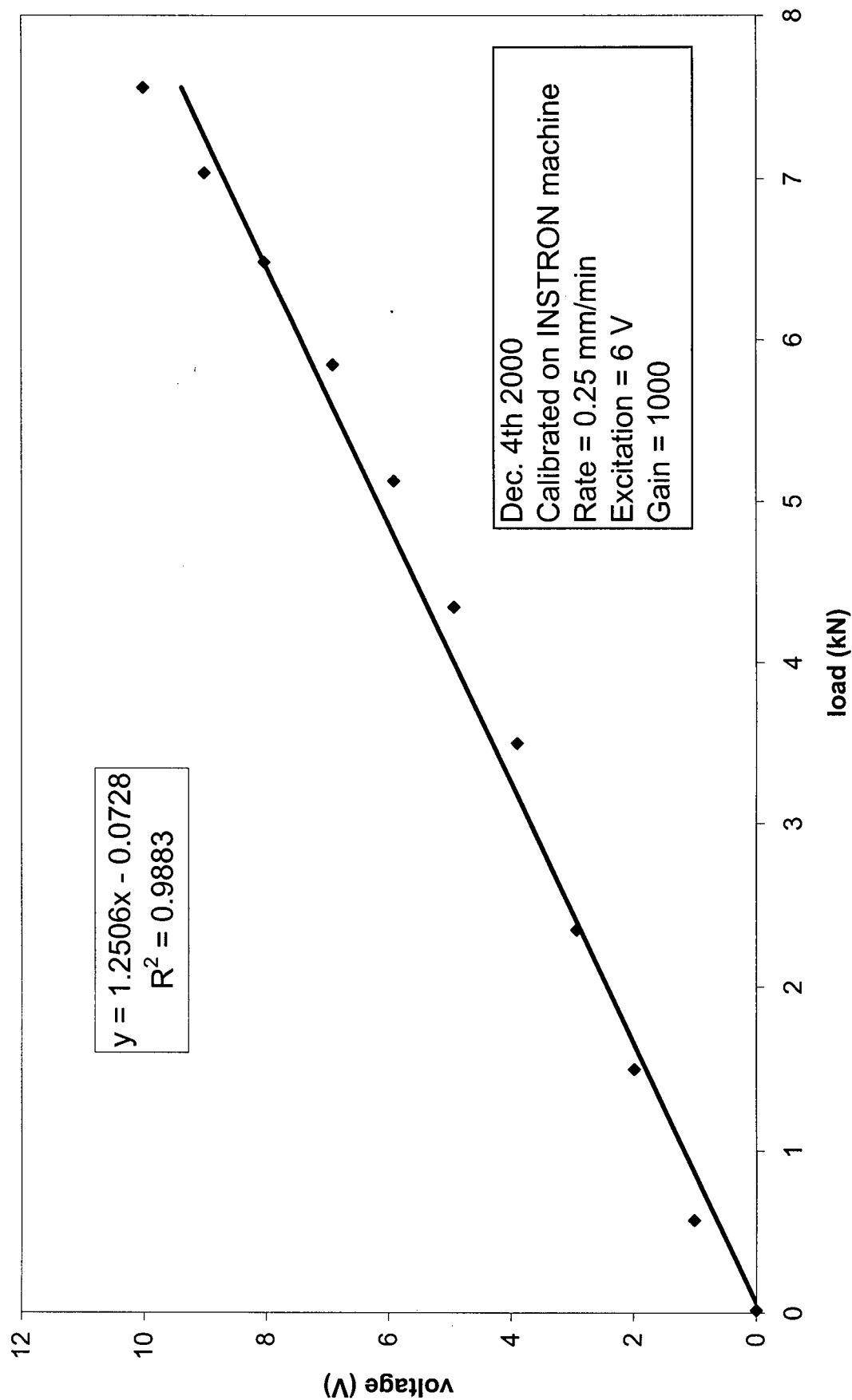
6" Blade Load Cell (Large and Medium Impact Machines)

$y = 10.032x + 0.2918$
$R^2 = 0.9993$

Dec. 16th 1999
Calibrated on INSTRON Machine
Rate = 0.25 mm/min
Excitation = 6V
Gain = 1000

load (kN)

Voltage (V)

Bolt Load Cell No. 2

$y = 6.5553x - 0.0221$
$R^2 = 1$

Nov. 22nd, 2000
Calibrated on INSTRON machine
Rate = 0.25 mm/min
Excitation = 6V DC
Gain = 1000

load (kN)

voltage (V)
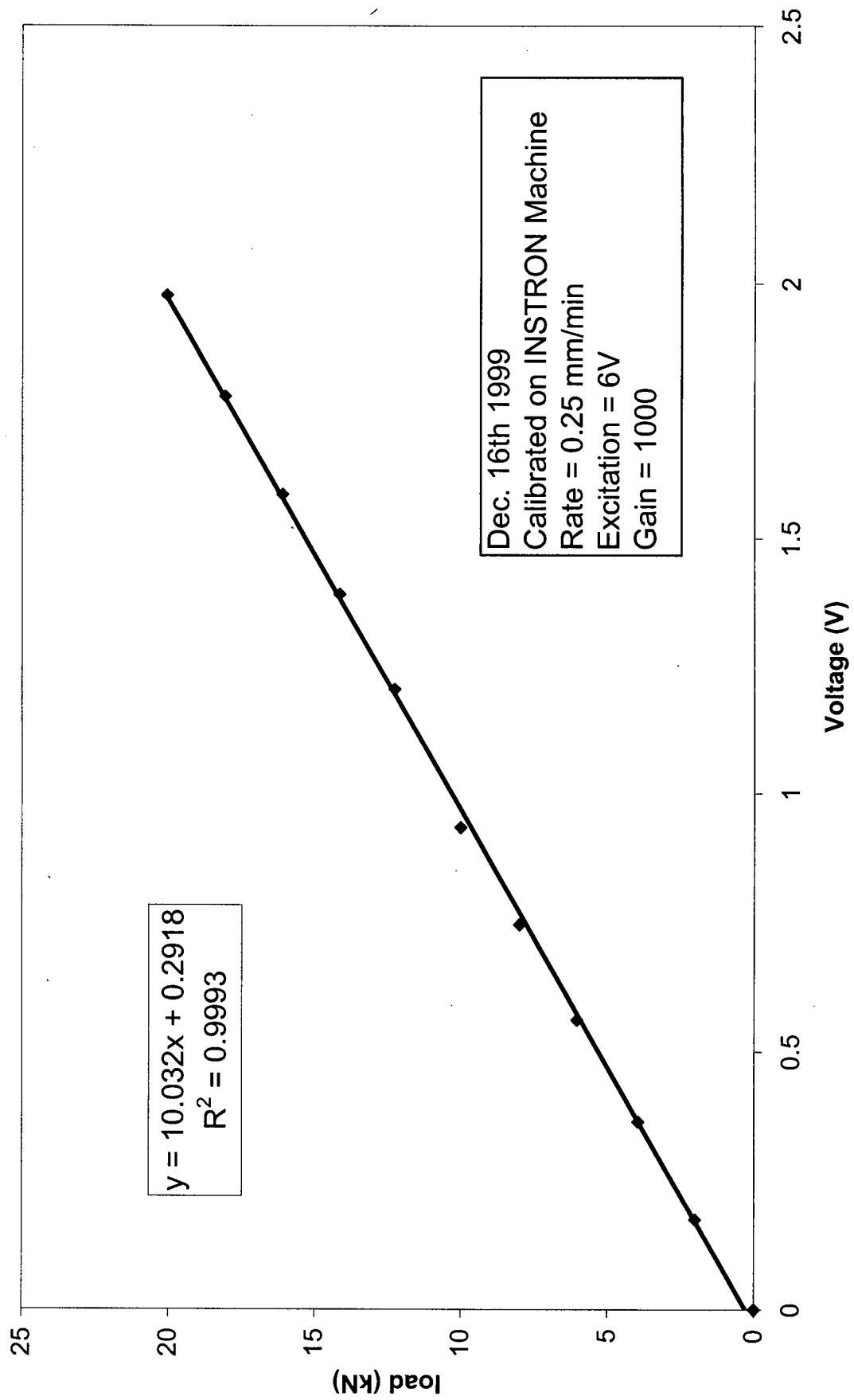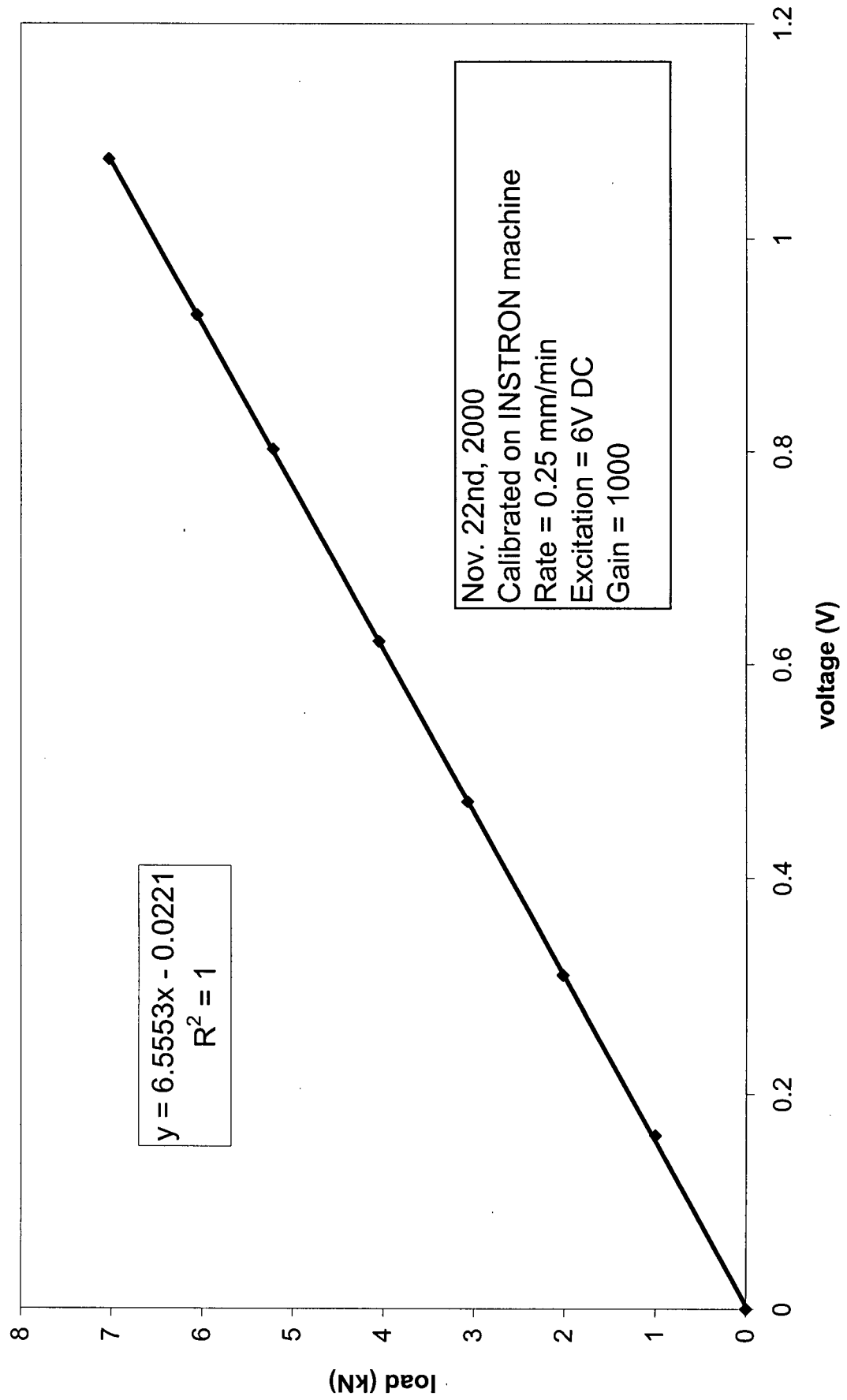
Bibliography

1.   Banthia, N., 'Fiber reinforced concrete: Present and the future', in Fiber Reinforced Concrete: Present and the Future, (Eds. N. Banthia, A. Bentur & A. Mufti), CSCE Montreal, Canada, Oct 1998, page 2.

2.   Bentur, A. and Mindess, S., 'Fiber reinforced cemetitious composites', Elsevier Applied Science, 1990, 449 pages

3.   Balaguru, P. N. and Shah, S. P., 'Fiber reinforced cement composites', McGraw Hill, 1992,.

4.   Banthia, N., Fiber reinforced concrete', Cement & Concrete: Science and Technology, (Ed. S.N. Ghosh et al.), ASI Publishers, India, 1991, pp. 288-320.

5.   Trottier, J-F and Mahoney, M, Innovative synthetic fibers', ACI Concrete International, Vol. 23, no. 6, Jun 2001, pp. 23-28.

6.   Banthia, N. and Armelin, H., 'A double anchored (DD) steel fiber for shotcrete', Proc. International Conf. on Eng. Developments in Shotcrete, Hobart, Tasmania, Apr 2-5, 2001, pp. 41-46.

7.   Naaman, A. E. and Sujivorakul, C., 'Pull-out mechanisms of twisted steel fibers embedded in concrete', Proc. International Conf. on Eng. Developments in Shotcrete, Hobart, Tasmania, Apr 2-5, 2001, pp. 197-204.

8.   Comite Euro-International du Beton (CEB), 'Concrete structures under impact and impulsive loading', Bulletin no. 187 1988, p. 3.6.

9.   Louw, J. M and Loedolff, M. J., 'RC cantilever column under lateral impact load: An experimental investigation', Proc: Conf. on Structures under Shock and Impact, Portsmouth, 1992, pp. 309-319.

10.   ASTM STP 563, 'Instrumented impact testing', Philadelphia, Jun 24-29, 1973.

11.   Grote, D. L., Park, S. W. and Zhou, M., 'Dynamic behaviour of concrete at high strain rates and pressures: I. Experimental characterization', Int. Journal of Impact Engineering, Vol. 25, 2001, pp. 869-886.

12. Kolsky, H., *'An investigation of the mechanical properties of materials at very high strain rates of loading'*, Proc. Phys. Soc. B, Vol. 62, 1949, pp. 676-699.

13. Ross, C. A., *'Review of strain rate effects in materials'*, Structures under extreme loading conditions, ASME Pressure Vessels and Piping Conf., Orlando, FL., 1997. pp. 255-262.

14. Tedesco, J. W., Ross, C. A. and Hughes, M. L., *'Load rate effects on concrete compressive strength'*, Structures Congress XII, Proc., Atlanta, GA., 1994, pp. 245-251.

15. Malvar, L. J. and Ross, C. A., *'Review of strain rate effects for concrete in tension'*, ACI Materials Journal, Vol. 95, no. 6, Nov-Dec 1998, pp. 735-739.

16. Tedesco, J. W., Ross, C. A. and Kuennen, S. T., *'Experimental and numerical analysis of high strain rate splitting tensile tests'*, ACI Materials Journal, Vol. 90, no. 2, Mar-Apr 1993, pp. 162-169.

17. Banthia, N. P. *'Impact resistance of concrete'*, Ph. D Thesis, The University of British Columbia, Vancouver, Canada, 1987.

18. Bentur, A., Mindess, S. and Banthia, N., *'Behaviour of reinforced concrete under impact: The effect of concrete strength'*, Publ. By Society for Experimental Mechanics Inc. Bethel, CT, 1987, pp. 449-458.

19. Sercombe, J., Ulm, F-J. and Toutlemonde, F., *'Viscous hardening plasticity for concrete in high rate dynamics'*, ASCE Journal of Engineering Mechanics, Vol. 124, no. 9, Sept 1998, pp. 1050-1057.

20. Banthia, N., Yan, C. and Sakai, K., *'Impact resistance of fiber reinforced concrete at sub-normal temperatures'*, Cement and Concrete Composites, Vol. 20, no. 5, 1998, 393-404.

21. Mindess, S., Banthia, N. Ritter, A. and Skalny, J. P., *Crack development in cementitious materials under impact loading'*, Mat. Res. Soc. Symp., Proc., Vol. 64, Cement-Based Composites: Strain Rate Effects on Fracture, (Eds. S. Mindess & S. P. Shah), 1985, pp.217-224.

22. Guo, Z. K., Kobayashi, A. S. and Hawkins, N. M., *'Dynamic mixed mode fracture of concrete'*, Int. Journal of Solids and Structures, Vol. 32, no. 17/18, 1995, pp. 2591-2607.

23. Chen, E. P. and Sih, G. C., *Transient response of cracks to impact loads'*, Mechanics of Fracture Vol. 4: Elastodynamic crack problems, 1977, pp. 1-58.

24. Cotterell, B., *'Fracture toughness and the Charpy V-notch impact tests'*, British Welding Journal, Vol. 9, no. 2, 1962, pp. 83-90.

25. Hibbert, A. P., *'Impact resistance of fiber concrete'*, Ph. D Thesis, The University of Surrey, UK, 1979.

26. Suaris, W. and Shah, S. P., *'Properties of concrete subjected to impact'*, Journal of Structural Eng., Proc. of ASCE, Vol. 109, no. ST7, 1983, pp. 1727-1741.

27. Saxton, H. J., Ireland, D. R. and Server, W. L., *'Analysis and control of inertial effects during instrumented impact testing'*, Instrumented Impact testing, ASTM STP 563, 1974, pp. 50-73.

28. Server, W. L., Walluaeert, R. A. and Sheckhard, J. W., *'Evaluation of current procedures of dynamic fracture toughness testing'*, Flaw Growth and Fracture, ASTM STP 631, 1977, pp. 446-461.

29. Gopalaratnam, V. S., Shah, S. P. and Reji, J., *'A modified instrumented Charpy test for cement based composites'*, Experimental Mechanics, Vol. 24, no. 2, 1984, pp. 102-111.

30. Banthia, N. P., Mindess, S., Bentur, A. and Pigeon, M., *'Impact testing of concrete using a drop-weight impact machine'*, Experimental Mechanics, Mar 1989, pp. 63-39.

31. Dowling, A. R. and Harding, J., In Proceedings, 1st HERF Conference, University of Denver, Vol. 2 1967, 7.3.1.

32. Harding, J., Metals Technologies, Vol. 4, 1977, page 6.

33. Harding, J, *'The effect of high strain rate on material properties'*, in Materials at High Strain Rates (Ed. T. Z. Blazynski), 1987, pp. 137-186.

34. Malvar, L. J., *'Review of static and dynamic properties of steel reinforcing bars'*, ACI Materials Journal, Vol. 95, no. 5, Sep-Oct, 1998, pp. 609-616.

35. Kawahara, W. A., Totten, J. T. and Korellis, J. S., *'Effects of temperature and strain rate on the nonlinear compressive mechanical behaviour of polypropylene'*, SANDIA Report: SAND89-8233, UC-13, 1989, pp. 3-39.

36. Nielsen, L.E., *'Mechanical properties of polymers and composites'*, Vol. 2, 1974, pp.313-320.

37. Williams, J. G., *'Fracture mechanics of polymers'*, Ellis Horwood Series in Eng. Sc., 1984, pp. 238-292.

38. Xu, T., Yu, J. and Jin, Z., *Effect of crystalline porphology on the impact behaviour of polypropylene'*, Materials and Design, Vol. 22, 2001, pp. 27-31.

39. Bartos, P., *'Review paper: Bond in fiber reinforced cements and concretes'*, The Int. Journal of Cement Composites, Vol. 3, no. 3, Aug 1981, pp.159-177.

40. Bentur, A., Wu, S.T., Banthia, N., Bagott, R., Hansen, W., Katz, A., Leung, C. K. Y., Li, V. C., Mobasher, B., Naaman, A. E., Robertson, R., Soroushian, P., Stang, H. and Taerwe, L. R., *'Fiber-matrix interfaces'*, RILEM Proc. 2nd Int. Workshop (HPFRCC 2) (Eds. A. E. Naaman & H. W. Reinhardt), 1995, pp. 149-192.

41. Maage, M., *'Interaction between steel fibers and cement based matrices'*, Materials and Structures, Res. and Testing (RILEM), Vol. 10, no. 59, 1977, pp. 297-301.

42. Hughes, B. P. and Fattuhi, N. I., *'Fiber bond strengths in cement and concrete'*, Magazine of Concrete Research, Vol. 27, no. 92, 1975, pp. 161-166.

43. Banthia, N. and Trottier, J-F., *'Concrete reinforced with deformed steel fibers, Part 1: Bond-slip mechanisms'*, ACI Materials Journal, Vol. 91, no. 5, Sep-Oct, 1994, pp. 435-459.

44. Banthia, N. and Trottier, J-F., *'Concrete reinforced with deformed steel fibers, Part 2: Toughnes characterization'*, ACI Materials Journal, Vol. 92, no. 2, Mar-Apr, 1995, pp. 146-154.

45. Rossi, P. and Chanvillard, G., *'New geometry of steel fiber for fiber reinforced concrete'*, HPFRCC, (Eds. H.W. Reinhardt and A.E. Naaman),1991 pp.129-139.

46. Dubey, A. and Banthia, N. *'Development of high-performance polypropylene fibers for fiber-reinforced concrete and shotcrete'*, Unpublished Technical Report, The University of British Columbia, 1997.

47. Chanvillard, G., and Aïtcin, P-C., *'Pull-out behaviour of corrugated steel fibers:Quantitative and statistical analysis'*, ACBM, 1996, pp. 28-41.

48. Gray, R. J., in Journal of Material Science, 1984, pp. 861-870.

49. Nammur, G. and Naaman, A. E., *'Bond stress model for fiber reinforced concrete based on bond stress-slip relationship'*, ACI Materials Journal, Vol. 86, no. 1 Jan-Feb, 1989, pp. 45-57.

50. Wang, Y., Li., V.C. and Backer, S., *'Analysis of synthetic fiber pullout from a cement matrix'*, Bonding in Cementitious Composites, Materials Research Society Symp. Proc. Vol. 114, 1987. pp. 159-174.

51.   Naaman, A. E. and Shah, S. P., *'Pullout mechanisms in steel fiber reinforced concrete'*, Journal of the Structural Division, ASCE, Aug 1976, pp. 1537-1548.

52.   Igarashi, S. I. And Kawamura, M., *'Effects of the addition of silica fume and fine aggregate on the fracture toughness for steel fiber-matrix interfacial zone'*, Proc. Fracture Processes in Concrete, Rock and Ceramics, (Eds. J.G.M. van Mier, J.G. Rots and A. Bekker), E & FN Spon, 1991, pp. 307-315.

53.   Wei, S., Mandel, J.A. and Said., S. *'Study of the interface strength in steel fiber reinforced cement-based composites'*, ACI Journal, vol. 83, no. 4, Jul-Aug 1986, pp. 597-605.

54.   Al-Khalaf, M. N., Page, C. L. and Ritchie, A.G.B., *'Effects of fiber surface composition on mechanical properties of steel fiber reiforced mortars'*, Cement and Concrete Research, Vol. 10, no. 1, 1980, pp. 71-77.

55.   Mayfield, B. and Zelly, B. M., *'Steel fiber treatment to improve bonds'*, Concrete, Vol. 7, no. 3, 1973, pp. 35-37.

56.   Banthia, N. and Trottier, J-F., *'Effects of curing temperature and early freezing on the pull-out resistance of steel fibers from a cementitious matrix'*, Cement and Concrete Research, Vol. 19, no. 5, 1989, pp. 727-736.

57.   Cox, H. L., *'The elasticity and strength of paper and other fibrous materials'*, Brit. Journal of Applied Physics, Vol. 3, Mar 1952, pp. 72-79.

58.   Chanvillard, G., *'Modeling the pullout of wire-drawn steel fibers'*, Cement and Concrete Research, Vol. 29, 1999, pp. 1027-1037.

59.   Pinchin, D. J. and Tabor, D., *'Interfacial phenomena in steel fiber reinforced cement II: Pull-out behaviour of steel wires'*, Cement and Concrete Research, Vol. 8, no. 2, Mar 1978, pp. 139-150.

60.   Ouyang, C., Pacios, A. and Shah, S. P., *'Pullout of inclined fibers from cementitious matrix'*, Journal of Engineering Mechanics, ASCE, Vol. 120, no. 12 Dec. 1994, pp. 2641-2659.

61.   Morrison, J. K., Shah, S. P. and Jenq, Y-S., *'Analysis of fiber debonding and pullout in composites'*, Journal of Engineering Mechanics, ASCE, Vol. 114, no. 2, 1988, pp. 277-294.

62.   Stang, H. and Shah, S. P. *'Fracture mechanical interpretation of the fiber/matrix debonding process in cmentitious composites'*, Fracture Toughness and Fracture Energy of Concrete, (Ed. F.H. Wittmann), 1986, pp. 513-523.

63. Dubey, A., *'Fiber reinforced concrete: Characterization of flexural toughness & some studies on fiber-matrix bond-slip interaction'*, Ph. D. Thesis, The University of British Columbia, 1999.

64. Mallikarjuna, M., Fafard, M. and Banthia, N. *'A new three-dimensional interface (contact) element for fiber pull-out behaviour in composites'*, Computers and Structures, Vol. 44, no. 4, 1992, pp. 753-764.

65. Li, C. Y. and Mobasher, B., *'Finite element simulation of fiber pullout toughnening in fiber reinforced cement based composites'*, ACBM, 1998, pp. 123-132.

66. Tu, L, Kruger, D., Wagener, J. B. and Carstens, P. A. B., *'Wettability of surface oxyfluorinated polypropylene fibers and its effects on interfacial bonding with cementitious matrix'*, Journal of Adhesion, Vol. 62, nos. 1-4, 1007, pp. 187-211.

67. Gokoz, U. and Naaman, A. E., *'Effect of strain rate on the pull-out behaviour of fibers in mortar'*, Int. Journal of Cement Composites and Light Weight Concrete, Vol.3, no. 3, 1981, pp. 187-202.

68. Banthia, N. and Trottier, J-F., *'Deformed steel fiber-cementitious matrix bond under impact'*, Cement and Concrete Research, Vol. 21, 1991, pp. 158-168.

69. Gray, R. J. and Johnston, C. D., *'The measurement of fiber-matrix interfacial bond strength in steel-fiber reinforced cementitious composites'*, Testing and Test Methods of Fiber Cement Composites, RILEM Symposium, 1978.

70. Kaadi, G. W., *'Behaviour of fiber-reinforced concrete under high rate tensile loading'*, MS Theis, The University of Illinois, Chicago, 1983.

71. Pacios, A., Ouyang, C. and Shah, S. P., *'Rate effect on interfacial response between fibers and matrix'*, Materials and Structures, RILEM, Vol. 28, 1995, pp. 83-91.

72. Gopalaratnam, V. S. and Shah, S. P., *'Properties of steel fiber reinforced concrete subjected to impact loading'*, Journal of ACI, Vol. 83, 1986, pp. 117-126.

73. Li, X, Lok, T. S., Zhao, P., Liu, D. and Lan, S., *'Methodology for the study of dynamic property of steel fiber reinforced concrete subjected to high strain rate'*, CONSEC '01, Proc., Vol. 1, (Eds. N. Banthia, K. Sakai & O.E. Gjørv, UBC, Vancouver, 2001, pp. 683-690.

74. Banthia, N., Mindess, S. and Bentur, A., *'Steel fiber reinforced concrete under impact'*, Int. Symp. On Fiber Reinforced Concrete, Madras, India, Dec 1987, pp. 4.29-4.39.

75. Bhargava, A. and Rehnstrom, A., *'Dynamic behaviour of polymer modified and fiber reinforced concrete'*, Cement and Conrete Research, Vol. 7, 1977, pp. 199-207.

76. Gupta, P., Banthia, N. and Yan, C., *'Fiber reinforced wet-mix shotcrete under impact'*, ASCE Journal of Materials, Vol. 12, no. 1, 2000, pp. 81-90.

77. Chanvillard, G., *'Characterization of fiber reinforced concrete mechanical properties: A review'*, BEFIB 2000, RILEM Proc. 15, (Eds. P. Rossi & G. Chanvillard), 2000, pp. 29-50.

78. Jenq, Y. S. and Shah, S. P., *'A two parameter fracture model for concrete'*, Journal of Engineering Mechanics, ASCE, Vol. 111, no. 4, 1985, pp. 1227-1241.

79. Jenq, Y. S. and Shah, S. P., *'Application of two parameter fracture model to concrete and fiber reinforced concrete'*, Fracture Toughness and Fracture Energy of Concrete, (Ed. F.H. Wittmann), 1986, pp. 499-512.

80. Armelin, H. and Banthia, N., *'Predicting the flexural postcracking performance of steel fiber reinforced concrete from the pullout of single fibers'*, ACI Materials Journal, Vol. 94, no. 1, Jan-Feb 1997, pp. 18-31.

81. Ziegeldorf, S., *'Phenomenological aspects of the fracture of concrete'*, Fracture Mechanics of Concrete, (Ed. F.H. Wittmann), 1983, pp. 31-41.

82. Broek, D., *'Elementary engineering fracture mechanics'*, Martinus Nijhoff Publishers, 1982.

83. Hillerborg, A., Modeer, M. and Petersson, P-E., *'Analysis of crack formation and crack growth in concrete by means of fracture mechanics and finite elements'*, Cement and Concrete Research, Vol. 6, 1976, 773-782.

84. Bažant, Z. P. and Oh, B. H., *'Crack band theory for fracture of concrete'*, Materials and Structures, RILEM, Vol. 16, no. 93, 1983, pp. 155-177.

85. Ouyang, C. and Shah, S. P., *'Geometry-dependent R-curve for quasi-brittle materials'*, Journal of American Ceramic Soc., Vol. 74, no. 11, 1991, pp. 2831-2836.

86. Cotterell, B. and Mai, Y-W., *'Crack growth resistance curve and size effect in the fracture of cement paste'*, Journal of Materials Science, Vol. 22, pp. 2734-2738.

87. Bažant, Z. P., *'Size effect in blunt fracture: concrete, rock, metal'*, Journal of Engineering Mechanics, ASCE, Vol. 110, 1984, pp. 518-535.

88. Baldie, K. D. and Pratt, P. L., *Crack growth in hardened cement paste'*, Materials Research Society Proc. Vol. 64, (Eds. S. Mindess & S.P. Shah), 1986, pp. 47-62.

89. Shah, S. P. and John, R., *'Rate-sensitivity of mode I and mode II fracture of concrete'*, Materials Research Society Proc. Vol. 64, (Eds. S. Mindess & S.P. Shah), 1986, pp. 21-38.

90. Belytschko, T., Organ, D. and Gerlach, C., *'Element-free Galerkin methods for dynamic fracture in concrete'*, Computer Methods in Applied Mechanics and Engineering, Vol. 187, 2000, pp. 385-399.

91. Shah, S. P., *'Concrete and fiber reinforced concrete subjected to impact loading'*, Materials Research Society Proc. Vol. 64, (Eds. S. Mindess & S.P. Shah), 1986, pp. 181-202.

92. Ansari, F. and Navalurkar, R. K., *'Fracture properties of fiber reinforced concrete subjected to impact loading'*, Materials Research Society Proc. Vol. 211, (Eds. S. Mindess & J.P. Skalny), 1991, pp. 159-168.

93. Sukontasukkul, P., Mindess, S., and Banthia, N., *'Fracture of fibre reinforced concrete notched beam under impact loading'*, BEFIB, 5th RILEM Symposium on Fibre Reinforced Concrete (FRC), (Eds. P. Rossi & G. Chanvillard), Lyon, France, September 2000, pp. 531-540.

94. Yon, J-H., Hawkins, N. M. and Kobayashi, A. S., *'Strain rate sensitivity of concrete mechanical properties'*, ACI Materials Journal, Mar-Apr, 1992, pp. 146-153.

95. Yon, J-H., Hawkins, N. M. and Kobayashi, A. S., *'Fracture process zone in dynamically loaded crack-line wedge-loaded, double-cantilever beam concrete specimens'*, ACI Materials Journal, Vol. 88, No. 5, Sept.-Oct., 1991, pp. 470-479.

96. Yon, J-H., *'Dynamic fracture of concrete'*, Ph. D Thesis, The University of Washington, Seattle, 1990.

97. Camacho, G. T. and Ortiz, M., *'Computational modelling of impact damage in brittle materials'*, Int. Journal of Solids and Structures, Vol. 33, nos. 20-22, 1996, pp. 2899-2938.

98. Ruiz, G., Pandolfi, A. and Ortiz, M., *'Three-dimensional cohesive modeling of dynamic mixed-mode fracture'*, Int. Journal for Numerical Methods in Engineering, Vol. 52, 2001, pp. 97-120.

99. Sierakowski, R. L., *'Dynamic effect in concrete materials'*, Application of Fracture Mechanics to Cementitious Materials, (Ed. S.P. Shah), NATO ASI Series, 1984, pp. 535-557.

100. Evans, A. G., *'Slow crack growth in brittle materials under dynamic conditions'*, Int. Journal fo Fracture, Vol. 10, 1974, pp. 251-259.

101. Nadeau, J. S., Bennett, R. and Fuller, E. R. (Jr), *'An explanation for the rate-of-loading and the duration-of-load effects in wood in terms of fracture mechanics'*, Journal of Materials Science, Vol. 17, (1982), pp. 2831-2840.

102. Reinhardt, H. W., *'Strain rate effects on the tensile strength of concrete as predicted by thermodynamic and fracture mechanics models'*, Materials Research Society, Proc. Vol. 64, (Eds. S. Mindess & S.P. Shah), 1985, pp. 1-14.

103. Zieliński, A. J., *'Model for tensile fracture of concrete at high rates of loading'*, Cement and Concrete Research, Vol. 14, no. 2, 1984, pp. 215-224.

104. Körmeling, H., *'A model for concrete under impact loading'*, Concrete Structures under Impact and Impulsive Loading, Proc. RILEM-CEB-IABSE-IASS-Interassociate Symp., 1982, pp. 125-133.

105. Malvar, L. J. and Ross, C. A., *'Review of strain rate effects for concrete in tension'*, ACI Materials Journal, Vol. 95, no. 6, pp. 735-773.

106. Walsh, P. F., *'Fracture of plain concrete'*,, Indian Concrete Journal, Vol. 46, no. 11, 1972, pp. 469-477.

107. Wright, P. J. F., *'The effect of the method of test on the flexural strength of concrete'*, Magazine of Concrete Research, Oct 1952, pp. 67-76.

108. Leicester, R. H., *'The size effect of notches'*, Proc., 2nd Australasian Conf. on Mechanics of Materials and Structures, Melbourne, 1969, pp. 4.1-4.20.

109. Bažant, Z. P. and Chen, E. P., *'Scaling of structural failure'*, Applied Mechanics Reviews, Vol. 50, 1997, pp. 593-627.

110. Weibull, W., *'A statistical theory of the strength of materials'*, Proc. of the Royal Swedish Institute for Engineering Research, Vol. 153, 1939, pp. 1-55.

111. Cotterell, B., Mai, Y. W. and Lam, K. Y., *'Statistics and size effect in cementitious materials'*, Cement and Concrete Research, Vol. 25, no. 2, 1995, pp. 408-416.

112. Carpinteri, A. and Chiaia, B., *'Multifractal scaling laws in the breaking behaviour of disordered materials'*, Chaos, Solitons & Fractals, Vol. 8, no. 2, 1997, pp. 135-150.

113. Carpinteri, A., Ferro, G. and Invernizzi, S., *'The nominal tensile strength of disordered materials: A statistical fracture mechanics approach'*, Engineering Fracture Mechanics, Vol. 58, nos. 5-6, 1997, pp. 421-435.

114. Arslan, A. and Ince, R., *'The neural network approximation to the size effect in fracture of cementitious materials'*, Engineering Fracture Mechanics, Vol. 54, no. 2, 1996, pp. 249-261.

115. Karihaloo, B. L., *'Size effect in shallow and deep notched quasi-brittle structures'*, Int. Journal of Fracture, Vol. 95, 1999, pp. 379-390.

116. Planas, J., Bažant, Z. P. and Jirásek, M., *'Reinterpretation of Karihaloo's size effect analysis for notched quasibrittle structures'*, Int. Jounral of Fracture, Vol. 111, 2001, pp. 17-28.

117. Bažant, Z. P. and Prat, P. C., *'Effect of temperature and humidity on fracture energy of concrete'*, ACI Materials Journal, Vol. 87, no. 4, Jul-Aug 1988, pp. 262-271.

118. Şener, S., *'Size effect tests of high strength concrete'*, Private Communication.

119. Gettu, R., Saldívar, H. and Kazemi, M. T., *'Implications of the size effect method for analyzing the fracture of concrete'*, Int. Journal of Solids & Structures, Vol. 35, nos. 31-32, 1998, pp. 4121-4132.

120. Bažant, Z. P. and Pfeiffer, P. A., *'Determination of fracture energy from size effect and brittleness number'*, ACI Materials Journal, Vol. 84, no. 6, Nov-Dec, 1987, pp. 463-480.

121. Perdikaris, P. C. and Romeo, A., *'Effect of size and compressive strength on the fracture energy of plain concrete'*, Proc. FRAMCOS, (Ed. Z.P. Bažant), 1992, pp. 550-555.

122. Mindess, S., *'The effect of specimen size on the fracture energy of concrete'*, Cement and Concrete Research, Vol. 14, 1984, pp. 431-436.

123. Li, V. C., Lin, Z. and Matsumoto, T., *'Influence of fiber bridging on structural size effect'*, Int. Journal of Solids and Structures, Vol. 35, no. 31-32, 1998, pp. 4223-4238.

124. Chen, L., *'Flexural toughness of fiber reinforced concrete'*, Ph. D thesis, The University of British Columbia, 1995.

125. Bažant, Z. P. and Gettu, R., *'Rate effects and load relaxation in static fracture of concrete'*, ACI Materials Journal, Vol. 89, no.5, Sep-Oct, 1992, pp. 456-468.

126. Wittmann, F. H., *'Influence of time on crack formation and failure of concrete'*, Application of Fracture Mechanics to Cementitious Composites, (Ed. S.P. Shah), NATO ASI Series, 1984, pp. 593-615.

127. Morton, J., *'Scaling of impact-loaded carbon-fiber composites'*, AIAA Journal, Vol. 26, no. 8, Aug, 1988, pp. 989-994.

128. Qian, Y., Swanson, S. R., Nuismer, R. J. and Bucinell, R. B., *'An experimental study of scaling rules for impact damage in fiber composites'*, Journal of Composite Materials, Vol. 24, May, 1990, pp. 559-570.

129. Liu, D., Raju, B. B. and Dang, X., *'Size effects on impact response of composite laminates'*, Int. Journal of Impact Engineering, Vol. 21, no. 10, 1998, pp. 837-854.

130. Richard, P., *'Reactive powder concrete: A new ultra-high-strength cementitious material'*, BHP 96, 4th Int. Symp. on Utilization of High-Strength/High-Performance Concrete, 1996.

131. Tjiptobroto, P. and Hansen, W., *'Flexural behaviour of ultra-high strength concrete with high volume fraction of discontinuous steel fibers'*, Ceramic Transactions (Ed. Sidney Mindess), Vol. 16, Advances in Cementitious Materials, 1991, pp. 581-601.

132. Bache, H. H., *'Densified cements ultra-fine particle-based materials'*, 2nd Int. Conf. on Superplasticizers in Concrete, Ottawa, 1981.

133. Bischoff, P. H. and Perry, S. H., *'Impact behaviour of plain concrete loaded in uniaxial compression'*, ASCE Journal of Eng. Mech., Vol. 121, no. 6, June, 1995, pp. 685-693.

134. Lee, T-F F., Shi, L-P and Yao, H-L, *'The comparison of structural concrete, self-compacting high-performance concrete and self-compacting reactive powder concrete under severe impact loading conditions'*, Concrete under Severe Conditions: Environment and Loading, (Eds. N. Banthia, K. Sakai and E. Gjørv), Vancouver B.C., June-17th –20th, 2001, pp. 676-682.

135. Aalborg Portland, *'In-house report for the Swedish Military'*, 44, Rørdalsvej, Dk-9100, 2000.

136. Wang, N., *Resistance of concrete railroad ties to impact loading'*, Ph.D Thesis, The University of British Columbia, Vancouver, May, 1996.

137. Banthia, N. and Sheng, J., *'Fracture toughness of micro-fiber reinforced cement composites'*, Cement and Concrete Composites, Vol. 18, 1996, pp. 251-269.

138. Banthia, N. P., Mindess, S. and Bentur, A., *'Energy balance in instrumented impact testing of plain concrete beams'*, Fracture of Concrete and Rock, (Eds. S.P. Shah & S.E. Swartz), SEM-RILEM Int. Conf., Jun 17-19, Houston, TX, USA, 1987, pp. 26-36.

139. ——, *'Mathcad 2001Professional: User's Guide with Reference Manual'*, Math Soft, Cambridge, MA., 2001.

140. Oh, B. H., and Chung, C. H., *'Fracture energy of concrete under static and dynamic'*, Fracture Toughness and Fracture Energy: Test Methods for Concrete and Rock, Int. Workshop on Fract. Toughness and Fract. Energy, Sendai, Japan, 1988, pp.

141. Banthia, N., Mindess, S. and Bentur, A., *'Impact behaviour of concrete beams'*, Materials and Structures RILEM, Vol. 20, 1987, pp. 293-302.

142. Mindess, S. and Yan, C., *Properties of plain and fiber reinforced concrete subjected to low velocity impact loading'*, Cement and Concrete Research, Vol. 23, no. 1, 1993, pp. 83-92.

143. Shah, S. P. and Rangan, B. V., *'Fiber reinforced concrete properties'*, ACI Journal Proc., Vol. 68, no. 2, Feb 1971, pp. 126-134.

144. Banthia, N. *'Study of some factors affecting the fiber-matrix bond in steel fiber reinforced concrete'*, Canadian Journal of Civil Engineering, Vol. 17, no. 4, 1990, pp. 610-620.

145. Banthia, N. and Trottier, J-F., *'Test methods for flexural toughness characterization of fiber-reinforced concrete: Some concerns and a Proposition'*, ACI Materials Journal, Vol. 92, no.1, Jan-Feb 1995, pp. 48-57.

146. Banthia, N., Mindess, S. and Trottier, J-F., *'Impact resistance of steel fiber-reinforced concrete'*, ACI Materials Journal, Vol. 93, no. 5, Sep-Oct 1996, pp. 472-479.

147. Bažant, Z. P. and Planas, J., *'Fracture and size effect in concrete and other quasibrittle materials'*, CRC Press, 1998.

148. Du, J., Yon, J-H., Hawkins, N. M. Arakawa, K. and Kobayashi, A. S., *'Fracture process zone for concrete dynamic loading'*, ACI Materials Journal, Vol. 89, no. 3, May-Jun, 1992, pp. 252-258.

149. Lambert, D. E. and Ross, C. A., *'Stain rate effects on dynamic fracture and strength'*, Int. Journal of Impact Engineering, Vol. 24, 2000, pp. 985-998.

150. Banthia, N. and Genois, I., *'Controlled crack growth tests for optimization of micro-fiber reinforced cement composites'*, ACI SP 201, Fracture Mechanics for Concrete Materials: Testing and Applications, 2001, pp. 55-73.

151. Mostovoy, S. Crosley, P.B. and Ripling, E. J., *'Use of crackline loaded specimens for measuring plane-strain fracture toughness'*, Journal of Materials, ASTM, Vol. 2, no. 3, 1967, pp. 661-681.

152. Srawley, J.E. and Gross, B., *'Stress intensity factors for crack line loaded edge-crack specimens'*, Materials Res. Stand., Vol. 7, no. 4, 1967, pp. 155-162.

153. Humar, J.L., *'Dynamics of structures'*, Prentice Hall, New Jersey, 1990, pp. 39-42.

154. Vanzi, S. Priest, A. and May, M. J., *'Influence of inertial loads on instrumented impact tests'*, Impact testing of metals, ASTM STP 466, 1970, pp. 165-180.

155. Loukili, A., Khelidj, A. and Richard, P, *'Hydration kinetics, change of relative humidity and autogenous shrinkage of ultra-high-strength concrete'*, Cement and Concrete Research, Vol. 29, 1999, pp. 577-584.

156. Andrade, M.C., Frias, M. and Aarup, B., *'Durability of ultra-high strength concrete: Compact Reinforced Composite'*, 4th Int. Symp. On Utilization of High-strength/High-performance Concrete, ENPC Press, Paris, 1996, pp. 529-534.

157. Dancygier, A. N. and Yankelevsky, D. Z., *'High strength concrete response to hard projectile impact'*, Int. Journal of Impact Engineering, Vol. 18, no. 6, 1996, pp. 583-599.

158. Luo, X., Sun, W. and Chan, S. Y. N., *'Characteristics of high performance steel fiber-reinforced concrete subject to high velocity impact'*, Cement and Concrete Res., Vol. 30, 2000, pp. 907-914.